

Physical Processes and Sediment Transport in Stormwater Wet Ponds and Constructed Wetlands

by

Sherif Salah Ahmed

A thesis submitted in partial fulfillment of the requirements for the degree of

Doctor of Philosophy

in

Water Resources Engineering

Department of Civil and Environmental Engineering
University of Alberta

© Sherif Salah Ahmed, 2023

Abstract

Wet ponds and wetlands can improve stormwater quality by removing sediment before being discharged into receiving water bodies. Despite a large amount of published information, their optimal design, operation, and management have not yet been determined due to the lack of adequately monitored sites over long periods that span a wide range of environmental conditions. In addition, performing computer modelling alone would provide a simplified picture of reality. As a result, a mixed problem-solving approach of a comprehensive two-year field monitoring program during the ice-free seasons between May and October in 2018 and 2019 and computer modelling investigations were carried out in two stormwater wet ponds and two constructed wetlands in Calgary, Alberta, Canada. Although stormwater wet ponds and wetlands are similar in many aspects, a wet pond has a greater portion of deep water zones, 2-3 m, while wetlands are dominated by shallower water and are often thoroughly and densely vegetated. The study aims to investigate the key factors affecting the water quality, physical processes, sediment transport and fate and the difference in the function of a wet pond and a wetland to point the direction for improved design and operation guidelines. First, field data were used to investigate thermal and chemical stratification in the ponds and wetlands as a fundamental physical process that may impact their water quality. Second, the field data supported the application of the Environmental Fluid Dynamics Code (EFDC) hydrodynamic model to simulate the physical processes and evaluate the hydraulic performance of one wet pond and one wetland. Finally, the sediment transport compartment of the EFDC model was applied to the calibrated hydrodynamic model to evaluate the current design and operation by predicting the annual mass of deposits and sediment removal efficiency. In addition, the model simulated different scenarios of permanent pool depth, thermal stratification, wind speed and vegetation design.

The field data showed that the wet ponds had vertical water temperature differences >1 °C for up to 83% of the time from May to October. In addition, salt-laden inflows from road deicing salts led to a significant densimetric stratification (i.e., at vertical density difference > 0.25 Kg/m³, equivalent to the density change in freshwater between 24 and 25 °C) for up to 96% of the time. Significant densimetric stratification was also thoroughly and intensely present in the wetlands for up to 79% of the time, in contrast to the assumption of urban wetlands being well-mixed. The stratification forced the runoff from the inlet to the outlet to move above or below the pycnocline, creating dead zones. Wind-induced surface currents in ponds/wetlands were insignificant, scaling at 0.3% of the wind speed. Strong densimetric stratification and low wind stress on the water surface caused anoxic conditions near the bed, potentially adversely affecting water quality and downstream aquatic communities. Hence, additional consideration of stratification is required when designing new stormwater wet ponds and constructed wetlands.

The hydrodynamic modelling in the current study simulated water depths, velocities, temperatures and salinities in a stormwater wet pond and a constructed wetland with reasonable accuracy. The calibrated/validated hydrodynamic models represent an essential step toward incorporating hydraulic complexity into sediment transport and fate to explore optimum design and operation guidelines for better sediment removal efficiency. The sediment transport compartment of the EFDC model revealed that sediment removal efficiency during individual inflow events varied between 70-100%. The fluctuation of removal efficiencies was investigated against inflow characteristics, sediment inflow load, vegetation design, wind, stratification, and others. For instance, the sediment removal efficiency was negatively correlated with the inflow duration at R^2 up to 0.71. Yet, the sediment removal efficiency was least sensitive to the inflow rate as the submerged berms efficiently dissipated the inflow momentum before transporting sediment to the

outlet. Furthermore, stratification significantly influenced the internal hydrodynamic behaviour and the movement of suspended particles in the water column, increasing or decreasing the sediment removal efficiency based on the inflow characteristics and interaction with variations in internal flow paths. The study models are promising tools for predicting sediment removal efficiency and optimizing design and operation by simulating various remediation options. Yet, coupled sediment transport and biogeochemical models are needed in future studies to predict the internal loading of the algal biomass and suspended matter.

Preface

This thesis is an original work by Sherif Ahmed under the supervision of Dr. David Z. Zhu and Mark R. Loewen. This study is a part of a collaborative research project by the Natural Sciences and Engineering Research Council of Canada (NSERC) and the City of Calgary, Water resources. It is presented in a paper format and consists of seven chapters.

Chapter 1 is a general introduction to the study's background, scope, and objectives.

Chapter 2 is the literature review with a special focus on the fundamentals of hydrodynamics, physical processes and sediment transport in urban stormwater wet ponds and constructed urban stormwater wetlands.

Chapters 3 to 7 are the main contents of this thesis.

Chapter 3 was published as: Ahmed, S.S., Loewen, M.R., Zhang, W., et al. (2022). Field Observations of Stratification in Stormwater Wet Ponds. *Journal of Environmental Management*, **322**, <https://doi.org/10.1016/j.jenvman.2022.115988>

Chapter 4 has been submitted as a journal manuscript: under review. Ahmed, S., Zhang, W., Loewen, M.R., et al. (2023). Stratification and its Consequences in Two Constructed Urban Stormwater Wetlands. *Science of The Total Environment*, Manuscript ID STOTEN-D-22-24906

Chapter 5 is currently being prepared as a journal manuscript.

Chapter 6 is currently being prepared as a journal manuscript.

Chapter 7 contains the general conclusions of this thesis and suggestions for future research on physical processes and sediment transport modelling.

I was responsible for the two-year field monitoring program, data analysis, computational modelling and manuscript composition. Drs. David Z. Zhu and Mark R. Loewen were the supervisory authors involved with concept formation, data analysis and manuscript composition. Dr. Wenming (William) Zhang contributed to the manuscript edits of Chapters 3 through 6. Dr. Bert van Duin and Mr. Khizar Mahmood facilitated data collection and contributed to manuscript edits of Chapters 3 through 6.

I also contributed to the following publications:

- ✓ **Ahmed, S.**, Ghobrial, T.R., Zhang, W., Zhu, D.Z., Loewen, M.R., Mahmood, K., and van Duin, B. (2019). Field Monitoring of Physical Processes in Stormwater Wet Ponds and Wetlands in Calgary, Alberta. 24th Canadian Hydrotechnical Specialty Conference, CSCE Annual Conference, Laval (Greater Montreal), QC, June 12 - 15, 2019, [Link to paper](#)

- ✓ Ghobrial, T.R., **Ahmed, S.**, Zhang, W., Zhu, D.Z., Loewen, M.R., Mahmood, K., and van Duin, B. (2019). Bottom Sediment Characteristics in Stormwater Ponds and Wetlands in Calgary, Alberta. 24th Canadian Hydrotechnical Specialty Conference, CSCE Annual Conference, Laval (Greater Montreal), QC, June 12 - 15, 2019. My role as co-author was to assist the author in collecting the data and presenting the results in figures using MATLAB code, [Link to paper](#)

Acknowledgement

First and foremost, I thank god for always being by my side; all good deeds are always because of his guidance. Second, I would like to dedicate this dissertation to the spirit of my beloved sister Shimaa (may her pure soul rest in pieces).

After that, I would like to express my sincere gratitude to my advisors, Prof. Dr. David Zhu and Prof. Dr. Mark Loewen, for offering me this excellent opportunity to pursue my doctoral degree and for giving me their guidance, continuous support and precious remarks. In addition, I sincerely thank Dr. Tadros Ghobrial and Dr. Wenming (William) Zhang for their invaluable input and the enormous amount of time and effort they dedicated to the work. Furthermore, I thank my colleagues Arlette Fernandez, Brendan Troitsky, and Shuntian Liang for their assistance in the fieldwork. I would also like to thank Bert van Duin, Khizar Mahmood, Chen Lei and others at the City of Calgary, Water Resources, for facilitating and securing our field program. I am also very grateful to Dr. Xing Fang (Auburn University), Dr. Kevin Devito, and Dr. Yuntong She for serving on the Ph.D. examining committee. Their insightful suggestions on this thesis are much appreciated. This research is being funded by The City of Calgary and the Natural Sciences and Engineering Research Council of Canada (NSERC) through a Collaborative Research and Development grant (CRDPJ 506201-16). This support is gratefully acknowledged.

Finally, this research could have never been completed without my family's continuous support, love, and encouragement. They have been a great inspiration to me. Therefore, I dedicated this dissertation to them, especially my mother, Mrs. Kawsar Abdel-Aziz, my father, Mr. Salah Zaky and my wife, Mrs. Yasmeen Ali. Last but not least, my extraordinary love goes to my lovely daughter, Shimaa, the most significant gift in my entire life.

Table of Contents

| | |
|---|------------|
| Abstract..... | ii |
| Preface..... | v |
| Acknowledgement..... | vii |
| List of Tables..... | xii |
| List of Figures..... | xv |
| 1. General introduction..... | 1 |
| 1.1 Research background and motivation..... | 1 |
| 1.2 Thesis outline..... | 3 |
| 2. Literature review..... | 5 |
| 2.1 Stormwater ponds..... | 5 |
| 2.2 Physical processes and hydrodynamic modelling in stormwater ponds..... | 6 |
| 2.3 Sediment transport and fate in stormwater ponds..... | 11 |
| 2.4 Knowledge gaps..... | 15 |
| 3. Field observations of stratification in stormwater wet ponds..... | 17 |
| 3.1 Introduction..... | 17 |
| 3.2 Study ponds and methods..... | 20 |
| 3.2.1 Study wet ponds..... | 20 |
| 3.2.2 Field measurement in the wet ponds..... | 21 |
| 3.2.3 Analysis methodology..... | 24 |
| 3.3 Results and discussion..... | 27 |

| | | |
|-----------|---|------------|
| 3.3.1 | Thermal and chemical stratification..... | 27 |
| 3.3.2 | Thermocline | 33 |
| 3.3.3 | Densimetric stratification..... | 35 |
| 3.3.4 | Wind-induced currents..... | 37 |
| 3.3.5 | Meteorological forcing and stratification..... | 38 |
| 3.4 | Conclusions..... | 41 |
| | Notation | 43 |
| 4. | Stratification and its consequences in two constructed urban stormwater wetlands ... | 61 |
| 4.1 | Introduction..... | 61 |
| 4.2 | Study wetlands and methods..... | 65 |
| 4.2.1 | Study wetlands | 65 |
| 4.2.2 | Field measurement in the wetlands..... | 67 |
| 4.2.3 | Analysis methodology..... | 69 |
| 4.3 | Results and discussion | 71 |
| 4.3.1 | Thermal stratification..... | 71 |
| 4.3.2 | Chemical stratification..... | 77 |
| 4.3.3 | Consequences of stratification | 81 |
| 4.3.4 | Hydrodynamics and mixing..... | 82 |
| 4.4 | Conclusions..... | 85 |
| | Notation | 88 |
| 5. | Hydrodynamic and physical processes modelling in an urban stormwater wet pond and a constructed wetland..... | 113 |
| 5.1 | Introduction..... | 113 |

| | | |
|-----------|---|------------|
| 5.2 | Methodology | 116 |
| 5.2.1 | Study sites and field measurements for the hydrodynamic modelling..... | 116 |
| 5.2.2 | Model description | 118 |
| 5.2.3 | Model setup..... | 121 |
| 5.2.4 | Model calibration | 123 |
| 5.2.5 | Hydraulic performance analysis..... | 127 |
| 5.3 | Results and discussion | 128 |
| 5.3.1 | Sensitivity analysis..... | 128 |
| 5.3.2 | Calibration and validation..... | 129 |
| 5.3.3 | Hydraulic performance | 135 |
| 5.3.4 | Design and operation guidelines | 136 |
| 5.4 | Conclusions..... | 139 |
| | Notation | 142 |
| 6. | Suspended sediment transport in an urban stormwater wet pond and a constructed wetland | 173 |
| 6.1 | Introduction..... | 173 |
| 6.2 | Materials and methods | 178 |
| 6.2.1 | Field measurements and data analysis of suspended sediment transport..... | 178 |
| 6.2.2 | Model description | 181 |
| 6.2.3 | Model implementation..... | 183 |
| 6.3 | Field measurement results..... | 184 |
| 6.4 | Model calibration and sensitivity analysis..... | 186 |
| 6.4.1 | Model calibration | 187 |
| 6.4.2 | Sensitivity analysis..... | 190 |

| | | |
|-----------|---|------------|
| 6.5 | Model application and discussion..... | 191 |
| 6.5.1 | Effect of lowering the operational NWL..... | 191 |
| 6.5.2 | Effect of inflow characteristics..... | 192 |
| 6.5.3 | Effect of vegetation..... | 193 |
| 6.5.4 | Effect of wind..... | 194 |
| 6.5.5 | Effect of stratification..... | 196 |
| 6.5.6 | Model limitation and future work..... | 198 |
| 6.6 | Conclusions..... | 199 |
| | Notation..... | 201 |
| 7. | Conclusions and recommendations..... | 234 |
| 7.1 | Conclusions..... | 234 |
| 7.2 | Recommendations..... | 237 |
| | Bibliography..... | 239 |

List of Tables

| | |
|---|----|
| Table 3-1 Study ponds’ physical and drainage characteristics. | 45 |
| Table 3-2 Summary of the seasonal statistics of the meteorologic data at the Auburn Bay and Cranston ponds between May and October in 2018 and 2019. W is the wind speed measured at 10 m above the ground, T_a is the air temperature, μ is the mean and σ is the standard deviation. | 46 |
| Table 3-3 Summary of the percentage of time (May- October) the water column was thermally stratified and strongly stratified along with the maximum top-bottom water temperature differences (ΔT). No data is available for Cranston in 2019 due to the draining of the pond for maintenance. | 47 |
| Table 3-4 Summary of the seasonal statistics (seasonal average \pm standard deviation) for the daily thermocline depth and strength and maximum seasonal thermocline strength at the two ponds between May and October in 2018 & 2019, except for the pink highlighted data for the Cranston pond in 2019, which are computed for July to October due to the draining of the pond in May 2019. N/A indicates missing data due to an equipment failure. | 48 |
| Table 3-5 Results of a linear regression analysis (slope and correlation coefficient R^2) using 2019 data between the absolute surface velocity (V) and wind speed (W) in the Auburn Bay and Cranston ponds at location V_m . All regressions are statistically significant at a 0.1% level ($p < 0.001$ using a t-test). | 49 |
| Table 3-6 Calculated wind durations in hours needed to mix two scenarios of $\Delta\rho$ and the maximum observed wind durations in the two study ponds. The highlighted cells are the calculated durations below the maximum observed durations in ponds when the wind can induce mixing. | 50 |
| Table 4-1. Study wetlands’ physical and drainage characteristics. | 90 |
| Table 4-2. Summary of the meteorologic data statistics at the wetlands between May and October in 2018 and 2019. T_a dry and T_a wet are the air temperature during zero rain depth and rain depth > 0.2 mm. μ is the mean. The first six rows of the table are mean values (μ). | 91 |
| Table 4-3. Average temperatures between May and October at the three monitored locations of the two wetlands. T_{wc} , T_s and T_a are the depth-averaged water temperature, water surface temperature, and air temperatures. | 92 |
| Table 4-4. Summary of the percentage of time between May and October when the water column in the two wetlands at the three locations IN, MID and OUT were thermally stratified by a vertical temperature gradient ($\Delta T/ \Delta z > 1$ °C) and ($\Delta T/ \Delta z < -1$ °C). | 93 |

| | |
|--|-----|
| Table 4-5. Summary of the statistics (mean \pm standard deviation) for the continuous temperature gradient at the two wetlands between May and October in 2018 & 2019..... | 94 |
| Table 4-6. Results of a linear regression analysis (slope and correlation coefficient R^2) between the absolute surface velocity (V) and wind speed (W) in the Royal Oak and Rocky Ridge wetlands at location V_m . All regressions are statistically significant at a 0.1% level ($p < 0.001$).95 | |
| Table 5-1 Physical and drainage characteristics of the study sites. | 146 |
| Table 5-2 Start and end dates of the model runs in Auburn Bay and Royal Oak..... | 147 |
| Table 5-3 Model parameters used in the vegetation submodel of the Royal Oak wetland | 148 |
| Table 5-4 Model parameters used in the simulations in Auburn Bay wet pond and Royal Oak wetland..... | 149 |
| Table 5-5 Root mean square errors (RMSE) between the observed data and modelled Water Surface Elevation (WSE), water temperature (T_w) and water salinity (S) in Auburn Bay and Royal Oak during calibration and validation runs. | 150 |
| Table 5-6 Comparison of the percentage of the time when the water columns at IN and OUT had vertical temperature difference > 1 °C (difference of near-surface and bottom temperatures) in the model and observation | 151 |
| Table 5-7 Comparison of the average near-surface and bottom temperature difference between the model and observation | 152 |
| Table 5-8 Simulated HRT, computed nominal residence time, t_n , and hydraulic efficiency, HRT/t_n results at both study sites in both years. | 153 |
| Table 5-9 The modelled duration as a percentage of the time between May and September 2019 when the water columns at IN, MID and OUT in Auburn Bay had vertical temperature differences > 1 °C for three NWL scenarios..... | 154 |
| Table 5-10 The modelled duration as a percentage of the time between May and September 2019 when the water columns in Auburn Bay and Royal Oak had vertical temperature differences > 1 °C for the scenario of inlets located at the NWL versus the base case scenario of inlets located at the bed..... | 155 |
| Table 5-11 The modelled duration as a percentage of the time between May and September 2019 when the water columns in Auburn Bay and Royal Oak had vertical temperature differences > 1 °C for three wind speed scenarios..... | 156 |
| Table 6-1 Information on the observed inflow/outflow events and the collected aliquots representativeness, defined as the inflow volume between the start and end of sampling to the total inflow volume during 11 rainfall events in the AB wet pond and the RO wetland. "√" | |

represents successful composite sampling, "√D" represents successful discrete sampling, and red highlighted cells labelled "X" represents unsuccessful sampling. 203

Table 6-2 The mean particle size distribution for the water samples collected at the inflow/ in-pond and outflow in the AB wet pond and the RO wetland. "n" are the number of water samples collected at each location. 204

Table 6-3 The characteristics of the bed sediment core samples collected in the AB wet pond and RO wetland. Locations I, M and O, where the bed sediment core samples were collected in AB and RO, are shown in Figure 6-1. 205

Table 6-4 Simulated and observed sediment removal efficiency (RE) for different sediment classes in the RO wetland 206

Table 6-5 Simulated and observed sediment removal efficiency (RE) for different sediment classes in the AB wet pond 207

Table 6-6 Root mean square errors (RMSE) between the simulated and measured TSS concentrations. Locations IN, MID and OUT are shown in Figure 5-1. 208

Table 6-7 Results of the sensitivity run for different sediment transport parameters..... 209

Table 6-8 Simulated sediment removal efficiency (RE) for different inflow events in the AB wet pond and RO wetland in 2019 210

List of Figures

Figure 3-1(a) Map of the City of Calgary, Canada, showing the location of the two study sites; (b) and (c) satellite images of the Auburn Bay and Cranston wet ponds, respectively. The red and yellow lines in (b) and (c) indicate the normal and high water level boundaries, respectively, and the white arrows show the location of inlets and outlets. Yellow pins labelled IN, MID, and OUT in each pond are in-pond monitoring locations near the inlet(s), middle, and outlet, respectively. Red dots labelled V_m and V_f are the deployment locations of the current profilers. [Images' source: Google Earth Pro 7.3.4.8248. (August 31, 2017). City of Calgary, Alberta, Canada. <<http://www.google.com/earth/index.html> > (Accessed January 22, 2022)]. [Map's source: Google Maps. Retrieved January 22, 2022, from <https://goo.gl/maps/22uRPTqEVXdxUaYSA>]

Figure 3-2 Time series measured in the Auburn Bay and Cranston ponds in 2018. (a,c) measured water depth (η) above NWL, 1041 m, (left axis) and rainfall intensity (right axis), (b) air temperature and water temperature at locations IN & OUT ~ 35 cm above the bed for IN_b & OUT_b and ~ 20 cm below the NWL for IN_s & OUT_s , IN_s time series ended on July 11 due to instruments battery depletion, (d) air temperature and water temperature at locations IN & OUT, ~35 cm from the bed for IN_b & OUT_b , and ~ 35 cm from the NWL for IN_s & OUT_s , and (e) water salinity at OUT ~ 40 cm from the bed for OUT_b , and ~ 80 cm from NWL for OUT_s . In July, the gap in data was when the instruments were retrieved for maintenance and battery change. 52

Figure 3-3 Time series measured in the Auburn Bay pond in 2019. (a) the measured water depth (η) above NWL, 1041m (left axis) and rainfall intensity (right axis), (b) air temperature and water temperature at locations IN & OUT, ~ 25 cm above the bed for IN_b & OUT_b , and ~ 10 cm below the NWL for IN_s & OUT_s , and (c) water salinity at locations IN & OUT above the bed by one-third of the water depth for $IN_{1/3}$ & $OUT_{1/3}$ and two-thirds of the water depth for $IN_{2/3}$ & $OUT_{2/3}$. $IN_{1/3}$ time series ended on September 15, and $OUT_{2/3}$ ended on October 8 due to instrument battery depletion. Data inside the zoomed-in plot show more details for May 6-10.. 54

Figure 3-4 Results from Auburn Bay (AB) and Cranston (CR) in 2018 of (a) surface-bed density differences $\Delta\rho$, and (b) the ratio of the freshwater surface-bed density difference and the in-pond water surface-bed density difference computed from the fortnightly profile data in 2018. 55

Figure 3-5 Water salinity profiles in the Auburn Bay pond in 2019 at locations (a) IN, (b) MID, and (c) OUT. 56

Figure 3-6 Results from the Auburn Bay pond in 2019 showing time series of (a) air temperature (left axis) and rain intensity (right axis), (b), (c) & (d) colour contour plots of vertical water temperature profiles versus geodetic elevation at IN, MID, and OUT, respectively, black circles are the average daily thermocline elevation, and (e) daily averaged thermocline strength time series at the three monitored locations. Gaps in data at the bottom of the water column at IN and OUT and at the top of the water column at MID are due to equipment loss. 57

Figure 3-7 Results from the Auburn Bay pond in 2019 showing time series of (a) the surface-bed density differences $\Delta\rho$ and (b) $\Delta\rho_0/\Delta\rho$, the ratio of the freshwater surface-bed density difference to the surface-bed density difference. The dashed and the solid horizontal lines in the plot (a) at 0.25 and 2 Kg/m³ are the thresholds between mixed, stratified, and strongly stratified water columns. The IN time series in plot (a) ended on September 15 due to a battery depletion of the conductivity sensor. 58

Figure 3-8 Water velocity vertical profiles at the Cranston pond, location V_f on (a) September 13, 2019, (b) September 15, 2019, and (c) September 20, 2019. Positive velocity flows towards the northeast or 60° clockwise from the north, and negative velocity flows towards the southwest or 240° clockwise from the north..... 59

Figure 3-9 Data measured at the Cranston pond, location V_m , between July 17 and 30, 2019, (a) air temperature and rain depth, (b) wind speed, (c) wind direction, (d) 2D vertical water temperature profiles at location IN, white circles are the thermocline height averaged over 3 hours, and (e) 2D absolute water velocity profiles versus height above the bed (h) at location V_m (left axis), and the black line is the pond averaged water column density gradient, $\Delta\rho/\Delta z$ (right axis)..... 60

Figure 4-1 (a) Map of the City of Calgary, Canada, showing the location of the Royal Oak (RO) and the Rocky Ridge (RR) wetlands; (b) and (c) satellite images of the Royal Oak and Rocky Ridge wetlands, respectively. The red and yellow lines in (b) and (c) indicate the normal and high water level boundaries, respectively. The white arrows show the location of inlets and outlets. Yellow pins labelled IN, MID, and OUT in each wetland are in-pond monitoring locations near the inlet(s), middle, and outlet. The red dot, V_m , is the velocity measurement location. [Images' source: Google Earth Pro 7.3.4.8248. (August 31, 2017). City of Calgary, Alberta, Canada. <<http://www.google.com/earth/index.html> > (Accessed January 22, 2022)]. [Map's source: Google Maps. Retrieved January 22, 2022, from <https://goo.gl/maps/22uRPTqEVXdxUaYSA>] 96

Figure 4-2 Boundaries and extents of the riparian and aquatic vegetation species at (a) the Royal Oak wetland and (b) the Rocky Ridge wetland. 97

Figure 4-3 Image from a game camera mounted at the weather station pole in (a) Rocky Ridge showing the dense submerged aquatic vegetation in July 2019, and in (b) Royal Oak showing the dense riparian vegetation at the outlet basin. The water level in the two images is the normal water level (NWL) 98

Figure 4-4 Results from the Royal Oak wetland in 2019 show time series of (a) air temperature (left axis) and rainfall intensity, I, (right axis), (b) measured water depth above the NWL, η , (c) vertical temperature gradients, $\Delta T/\Delta z$, (d), (e) & (f) colour contour plots of vertical water temperature profiles versus height above the bed at IN, MID, and OUT, respectively, numbers in boxes at the top of each colour contour plot and the black staircase lines represent days with continuous thermal stratification..... 99

| | |
|--|-----|
| Figure 4-5 Results from the Rocky Ridge wetland in 2019 similar to that in Figure 4-4. | 100 |
| Figure 4-6 Results from the Royal Oak wetland in 2018 similar to that in Figure 4-4. | 101 |
| Figure 4-7 Results from the Rocky Ridge wetland in 2018 similar to that in Figure 4-4. | 102 |
| Figure 4-8 Linear correlation of the daily averaged air temperature, T_a , and the vertical water temperature gradient, $\Delta T/\Delta z$, daily averaged and averaged over the entire wetland between May and August in 2018 and 2019 in (a) Royal Oak and (b) Rocky Ridge. | 103 |
| Figure 4-9. Linear correlation between the atmospheric instability, $T_s - T_a$, and the vertical water temperature gradient, $\Delta T/\Delta z$, daily averaged and averaged over the entire wetland between May and August in 2018 and 2019 in (a) Royal Oak and (b) Rocky Ridge. | 104 |
| Figure 4-10 Water salinity profiles in 2019 at locations (a) IN, (b) MID, (c) OUT in the Royal Oak wetland, and (d) IN, (e) MID, and (f) OUT of the Rocky Ridge wetland. | 105 |
| Figure 4-11 Results from the Royal Oak wetland in 2019 show time series of (a) the vertical density gradient $\Delta\rho/\Delta d$ at IN, MID and OUT and (b) $(\Delta\rho - \Delta\rho_o)/\Delta\rho$, the ratio of the real minus freshwater bed- surface density difference to the real bed- surface density difference. | 106 |
| Figure 4-12 Results from the Royal Oak wetland in 2019 show the time series of water salinity measured at IN 30cm above the bed for INb and 30 cm below the NWL for INs (left axis) and rainfall intensity (right axis). | 107 |
| Figure 4-13 Vertical density gradient $\Delta\rho/\Delta d$ at the Rocky Ridge wetland in 2019 at locations IN, MID and OUT for plots (a,b,c). | 108 |
| Figure 4-14 Data measured at the Rocky Ridge wetland in 2019, (a) air temperature (left axis) and rainfall intensity (right axis), (b) vertical density gradient $\Delta\rho/\Delta d$ at OUT, (c) colour contour plots of vertical water temperature profiles versus height above the bed at OUT, numbers in boxes at the top of the plot are days with continuous thermal stratification, and (d) colour contour plots of vertical dissolved Oxygen (DO) profiles versus height above the bed measured at h of 10, 37.5 and 62.5 cm at OUT. | 109 |
| Figure 4-15 DO profiles in the Royal Oak wetland at IN and OUT between July 5 and September 13, 2018. | 110 |
| Figure 4-16 Data measured at the Royal Oak and Rocky Ridge wetlands show (a,c) wind components (u_w : positive eastward, v_w : positive northward, and W_{abs} : magnitude) (left axis), and 5-minute interval rain depth (I, right axis), (b,d) water surface velocity, location V_m , (V_E : positive eastward, V_N : positive northward, and V_{abs} : magnitude). | 111 |
| Figure 4-17 Data measured at the Royal Oak wetland between July 24 and August 6, 2019, (a) wind components (u_w : positive eastward, v_w : positive northward, and W_{abs} : magnitude) (left | |

axis), and 5-minute interval rain depth (right axis), (b) water surface velocity (V_E : positive eastward, V_N : positive northward, and V_{abs} : magnitude), (c) solar radiation, (d) air temperature and water temperature at ~ 0 cm above the bed for MID_b and ~ 10 cm below the NWL for MID_s , and (e) vertical density gradient, location MID 112

Figure 5-1 Model domain of (a) the Auburn Bay wet pond and (b) the Royal Oak wetland, indicating their permanent pool depths in Auburn Bay and Royal Oak. Note that dark blue values are zero water depth only during the NWL condition, i.e., during no live storage or rainstorm inflow events. The outer boundaries of the model domains cover the inundated area during the design High Water Level (HWL), 1043m and 1266m in Auburn Bay and Royal Oak. Black arrows show the location of inlets and outlets. Black circles labelled IN, MID and OUT are in-pond monitoring locations near the inlet, middle, and outlet. Blue triangles are the deployment locations of the current meters. 157

Figure 5-2 Time series from the Auburn Bay weather station showing the meteorological data versus Julian day in 2019. Gray and black time series are the continuous 5-minute interval and the 24 hr running average data. 158

Figure 5-3 Two-dimensional RMSE contour plots of water temperature generated based on the calibration sensitivity analysis in Auburn Bay in (a,b,c) and Royal Oak in (d,e,f) for 16 scenarios of turbulent heat exchange coefficients and albedo in (a,d), 24 scenarios of light extinction coefficient at IN and albedo in (b,e), and 24 scenarios of light extinction coefficient at OUT and albedo in (c,f). Red arrows and dots are the scenarios for the calibration parameters with the least temperature RMSE. 159

Figure 5-4 Results from the Auburn Bay pond in 2019 at V_2 show time series of (a) wind speed (left axis) and 5-minute interval rain depth (right axis), (b) colour contour plots of observed absolute water velocity profiles versus range from the bed, and (c),(d) colour contour plots of modelled absolute water velocity profiles versus range from the bed using horizontal eddy viscosities of 0.05 and 0.1 m^2/s , respectively. 160

Figure 5-5 Time series of the modelled and measured water surface elevation in Auburn Bay (a,b) and Royal Oak (c,d) during calibration (a,c) and validation runs (b,d) in 2019 and 2018. The start date of each run is presented in Table 2. 161

Figure 5-6 Results from the Auburn Bay wet pond in 2019 show time series of (a) air temperature (left axis) and rain depth (I, right axis), (b), (c), (d) and (e) colour contour plots of observed and modelled vertical water temperature profiles versus height above the bed (z) at IN, and MID. The black circles are the average daily thermocline height above the bed (z). 162

Figure 5-7 Results from the Royal Oak wetland in 2019 show time series of (a) air temperature (left axis) and rain depth (I, right axis), (b), (c), (d) and (e) colour contour plots of observed and modelled vertical water temperature profiles versus height above the bed (z) at IN, and MID. The black circles are the average daily thermocline height above the bed (z). 163

Figure 5-8 Observed and modelled time-depth variations of the water salinity in Auburn in 2019 at IN and OUT and heights above the bed (z) of 1.0 and 2.0 m. The start date of the calibration run in 2019 is presented in Table 2. 164

Figure 5-9 Results from the Auburn Bay pond in 2019 show time series of (a) wind components (u_w : positive eastward, v_w : positive northward, and magnitude, W) (left axis) and 5-minute interval rain depth (right axis), (b), (c), (d) observed and modelled east, V_x , north, V_y , and absolute, V_{abs} , water surface velocity at V_2 , (e), and (f) colour contour plots of observed and modelled absolute water velocity profiles versus depth ratio (d/H) at V_2 165

Figure 5-10 Observed and modelled East velocity, V_x , profiles versus depth ratio (d/H) at V_2 on (a) June 8, 2019, and (b) June 13, 2019. 166

Figure 5-11 The vertical distribution of normalized Fourier norms between the modelled and observed currents at stations V_1 , V_2 and V_3 in Auburn Bay. 167

Figure 5-12 Results from the Royal Oak Wetland in 2019 show time series of (a) wind speed (left axis) and 5-minute interval rain depth (right axis), (b), (c) and (d) observed and modelled east, north and absolute water surface velocity at V_4 168

Figure 5-13 Results from the Auburn Bay wet pond model show time series of water depth at MID (left axis) and the modelled HRT averaged over the entire domain (right axis) in (a) 2019 and (b) 2018. Start dates are April 27 and June 15 in 2019 and 2018, respectively, Avg. HRT is the hydraulic residence time averaged over the entire model domain and run time. T_n is the nominal residence time in a given year. 169

Figure 5-14 Linear correlation of the water depth rise normalized to the average pond depth, $\Delta d/H$, and the corresponding reduction in the domain HRT normalized to the initial HRT, $\Delta HRT/HRT_o$ in (a) Auburn Bay and (b) Royal Oak. 170

Figure 5-15 Model grids indicating the modelled HRT averaged over the entire run time in 2019 for four scenarios of the observed wind speed consistently blowing from north, south, east and west in (a) Auburn Bay and (b) Royal Oak. 171

Figure 5-16 The wind rose plots in 2019 at (a) Auburn Bay and (b) Royal Oak, along with the HRT for the base case scenario for wind and scenarios of half and double the observed wind speed at (c) Auburn Bay and (d) Royal Oak. 172

Figure 6-1 Satellite images of the (a) AB wet pond and (b) RO wetland. The red lines indicate the normal water level boundaries, and the white arrows show the location of inlets and outlets. Yellow circles labelled I, M, and O are bed sediment cores sampling locations along the flow path near the inlet, middle, and outlet, respectively. Red arrows show the location of the branch pipes to the inlet in AB. [Images' source: Google Earth Pro 7.3.4.8248. (August 31, 2017). City of Calgary, Alberta, Canada. <<http://www.google.com/earth/index.html> > (Accessed January 22, 2022)]. 211

Figure 6-2 Time series measured in the AB wet pond showing the measured (a) inflow rate from branch pipe 1 (left axis) and rainfall depth (I, right axis), (b) inflow rate from branch pipe 2, and (c) outflow rate. Crosses in (a), (b), and (c) indicate the timing of the successfully collected aliquots. 212

Figure 6-3 Time series measured in the RO wetland showing the measured (a) inflow rate (left axis) and the rainfall depth (I, right axis), (b) outflow rate. Crosses in (a) and (b) indicate the timing of the successfully collected aliquots. 213

Figure 6-4 Linear correlation between TSS in (mg/L) and Turbidity level in (FNU) from water samples collected in the RO wetland. 214

Figure 6-5 Comparison of the simulated and measured outflow’s TSS concentration in the (a) RO wetland and (b) AB wet pond..... 215

Figure 6-6 Comparison of the model-predicted and measured water column TSS concentration in the RO wetland at locations (a) IN, (b) MID and (c) OUT. Locations are shown in Figure 5-1b. 216

Figure 6-7 Comparison of the model-predicted and measured water column TSS concentration in the AB wet pond at locations (a) IN, (b) MID and (c) OUT. Locations are shown in Figure 5-1a. 217

Figure 6-8 Time series of the measured chlorophyll-a concentration in (RFU) at mid-depth of location "OUT" in the AB wet pond. Location OUT in AB is shown in Figure 5-1a. 218

Figure 6-9 Pictures from the AB wet pond were taken on August 14, 2019..... 219

Figure 6-10 Model sensitivity results for different parameters in the RO wetland. 220

Figure 6-11 Model sensitivity results for different runs of the settling velocity of the cohesive sediment in AB. 221

Figure 6-12 Comparison of the model-predicted outflow’s TSS concentration in the AB wet pond between the base scenario and lowered NWL scenario..... 222

Figure 6-13 Comparison of the model-predicted TSS concentration using longitudinal sections from the inlet to the outlet in the AB wet pond on June 28 following the significant inflow event on June 27 during two scenarios of the operational NWL: (a) the base case scenario of NWL at 1041m and (b) the lowered NWL scenario at 1040m..... 223

Figure 6-14 Linear correlation between the TSS removal efficiency and inflow characteristics in the AB wet pond. 224

Figure 6-15 Linear correlation between the TSS removal efficiency and inflow characteristics in the RO wetland. 225

Figure 6-16 Modelling results during the highest observed wind speed in the AB wet pond on July 1, showing (a) a plan view for the surface velocity vector, (b) a longitudinal section from the inlet to the outlet for the velocity vector, and (c) a longitudinal section from the inlet to the outlet for the TSS concentration. 226

Figure 6-17 Modelling results during a significant wind event in the RO wetland on July 24, showing (a) a plan view for the surface velocity vector, (b) a longitudinal section from the inlet to the outlet for the vertical velocity vector, and (c) a longitudinal section from the inlet to the outlet for the TSS concentration. 227

Figure 6-18 Comparison of the model-predicted outflow’s TSS concentration under three wind speed scenarios: the observed wind speed, double and half the observed wind speed in the (a) AB wet pond and (b) RO wetland. 228

Figure 6-19 Modelling results in the AB wet pond on April 28 show longitudinal sections from the inlet to the outlet for the TSS concentration and velocity vector during the scenarios of (a) half the observed wind speed and (b) double the observed wind speed. 229

Figure 6-20 Modelling results in the AB wet pond on June 28 show longitudinal sections from the inlet to the outlet for the TSS concentration and velocity vector during the scenarios of (a) half the observed wind speed and (b) double the observed wind speed. 230

Figure 6-21 Comparison of the model-predicted outflow’s TSS concentration in the RO wetland between the base scenario and stratification scenarios. 231

Figure 6-22 Modelling results in the RO wetland during the peak outflow concentration following the April 27 inflow event, showing plan views for the depth average TSS concentration and longitudinal section from the inlet to the outlet for the TSS concentration for (a) the base case scenario, and (b) the stratification scenario. 232

Figure 6-23 Modelling results in the RO wetland during the peak outflow concentration following the May 16 inflow event, showing plan views for the depth average TSS concentration and longitudinal section from the inlet to the outlet for the TSS concentration for (a) the base case scenario, and (b) the stratification scenario. 233

1. General introduction

1.1 Research background and motivation

Stormwater sediments can cause many negative impacts on receiving water bodies. Studies have noted that excessive sediment, in addition to heavy metals, nutrients, and other pollutants absorbed into fine sediment particulates, can adversely impact aquatic life and fisheries, source waters for drinking water supplies, and recreational uses of receiving waters (USEPA 1999; Aryal and Lee, 2009; Jin and Ji 2015). As a result, several structural and nonstructural best management practices (BMPs) have been developed to reduce sediment and pollutant loadings in receiving waters. Stormwater wet ponds and constructed wetlands are structural best management practices used extensively for stormwater management (Gu et al., 2017). They commonly control excess runoff in urban areas by temporarily storing surface runoff and then releasing it to the downstream receiving waters and/or downstream conveyance systems at a controlled rate (Gu et al., 2017). Wet ponds and constructed wetlands can also improve the water quality of stormwater runoff by removing sediments, nutrients and other pollutants before being discharged into receiving water bodies (Song et al., 2013; Gu et al., 2017). However, the physical processes involved in transporting sediments and pollutants in stormwater facilities are complex and not yet fully understood (Gu et al., 2017).

The general objective of the study is to understand how existing stormwater facilities perform in improving stormwater quality and how to improve future designs and optimize their operations. Specific goals include understanding stormwater quality and processes such as deoxygenation of the water near the bed, transport, settling, and resuspension of sediments and filtration by vegetation in stormwater wet ponds and constructed wetlands as a function of the hydrodynamics

and physical processes. A deeper understanding of the sediment transport processes and the dominant factors controlling them will help predict the performance of existing facilities. This can lead to better operation of existing facilities and can assist in improving future designs for increasing sediment capture in ponds/wetlands.

Numerical modelling has been broadly developed and applied to investigate sediment dynamics in ponds, wetlands, and shallow lakes (Bentzen, 2009; Chung et al., 2009; Wang et al., 2013; Lv et al., 2013; Ji and Jin, 2014; Jin and Ji 2015; Liu et al. 2016). Yet, numerical modelling alone can never contain all the features of the real system (Jørgensen & Fath, 2011). As a result, a mixed approach of a comprehensive field monitoring program and computer modelling investigations has been carried out in the current study. A comprehensive 2-year field monitoring program was undertaken to continuously monitor two stormwater wet ponds and two constructed wetlands in Calgary, Alberta, during two ice-free seasons (May to October) in 2018 and 2019. The collected data from the field program were used to investigate the role of thermal and chemical stratifications and hydrodynamics in governing physical and water quality processes in the wet ponds and the constructed wetland. The field data also supported the application, calibration and validation of two 3D hydrodynamic Environmental Fluid Dynamics Code (EFDC) models in a stormwater wet pond and a constructed wetland. The validated hydrodynamic models were used to retrieve poorly known model parameters in the relatively small inland stormwater ponds and wetlands, such as horizontal eddy viscosity, turbulent heat exchange coefficient, albedo and light extinction coefficient. In addition, the hydrodynamic models investigated the hydraulic efficiency of the wet pond and the wetland and the governing physical processes. Then the sediment transport compartment of the EFDC was applied to the validated hydrodynamic models to simulate sediment transport in the stormwater wet pond and the constructed wetland. The sediment transport models

were used to assess the study pond and wetland's ability to remove sediments, investigate the governing factors that control sediment transport, and explore design/operation improvements to increase sediment capture.

1.2 Thesis outline

The structure of this thesis is organized as follows:

Chapter 2 is a comprehensive literature review of the physical processes in wet ponds and constructed wetlands and computational modelling of the hydrodynamics and sediment transport in wet ponds and constructed wetlands. The knowledge gaps are identified.

Chapter 3 reported a comprehensive two ice-free seasons (May – October) field monitoring program on the governing factors that control the strength and duration of thermal, chemical and densimetric stratification and the interaction between stratification and hydrodynamics in two stormwater wet ponds in Calgary, Canada.

Chapter 4 reported a comprehensive two ice-free seasons (May – October) field monitoring program on the stratification and hydrodynamics in two constructed urban stormwater wetlands in Calgary, Canada, with different inlet, outlet, morphometric and vegetation designs to understand the role of stratification in governing physical and water quality processes.

Chapter 5 proposes two well-calibrated and validated EFDC hydrodynamic models using the two ice-free seasons field data in one urban stormwater wet pond and one constructed urban stormwater wetland to explore their physical processes, evaluate their hydraulic performance and define appropriate remediation design strategies to ensure better hydraulic efficiency.

Chapter 6 reported the field investigation of suspended sediment transport and the application and validation of the sediment transport compartment of the EFDC based on the previously calibrated/validated hydrodynamic model in chapter 5 to investigate the key factors governing sediment transport and removal efficiencies in the study urban stormwater wet pond and constructed wetland.

Chapter 7 concludes the thesis and discusses the future directions of this research.

2. Literature review

In Calgary and Edmonton, stormwater runoff is a major sediment source to the Bow, Elbow and North Saskatchewan Rivers (AENV, 2007). In 2005, for instance, a water quality study found that 90% of sediment that had entered the Bow River from Calgary, Alberta, was from the stormwater system. In addition, thousands of tons of sediment in Edmonton are released to the North Saskatchewan River annually, with about 70% of this loading attributed to stormwater runoff (Shammaa et al., 2002). Stormwater sediments can cause many negative impacts on receiving water bodies (Megahan, 1999; USEPA, 1999; Bash et al., 2001; EPA, 2002; Vaze and Chiew, 2004; Aryal and Lee, 2009; Choi et al., 2012; Gatch, 2019; Nakhaei et al., 2021). For instance, high sediments increase turbidity, limit sunlight penetration, inhibit aquatic plants' growth (Aryal and Lee, 2009) and negatively impact water aesthetics (Nakhaei et al., 2021). Sedimentation can also clog fish spawning grounds resulting in a loss of fish habitat, and it can irritate fish gills and suffocate organisms if significant concentrations and durations occur (Megahan, 1999; Gatch, 2019). Additionally, pollutants adhering to sediments, including heavy metals, salt, hydrocarbons and high concentration of nutrients, pose direct threats to aquatic life and water quality (Bash et al. 2001; EPA 2002; Vaze and Chiew 2004; Choi et al. 2012). As a result, several structural and nonstructural best management practices (BMPs) have been developed over the years to reduce sediment loadings in receiving waters (City of Calgary, 2011).

2.1 Stormwater ponds

One of the structural BMPs being used extensively for stormwater management is stormwater ponds, including wet ponds and wetlands (City of Calgary, 2011). Wet ponds and constructed wetlands are permanent bodies of water with additional temporary storage provided above the

permanent or normal water level (NWL) for the stormwater runoff entering during rainfall events. After the rainstorm, the water level gradually recedes to its normal water level (City of Calgary, 2011). Although stormwater wet ponds and constructed wetlands are similar in many aspects, the main differences are the vegetation design and permanent depth (City of Calgary, 2011). Constructed wetlands are generally designed to resemble natural marshes, with emergent and submerged vegetation and shallower average depths than wet ponds, at depths less than the photic zone at ~ 1.5m (City of Calgary, 2011). Conversely, wet ponds have a greater portion of deep water zones, 2-3 m, and aquatic vegetation is concentrated along the ponds' perimeter (City of Calgary 2011). Ponds and wetlands can improve the water quality of stormwater runoff by removing sediments, nutrients and other pollutants before being discharged to the receiving water bodies (Song et al., 2013 & 2015; Gu et al., 2017). Many physical, biological, and chemical processes may contribute to pollutant removal in these ponds at any time. A permanent pool in a wet pond acts as a settling chamber where suspended particulate pollutants settle to the bottom (City of Calgary, 2011; Jin and Ji, 2015). Dissolved pollutants such as nutrients can be removed via sorption onto suspended sediment particles and uptake by vegetation and algae (Reed et al., 1995; Wand et al., 2007; City of Calgary, 2011; Schwammberger et al., 2020; Nakhaei et al., 2021). However, the processes involved in transporting sediments and pollutants in stormwater facilities are complex and not yet fully understood (Song et al., 2013 & 2015; Gu et al., 2017; Ji and Jin, 2020).

2.2 Physical processes and hydrodynamic modelling in stormwater ponds

Stratification in stormwater ponds is one of the key physical phenomena that affect hydrodynamics and hence the transport and fate of sediments and pollutants. Chemical stratification caused by

accumulated road deicing salts in northern climates is known to occur in stormwater management facilities (Marsalek 2003; Semandeni-Davies 2006; She et al. 2016). Common sodium chloride and calcium dichloride are the de-icers of choice in most parts of Canada and the US, with Canadian use estimated at nearly 5 million tonnes per year and Alberta use at ~ 200,000 tonnes per year as the sixth highest province in Canada using road salts (Environment Canada and Health Canada, 2001). Based on data from Marsalek et al. (2000), chemical stratification appears stronger than thermal stratification in urban stormwater ponds in the winter and early spring. Water column stability is a measure of the strength of thermal plus chemical stratification (Wetzel 2001). In general, water column stability is controlled by a combination of surface heating, horizontal advection, as well as the applied road salt and associated concentrations of dissolved solids (Marsalek et al. 2000). Precipitation may also affect water column stratification in stormwater wet ponds and constructed wetlands, as it can generate storm runoff that has collected heat from impervious surface areas (McEnroe et al. 2013). Thermal and chemical stratification in stormwater ponds may divide the water column into layers based on the density gradient and relative stability of the water column (Marsalek 2003; Semandeni-Davies 2006; McEnroe et al. 2013; Song et al. 2013; Chiandet & Xenopoulos 2016; She et al. 2016; Gu et al., 2017). Several recent studies of stormwater ponds have found that despite being small and very shallow, the water column was frequently observed to be stratified for extended periods (Song et al., 2013; McEnroe et al., 2013; Chiandet & Xenopoulos, 2016).

The hydrodynamics in stormwater ponds can be complex and dynamic because of the combined effect of inflow, wind, stratification, morphometry and vegetation design (Jenter and Schaffranek, 2003; Bentzen et al., 2008 and 2009; Gu et al., 2017; Ji and Jin, 2020; Rey et al., 2020 and 2021). In many studies, the wind was identified as the primary driver of the turbulent, three-dimensional

flow patterns in ponds (Andradóttir and Mortamet, 2016; Rey et al., 2020). For instance, high-resolution velocity measurements in a stormwater pond showed that despite the small size of stormwater ponds, wind-induced vertical and basin scale mixing creates a complex 3D flow (Andradóttir and Mortamet 2016). However, other studies suggested that flow patterns were driven primarily by the circulation between inlets and outlets (Shilton and Harrison, 2003; Passos et al., 2014). The vertical thermal and chemical stratification can also affect the hydrodynamics in ponds as they were reported to force the runoff from the inlet to the outlet to move above or below the thermocline, creating dead zones and reducing the pollutants' retention capacities (Novotny and Stefan, 2012; Yang et al., 2022). In addition, some studies reported that the speed and direction of the wind-induced currents change with depth in ponds and that wind forces are more efficiently transferred to the bottom of shallower ponds (Novotny and Stefan, 2012; Józsa, 2014; Andradóttir and Mortamet, 2016). Although wind forces were reported to transfer momentum more efficiently to the bottom of shallower water bodies with a depth of $< 2\text{m}$ (Józsa, 2014; Andradóttir and Mortamet, 2016), the flow resistance caused by the submerged/emergent aquatic vegetation in wetlands can significantly reduce the flow velocity and change the flow pattern (Jin and Ji, 2015; Gu et al., 2017). Hence, in slowly flowing wetlands, thermally-driven convection can be the dominant mixing mechanism (Jenter and Schaffranek, 2003). In addition, wetland vegetation contributes to the physical processes by altering light and water temperature (Chimney et al. 2006).

The complex flow fields in stormwater ponds need to be modelled realistically to evaluate the hydraulic performance of ponds and wetlands and define appropriate remediation design strategies to ensure desirable water quality. Several previous attempts have used two-dimensional (2D) models to simulate the hydrodynamics in stormwater ponds (e.g. German et al. 2003; Gharabaghi et al. 2006; Torres et al. 2008). However, there is a growing consensus that the complex flow fields

created by the wind and submerged and emergent vegetation and the strong vertical stratification can only be modelled realistically with a three-dimensional model (3D) (German et al. 2003; Bentzen et al. 2008, 2009; Hart et al. 2014; Nakhaei et al., 2019). In one of the first studies involving the application of 3D hydrodynamic models to stormwater ponds, Shaw et al. (1997) used the 3D finite-volume hydrodynamic commercial software package PHOENICS to perform steady-state simulations of flows in a stormwater pond located in Kingston, Ontario. Analysis of field data and computer simulations revealed that the pond's horizontal and vertical flow patterns were very complex and dynamic because of the combined effects of wind stress on the water surface and inflow momentum. Bentzen et al. (2008 and 2009) applied the 3D computational fluid dynamics (CFD) model MIKE3 to a stormwater pond in the northern part of Denmark. They concluded that wind-induced flows in shallow stormwater ponds are the dominant transport mechanism and that short-circuiting increased exponentially with wind speed. Nakhaei et al. (2019) applied the 3D hydrodynamic and biogeochemical model, ELCOM, to three stormwater ponds in the City of Edmonton. They could not accurately simulate water temperature and thermocline depth in densely vegetated areas. As a result, they recommended applying vegetated flow models for hydrodynamic modelling in stormwater wetlands. These studies clearly demonstrated that 3D models are required to accurately simulate the complex temporal and spatial variations in the flows that occur in stormwater ponds.

The current study uses the EFDC+ software based on the Environmental Fluid Dynamics Code (EFDC) developed in the late 1980s by Dr. John M. Hamrick (<https://www.eemodelingsystem.com/ee-modeling-system/efdc-plus/overview>). The model is a general-purpose modelling package for simulating 3D flow, sediment transport, and chemical fate and transport in surface water (Hamrick 1992; Hamrick and Wu 1997). The EFDC model was

initially developed at the Virginia Institute of Marine Science for estuarine and coastal applications and is a public domain, open-source, surface water modelling system that can be downloaded at <https://www.epa.gov/exposure-assessment-models/efdc>. It has been extensively tested and documented in more than 100 modelling studies, including lakes, reservoirs, and wetlands (e.g., Jin et al., 2000, Arifin et al., 2016; Gong et al., 2016; Shin et al., 2019; Dong et al., 2019; Chen et al., 2020; Ji and Jin, 2020). In addition, the model has been shown to accurately simulate the dynamics of water surface elevations, velocities, temperatures, water quality and submerged aquatic vegetation from large natural systems, such as Lake Okeechobee, Lake Ontario and Lake Arendsee (Jin and Ji 2004, 2005; Ji and Jin 2006; Jin et al., 2007; Arifin et al., 2016; Dong et al., 2019) to smaller wetlands (e.g., Ji and Jin 2020). However, it does not appear that it has been previously applied to an urban stormwater wet pond and an urban constructed wetland as in the present application.

Recent applications of the hydrodynamic compartment of the EFDC model include a 3D hydrodynamic and heat transport model for Lake Okeechobee developed by Jin and Hamrick (2000), which showed that the model reproduced general observed trends and short-term fluctuations. They concluded that adding wind-wave and vegetation resistance algorithms to the model may improve the simulation accuracy. The hydrodynamic, sediment and water quality modules of the EFDC were used in St. Lucie Estuary and Indian River Lagoon (Ji et al. 2007; Wan et al. 2012). This study indicated that stratification and circulation induced by freshwater inflows may contribute significantly to bottom water hypoxia in the estuary. The integrated 3D hydrodynamic, sediment transport, water quality, and submerged aquatic vegetation Lake Okeechobee Environmental Model (LOEM) was developed within the Environmental Fluid Dynamics Code (EFDC) framework. The LOEM model was used for Lake Okeechobee to

simulate water surface elevations, velocities, temperatures, water quality and submerged aquatic vegetation (Jin and Ji 2004, 2005; Ji and Jin 2006; Jin et al. 2007). Based on the calibration results, the authors concluded that the model simulates water surface elevations, velocities, and temperatures with reasonable accuracy and that the model's heat transport and turbulence closure schemes behave as expected with regard to water column stratification and mixing. The submerged aquatic vegetation model could represent the spatial and temporal variations of the aquatic vegetation in the lake well. In the past seven years, the LOEM-CW model, modified from the EFDC code, has been used to simulate hydrodynamics and transport processes in the constructed wetland environment (Jin and Ji 2015; Jin and Ji 2020). The hydrodynamic and sediment model of LOEM-CW was applied to Stormwater Treatment Areas (STAs) Cells 3A and 3B in South Florida. It was shown that the flow pattern is primarily driven by rain and inflows/outflows. The flow resistance caused by the submerged/emergent aquatic vegetation was important in reducing the flow velocity and changing the flow pattern (Jin and Ji 2015).

2.3 Sediment transport and fate in stormwater ponds

The proportion of the incoming sediment that is removed (i.e., removal efficiency or trap efficiency) is one of the most critical properties of stormwater ponds. The Alberta guideline (AENV 2001) calls for removing a minimum of 85% of sediment with a particle size of 75 μm or greater. In Ontario, the facilities are required to meet the water quality objectives of the long-term average removal of 80, 70 and 60% of suspended solids in the total runoff volume for enhanced, normal and basic protection levels, respectively (OMOE 2003). The City of Calgary has mandated the removal of a minimum of 85% of total suspended solids (TSS) for particle sizes greater than or equal to 50 μm (City of Calgary 2011). Data from the 2017 international stormwater BMP

database were used to compute removal efficiencies for various pollutants, including suspended sediment in stormwater ponds and constructed wetlands (WWEI & GCI, 2017). The median removal efficiencies of TSS were 75% and 55% in stormwater wet ponds and constructed wetlands, respectively. These indicate that, generally, ponds perform better than wetlands. What may not be evident from the median values is the widely variable removal efficiencies reported in the literature for commonly used stormwater BMPs. For example, in a study by Birch et al. (2006), TSS in stormwater entering the stormwater ponds was highly variable, resulting in significant variations in removal efficiencies (range -12% to 93%; mean: 40%). The high intra- and inter-event variability of the TSS concentrations in stormwater influent and effluent resulted in reduced predictability of the overall removal efficiency of the facilities.

Knowledge of sediment fate (i.e. transport, deposition, and resuspension) in stormwater ponds and constructed wetlands is essential to predicting and managing the cumulative effect of sediment loadings to receiving water bodies. Key considerations, including physical particle characteristics, water salinity (e.g., from road deicing salts) and density stratification in ponds/wetlands, wind effects, pond geometries, and inflow/outflow configurations will all affect sediment fate (Marsalek 2003; Bentzen et al. 2008; Novotny et al. 2008; Song et al. 2013; Gu et al., 2017). These key factors should be properly represented in numerical models used to evaluate the performance and operation of stormwater ponds (Takamatsu et al., 2010; Gu, 2017). For instance, the flux of bed sediment resuspension and deposition can be calculated using the concept of flow-induced bed shear stress (Aalderink et al. 1985). In this respect, the characterization of sediments in cohesive and non-cohesive fractions is necessary (Bloesch 1994). On the other hand, parameters such as grain size, shape and density and the characteristics of the ambient medium should govern the settling velocity of suspended particles (Gu et al., 2017; Nasiha et al., 2018). Analysis of the field

data and computer simulations by Shaw et al. (1997) revealed that the shear velocities associated with wind-generated currents in stormwater ponds may be sufficiently large to prevent particle settling and, in extreme cases, to cause resuspension of deposited and contaminated sediment. Higher flow rates at an inlet will cause particles to move a greater distance before settling (Gu et al., 2017). The resuspension of deposited sediment and the tendency toward short-circuiting occur mainly during larger influent flow rates (Gu et al. 2017). The physical interactions between the flow and aquatic vegetation in wetlands also need to be incorporated into the models to account for sediment filtration by vegetation (Wakelin et al., 2003, Hart et al., 2014; Ji and Jin, 2020). Sediment filtration by vegetation is an important factor governing sediment transport and deposition in stormwater wetlands. Sediment transport and deposition through the filter are usually affected by the flow field within the filter area, sediment concentration and characteristics (e.g., particle size, fall velocity and sediment density), vegetation type and density (Mun˜oz-Carpna 1999).

The suitability of widely used 3D sediment transport computer models such as the Environmental Fluid Dynamics Code (EFDC), Water Quality Analysis Simulation Program (WASP), MIKE3, and Delft-3D for application in stormwater ponds and constructed wetlands has been assessed. Some relative strengths and weaknesses of the models have been drawn from their respective literature and from reviews by Anagnostou et al. (2017) and Troitsky et al. (2019). For instance, the WASP model performs poorly with mixing zones and settling/floating particles, thus, is often coupled with a more robust hydrodynamic model (Troitsky et al. 2019). In addition, WASP includes oversimplified sediment flux calculation, and the sediment transport processes are unrelated to shear stress (Anagnostou et al. 2017). MIKE3 cannot separate the total sediment load into bedload and suspended load (MIKE 2023). The delft-3D model is primarily a river and estuary

management model and has limited usage with wetlands and wet ponds (Troitsky et al. 2019). As a result, the EFDC model endorsed by the Alberta Government was the most relevant for our study because it was recently used with case studies similar to ours, including wetlands and shallow lakes (Liu et al., 2015; Jin and Ji, 2015; Gong et al., 2016; Ji and Jin, 2020). In addition, it can simulate cohesive and non-cohesive sediment transport and separate the non-cohesive sediment transport into bed load and suspended load (DSI 2022).

First, the hydrodynamic model of the EFDC+ software predicts water depth, temperature, salinity and velocity. Then the sediment transport model uses the hydrodynamic model results to calculate the settling of suspended sediment, resuspension of bottom sediments, and bed load movement of non-cohesive sediments (DSI 2022). Recent applications of sediment transport modelling using the EFDC include the three-dimensional hydrodynamic and sediment transport modelling in the Yuan-Yang lake (YYL) in the north-central region of Taiwan by Liu et al. (2015). This study used field-observed data to determine poorly known model parameters such as sediment settling velocity and resuspension rate. Sensitivity analysis indicated that the settling velocity is the most sensitive parameter to the suspended sediment concentration. The model was also used to probe the lake's mean current and suspended sediment distribution. The hydrodynamic and sediment model of LOEM-CW, modified from the EFDC code, revealed that the flow resistance caused by the submerged/emergent aquatic vegetation in stormwater treatment wetlands in South Florida significantly reduced the flow velocity and changed the flow pattern, which helped increase sediment settling (Jin and Ji 2015). The hydrodynamic and sediment transport modules of the EFDC were also used by Shin et al. (2019) as a receiving water-body model. The EFDC model was coupled with a watershed loading model, Soil and Water Assessment Tool (SWAT). The

modelling framework in this study was applied to predict the spatial distributions of sediment depositions in an agricultural reservoir and quantify their uncertainty.

2.4 Knowledge gaps

In general, knowledge gaps about physical processes and sediment transport in stormwater wet ponds and constructed wetlands were identified as follows:

- 1) The role of thermal and chemical stratifications in governing water quality processes in stormwater ponds is not fully understood. This is partly due to the lack of detailed field measurements of sufficient governing parameters over periods that span a wide range of environmental conditions.
- 2) The knowledge of the complex and dynamic hydrodynamics in stormwater ponds is still limited due to a lack of reliable and continuous field observations focusing on the strength and duration of thermal and chemical stratification and continuous velocity measurements at different locations in stormwater ponds.
- 3) The optimal design, operation and management of stormwater ponds have not yet been determined due to the lack of adequately monitored sites over long periods that span many environmental conditions.
- 4) The EFDC model has been shown to accurately simulate the dynamics of water surface elevations, velocities, temperatures, water quality and submerged aquatic vegetation from large natural systems, such as Lake Okeechobee, Lake Ontario and Lake Arendsee (Jin and Ji 2004, 2005; Ji and Jin 2006; Jin et al., 2007; Arifin et al., 2016; Dong et al., 2019) to smaller wetlands (e.g., Ji and Jin 2020). However, it does not appear that it has been

previously applied to an urban stormwater wet pond and an urban constructed wetland for extended periods with extensive data sets for model calibration and verification as in the present application.

3. Field observations of stratification in stormwater wet ponds*

3.1 Introduction

Stormwater wet ponds are commonly used to control excess runoff in urban areas by temporarily storing surface runoff and then releasing it to the downstream stormwater network and/or recipient water body at a controlled rate to reduce the risk of downstream flooding. Ponds can also improve the water quality of stormwater runoff by removing or transforming pollutants prior to release downstream. Many physical, biological, and chemical processes may contribute to pollutant removal at any given time in these ponds. A permanent pool in a wet pond acts as a settling chamber where suspended particulate pollutants settle to the bottom. Dissolved pollutants such as nutrients can be removed via sorption onto suspended sediment particles and uptake by vegetation and algae (Schwammberger et al., 2020). However, the processes involved in transporting sediments and pollutants in stormwater facilities are complex and not yet fully understood (Song et al., 2013 & 2015).

Stratification in stormwater wet ponds is one of the key physical phenomena that affect hydrodynamics and hence the transport and fate of sediments and pollutants. Previous studies of stormwater wet ponds have shown that despite being small and shallow (typically 2-3 m), the water column can be stratified frequently and for extended periods, which inhibits vertical mixing and affects pond hydrodynamics and water quality (Bentzen et al., 2008; Marsalek, 2003; McEnroe et al., 2013; Novotny et al., 2008; Rey et al., 2021; Song et al., 2013). Thermal and chemical

* The content of this chapter has been published as: Ahmed, S.S., Loewen, M.R., Zhang, W., et al. (2022). Field Observations of Stratification in Stormwater Wet Ponds. *Journal of Environmental Management*, **322**, <https://doi.org/10.1016/j.jenvman.2022.115988>

stratification can alter processes such as the settling and resuspension of sediments, the uptake of nutrients by vegetation and algae, and the release of nutrients from the bottom sediments in stormwater facilities (Olding et al., 2000; Song et al., 2013). Persistent stratification in wet ponds may cause the water at depth to become hypoxic or even anoxic (Mayer et al. 2008). Potential adverse effects on water quality include the remobilization of metals and nutrients (e.g., Oberts, 2003; Song et al., 2013) and the generation of toxicants such as hydrogen sulphide and ammonia (Chen et al., 2019; Teichreb, 2012). Stratification has also been observed to cause short-circuiting in ponds, decrease the residence time and degrade the quality of the water discharged downstream (Torres et al., 1997; Kellner and Pires, 2002). For example, Torres et al. (1997) found that the active pond volume in a waste stabilization pond in Spain was reduced by almost a factor of five in the summer due to thermal stratification.

Thermal stratification in stormwater ponds is a dynamic process influenced by local climate conditions as well as the design of the facility (McEnroe et al., 2013; Song et al., 2013; He et al., 2015; Rey et al., 2021). Rey et al. (2021) found that thermal stratification in a 1.6 m deep operational waste stabilization pond in eastern Ontario was primarily caused by warmer air temperatures and solar radiation heating surface waters, but this was balanced by wind events mixing the pond. Precipitation may also affect water column stratification in stormwater ponds when it generates colder or warmer runoff than the receiving water body, and the resultant inflow can promote mixing (McEnroe et al., 2013). He et al. (2015) observed diurnal water temperature cycles with a temperature difference of 1.5-3.0 °C in the upper 1.2-1.7 m of the water column in a 3.8 m deep stormwater pond in southeast Calgary, Canada. They reported that stratification gradually broke down and vanished several hours after sunset due to air cooling combined with wind action. Song et al. (2013) found that thermal stratification through the summer and fall in 10

shallow stormwater ponds in southern Ontario was negatively correlated with rainfall and wind speed but strongly positively correlated with air temperatures and maximum pond depth.

In northern climates, chemical stratification caused by the accumulation of dissolved solids is also known to occur in stormwater ponds (Olding et al., 2000; Marsalek, 2003). Seasonal cycles of chemical stratification, high in winter and early spring and low in summer, are due to inflows of salt-laden stormwater from road deicing salts (McEnroe et al., 2013; Novotny et al., 2008). However, the importance of water temperature and dissolved solids in controlling water column densimetric stratification varies with the season and the prevalence and intensity of the application of deicing compounds. For instance, in a stormwater pond in Ontario, chemical stratification appeared stronger than thermal stratification in winter and early spring (Marsalek et al., 2000). Conversely, temperature differences between surface and bottom waters, rather than the salinity difference, were more closely related to water column stratification during the summer in 45 stormwater ponds in southern Ontario (McEnroe et al., 2013).

In many studies, wind was identified as the primary driver of the turbulent, three-dimensional flow patterns in ponds (Andradóttir and Mortamet, 2016; Rey et al., 2020). However, other studies suggested that flow patterns were driven primarily by the circulation between inlets and outlets (Shilton and Harrison, 2003; Passos et al., 2014). The horizontal and vertical flow patterns in stormwater ponds can also be complex and dynamic because of variable water column stratification (Bentzen et al., 2008 and 2009). For instance, Novotny and Stefan (2012) reported that the thermocline formed after the ice cover melts in the spring effectively reduced the transport of wind energy from the epilimnion to the hypolimnion. Other studies found that the speed and direction of the wind-induced currents change with depth in ponds and that wind forces are more

efficiently transferred to the bottom of shallower ponds (Józsa, 2014; Andradóttir and Mortamet, 2016).

Reliable and continuous field observations focusing on the strength and duration of thermal and chemical stratification at different locations in stormwater ponds are needed to improve understanding of pond hydrodynamics. In addition, measurements of vertical velocity profiles in stormwater ponds over multiday periods are required to more fully understand the importance of wind-driven currents and storm event inflows in these relatively small water bodies. For this purpose, a comprehensive 2-year field monitoring program was undertaken to continuously monitor two stormwater wet ponds in Calgary, Alberta, Canada, during the ice-free seasons from May to October in 2018 and 2019. A detailed analysis of the field measurements was undertaken to investigate the interaction between thermal and chemical stratification and the ponds' hydrodynamics. In addition, the responses of the water column stratification at different locations in the two wet ponds to atmospheric forcing, including precipitation, wind, and air temperatures, were examined. Spatial and temporal variations in thermal, chemical, and densimetric stratifications were also investigated. Finally, the interactions between wind forcing, inflow, stratification, and flow patterns in the ponds are discussed.

3.2 Study ponds and methods

3.2.1 Study wet ponds

The study sites are two stormwater wet ponds in the communities of Auburn Bay and Cranston ($50^{\circ} 53.53'N$ and $113^{\circ} 58.05'W$) in southeast Calgary, Alberta, Canada (Figure 3-1a). The characteristics of the two facilities and their catchments are presented in Table 3-1. The study sites have different shapes, inlet configurations, local landscaping, and catchment characteristics, see

Figure 3-1b,c and Table 3-1. The Auburn Bay pond has a single inlet pipe and outlet pipe with 2.7 m and 2.1 m diameters, respectively. The pond was built with a submerged berm that separates the sediment forebay from the main water body. The Cranston pond has two inlet pipes with diameters of 1.5 m and 1.95 m for Inlets 1 and 2, respectively; one outlet with a diameter of 1.5 m, and a vegetated berm that separates its sediment forebay from the main cell. All inlet and outlet pipes are located with their inverts at or slightly below the pond bed. The climatic conditions at the two ponds are very similar since they are only 1.5 km apart (Figure 3-1a). However, Auburn Bay has a significantly larger catchment area (232 vs. 122 ha) and a slightly larger imperviousness ratio (58 vs. 52%) than Cranston. Hence more stormwater runoff enters Auburn Bay each season. The discharge out of each pond is controlled by an outlet control structure equipped with a rectangular orifice that maintains the Normal Water Level (NWL) and a weir at the high water level (HWL). Both ponds were designed to store the runoff from the 1:100-year design event in accordance with the City of Calgary design standards (City of Calgary Water Resources 2011).

Three locations in each pond were selected for continuous water quality monitoring: location IN near the inlet and within the sediment forebay, location MID near the middle of the pond and away from the main flow path, and location OUT near the outlet (Figure 3-1b,c). The two ponds have a permanent design depth of 3.0 m (Table 3-1). In Auburn Bay, the location IN was located 30 m from the inlet. In Cranston, IN was located ~ 120 m from Inlet 1 and ~70 m from Inlet 2, at a point where the flow exits the sediment forebay. In Auburn Bay, the average water depths at the three monitored locations were 3.0 m, 3.2 m and 3.1 m, respectively. However, in Cranston, the average water depth at IN was only 2.4 m due to sediment accumulation in the sediment forebay, while it was 3.3 m at MID and 3.1 m at OUT.

3.2.2 Field measurement in the wet ponds

Field measurements were conducted from May to October 2018 and 2019 at the two ponds. However, no in-pond data were collected in May and June 2019 in Cranston because the pond was drained for maintenance in early May, and it took two months for runoff to fill it back to the design NWL. The field program included continuous and intermittent measurements using a wide array of instrumentation.

Weather stations (Onset, USA) were installed at each pond on the top of a hinged flagpole 10 m above the ground. Solar-powered weather data loggers were used at Auburn Bay (HOBO U30) and Cranston (HOBO RX3000). Six sensors were connected to the data loggers, including a rain gauge (S-RGB-M002), a temperature/relative humidity sensor (S-THB-M002), a solar radiation sensor (S-LIB-M003), a barometric pressure sensor (S-BPB-CM50) and wind speed and direction sensors (S-WSB-M003, S-WDA-M003, S-WCG-M003). The data loggers were programmed to sample every 10 seconds and then record average values at 5-minute logging intervals. The data was then periodically downloaded via USB on-site or via the internet using the RX3000 data logger that supports cloud-based data logging over cellular networks.

Seasonal statistics of the meteorological data gathered at the two ponds are presented in Table 3-2. The average air temperatures were approximately equal at the two ponds at ~ 13.5 and 12.4°C in 2018 and 2019, respectively. The total rainfall at the two ponds ranged from 273 to 286 mm. Although the most significant rainfall events occurred in June and July 2018, more wet days occurred in 2019 at 68 days versus only 56 days in 2018. The mean wind speed at Auburn Bay was slightly larger than at Cranston, likely due to increased sheltering by the mature vegetation and houses at Cranston. The prevailing wind directions were from the north and south, and the maximum recorded wind speeds were ~ 12 m/s at both ponds. Several gaps in the meteorologic data (May 10 to July 4, 2018, in Auburn Bay and July 10 to August 2, 2018, in Cranston) occurred

during the study due to equipment malfunctions. The two ponds are only 1.5 km apart (see Figure 3-1a); therefore, a gap at one pond was filled using data from the other pond.

Vertical arrays of moored instruments were deployed at three locations in each pond to capture the temporal and spatial variations in various water quality parameters. The water temperature was sampled at 5-minute intervals using HOBO MX2203 TidbiT (Onset, USA) installed at a vertical resolution of 25 cm. In addition, the water depth, temperature and conductivity were sampled at 5-minute intervals using TD-Diver or CTD-Diver or Micro-Diver (Van Essen Instruments, Netherlands) and at 15-minute intervals using EXO2 or EXO3 (YSI, USA). Furthermore, HOBO U26-001 DO (dissolved oxygen) loggers (Onset, USA) were deployed at various depths and locations, sampling at 5-minute intervals.

Velocity profile measurements were collected in 2019 using two bottom-mounted upward-looking acoustic Doppler current profilers (Aquadopp Profiler 1 MHz, Nortek, Norway) in both ponds, Figure 3-1b,c. The velocity profilers were deployed in a high-resolution mode with a vertical cell size of 3 cm and programmed to collect 100 samples at a rate of 1 Hz every 15 minutes, which resulted in a two-week battery life. The 100 samples for each cell were then averaged to create vertical profiles of the mean velocities every 15 minutes. The data collected from the profilers' depth sensor was used to detect the vertical location of the water surface, and surface velocities were extracted from the measurement cell located just below the surface. Velocity profiles were collected in the middle of the two wet ponds at location V_m between May and June in Auburn Bay and between July and August in Cranston. In addition, velocity measurements were made in the sediment forebay of Cranston at location V_f between September and October.

A total of 25 fortnightly field trips to the ponds were conducted over the two years, from June 6 until October 25, 2018, and from April 23 until October 25, 2019. During each field trip, vertical temperature and conductivity profiles with a vertical resolution of 30 cm were collected manually from a boat at the three monitoring locations using an EXO2 water quality sonde (YSI, USA).

3.2.3 Analysis methodology

Water level fluctuations in the study ponds were used to represent the magnitude and duration of runoff events. The continuous accurate measurements of water level over the entire season in the two ponds were presented instead of the inflow and outflow discharge measurements that were intermittent due to issues of occasional malfunction of the flow meters. A temperature difference of >1 °C between surface and bottom waters was used to identify the presence of thermal stratification. This value has been widely used in the literature as an indicator of thermal stratification in ponds and shallow lakes (Kellner and Pires, 2002; Abis and Mara, 2006; McEnroe et al., 2013; Nakhaei et al., 2019). A 10 °C surface-bottom water temperature difference was used as a threshold to define strong thermal stratification. In this study, the water column thermocline strength is defined as the maximum temperature gradient (dT/dz) of the column and the corresponding location as the thermocline depth (Kellner and Pires 2002). The thermocline strength and depth were computed at 5-minute intervals at the three monitoring locations in both ponds using the water temperature logger data. Daily averaged values of the thermocline strength and depth were calculated to reduce the noise in the data.

Salinity and water density were calculated from conductivity and temperature measurements using standard equations (APHA 1989) as follows:

$$\rho_o = 1000 \left\{ 1 - \left(\frac{T+288.9414}{508929.2(T+68.12963)} \right) (T - 3.9863)^2 \right\} \quad (\text{Equation 3-1})$$

where ρ_o is the density of fresh water as a function of temperature only in kg/m^3 ; T is the water temperature in $^{\circ}\text{C}$.

To determine the density contribution from salinity, first, the specific conductance (R_t) was converted to salinity as follows:

$$S = 0.008 - 0.1692R_t^{0.5} + 25.3851R_t + 14.0941R_t^{1.5} - 7.0261R_t^2 + 2.7081R_t^{2.5} - \frac{0.008}{1+(1.5 \times 400 \times R_t) + (400R_t)^2} \quad (\text{Equation 3-2})$$

where R_t is the ratio between the specific conductance values at 25°C and the conductivity of standard seawater with a salinity of 35 g/L and 25°C ; S is the water salinity in g of salt per kg of water or parts per thousand (ppt).

Then the water density as a function of temperature and salinity is calculated as follows:

$$\rho = \rho_o + AS + BS^{3/2} + CS^2 \quad (\text{Equation 3-3})$$

where ρ is the water density in kg/m^3 , A, B, and C are as follows:

$$A = 8.24493 \times 10^{-1} - 4.0899 \times 10^{-3}T + 7.6438 \times 10^{-5}T^2 - 8.2467 \times 10^{-7}T^3 + 5.3875 \times 10^{-9}T^4 \quad (\text{Equation 3-4})$$

$$B = -5.72466 \times 10^{-3} + 1.0227 \times 10^{-4}T - 1.6546 \times 10^{-6}T^2 \quad (\text{Equation 3-5})$$

$$C = 4.8314 \times 10^{-4} \quad (\text{Equation 3-6})$$

The densimetric stratification in the ponds is quantified in this study using the bed-surface density difference, $\Delta\rho$. In addition, the freshwater bed-surface density difference, $\Delta\rho_o$, is calculated as a function of temperature, and the ratio $\Delta\rho_o/\Delta\rho$ is used to quantify the relative importance of thermal stratification. This study used threshold values of $\Delta\rho$ of 0.25 and 2 kg/m³ to define mixed ($\Delta\rho < 0.25$ kg/m³), stratified ($0.25 < \Delta\rho < 2$ kg/m³), and strongly stratified ($\Delta\rho > 2$ kg/m³) water columns. Note that $\Delta\rho$ of 0.25 and 2 kg/m³ are equivalent to the density change that occurs in freshwater when the temperature varies between 24 and 25 °C and 15 and 25 °C, respectively. Similarly, McEnroe et al. (2013) defined thermal and chemical stratifications using thresholds equivalent to a density change of 1 °C.

Small ponds are dynamic systems with wind-induced internal waves and thermocline tilting (MacIntyre et al., 2018). Therefore, the period of the first mode internal gravity waves (T) was calculated for the two ponds in 2019 using biweekly density profiles as follows,

$$T = \frac{2L}{\sqrt{g(\rho_h - \rho_e) / (\frac{\rho_h}{z_h} + \frac{\rho_e}{z_e})}} \quad \text{(Equation 3-7)}$$

where g is the gravitational acceleration (m/s²); T is the period (s); L is the fetch (m); ρ_h and ρ_e are the hypolimnion and epilimnion densities (kg/m³); z_h and z_e are the hypolimnion and epilimnion depths (m) (Kalff, 2002).

In the middle of the two wet ponds (location V_m in Figure 3-1b,c), linear regression was performed between the magnitude of the water surface velocity, V , and the wind speed, W , for each of the eight cardinal wind directions. For example, the north wind direction includes directions within an angle of 45° between -22.5° and +22.5° and similarly for the other directions. The location V_m in the middle of the ponds was chosen because it is far from inlets and outlets, and this will minimize

the effects of currents generated by inflows and outflows and maximize the effects of wind-generated currents. The linear regressions were computed using continuous 15-minute interval data spanned two months.

Rey et al. (2021) used an approach developed by Boegman et al. (2008) to estimate the wind speed required to thoroughly mix a stratified water column. This approach resulted in the following Equation:

$$0.3 C_D \rho_a W_m^2 \sqrt{\frac{C_D \rho_a W_m^2}{\rho_m}} S = \frac{g(\rho_b - \rho_s)H^2}{12} \quad (\text{Equation 3-8})$$

where C_D is the drag coefficient (1.3×10^{-3}) (Fischer et al., 1979); ρ_a is the air density (1.2 kg/m^3); ρ_m is the average water density (kg/m^3); W_m is the wind speed needed to mix a stratified water column (m/s); H is the water depth (m); ρ_s , and ρ_b are near-surface, and near-bed water densities (kg/m^3); and S is the time required for the applied wind shear stress to be converted to mixing work (s). In the current study, the time S needed to fully mix two scenarios of stratification of $(\rho_b - \rho_s) = 0.25$ and 0.50 kg/m^3 was calculated for given wind speeds and compared to the maximum durations observed for the same wind speeds in the two ponds.

3.3 Results and discussion

3.3.1 Thermal and chemical stratification

Time series of rainfall depth, pond depth, air temperature, water temperatures, and salinity are plotted for the two ponds in 2018 in Figure 3-2 and for Auburn Bay in 2019 in Figure 3-3. Note that data are not presented for Cranston in 2019, as the pond was drained for maintenance at the start of the season. The water depth increased in both ponds in response to each rainfall event

before it decreased slowly as the pond drained to the NWL afterwards (see Figures 3-2a,c and 3-3a). Diurnal fluctuations in air temperature are evident in Figures 3-2b,d and 3-3b and typically generated diurnal fluctuations in near-surface water temperatures at both IN and OUT. Attenuations in the diurnal amplitudes of the near-surface water temperature fluctuations were notable during wet days and following abrupt drops in the air temperature (e.g., May 28-31, 2018, May 15-20, 2019, and September 25-30 in 2018 and 2019).

The geometry of the two sediment forebays and the proximity of IN location to the inlets are quite different in the two ponds (Figure 3-1b,c). However, the water temperatures measured near the bottom at IN_b in the two ponds were very similar during the same rainstorm events, increasing or decreasing in response to warmer or cooler inflow temperatures (Figure 3-2b,d). This indicates that perhaps the difference in the proximity of IN location was approximately cancelled out by the different sediment forebay geometries. Between May 17 and July 23, 2018, the water temperature measured near the bed at IN_b in Cranston was significantly higher than at IN_b in Auburn Bay; the average temperatures were 12.5 and 11.0 °C, respectively (Figure 3-2b,d). At the same time, the average temperatures at 2.4 m depths at IN in both ponds were 12.5 °C, indicating that the warmer water at IN_b in Cranston was simply due to the fact it is only 2.4 m deep compared to 3.0 m in Auburn Bay.

In Auburn Bay, the most significant increase in water depth was in 2018 at ~1.3 m, three times the maximum rise in 2019, and was generated by a total rainfall depth of 102 mm over two days on June 22-23, 2018 (Figure 3-2a). The inflow caused by this rainfall event was significant enough to thermally mix the entire pond to an approximately constant temperature of 16 °C (Figure 3-2b). The runoff volume was ~65% of the permanent pool volume or 35,500 m³. This large volume inflow caused the entire pond to remain thermally mixed for one day (Figure 3-2b). In Cranston,

the same rainfall event on June 22-23, 2018, resulted in a water level increase of 85 cm (see Figure 3-2c), equivalent to a runoff volume of 44% of the permanent pool volume or 19,800 m³. This significantly smaller runoff volume compared to Auburn Bay is due to the fact that the catchment area of Cranston is ~50% smaller (see Table 3-1). As a result, only the sediment forebay in Cranston was thermally and temporarily mixed during this event, while the main cell remained thermally stratified. The temperature and salinity at OUT_b did not respond significantly to this large inflow event on June 22-23 (Figure 3-2d,e), but the salinity decreased from 0.5 to 0.2 ppt at OUT_s because the inflow was 3.5°C warmer than the pond water. As this lighter-warmer water exited the inlet pipe, it rose and entered the epilimnion, where it then flowed to the outlet, producing the 0.3 ppt decrease in salinity while the salinity in the hypolimnion remained unchanged. The strength of the densimetric stratification prior to this rainfall event at both IN and OUT in Cranston was ~2 kg/m³ (Figure 3-4a), and this strong stratification inhibited vertical mixing of the fresher-warmer inflow water as it flowed to the outlet. This is a clear example of how inflow properties (i.e., temperature and salinity) and ambient stratification can reduce a pond's active volume (Kellner and Pires, 2002).

On July 23, the second-largest rainfall event in 2018 caused a water surface elevation rise of ~60 cm in Auburn Bay and ~35 cm in Cranston (Figure 3-2a,c). The relatively cold runoff on July 23 decreased the water temperature at IN_b in both ponds by ~8 °C, see Figure 3-2b,d. This event had a pond-wide effect in Auburn Bay, decreasing the water temperature in the main cell by 5 °C due to the cooling effect of the rainstorm inflow. A pond-wide effect was also evident in Cranston when the cold inflow water remained in the hypolimnion as it flowed through the main cell, flushing saline bottom water into the outlet. This event caused the near-bed salinity to decrease from 1.6 to 0.8 ppt while the near-surface salinity remained unchanged (Figure 3-2e).

Hence, during the two biggest rainfall events in 2018, runoff moved above or below the thermocline from inlet to outlet, depending on its relative density, without any significant vertical mixing. The stratification was strong enough in June and July, as indicated by relatively high values of $\Delta\rho$ in Figure 3-4a, that either scenario of runoff moving above or below the thermocline is possible. In both cases, this would significantly reduce the effective residence time, causing inflow pollutants to be transported from the inlet to the outlet in a shorter time than the nominal residence time and potentially lowering the outflow water quality.

Significantly cooler air temperatures and decreasing solar radiation caused bed and surface water temperatures at IN and OUT in both ponds to converge in mid to late September (Figures 3-2b,d and 3-3b). Complete mixing of the water columns occurred following abrupt decreases in air temperature from ~ 16 °C to -1 °C, which started on Sept. 11th and 25th in 2018 and 2019, respectively. Starting the second week of October, inverse thermal stratification was observed at IN, in both ponds in both years, when the bottom waters were 2-4 °C warmer than the surface waters (Figures 3-2b,d and 3-3b). Simultaneously, OUT was thermally mixed, and no inverse thermal stratification was observed. This was due to warm salt-laden inflows following early snowmelt events in October. For example, on October 8, 2019, salt-laden runoff entered Auburn Bay following a snowstorm and increased the near-bed salinity at IN from 0.2 to 1.4 ppt, Figure 3-5a.

The percent durations and maximum strength of the thermal stratification observed at IN and OUT computed over the entire measurement seasons (May- October) are presented in Table 3-3 for both ponds. The two ponds were observed to be thermally stratified (i.e., > 1 °C temperature difference) 70-83% of the time at IN and 70-79% at OUT. During shorter monitoring periods between May and August, Nakhaei et al. (2019) observed thermal stratification 56-88% of the time in three 0.4-

1.8 m deep stormwater ponds in Edmonton, Canada, and Abis and Mara (2006) for 50-90% of the time, May to August, in waste stabilization ponds of 1.5 m depth in the UK. Over the same period, May to August, the two ponds in this study were thermally stratified for > 99% of the time. Hence, the stratification in our study ponds persisted for longer than what has been previously observed in shallower ponds.

The air temperature in the fall of 2018 dropped below 0 °C 15 days earlier than in 2019, Figures 3-2b and 3-3b. As a result, the two ponds were thermally stratified for less time in 2018, Table 3-3. Strong thermal stratification (i.e., > 10 °C temperature difference) occurred 6-14% of the time. The strongest thermal stratification in the ponds occurred between late May and early June when surface-bed temperature differences reached 14-20 °C and coincided with relatively cold waters near the beds at 6-8 °C and peak air temperatures that ranged from 28 to 30 °C. Both the duration and maximum strength were higher in 2018 compared to 2019. This was largely due to the air temperatures that were, on average, 4 °C higher in May 2018 compared to 2019, Figures 3-2b and 3-3b. In 2018, the strong thermal stratification (i.e., > 10 °C temperature difference) persisted at IN in Auburn Bay for 13% of the time between May and October, while in Cranston, it occurred for only 6% of the time between May and October (Table 3-3). This is attributed to the fact that the depth at IN in Cranston was 2.4 m compared to 3.0 m in Auburn Bay. Therefore, a 20% reduction in the depth appears to have caused a factor of approximately two reduction in the duration of strong stratification and a significant reduction in the maximum ΔT .

Previous studies of small lakes and ponds have observed salinity increased in stormwater ponds due to runoff from salted roads in the spring (e.g., Marsalek, 2003). The City of Calgary uses ~35,000 tons of sodium chloride and calcium chloride annually for snow and ice control (City of

Calgary, 2022). During snowmelt or rain-on-snow events in April, accumulated water and chemicals in the catchment may be suddenly released and contribute to acute and chronic impacts on receiving waters (Environment Canada and Health Canada, 2001). As a result, elevated salinity concentrations were observed in both study ponds from April to as late as August, particularly near the bed (Figures 3-2e and 3-3c). In 2019, the salinity decreased abruptly at IN_{1/3} on April 28, May 17, and June 7 (Figure 3-3c) due to the flushing effect of significant stormwater inflows (Figure 3-3a). Mild inflows on May 5, 8, 21 and 25 that induced water surface elevation rises of less than 10 cm had a minor effect on the salinity at IN_{1/3}. In 2018, the runoff from the inlet to the outlet in Cranston flushed the salinity above and below the thermocline on June 22 and July 23, depending on its relative density (Figure 3-2e). Therefore, stormwater may increase or decrease chemical stratification depending on the runoff volume, temperature and salinity.

It has been previously reported that chemical stratification due to the accumulation of salts in stormwater ponds dissipates by the first significant runoff event in spring (Marsalek, 2003; Mayer et al., 2008). However, in this study, it was observed that multiple runoff events were required to reduce salinity concentrations to background levels. A persistent salinity of 1-2 ppt near the outlets was observed until mid-July in the two study ponds (Figures 3-2e and 3-5c). This is a concern since concentrations > 1 ppt are high enough to pose a risk to the receiving waters downstream (Crowther and Hynes 1977). The outflow of high salinity water from stormwater ponds into downstream water bodies could potentially reduce biodiversity and prevent the oxygenation of bottom waters (Marsalek et al., 2000; Marsalek, 2003; Mayer et al., 2008).

Rapid fluctuations in the salinity time series were evident at all monitored locations in Auburn Bay in 2019. Salinity fluctuations of amplitudes up to 0.5 ppt with periods 1-3 hours were most notable in May near the bed at IN_{1/3} and OUT_{1/3}, as shown in the zoomed-in plot in Figure 3-3c. These

fluctuations were smaller or even disappeared overnight when winds were weak. Similar fluctuations in water temperature at OUT_b with amplitudes up to 2 °C and periods of 1-3 hours were also observed (see Figure 3-3b). Both types of rapid fluctuations are most likely due to internal wave activity since theoretical estimates of the period of first-mode internal waves also ranged from 1-3 hours. In ponds and shallow lakes, internal wave motions may break near sloping boundaries and berms, inducing vertical mixing or resuspension of sediment and pollutants. For example, the breaking of nonlinear internal waves in Toolik Lake, Alaska, was found to cause vertical fluxes of heat, solutes, and particulates (MacIntyre et al., 2009).

3.3.2 Thermocline

Rainfall depth, air temperature, 2D colour contour plots of vertical water temperature profiles and the daily averaged thermocline elevation and strength at Auburn Bay in 2019 are presented in Figure 3-6. Varying air temperatures generated similar diurnal fluctuations and longer-term trends in the near-surface water temperatures at the three monitoring locations (Figure 3-6,b-d). The thermocline was significantly deeper most of the time at MID and OUT than IN. In May 2019, the temperature of the near-bed water at all locations was still relatively cold (<10 °C), while the air temperatures increased to >20 °C in mid-May. This combination of cold bottom waters and rising air temperatures caused the thermocline strength to increase from ~5 °C/m to ~10 °C/m. At the start of June 2019, the thermocline strengths at all locations were ~10 °C/m before they decreased to ~5 °C/m by mid-July. The thermocline strength fluctuated more frequently at IN due to the influence of rainstorm inflows carrying varying amounts of heat and salinity. On July 24, the thermocline strength at IN in Auburn Bay peaked at ~ 12 °C/m due to the combined effect of a cold inflow on July 18 and increased air temperatures. Starting the last week of September 2019,

the thermocline strength at all locations decreased below 2 °C/m when the air temperature abruptly decreased.

Statistics for the thermocline depth and strength in the two ponds in 2018 and 2019 are presented in Table 3-4. The average thermocline depth below the NWL was the smallest at IN and the largest away from the main flow path at MID in the two ponds. The mean thermocline strength at IN was significantly larger than at MID and OUT (statistical significance $P < 0.001$ using t-test), see Table 3-4. Furthermore, the thermocline strength at IN had the highest standard deviation compared to MID and OUT, confirming that thermocline strength fluctuates more frequently at IN, see Figure 3-6e. The strong thermal stratification and shallow thermocline depth in the sediment forebays are explained by the relatively cold summer inflows at times entering the ponds near the bed following rainfall events. Ambient climatic conditions prior to and during storm events govern the temperature of the inflows. For example, McEnroe et al. (2013) suggested that the heat transferred from impervious surfaces could result in warm pond inflows that enhance mixing. Note that the time series plotted in Figure 3-3b suggests that cold inflows are preceded by or are coincident with significantly colder air temperatures.

The average thermocline strengths in the two ponds were 5-7 °C/m, and the maximum values were as large as 18 °C/m in the two study ponds (Table 3-4). Song et al. (2013) reported that the average thermocline strengths in 10 urban ponds with maximum depths between 0.7-2.5 m in southern Ontario, Canada, were 2.9 °C/m, which is ~50% of what was observed in this study. In their study, the mean thermal stratification in each pond was strongly correlated with the maximum water depth ($R^2 = 0.72$), suggesting their lower thermocline strength was mainly due to their shallower depth compared to the current study. Abis and Mara (2006) observed strong daytime stratification (i.e., temperature gradients >20 °C/m) in three 1.5 m deep waste stabilization ponds in the UK,

followed by night-time destratification. This indicates that in shallower ponds, diurnal cycles of stratification are the norm, while in deeper ponds such as our study ponds, persistent stronger stratification is the norm.

Therefore, designing shallower ponds would almost certainly reduce the occurrence of persistent strong stratification. However, at depths shallower than the photic zone, wet ponds tend to become overgrown with submerged macrophytes and may become hypereutrophic, leading to complaints from the public (Nakhaei et al., 2021). Nonetheless, it may be possible to determine an optimum wet pond depth that is shallow enough to avoid persistent stratification and deep enough that ponds do not become hypereutrophic. According to the City of Calgary (2011), the minimum depth to control weed growth is 1.5 m in the sediment forebay and 2.0 m in the main cell. Locating inlets at or near the NWL surface as opposed to the pond bottom may also enhance mixing in forebays. If relatively lighter or denser inflows can be mixed fully with ambient pond water in the near-field of inlets, this would prevent the short-circuiting that occurs when the flow is confined above or below the thermocline, reducing the residence time. However, ice dams may form in near-surface inlets in cold regions, causing blockages and high backwater levels. The strength of stratification can also be reduced using design features such as fountains, aerators, and circulating pumps that mix and circulate the water. However, a major disadvantage of these options is their construction, maintenance, and operational costs. Hence, more research is needed to demonstrate that these are economical and effective methods for enhancing vertical mixing in wet ponds.

3.3.3 Densimetric stratification

The time series of surface-bed density differences, $\Delta\rho$, at IN and OUT in Auburn Bay in 2019 are presented in Figure 3-7a. Diurnal cycles in $\Delta\rho$ with amplitudes up to 1 kg/m³ were typically

generated due to daily fluctuations in the near-surface water temperatures. In early May at IN, the densimetric stratification was ~4.5 times larger than at OUT due to strong chemical stratification. Flushing caused by runoff events on April 28, May 17, and June 7 decreased $\Delta\rho$ significantly at IN, see Figure 3-3a,c. Following June 7, $\Delta\rho$ at IN and OUT was approximately equal and remained above 0.25 kg/m^3 most of the time until mid-September. This data shows that the pond was stratified (i.e., $\Delta\rho > 0.25 \text{ Kg/m}^3$) between May and mid-September 2019 for 96% and 90% of the time and was strongly stratified (i.e., $\Delta\rho > 2 \text{ Kg/m}^3$) for 34% and 9% of the time at IN and OUT, respectively. These percentages are larger than the corresponding thermal stratification (i.e., $\Delta\rho_o > 0.25 \text{ Kg/m}^3$) percentages at 88 and 85% and significantly larger than the strong thermal stratification (i.e., $\Delta\rho_o > 2 \text{ Kg/m}^3$) percentages at 4 and 2%. In 2018, the $\Delta\rho$ computed from the fortnightly profiles (Figure 3-4a) between June and mid-September showed that the two ponds were stratified for 75-88% and strongly stratified for 13-38% of the time versus thermal stratification of 75-88% and strong thermal stratification of 0-25%. This highlights the importance of chemical stratification in these ponds.

A times series of the relative strength of thermal stratification to the total or densimetric stratification in Auburn Bay in 2019 is presented in Figure 3-7b. At IN in early May, thermal stratification was negligible, and the densimetric stratification was due almost entirely to chemical stratification (Figure 3-5a). However, by the third week of June, $\Delta\rho_o/\Delta\rho$ at IN reached ~1.0, indicating that chemical stratification was now negligible because most of the water column salinity had been flushed (Figure 3-5a). At OUT, $\Delta\rho_o/\Delta\rho$ in early May was ~0.25, and while it did fluctuate a lot, it did not reach 1.0 until mid-August. In 2018, $\Delta\rho_o/\Delta\rho$ in both ponds was 0.40-0.75 in early June before it increased gradually to reach 1.0 in mid-July, except for OUT in Cranston, where it stayed at 0.75 during all profiles between mid-July and mid-September (Figure 3-4b).

This data shows that chemical stratification can persist in the main cell of these ponds and contribute to densimetric stratification until mid-September (Figure 3-4b).

In the two ponds, low DO concentrations were observed in the bottom waters in both years. For example, the average DO concentrations varied vertically, bed to surface, from 1.2-10.1 mg/L in Auburn Bay and from 0.8-4.3 mg/L in Cranston. The DO measurements at 50 and 30 cm above the bed indicated that conditions were anoxic at < 1 mg/L for 70% and 88 % of the time between May and mid-September in Auburn Bay and Cranston, respectively. Similarly, Mayer et al. (2008) observed DO concentrations of 1.0 mg/L at a depth of 2.5 m and below in a strongly stratified 4 m deep stormwater pond in Toronto, Canada, indicating anoxic conditions. Furthermore, He et al. (2015) observed DO concentrations < 5 mg/L in the upper 1 m of the water column in a 3.8 m deep stormwater pond in Calgary, which violated the requirements for receiving water (Alberta Environment, 1999). Evidently, the persistent densimetric stratification in the two wet ponds inhibited vertical mixing, causing the water at depth to become anoxic at DO concentrations < 1 mg/L. This can significantly and negatively impact water quality by enhancing the remobilization of metals and nutrients and the generation of toxicants such as hydrogen sulphide and ammonia (Oberts, 2003; Teichreb, 2012; Song et al., 2013; Chen et al., 2019).

3.3.4 Wind-induced currents

Average wind speeds of 2.1 m/s and 1.8 m/s and average surface drift currents of 0.9 cm/s and 0.8 cm/s were observed in the main cells in Auburn Bay and Cranston, respectively. Results from a linear regression analysis between the absolute surface drift velocity, V , and wind speed, W , are presented in Table 3-5. The wind speed was found to be correlated with the surface drift current at Auburn Bay with a coefficient of determination, $R^2 = 0.62$, regardless of wind direction, and a

regression slope $V/W = 0.35\%$. The correlation was slightly weaker at Cranston with $R^2 = 0.56$ and a regression slope $V/W = 0.26\%$. This is likely due to the smaller wind speeds at Cranston caused by increased sheltering by mature vegetation and houses. The strongest correlation was between the surface drift and winds blowing from the south and southeast in Auburn Bay and Cranston, with R^2 of 0.74 and 0.64, see Table 3-5. These V/W ratios are within the 0.2-0.5% range observed in a small 2 m deep stormwater pond in Iceland (Andradóttir and Mortamet 2016). Therefore, the V/W ratios can be used as a simple tool to estimate wind-driven currents in the study ponds.

Water velocity profiles from the sediment forebay of Cranston at V_f are plotted in Figure 3-8 for September 13, 15, and 20 during three windstorm events with average wind speeds of 6.8, 4.4, and 3.8 m/s, respectively. These three wind events were due to northwest or southwest winds and generated similar longitudinal surface currents in the forebay. Wind-driven surface currents were observed along the longitudinal axis of the forebay towards the northeast, and deep return currents were in the opposite direction (Figure 3-8). The surface currents ranged from 1.0-3.5 cm/s, similar to the 1.0-4.0 cm/s reported in Andradóttir and Mortamet (2016) but the bottom counter-current magnitudes of 1.0-5.5 cm/s were sometimes significantly higher than the 1.0-1.6 cm/s that they observed. This is likely due to Cranston's longer and narrower sediment forebay and the fact that the return flow was forced to pass through a narrow gap to exit the forebay.

3.3.5 Meteorological forcing and stratification

Rainfall depth, air temperature, wind speed, and wind direction at Cranston for July 17-30, 2019, are plotted in Figure 3-9, a-c. Also plotted in Figure 3-9, d-e are 2D colour contour plots of profiles of the water temperature and absolute water velocity, along with time series of the thermocline depth and pond averaged water column density gradient. Generally, the water column density

gradient followed the air temperature diurnal fluctuations (Figure 3-9a,e). For example, the air temperature and pond average water column density gradient were positively correlated from July through September in Auburn Bay and Cranston with $R^2 = 0.44-0.51$ and a slope of $0.024 \text{ (kg/m}^3\text{)/(m }^\circ\text{C)}$, ($p < 0.0001$ in both cases using t-tests). Hence, varying air temperatures directly impacted the thermal stratification and vertical density gradient. Decreasing air temperature from July 17 to 20 caused the density gradient to decrease from 0.6 to $0.2 \text{ kg/m}^3\text{/m}$ (Figure 3-9a,e). Simultaneously, deep-water currents with magnitudes of $2-5 \text{ cm/s}$ and depths 1.5 to 2.5 m below the water surface were observed following rainfall events on July 18 and 20, Figure 3-9a,e. The inflow on July 18 was relatively cold and increased the thickness of the hypolimnion from $\sim 1.0 \text{ m}$ to $\sim 1.5 \text{ m}$, Figure 3-9d. These deep-water currents sank from a height above the bed of $\sim 1 \text{ m}$ to $\sim 0.25 \text{ m}$ between July 18 and 20 because the inflows were $3 \text{ }^\circ\text{C}$ colder than the ambient water. Starting July 21, the surface waters began warming, and the thermocline height fluctuated significantly, around 1.5 m , for several days before it started to deepen on July 25, after multiple days of surface heating and no inflows.

Higher magnitude wind-induced near-surface currents up to 5 cm/s were observed in the upper 1.5 m of the water column on July 21, 24, 25, and 27 (Figure 3-9e). They coincided with wind storms with maximum wind speeds of $\geq 8 \text{ m/s}$, average wind speeds of $4.5-5.5 \text{ m/s}$, and durations of ≥ 14 hours. No significant rainfall was observed between July 22 and 30 when daytime warming of surface waters by air temperatures ranging from 10 to $30 \text{ }^\circ\text{C}$ created diurnal fluctuations in the density gradient (see Figure 3-9d,e). The density gradient peaked at $0.8 \text{ kg/m}^3\text{/m}$ on July 23, following ~ 1.5 days of relatively low wind speeds. It then decreased abruptly and remained in the range of $0.30-0.55 \text{ kg/m}^3\text{/m}$ for the next two days while peak wind speeds exceeded 8 m/s and

significant surface currents were generated (see Figure 3-9b,d,e). This indicates that wind-induced vertical mixing had a certain impact on the strength of stratification in these ponds.

A linear regression analysis between daily averaged wind speed and pond averaged water column density gradient was performed in the two ponds using data from 12 days in July and August 2019 on days with rainfall depths < 0.4 mm and moderate air temperature between 12-24 °C. The goal was to identify the significance of wind on mixing when other factors like inflow and surface cooling were insignificant. During these 12 days, the average daily wind speed was 1.6-4.1 m/s at Cranston and 1.7-2.9 m/s at Auburn Bay. The wind speed was found to be negatively correlated with the pond-averaged water column density gradient with R^2 values of 0.62 and 0.75 ($p < 0.0025$ using t-tests) at Cranston and Auburn Bay.

The durations S of wind events with wind speeds of 4-8 m/s needed to mix two scenarios of stratified water columns ($\Delta\rho = 0.25$ and 0.5 kg/m^3) were calculated with Equation (3-8), and the results are presented in Table 3-6. The maximum observed durations of two and six wind events in Auburn Bay and Cranston exceeded that needed to fully mix a weaker stratified water column ($\Delta\rho = 0.25 \text{ kg/m}^3$). However, none of the observed wind events had sufficient durations to mix a more strongly stratified water column ($\Delta\rho$ of 0.50 kg/m^3). Note that $\Delta\rho$ in these ponds was $> 0.25 \text{ kg/m}^3$ between May and mid-September for 75-96% of the time, and therefore it was concluded that the impact of the observed wind events on vertical mixing was insignificant most of the time. Previous studies reported persistent and strong stratification in small ponds and concluded that this was likely explained by low wind stresses at the water surface (Folkard et al., 2007; Song et al., 2013). Furthermore, Mayer et al. (2008) suggested that vertical mixing due to the wind would be inhibited by strong water column stratification and depths exceeding 2 m in stormwater ponds, which was the case in both study ponds.

3.4 Conclusions

The main objective of this chapter is to report on the governing factors that control the strength and duration of thermal, chemical and densimetric stratification, as well as the interaction between stratification and hydrodynamics in stormwater wet ponds. The field measurements used in the current study were collected using over 90 instruments during two ice-free seasons, making our research one of the most comprehensive field studies of stormwater ponds so far reported in the literature.

In this investigation, stormwater wet ponds experienced strong and prolonged thermal and chemical stratifications, negatively affecting their performance. In particular, the vertical thermal and chemical structure forced the runoff from the inlet to the outlet to move above or below the thermocline at times, creating dead zones. In addition, vertical mixing due to wind was inhibited by a densimetric stratification of $\Delta\rho > 0.25 \text{ Kg/m}^3$, causing the water at depth to become anoxic (DO concentration $< 1 \text{ mg/L}$) for a long time. Potential consequences of the observed stratification include decreased pollutant retention capacity, discharge of poorer quality water downstream and increased stress on aquatic communities. As a result, additional consideration of stratification may be required when designing new stormwater wet ponds. For example, this study showed that the relatively cold summer inflows entering the pond near the bed caused the thermocline depth to be the shallowest in the sediment forebays. Notably, this finding suggests that stormwater pond designers should consider locating inlets at or near the NWL surface to allow complete mixing with ambient pond water in the near-field of the inlet. This can minimize the occurrence of stratification in the forebays. However, ice dams may also form in near-surface inlets in cold regions, causing blockages and high backwater levels. Decreasing pond depth would significantly

reduce the duration of the extreme thermal stratification. As a result, it is recommended to lower the design depth from 3 to 2 m to be shallow enough to avoid persistent stratification and deeper than the photic zone to prevent aquatic growth and eutrophication. In chapters 5 and 6, inflow/outflow and in-pond water quality measurements will be linked to the hydrodynamic and stratification results presented in the current chapter to explore in-depth the role of stratification in altering the hydraulic performance and the sediment transport and fate in stormwater wet ponds.

Notation

The following symbols are used in this chapter:

C_D = wind drag coefficient;

h = height above the bed;

H = water depth;

HWL = high water level;

I = rainfall depth;

L = pond fetch;

NWL = normal water level;

R_t = the ratio between the specific conductance values at 25°C and the conductivity of standard seawater with a salinity of 35 g/L and 25°C;

S = time required for the applied wind shear stress to be converted to mixing work;

S = water salinity;

T = water temperature;

T_a = air temperature;

w = wind speed;

W_m = wind speed needed to mix a stratified water column;

z = water surface elevation;

z_e = epilimnion depth;

z_h = hypolimnion depth;

ΔT = vertical top-bottom temperature differences;

$\Delta \rho$ = vertical bottom-top density differences;

$\Delta \rho_o / \Delta \rho$ = the ratio of the freshwater bed-surface density difference and the in-pond water bed-surface density difference;

η = water depth above normal water level;

ρ_a = air density;

ρ_b = near-bed water density;

ρ_e = epilimnion density;

ρ_h = hypolimnion density;

ρ_m = average water density;

ρ_o = density of fresh water;

ρ_s = near-surface water density;

Table 3-1 Study ponds' physical and drainage characteristics.

| | Units | Auburn Bay | Cranston |
|---|----------------|--------------------------|--------------------------|
| Catchment type | / | Residential & Commercial | Residential & Commercial |
| Catchment area | ha | 232 | 122 |
| Imperviousness ratio | % | 58 | 52 |
| Surface area at NWL¹ | m ² | 24,700 | 22,000 |
| Loading ratio² | / | 94 | 55 |
| Permanent wet pool volume | m ³ | 54,600 | 45,100 |
| Active storage volume at HWL³ | m ³ | 56,495 | 52,724 |
| Design bottom elevation | m | 1038 | 1038 |
| Design NWL elevation | m | 1041 | 1041 |
| Length-to-width ratio | - | 2:1 | 2:1 |
| Number of inlets/outlets | - | 1 / 1 | 2 / 1 |
| Depths at NWL¹ IN/MID/OUT⁴ | m | 3.0/ 3.2/ 3.1 | 2.4/3.3/3.1 |

1 Normal Water Level

2 Ratio of the catchment to the pond area

3 High Water Level

4 Monitoring locations in Figure 3-1b,c

Table 3-2 Summary of the seasonal statistics of the meteorologic data at the Auburn Bay and Cranston ponds between May and October in 2018 and 2019. W is the wind speed measured at 10 m above the ground, T_a is the air temperature, μ is the mean and σ is the standard deviation.

| Pond | Auburn Bay | | Cranston | |
|---|-------------------|------------|-----------------|------------|
| Year | 2018 | 2019 | 2018 | 2019 |
| T_a ($\mu \pm \sigma$), °C | 13.5 ± 8.1 | 12.5 ± 7.5 | 13.4 ± 8.1 | 12.3 ± 7.5 |
| W, m/s (μ/Max.) | 1.7 / 11.4 | 2.1 / 11.7 | 1.2 / 8.1 | 1.8 / 12.2 |
| Total Rain, mm (wet days)¹ | 273 (56) | 286 (68) | 283 (58) | 282 (67) |

¹ All days with rainfall greater than or equal to 0.2 mm.

Table 3-3 Summary of the percentage of time (May- October) the water column was thermally stratified and strongly stratified along with the maximum top-bottom water temperature differences (ΔT). No data is available for Cranston in 2019 due to the draining of the pond for maintenance.

| Pond | Auburn Bay | | | | Cranston | |
|--|-----------------------|-----------------------|-----------------------|-----------------------|-----------------------|-----------------------|
| Year | 2018 | | 2019 | | 2018 | |
| Location | IN* | OUT | IN | OUT | IN | OUT |
| $\Delta T > 1\text{ }^{\circ}\text{C}$ | 72 % | 71% | 83 % | 79% | 70% | 70 % |
| $\Delta T > 10\text{ }^{\circ}\text{C}$ | 13% | 14% | 11% | 8 % | 6% | 12% |
| Max. ΔT | 19 $^{\circ}\text{C}$ | 20 $^{\circ}\text{C}$ | 17 $^{\circ}\text{C}$ | 16 $^{\circ}\text{C}$ | 14 $^{\circ}\text{C}$ | 18 $^{\circ}\text{C}$ |

** Due to equipment failure, averaged temperature at MID_s and OUT_s was used to fill the gap at IN_s between Jul 20 and Oct 24, 2018.*

Table 3-4 Summary of the seasonal statistics (seasonal average \pm standard deviation) for the daily thermocline depth and strength and maximum seasonal thermocline strength at the two ponds between May and October in 2018 & 2019, except for the pink highlighted data for the Cranston pond in 2019, which are computed for July to October due to the draining of the pond in May 2019. N/A indicates missing data due to an equipment failure.

| Year / Location | Auburn Bay | | | Cranston | | | |
|-----------------|------------------------|---------------|---------------|---------------|---------------|---------------|---------------|
| | IN | MID | OUT | IN | MID | OUT | |
| 2018 | Depth ¹ (m) | N/A | 1.9 \pm 0.6 | 1.7 \pm 0.6 | 1.1 \pm 0.5 | 2.2 \pm 0.6 | 1.8 \pm 0.6 |
| | Strength (°C/m) | N/A | 5.1 \pm 4.3 | 4.5 \pm 3.5 | 7.1 \pm 4.6 | 5.2 \pm 3.6 | 5.8 \pm 4.4 |
| | Max. Strength (°C/m) | N/A | 17.9 | 13.1 | 18.5 | 11.5 | 16.7 |
| 2019 | Depth ¹ (m) | 1.1 \pm 0.4 | 2.2 \pm 0.7 | 1.7 \pm 0.6 | 1.3 \pm 0.5 | 2.2 \pm 0.7 | 2.0 \pm 0.5 |
| | Strength (°C/m) | 5.4 \pm 3.1 | 4.8 \pm 3.0 | 5.1 \pm 3.0 | 3.9 \pm 2.8 | 3.1 \pm 2.6 | 3.3 \pm 2.2 |
| | Max. Strength (°C/m) | 13.5 | 11.0 | 13.0 | 9.9 | 8.7 | 8.5 |

¹ Average seasonal depth below NWL for thermocline strength above 1 °C/m

Table 3-5 Results of a linear regression analysis (slope and correlation coefficient R^2) using 2019 data between the absolute surface velocity (V) and wind speed (W) in the Auburn Bay and Cranston ponds at location V_m . All regressions are statistically significant at a 0.1% level ($p < 0.001$ using a t-test).

| Wind Direction | Auburn Bay | | Cranston | |
|-----------------------|--------------------|-------------------------|--------------------|-------------------------|
| | Slope (V/W) | R^2 | Slope (V/W) | R^2 |
| N | 0.27% | 0.66 | 0.24% | 0.51 |
| NE | 0.29% | 0.65 | 0.29% | 0.53 |
| E | 0.29% | 0.67 | 0.33% | 0.50 |
| SE | 0.35% | 0.66 | 0.26% | 0.75 |
| S | 0.42% | 0.74 | 0.24% | 0.64 |
| SW | 0.47% | 0.65 | 0.37% | 0.58 |
| W | 0.50% | 0.53 | 0.31% | 0.37 |
| NW | 0.51% | 0.62 | 0.25% | 0.42 |
| All Directions | 0.35% | 0.62 | 0.26% | 0.56 |

Table 3-6 Calculated wind durations in hours needed to mix two scenarios of $\Delta\rho$ and the maximum observed wind durations in the two study ponds. The highlighted cells are the calculated durations below the maximum observed durations in ponds when the wind can induce mixing.

| Pond | Duration (hr) | Wind Speed (m/s) | | |
|------|---|------------------|-----|-----|
| | | 4 | 6 | 8 |
| AB | Calculated to mix $\Delta\rho = 0.50 \text{ Kg/m}^3$ | 27.3 | 8.1 | 3.4 |
| | Calculated to mix $\Delta\rho = 0.25 \text{ kg/m}^3$ | 13.7 | 4.1 | 1.7 |
| | Maximum observed | 14.1 | 5.8 | 1.8 |
| CR | Calculated to mix $\Delta\rho = 0.50 \text{ Kg/m}^3$ | 17.5 | 5.2 | 2.2 |
| | Calculated to mix $\Delta\rho = 0.25 \text{ kg/m}^3$ | 8.7 | 2.6 | 1.1 |
| | Maximum observed | 10.1 | 4.1 | 0.9 |

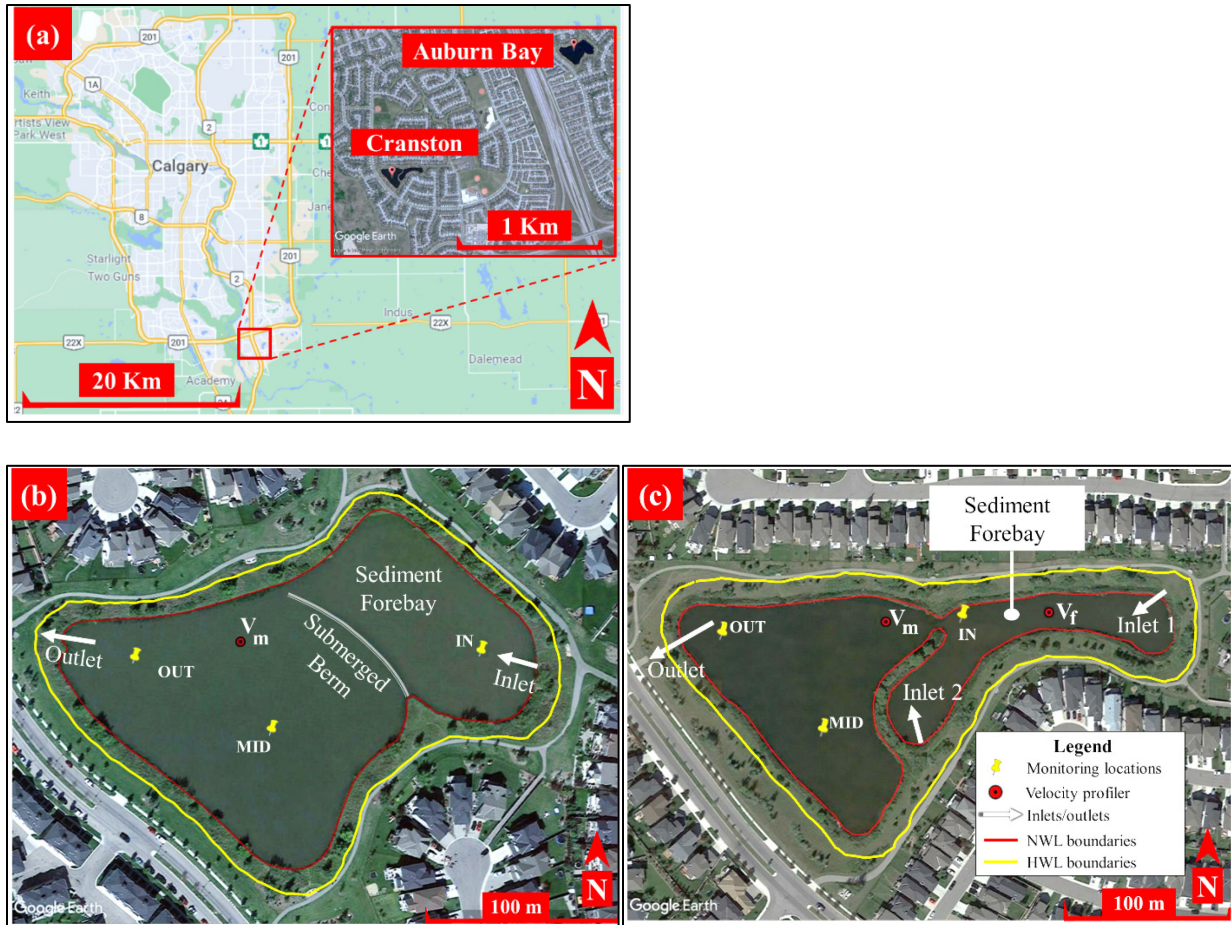


Figure 3-1(a) Map of the City of Calgary, Canada, showing the location of the two study sites; (b) and (c) satellite images of the Auburn Bay and Cranston wet ponds, respectively. The red and yellow lines in (b) and (c) indicate the normal and high water level boundaries, respectively, and the white arrows show the location of inlets and outlets. Yellow pins labelled IN, MID, and OUT in each pond are in-pond monitoring locations near the inlet(s), middle, and outlet, respectively. Red dots labelled V_m and V_f are the deployment locations of the current profilers. [Images' source: Google Earth Pro 7.3.4.8248. (August 31, 2017). City of Calgary, Alberta, Canada. <<http://www.google.com/earth/index.html>> (Accessed January 22, 2022)]. [Map's source: Google Maps. Retrieved January 22, 2022, from <https://goo.gl/maps/22uRPTqEVXdxUaYSA>]

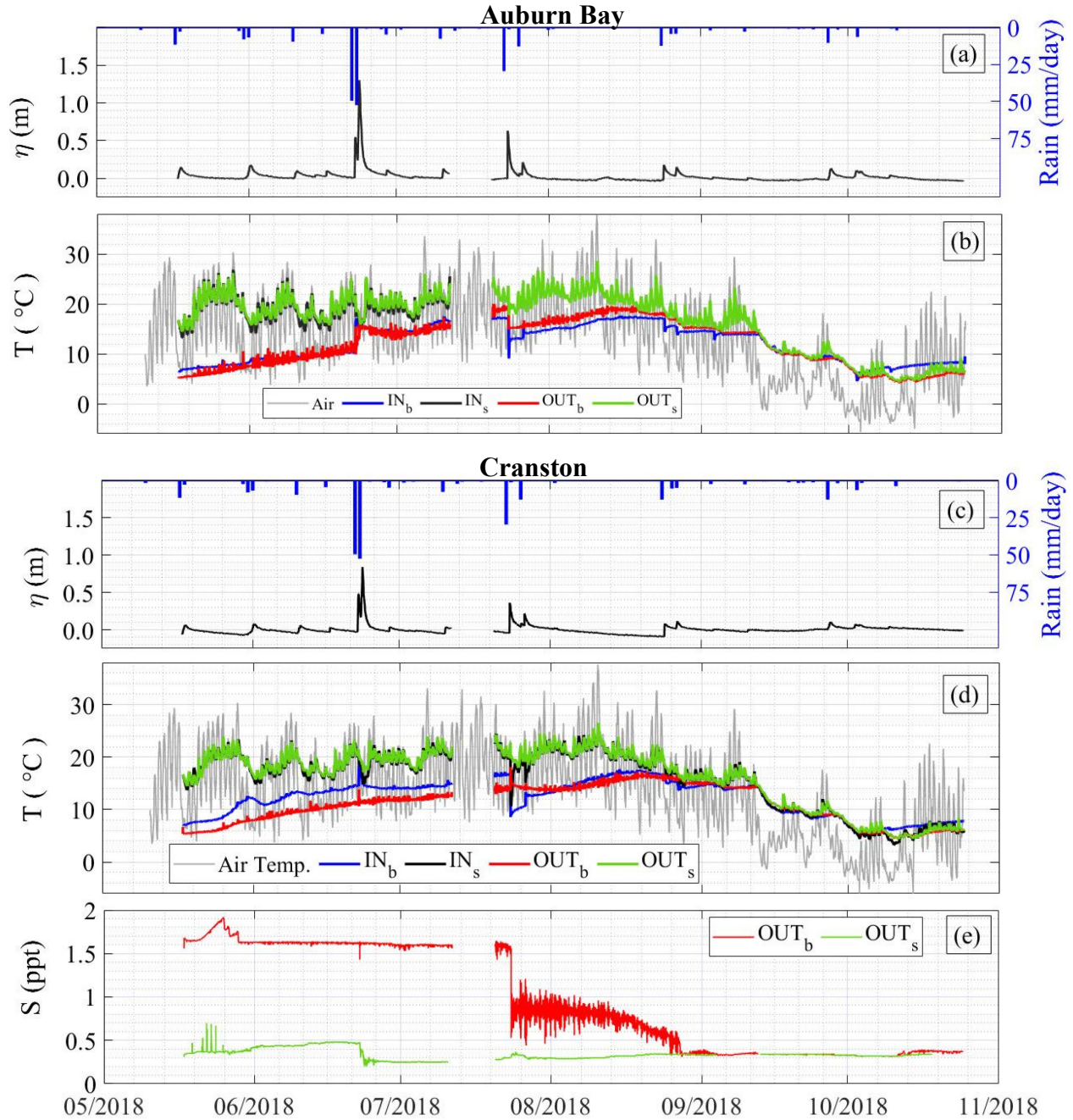


Figure 3-2 Time series measured in the Auburn Bay and Cranston ponds in 2018. (a,c) measured water depth (η) above NWL, 1041 m, (left axis) and rainfall intensity (right axis), (b) air temperature and water temperature at locations IN & OUT \sim 35 cm above the bed for IN_b & OUT_b and \sim 20 cm below the NWL for IN_s & OUT_s , IN_s time series ended on July 11 due to instruments

battery depletion, (d) air temperature and water temperature at locations IN & OUT, ~35 cm from the bed for IN_b & OUT_b, and ~ 35 cm from the NWL for IN_s & OUT_s, and (e) water salinity at OUT ~ 40 cm from the bed for OUT_b, and ~ 80 cm from NWL for OUT_s. In July, the gap in data was when the instruments were retrieved for maintenance and battery change.

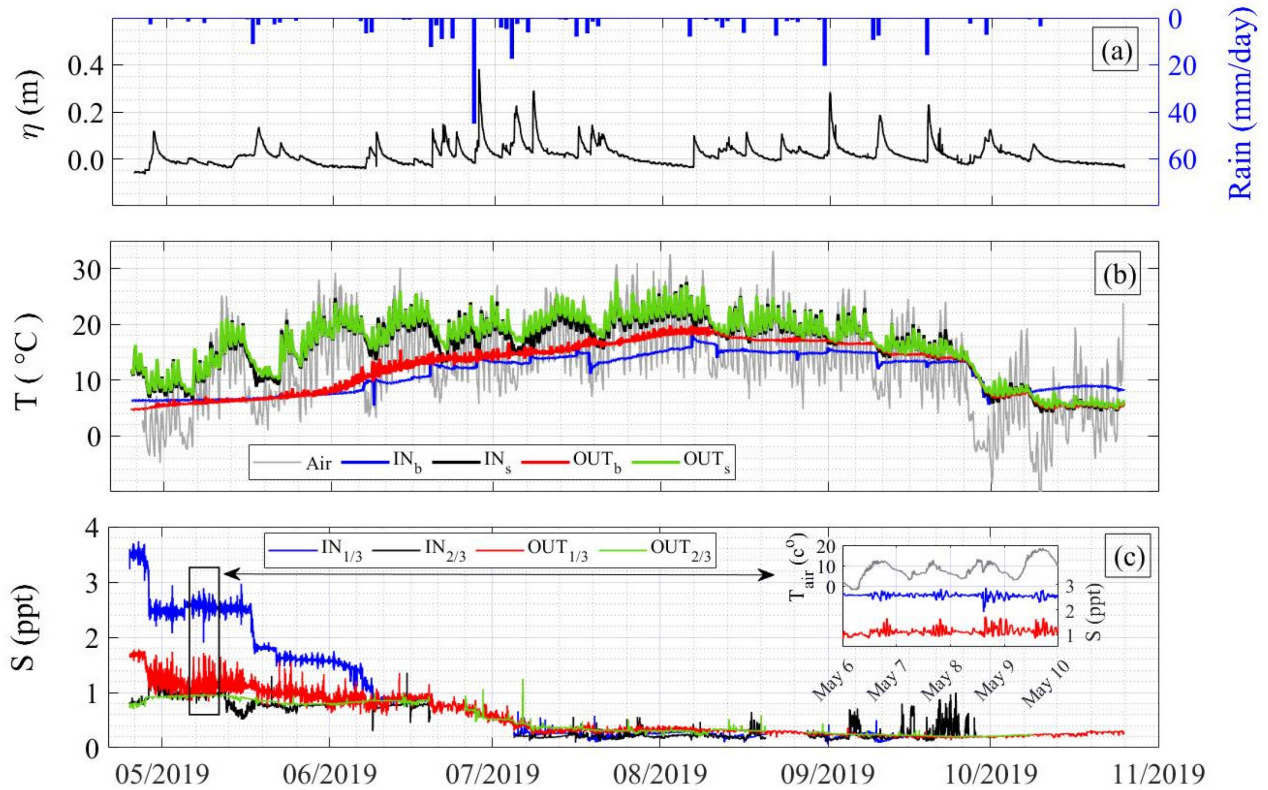


Figure 3-3 Time series measured in the Auburn Bay pond in 2019. (a) the measured water depth (η) above NWL, 1041m (left axis) and rainfall intensity (right axis), (b) air temperature and water temperature at locations IN & OUT, ~ 25 cm above the bed for IN_b & OUT_b , and ~ 10 cm below the NWL for IN_s & OUT_s , and (c) water salinity at locations IN & OUT above the bed by one-third of the water depth for $\text{IN}_{1/3}$ & $\text{OUT}_{1/3}$ and two-thirds of the water depth for $\text{IN}_{2/3}$ & $\text{OUT}_{2/3}$. $\text{IN}_{1/3}$ time series ended on September 15, and $\text{OUT}_{2/3}$ ended on October 8 due to instrument battery depletion. Data inside the zoomed-in plot show more details for May 6-10.

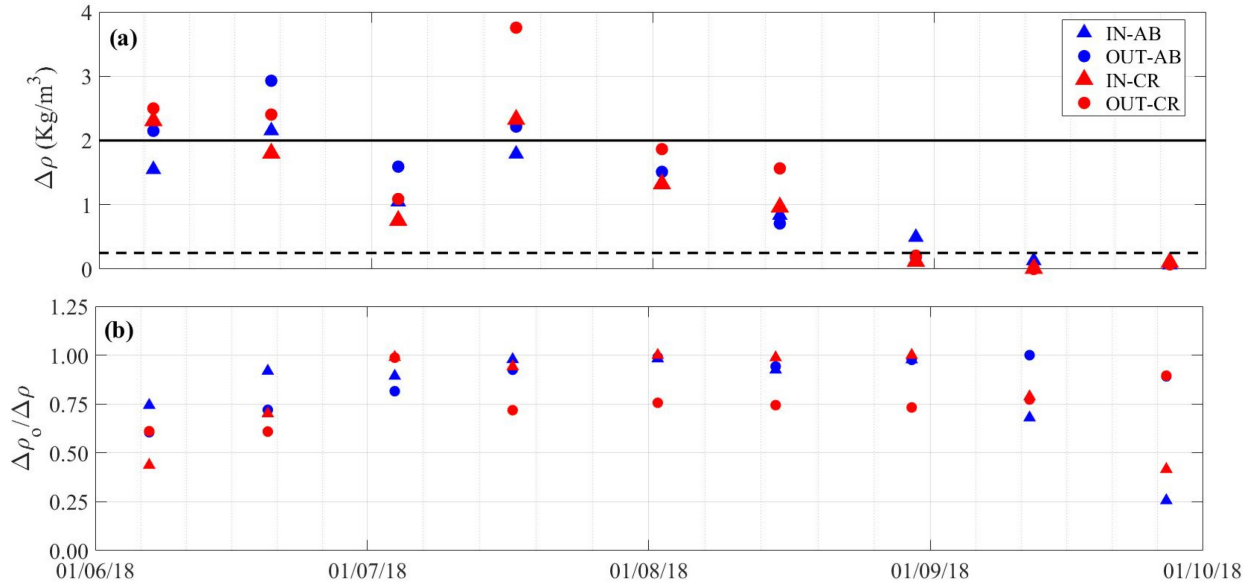


Figure 3-4 Results from Auburn Bay (AB) and Cranston (CR) in 2018 of (a) surface-bed density differences $\Delta\rho$, and (b) the ratio of the freshwater surface-bed density difference and the in-pond water surface-bed density difference computed from the fortnightly profile data in 2018.

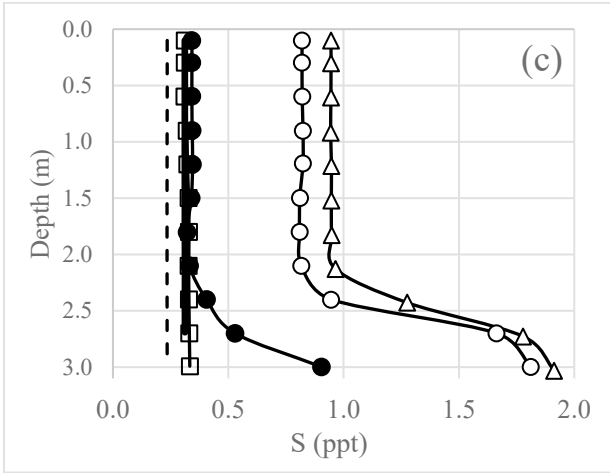
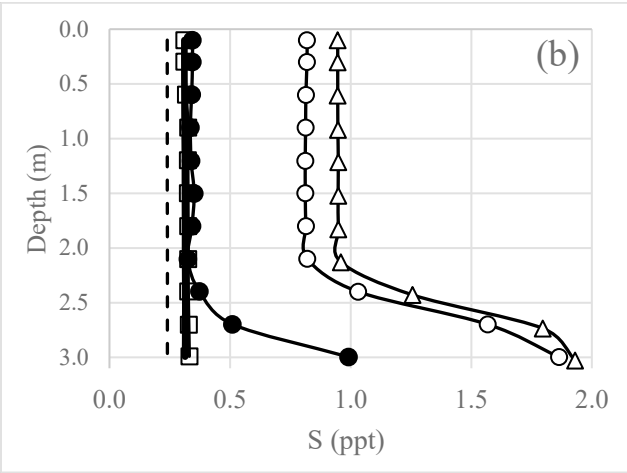
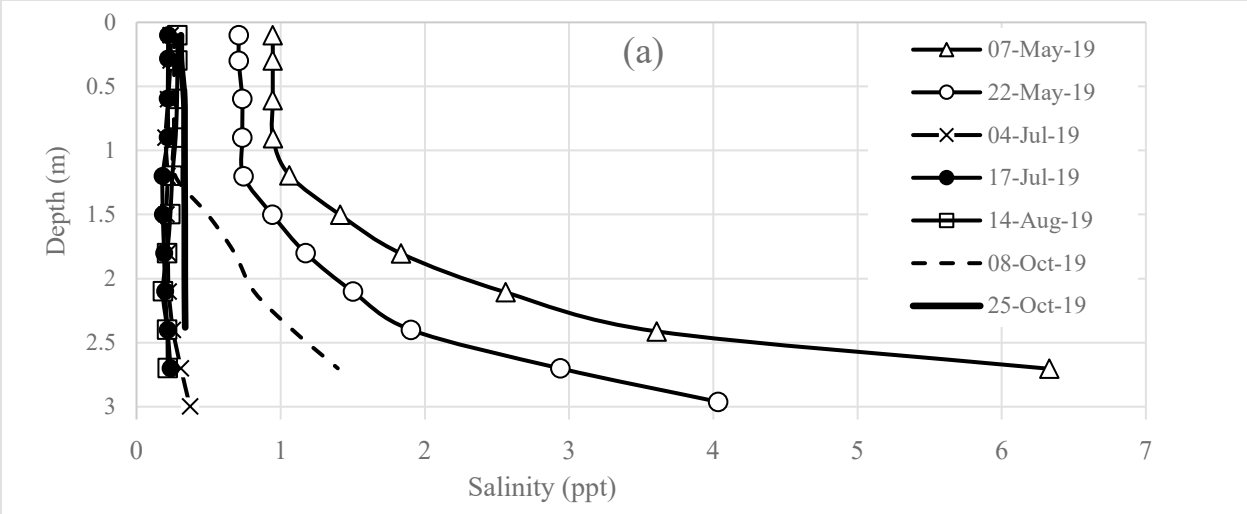


Figure 3-5 Water salinity profiles in the Auburn Bay pond in 2019 at locations (a) IN, (b) MID, and (c) OUT.

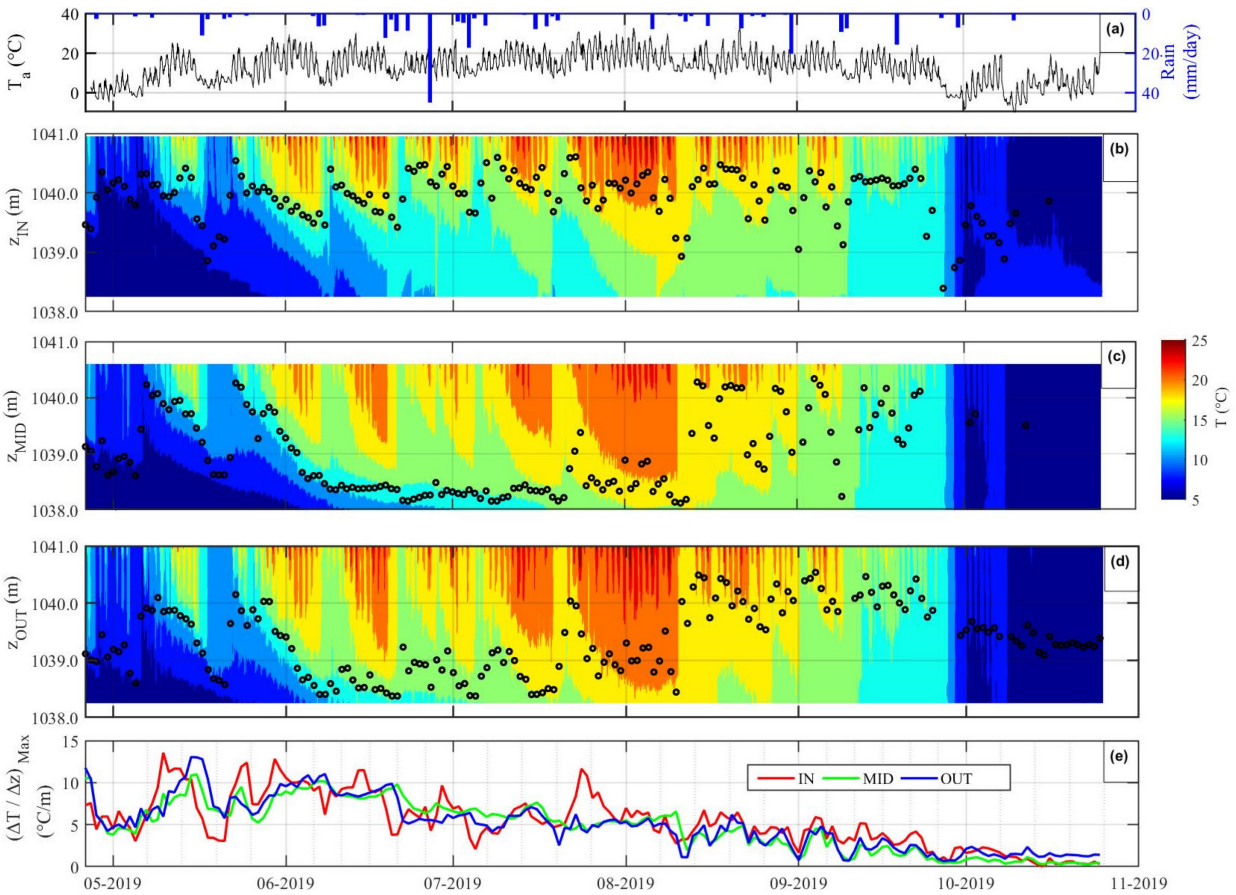


Figure 3-6 Results from the Auburn Bay pond in 2019 showing time series of (a) air temperature (left axis) and rain intensity (right axis), (b), (c) & (d) colour contour plots of vertical water temperature profiles versus geodetic elevation at IN, MID, and OUT, respectively, black circles are the average daily thermocline elevation, and (e) daily averaged thermocline strength time series at the three monitored locations. Gaps in data at the bottom of the water column at IN and OUT and at the top of the water column at MID are due to equipment loss.

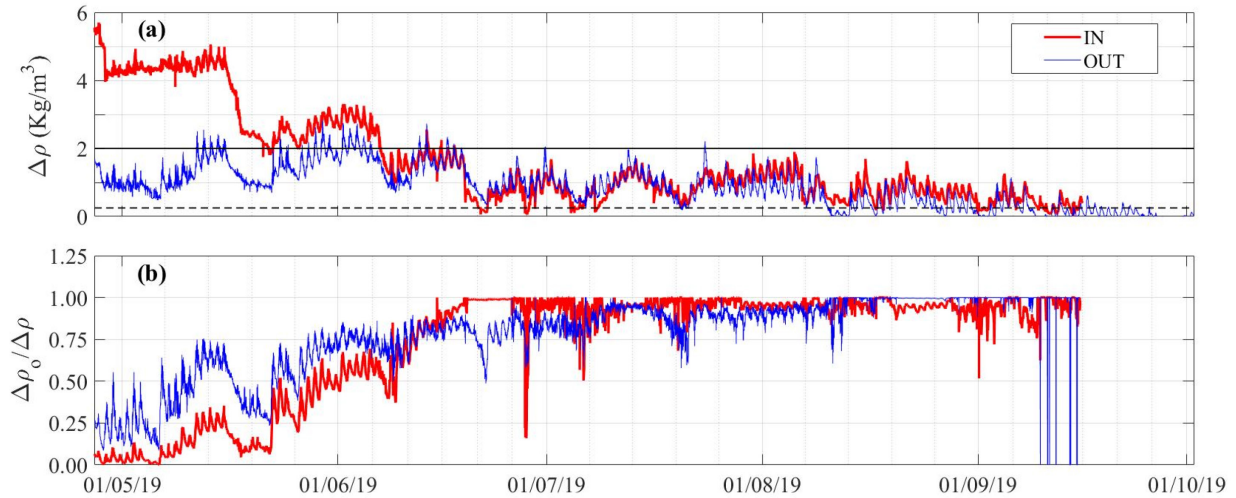


Figure 3-7 Results from the Auburn Bay pond in 2019 showing time series of (a) the surface-bed density differences $\Delta\rho$ and (b) $\Delta\rho_0/\Delta\rho$, the ratio of the freshwater surface-bed density difference to the surface-bed density difference. The dashed and the solid horizontal lines in the plot (a) at 0.25 and 2 Kg/m^3 are the thresholds between mixed, stratified, and strongly stratified water columns. The IN time series in plot (a) ended on September 15 due to a battery depletion of the conductivity sensor.

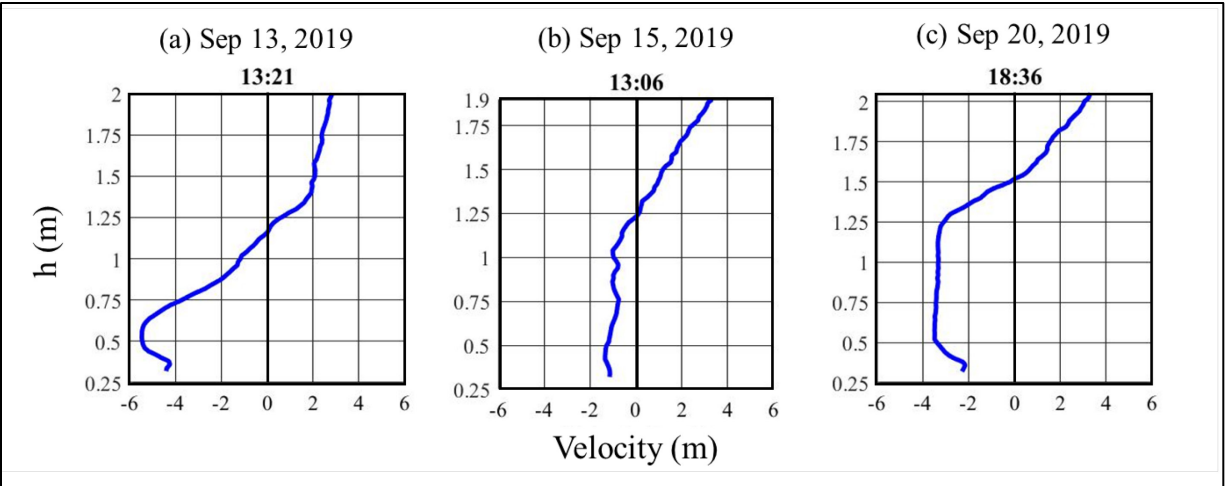


Figure 3-8 Water velocity vertical profiles at the Cranston pond, location V_f on (a) September 13, 2019, (b) September 15, 2019, and (c) September 20, 2019. Positive velocity flows towards the northeast or 60° clockwise from the north, and negative velocity flows towards the southwest or 240° clockwise from the north.

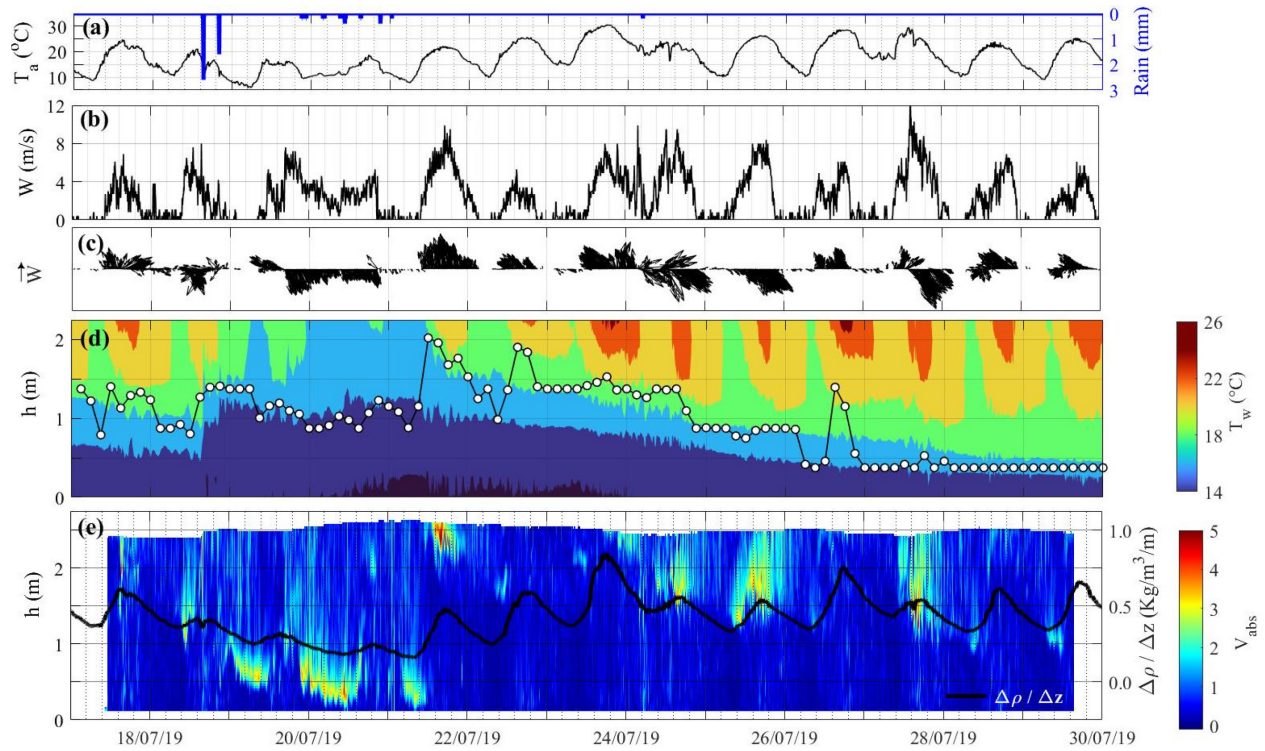


Figure 3-9 Data measured at the Cranston pond, location V_m , between July 17 and 30, 2019, (a) air temperature and rain depth, (b) wind speed, (c) wind direction, (d) 2D vertical water temperature profiles at location IN, white circles are the thermocline height averaged over 3 hours, and (e) 2D absolute water velocity profiles versus height above the bed (h) at location V_m (left axis), and the black line is the pond averaged water column density gradient, $\Delta\rho/\Delta z$ (right axis)

4. Stratification and its consequences in two constructed urban stormwater wetlands*

4.1 Introduction

Constructed urban stormwater wetlands are generally designed to resemble natural marshes with shallow pools and channels that allow for the growth of various plants (Cappiella et al., 2008). Although stormwater wet ponds and wetlands are similar in many aspects, they differ in vegetation design and water depth (City of Calgary, 2011). A wet pond has a greater portion of deep water zones, 2-3 m, and its aquatic vegetation is concentrated along the perimeter (City of Calgary, 2011). While wetlands are dominated by shallower water and are often thoroughly and densely vegetated (Chimney et al., 2006; City of Calgary, 2011; Ji and Jin, 2020). Constructed wetlands are one of many structural best management practices that have been extensively used over the years for stormwater management, and they are now widely used for water quality improvement (Carleton et al., 2001; Schulz and Peall, 2001; Chimney et al., 2006; Ji and Jin, 2020). Constructed stormwater wetlands mimic the naturally-occurring pollutant removal processes (physical, biological, and chemical processes) in natural wetlands, providing a low-maintenance and operationally simple water-treatment solution (Chimney et al., 2006; Rousseau et al., 2008; Headley and Tanner, 2012; Ji 2017; Melbourne Water, 2017; Schwammberger et al., 2020). The buffering and attenuation of stormwater flows by permanent pools and aquatic vegetation promote sedimentation by reducing bottom shear stresses and bed erosion (Mazda et al., 2006; City of Calgary, 2011; Jin and Ji, 2015). Other mechanisms for water quality improvement in wetlands

* The content of this chapter has been submitted as a journal manuscript: Ahmed, S.S., Zhang, W., Loewen, M.R., et al. (2022). Stratification and its Consequences in Two Constructed Urban Stormwater Wetlands. *Sci. Total Environ*, Manuscript ID STOTEN-D-22-24906, under review.

include filtration by vegetation, adsorption, and biological uptake (Reed et al., 1995; Wand et al., 2007; City of Calgary, 2011; Schwammburger et al., 2020). In addition, the microorganisms attach to roots and rhizomes form a biofilm that breaks down pollutants and organic matter (Stewart et al., 2008; Tanner et al., 2011; Winston et al., 2013).

Stratification in wetlands may inhibit vertical mixing and affect hydrodynamics and therefore nutrient and pollutant removal and the quality of outflow water (Kadlec and Knight, 1996; Ford et al., 2002; Jenter and Schaffranek, 2003; Chimney et al., 2006; Yang et al., 2018; Singh et al., 2019; Ji and Jin, 2020; Nakhaei et al., 2021). For instance, thermal and chemical stratification can alter physical, chemical and biological processes such as the settling and resuspension of sediments, the uptake of nutrients by vegetation and algae, and the release of nutrients from the bottom sediments (Olding et al., 2000; Ford et al., 2002; Chimney et al., 2006; Singh et al., 2019). The potential adverse effects of stratification on water quality include causing hypoxia or even anoxia near the bed (Singh et al., 2019; Ji and Jin, 2020). The water is anoxic when oxygen levels are at zero and hypoxic when dissolved oxygen concentrations are less than 2-3 mg/L (CENR, 2000; Lake Simcoe Region Conservation Authority, 2010; Chen et al., 2019; EPA, 2023). Anoxia and hypoxia can remobilize metals and nutrients from the bed (Singh et al., 2019), enhance the growth of algae blooms, causing eutrophication (Diaz and Rosenberg, 2008), and generate toxicants such as hydrogen sulphide and ammonia (Teichreb, 2012; D'Aoust et al., 2017; Chen et al., 2019). Eutrophication and algal blooms are one of the primary reasons for poor water quality in stormwater ponds and wetlands (Nakhaei et al., 2021). In addition, the discharge of stormwater water with low dissolved oxygen may harm the ecological functioning and biodiversity of the receiving water bodies (Diaz and Rosenberg, 2008; Yadav et al., 2016).

Thermal and chemical stratification in ponds, wetlands and shallow lakes are influenced by a combination of local climate conditions, the facility's design and others (Olding, 2000; Ford et al., 2002; Marsalek, 2003; Chimney et al., 2006; McEnroe et al., 2013; Song et al., 2013; Yang et al., 2018; Nakhaei et al., 2019; Singh et al., 2019). For example, thermal stratification in a stormwater pond in Calgary, Canada, was found to be primarily caused by warmer daytime air temperatures before it vanished several hours after sunset due to air cooling combined with wind action (He et al., 2015). Atmospheric instability, defined as air-water temperature difference, can also alter thermal stratification by changing the surface heat fluxes (Derecki, 1981; Imberger and Patterson, 1989). In wetlands, atmospheric instability can be more substantial relative to large lakes and oceans due to the more significant heating or cooling of the surrounding land surface (Katsaros, 1998). Precipitation may also affect stratification as it generates stormwater runoff that can be colder or warmer than that in the receiving wetland (McEnroe et al., 2013). Design features and morphometric characteristics, particularly pond depth, can influence thermal and chemical stratification (McEnroe et al., 2013; Song et al., 2013; Yang et al., 2018). In addition, wetland vegetation contributes to the physical processes by altering light and water temperature (Chimney et al. 2006). Furthermore, chemical stratification caused by accumulated road deicing salts in northern climates is known to occur in stormwater management facilities (Marsalek, 2003).

The hydrodynamics in wetlands and shallow lakes can be complex and dynamic because of the combined effect of inflow, wind, stratification, morphometry and vegetation design of the wetland (Jenter and Schaffranek, 2003; Bentzen et al., 2008 and 2009; Yang et al., 2018; Ji and Jin, 2020; Rey et al., 2020 and 2021). For instance, vertical thermal and chemical stratification can force the runoff from the inlet to the outlet to move above or below the thermocline, creating dead zones and reducing the pollutant's retention capacities (Yang et al., 2022; chapter 3 of the current study).

In addition, stratification can inhibit the transport of wind energy from the epilimnion to the hypolimnion, causing anoxic conditions near the bed (Novotny and Stefan, 2012). Although wind forces were reported to transfer momentum more efficiently to the bottom of shallower water bodies with a depth of < 2m (Józsa, 2014; Andradóttir and Mortamet, 2016), the flow resistance caused by the submerged/emergent aquatic vegetation in wetlands can significantly reduce the flow velocity and change the flow pattern (Jin and Ji, 2015). Hence, in slowly flowing wetlands, thermally-driven convection can be the dominant mixing mechanism (Jenter and Schaffranek, 2003). The physical processes occurring due to the interactions between the atmospheric forcing and the wetlands' design features must be understood to aid municipal water managers and engineers in designing stormwater wetlands to reduce nutrient and sediment release to downstream receiving waters.

Despite a large amount of research, the optimal design, operation and management of a constructed wetland have not yet been determined due to the high cost of gathering data accounts for the difficulty of accurately investigating the performance of existing stormwater facilities (City of Calgary, 2011; Nakhaei et al., 2019; Ji and Jin, 2020). As a result, stormwater wetlands have varying degrees of success in removing sediments, nutrients, and other pollutants before discharge into receiving water bodies (Carleton et al., 2001; Birch et al., 2007; Song et al., 2013; Chiandet and Xenopoulos, 2016; Ji and Jin, 2020). Consequently, there is an ongoing need to understand the complex physical processes affecting the hydrodynamics and contaminants' transport and fate in these stormwater facilities to improve future designs and optimize their operations (Ji and Jin, 2020). This was the motivation for a comprehensive 2-year field monitoring program that was undertaken to continuously monitor two nearby constructed stormwater wetlands in Calgary, Alberta, Canada, during the ice-free seasons (May - October) in 2018 and 2019. The effects of the

differences in the design characteristics of the two wetlands, including physical dimensions, water level fluctuations and vegetation design, were investigated and discussed. The response of the two wetlands to atmospheric forcing (e.g., rainfall, wind, solar radiation, air temperatures and atmospheric instability) were examined. The strength and persistence of thermal and chemical stratification at different locations within the wetlands were evaluated and compared with stormwater ponds and constructed wetlands in the literature.

The current study provides novel results regarding stratification, hydrodynamics and water quality in two 0.8m deep constructed wetlands. Although significant thermal, chemical, and densimetric stratification has been previously reported in wet ponds and shallow lakes (2-4m deep), causing hypoxia near the bed (Mayer et al., 2008; He et al., 2015; Yang et al., 2018), it does not appear that the implications of stratification and hydrodynamics on water quality have been previously investigated in shallow (<1.0 m deep) constructed wetlands. In addition, this study reports marked differences in temperature and thermal stratification in the two nearby study wetlands, which are only 0.25 km apart, due to differences in their design, which are relevant to the development of future design guidelines.

4.2 Study wetlands and methods

4.2.1 Study wetlands

The two constructed stormwater wetlands are located in the communities of Royal Oak and Rocky Ridge (51° 8.8'N and 114° 14.1'W) in northwest Calgary (Figure 4-1). Table 4-1 presents the characteristics of the two facilities and their associated catchments. The land use in the two catchment areas is predominantly single and multi-family residential, with the percent imperviousness ranging from 50% to 60% (Table 4-1). Royal Oak and Rocky Ridge wetlands have

catchment areas of 18.3 and 15.1 ha, and their surface areas at the normal water level (NWL) are 5,500 and 11,400 m², respectively. The average normal water depth in these two wetlands is about 0.8 m; however, the permanent pool volume is significantly bigger in Rocky Ridge than in Royal Oak at 5,750 and 2,500 m³, respectively. Royal Oak has two inlets: Inlet 1 discharges into the outlet basin, draining a small and negligible catchment area of less than 0.1 ha, and Inlet 2 drains a catchment area of 18.3 ha into a sedimentation forebay of ~1.3 m depth (Figure 4-1a). The forebay is designed to facilitate maintenance and improve pollutant removal by trapping larger particles near the inlet of the wetland and is intended to be the deepest area of the wetland to minimize the potential for particle resuspension. A submerged berm separates the forebay from the main water body to prevent the conveyance of the suspended materials to the outlet (Figure 4-1b). Downstream of the forebay, the depth decreases to ~0.7 m; the water then flows through a heavily vegetated narrow channel where the water depth reduces to ~0.3 m at NWL and then discharges into a smaller, deeper (~0.6 m) basin (referred to as the outlet basin) near the outlet pipe. Rocky Ridge does not have a sedimentation forebay; instead, the design of this facility includes an inlet structure that diverts the first flush of a storm event into a sedimentation vault (settling basin) with an overflow weir and bypass pipe upstream of the wetland. The sedimentation vault consists of one chamber where floatable debris is trapped, and gravity settling of coarse sediments occurs prior to discharging to the wetland. The average water depth of ~0.8 m is fairly uniform across the Rocky Ridge wetland (Table 4-1). Both wetlands have an outlet control structure equipped with a weir and an orifice to regulate the outflow discharge and maintain their NWL. Three locations were selected in each wetland, near the inlet, the middle and the outlet, for continuous water quality monitoring, i.e., locations IN, MID and OUT in Figure 4-1b,c.

The vegetation communities and their spatial distribution are presented in Figure 4-2. A total of two aquatic vegetation communities and one riparian vegetation community were identified during a ground-based field survey in June 2019. The dominant aquatic vegetation included pondweed species and spiked water milfoil, while the riparian vegetation was mainly the common cattail (*Typha latifolia*). In the two wetlands, patches of collapsing aquatic vegetation were evident (Figure 4-2). Rocky Ridge had denser submerged aquatic vegetation that grew up to the water surface (Figure 4-3a), with a canopy cover of over 90% of the water surface area at the NWL versus only 40% in Royal Oak. The riparian vegetation was much denser in Royal Oak, especially at the narrow channel and the outlet basin (Figures 4-2a and 4-3b).

4.2.2 Field measurement in the wetlands

Solar-powered meteorological data loggers on the top of hinged flagpoles at 10 m height were used at Rocky Ridge (HOBO U30, Onset, USA) and Royal Oak (HOBO RX3000, Onset, USA). Six sensors sampling at 5 minutes intervals were connected to the data loggers, including a rain gauge sensor (S-RGB-M002), a 12-bit temperature/relative humidity sensor with a solar radiation shield (S-THB-M002), a solar radiation sensor (S-LIB-M003), a barometric pressure sensor (S-BPB-CM50), a wind speed sensor (S-WSB-M003), and a wind direction sensor (S-WDA-M003). Both sites acquired continuous data from May 10 to October 25, 2018, and from April 25 to October 25, 2019. The data were downloaded in situ from the HOBO U30 logger every month, while the wireless cellular HOBO RX3000 data logger was used to schedule all data to be automatically uploaded online every 1 hour.

A summary of the meteorologic data statistics gathered at the two wetlands in 2018 and 2019 is shown in Table 4-2. The two wetlands are only 250 m apart (Figure 4-1a), and as a result, the

meteorological conditions at the two sites were very similar. The average air temperature was warmer in 2018 than in 2019 (11.9 and 10.8 °C). Fewer wet days with rainfall depth > 0.2 mm were observed in 2018 compared to 2019 (35% versus 43%). Wet weather had cooler air temperatures than dry weather in the two years (7.5 °C versus 11-12 °C) (Table 4-2). The total rainfall depth at the two ponds was significantly higher in 2019 than in 2018 at 397-400 mm compared to 185-201 mm. The prevailing wind directions were from the north and the west at both wetlands. The higher wind speed in Royal Oak than in Rocky Ridge, which was more evident in 2019, at 2.7 and 1.7 m/s, is likely because Royal Oak is less sheltered by mature vegetation and houses on the west side (Figure 4-1a). The consistently lower average wind speed in Rocky Rocky in the two years at 1.6-1.7 m/s is likely because this wetland is sheltered by houses and matured vegetation on the north, south and west sides (Figure 4-1a). The solar radiation was slightly higher in Royal Oak than in Rocky Ridge by < 5% (Table 4-2). The slight difference in solar radiation was because both weather stations were quite high (>10m) above the wetlands and mounted on the west side of Royal Oak and the east side of Rocky Ridge, which were less sheltered by mature vegetation and houses (Figure 4-1a).

Moored instruments were deployed at the three monitoring locations, IN, MID, and OUT, in the two wetlands to continuously sample various water quality parameters' horizontal and vertical variability. The water temperature was sampled at 5-minute intervals using HOBO MX2203 TidbiT (Onset, USA) loggers installed at a vertical resolution of 10 cm. The bed temperature, T_b , was measured using sensors on the bed, while the water surface temperature, T_s , was measured using sensors mounted within 10 cm below the NWL. In addition, TD-Diver or Micro-Diver and CTD-Diver (Van Essen Instruments, Netherlands) loggers were used to measure depth, conductivity and water temperature, and HOBO U26-001 dissolved oxygen (DO) data loggers

(Onset, USA) sampled at 5-minute intervals. The instruments were mounted on a vertical steel post attached to a horizontal base. In-pond measurements were collected from May 25 to October 25, 2018, and from April 25 to October 25, 2019. In addition, twenty-five (25) fortnightly field trips to the wetlands were conducted between June 6 and October 26, 2018, and from April 25 to October 25, 2019. During these trips, high-resolution vertical profiles for temperature and conductivity were conducted at the three locations in each facility using an EXO2 water quality sonde (YSI, USA).

In the middle of the two wetlands (location V_m in Figure 4-1b,c), an Acoustic Doppler Velocimeter (ADV) (Vector-300m Cable Probe GA, Nortek, Norway) with an accuracy level of 1 mm/s was deployed to measure 3D velocities at 10 cm below the water surface. The ADV was programmed to collect 100 samples at a rate of 1 Hz every 15 minutes. The 100 samples were then averaged to create mean velocities. The water velocity was measured continuously for four months between May 6 and July 3, 2019, in Rocky Ridge and July 3 to August 27, 2019, in Royal Oak. Location V_m was chosen away from the inlets and outlets to minimize the effects of currents generated by inflows and outflows and maximize the impact of wind-generated currents. Linear regression analysis was performed between the magnitudes of the water surface velocity, V , and the wind speed, W , for eight different wind directions. For example, the north wind includes directions within an angle of 45° between -22.5° and $+22.5^\circ$ with zero defined at true north.

4.2.3 Analysis methodology

The current study used water depth fluctuations in the wetlands to represent the magnitude and duration of rainfall-runoff events. Continuous accurate measurements of water levels in both

wetlands are presented instead of the intermittent inflow and outflow discharge measurements due to occasional malfunction of the flow meters that created significant gaps in the data.

The thermal gradient that characterizes the occurrence of thermal stratification is not consistent in the literature and varies from 0.1°C/m to 1.0°C/m (Keller and Pires, 2002; Abis and Mara, 2006; Boegman et al., 2008; McEnroe et al., 2013; Nakhaei et al., 2019). The current study used a vertical temperature gradient $\Delta T/\Delta z > 1$ °C/m to indicate the occurrence of a significant thermal stratification due to the precision of our temperature sensors at ± 0.2 °C. Even though a vertical temperature gradient as low as 0.14 °C/m could inhibit mixing in the water column (Boegman et al., 2008).

Salinity and water density were calculated using standard equations from conductivity and temperature measurements following (APHA 1989) (See equations 3-1 to 3-6). Densimetric stratification in the wetlands was quantified using a vertical density gradient between the surface and bottom water, $\Delta\rho/\Delta d$, where d is the water depth measured downward from the normal water level. Boegman et al. (2008) reported that a $\Delta\rho/\Delta d$ of 0.07 kg/m³/m could reduce vertical mixing in a 7 m deep lake in North America. The current study uses a vertical density gradient $\Delta\rho/\Delta d$ of 0.08 kg/m³/m as a threshold for the densimetric stratification, which is equivalent to a $\Delta\rho$ of 0.25 kg/m³ used in Chapter 3 in two 3 m deep stormwater ponds in Calgary, Alberta, Canada, to identify the presence of their densimetric stratification. Positive and negative values of $\Delta\rho/\Delta d$ indicate stable and unstable stratification, respectively. The freshwater bed-surface density difference, $\Delta\rho_o$, is calculated as a function of temperature only (i.e. assuming the salinity is zero). The ratio $(\Delta\rho - \Delta\rho_o)/\Delta\rho$ is used to quantify the relative strength of chemical stratification to the total or densimetric stratification in the wetlands.

4.3 Results and discussion

4.3.1 Thermal stratification

Time series of rainfall intensity I , water depth above the NWL η , air temperature T_a , vertical temperature gradient $\Delta T/\Delta z$, and 2D colour contour plots of water temperature profiles and the number of days of continuous thermal stratification are plotted for the two wetlands in 2019 in Figures 4-4 and 4-5. Similar results for the two wetlands in 2018 are presented in Figures 4-6 and 4-7. The maximum rainfall depths of 81, 31 and 28 mm on June 21, 27 and July 4 in 2019 resulted in water level increases above the NWL by 1.07, 0.54 and 0.27 m in Royal Oak and 0.48, 0.26 and 0.10 m in Rocky Ridge (Figures 4-4a,b and 4-5a,b), respectively. The water level increases in Rocky Ridge were approximately half as large as in Royal Oak following the same rainstorm events (Figures 4-4b and 4-5b) because the wetland surface area to the catchment area ratio in Rocky Ridge is ~ 2.5 times larger than in Royal Oak (Table 4-1).

Diurnal fluctuations in air temperature are evident in Figures 4-4a, 4-5a, 4-6a and 4-7a and typically generated diurnal fluctuations in the vertical temperature gradients $\Delta T/\Delta z$ in the two wetlands at IN, MID and OUT (see Figures 4-4c, 4-5c, 4-6c and 4-7c). For instance, the vertical water temperature gradient, $\Delta T/\Delta z$, daily averaged and averaged over the entire wetland was linearly correlated with air temperature in summer between May and August in the two years, with coefficients of determination R^2 of 0.72 in Royal Oak and Rocky Ridge (Figures 4-8). However, the correlation slope was higher in Rocky Ridge than in Royal Oak at 0.30 and 0.21 °C/m per 1 °C rise in air temperature (Figure 4-8), indicating stronger thermal stratification in Rocky Ridge. Thermal stratification was also reported to be primarily caused by fluctuating air temperatures in stormwater wetlands and ponds in a number of North American studies (Jenter and Schaffranek,

2003; He et al., 2015). In addition, the vertical water temperature gradient, $\Delta T/\Delta z$, daily averaged and averaged over the entire wetland was inversely correlated with the atmospheric instability $T_s - T_a$ between May and August in the two years. The correlation was slightly more robust in Royal Oak than in Rocky Ridge, with R^2 of 0.43 and 0.32, respectively (see Figure 4-9). For instance, Royal Oak and Rocky Ridge were thermally mixed at $\Delta T/\Delta z < 1$ °C/m during days of high $T_s - T_a$ above 5 and 8 °C, according to the correlation in Figure 4-9. Similarly, Derecki (1981) used the air and water surface temperature difference ($T_s - T_a$) as a stability index in the Great Lakes and found a difference of 3.5–10.5 °C indicative of unstable conditions with high evaporation rates and heat losses.

Attenuations in the diurnal amplitudes of the vertical temperature gradient $\Delta T/\Delta z$ at IN, MID and OUT were notable during most wet days due to the turbulent mixing by stormwater inflows to the wetlands, e.g., June 6, 21, 27 and July 4 (Figures 4-4a-c and 4-5a-c). In addition, most rainstorm events in the two wetlands coincided with a drop in the diurnal air temperature, contributing to the attenuations in the $\Delta T/\Delta z$ amplitudes (Figures 4-4a,c and 4-5a,c). For instance, the air temperature was, on average, cooler during wet weather at ~ 7.5 °C compared to 11-12 °C in dry weather in the two years (Table 4-2). As a result, the stormwater inflows entering the wetlands near the bed following rainfall events might have cooled the bed, likely increased water turbidity and reduced light penetration at IN. This probably caused the higher vertical temperature gradient at IN than MID and OUT during dry days and surface heating (Figures 4-4c, 4-5c). In Royal Oak, location IN experienced continuous thermal stratification for extended periods of up to 21 consecutive days compared to 2 days at MID and less than one day at OUT (Figure 4-4,d-f), likely due to the deeper water column at IN (Table 4-1). In Rocky Ridge, although the depths were uniform and all monitored locations were within one open water body with no berms or baffles, the thermal

stratification persisted for up to 19 days of continuous thermal stratification at IN versus 3 days at MID and OUT (Figure 4-5,d-f). Similar results of more extended periods of thermal stratification at IN than MID and OUT were observed in 2018 in both wetlands (Figures 4-6d-f and 4-7,d-f). Similarly, the current study in chapter 3 related the stronger thermal stratification and the shallower thermocline depth near the inlets in two stormwater wet ponds in Calgary, Alberta, Canada, to the relatively cold summer inflows entering the ponds near the bed following rainfall events.

During the fall's first freezing air temperature event in late September 2019, the vertical temperature gradients decreased more severely in Rocky Ridge than in Royal Oak when air temperature abruptly dropped from above 10 °C to below 0 °C (Figures 4-4a,c and 4-5a,c). As a result, the vertical temperature gradient in Rocky Ridge dropped to -9, -6 and -5 °C/m at IN, MID and OUT, while it dropped to a less value at -3 °C/m everywhere in Royal Oak as a response to the late-September cooling event (Figures 4-4c and 4-5c). Following the second significant cooling event in mid-October, the temperature gradient dropped less severely in Rocky Ridge to -7, -4 and -4 °C/m at IN, MID, and OUT, while it decreased dramatically at Royal Oak to -4,-7 and -1 °C/m at IN, MID and OUT (Figures 4-4c and 4-5c). Hence, the temperature gradient during fall in wetlands is very dynamic, complex, and site-specific. The same conclusion applies to fall 2018 in Figures 4-6c and 4-7c.

Seasonally averaged values of depth-averaged and surface water temperatures and atmospheric instability are presented in Table 4-3. In Royal Oak, the water temperature was relatively colder in 2019 than in 2018, likely due to the cooler air temperature averaged at 10.8 °C in 2019 versus 11.9 °C in 2018. In addition, the higher wind speed in 2019, which was 1.5 times that in 2018 (Table 4-2), might have contributed to the release of more latent and sensible heat (Rouse et al., 2003). Furthermore, the higher atmospheric instability in 2019 than in 2018 might have also

resulted in more heat loss and cooler T_s in Royal Oak in 2019. For example, the atmospheric instability increased the annual heat loss from Lake Tanganyika, East Africa, by up to 18% (Verburg and Antenucci, 2010) and the latent and sensible heat fluxes in Slave Lake, Alberta, Canada, by 9 times (Rouse et al., 2003). However, in Rocky Ridge, T_{wc} and T_s were almost consistent in the two years, i.e. within 0.4 °C or less (Table 4-3), despite the differences in the atmospheric forcings T_a , T_s-T_a , and the annual rainfall depth (Tables 4-2 and 4-3). This might be due to the lower wind speed in Rocky Ridge, which was approximately half that in Royal Oak in 2019 (Table 4-2), slowing down the rate of cooling and heat loss relative to Royal Oak.

The average water column temperature between May and August was significantly higher in Rocky Ridge than in Royal Oak, especially at OUT, by up to 1.5-2.0 C° in the two years (Table 4-3). This is because shading through deciduous and coniferous trees along the edges of the outlet basin in Royal Oak likely lowered the water temperatures compared to Rocky Ridge (Figure 4-6a). Similarly, Schwammberger et al. (2020) suggested that the lower water temperatures at a stormwater retention pond compared to an artificial lake in Australia were probably due to shading by the overhanging trees. The water column temperature at OUT in Rocky Ridge was higher by > 3 °C than in Royal Oak for 10% of the sunniest months, June, July and August in 2019 (see Figures 4-4f and 4-5f). The high water temperatures near the outlet in Rocky Ridge might be a concern because the discharge of stormwater with elevated temperatures more than 3°C above the receiving water temperature could adversely affect aquatic fish and invertebrates that require cold water temperature conditions (Alberta Environment, 1999; City of Calgary, 2011).

The persistence of the thermal stratification in the two wetlands between May and October in the two years was computed using the unfiltered data (i.e. 5-minute sampling interval) at the three monitoring locations, and the results are presented in Table 4-4. The thermal stratification persisted

more at IN (51-62%) than Mid (28-46%) and OUT (28-41%) due to the relatively cold summer inflows that frequently cooled the bed at IN before it heated as it moved from inlets to outlets by the action of warm air temperatures and solar radiation. For instance, the near-bed water temperature between May and October in the two wetlands was lower at IN by 1.0-2.1 °C than at MID and 0.7-1.1 °C at OUT in Royal Oak and Rocky Ridge. In 2019, thermal stratification lasted longer than in 2018 at IN and MID due to the early onset of the fall turnover in 2018 by two weeks ~ 8% of the time (Figures 4-4a and 4-6a). However, at OUT, especially in Royal Oak, thermal stratification lasted significantly longer in 2018 than in 2019 (Table 4-4). The small volume of the outlet basin in Royal Oak likely caused higher variability in stratification between the two years (Table 4-4) due to the greater heating and cooling by the surrounding land and the generally lower wind speeds due to the surrounding riparian vegetation (Katsaros 1998).

Abis and Mara (2006) and the current study in chapter 3 used the surface-bed temperature difference above 1 °C as a threshold for thermal stratification in deeper ponds in the UK and Canada. Using the same criteria, the average duration of the thermal stratification between May and October in our wetlands was 39% versus 67% in the 1.5 m deep waste stabilization ponds in the UK (Abis and Mara, 2006) and 74% in the 3 m deep stormwater ponds in Alberta, Canada (refer to chapter 3). Therefore, thermal stratification is relatively ephemeral in shallow wetlands compared to the deeper urban ponds, where persistent stratification is the norm.

Stratification in lakes was related to the lake geometry ratio defined as $A_s^{0.25}/H_{\max}$, where A_s is the lake surface area (a surrogate for wind fetch) and H_{\max} is the maximum lake depth used as indicators to differentiate between stratified and mixed lakes (Gorham and Boyce, 1989; Stefan et al., 1996). Stefan et al. (1996) divided lakes into 27 classes covering geometry ratios from 0.9 to 14.1. Mixed lakes have high geometry ratios, while strongly stratified lakes occur at the lowest

numbers, with a transitional ratio between a permanent seasonal stratification (dimictic lakes) and intermittently stratified lakes (polymictic lakes) occurring between $2-5 \text{ m}^{-0.5}$ (Gorham and Boyce, 1989). In the current study, the 3 m deep stormwater ponds in chapter 3 have a lake geometry ratio of 3.8 versus 6.6 and 12.9 for the Royal Oak and Rocky Ridge wetland. Hence the full range of stratification behavior is included in the ponds and wetlands selected for the current study.

A vertical temperature gradient lower than $-1.0 \text{ }^\circ\text{C/m}$ indicates significant inverse thermal stratification. For example, significant inverse thermal stratification was observed 10-24% and 1-20% of the time in Royal Oak and Rocky Ridge, respectively (see Table 4-4). In addition, inverse thermal stratification occurred continuously for up to 18 and 16 days in October 2019 in Royal Oak (Figure 4-4c) and Rocky Ridge (Figure 4-5c), respectively. Similarly, Yang et al. (2018) observed a temperature inversion near the surface of a shallow lake in East China in the fall when the sediment became a heat source warming the bottom waters.

A summary of the statistics for the vertical temperature gradients at the three monitoring locations of the two wetlands is presented in Table 4-5. The average temperature gradient was the highest at IN ($1.5-2.6 \text{ }^\circ\text{C/m}$) compared to MID ($0.2-1.6 \text{ }^\circ\text{C/m}$) and Out ($0.2-1.4 \text{ }^\circ\text{C/m}$) due to stormwater inflows which cooled the bottom waters, and likely also increased the turbidity and reduced light penetration at IN. In addition, IN had the highest standard deviation in temperature gradients ($2.2-4.5 \text{ }^\circ\text{C/m}$ compared to $1.6-2.4 \text{ }^\circ\text{C/m}$ at MID and $1.7-2.3 \text{ }^\circ\text{C/m}$ at OUT), confirming that the temperature gradient fluctuates more frequently at IN due to the frequent stormwater inflow events. Similarly, the thermocline strength near inlets in two stormwater ponds in Alberta, Canada, was higher than the main cell and fluctuated more regularly due to the cooling effect of the near-bed inflows (refer to chapter 3).

The temperature gradients were higher in Rocky Ridge (0.9-2.6 °C/m) than in Royal Oak (0.2-1.9 °C/m), likely due to its denser submerged aquatic vegetation filling 90% of its surface area versus only 40% in Royal Oak (Figure 4-2). This was likely because much of the light that fell on the leaves of submerged aquatic plants, which extended to the surface (see Figure 4-3a), was converted into heat and radiated back to the water, causing a localized increase in near-surface water temperature, which is a well-known mechanism in developing thermal stratification in wetlands (Dale and Gillespie, 1977; Chimney et al., 2006). The greater length-to-width ratio in Royal Oak at 2:1 versus 1.25:1 in Rocky Ridge (Table 4-1) and its higher water level fluctuations which were double that in Rocky Ridge (Figures 4-4b and 4-5b), might also have resulted in better mixing of the stormwater runoff in Royal Oak during most inflow events resulting in a weaker thermal stratification (Cappiella et al., 2008; City of Calgary, 2011). For instance, the two significant rainstorm events on June 27 and July 4 in 2019 could thermally mix IN at Royal Oak at $\Delta T/\Delta z$ of 0.4 and 0.3 °C/m versus 1.3 and 1.0 °C/m at IN of Rocky Ridge (Figures 4-4,a-d and 4-5,a-d).

The average temperature gradient in the two wetlands at 1.3 °C/m is lower than the 2.9 °C/m observed by Song et al. (2013) in 10 deeper stormwater ponds in southern Ontario, Canada, with maximum depths of 0.7-2.5 m. Song et al. (2013) reported that the mean thermal stratification in their 10 urban ponds was strongly correlated with the maximum pond depth ($R^2 = 0.72$). Hence, the shallower depths of our wetlands at ~ 0.8 m most likely resulted in their lower temperature gradients.

4.3.2 Chemical stratification

Vertical profiles of salinity collected in both wetlands in 2019 are plotted in Figure 4-10. In the sediment forebay of Royal Oak at IN, a high water salinity near the bed of 4.0-4.5 parts per

thousand (ppt) and vertical salinity difference, $\Delta S = 2.5\text{-}3.5$ ppt, was observed in early May and October 2019 (Figure 4-10a). These chemical stratification events were due to salt-laden inflows from road runoff following below-zero air temperatures and snowmelt events (Figure 4-4a). However, at MID and OUT in Royal Oak, the water column was observed to be chemically mixed at all times with salinity ranging from 0.50 to 1.75 ppt (Figure 4-10b,c). In Rocky Ridge, all locations were chemically mixed, and salinity concentration was much lower at 0.1-0.4 ppt (Figure 4-10,d-f). Previous studies in northern climates have similarly observed increased salinity and strong chemical stratification in stormwater ponds due to runoff from salted roads in the spring and fall (e.g., Semadeni-Davies, 2006; Mayer et al., 2008). The salinity concentration in Royal Oak might be a concern as the outflow of high salinity water > 1.0 ppt into downstream water bodies could potentially reduce biodiversity and prevent oxygenation of bottom waters (Crowther and Hynes, 1977; Marsalek et al., 2000; Marsalek, 2003; Mayer et al., 2008). Lower salt concentration and chemical stratification in Rocky Ridge are likely due to fewer deicing salts applied to its catchment, with only residential streets and no significant priority routes (e.g., bus routes) for snow and ice cleaning (City of Calgary, Snow and ice clearing update 2022). It might also be due to the Rocky Ridge's inlet design, with the sediment vault trapping some salt-laden runoff during these low-flow spring and fall snowmelt events before it is slowly released into the wetland.

Time series of the vertical density gradient, $\Delta\rho/\Delta d$, at IN, MID and OUT in Royal Oak are presented in Figure 4-11a. In addition, a time series of the relative strength of chemical stratification to the total or densimetric stratification, $(\Delta\rho-\Delta\rho_o)/\Delta\rho$, in Royal Oak in 2019 is presented in Figure 4-11b. In spring and fall, particularly late April, early May, late September and early October, $\Delta\rho/\Delta d$ at IN peaked at 2.4-3.6 $\text{kg}/\text{m}^3/\text{m}$. This was due almost entirely to chemical

stratification from salt-laden road runoff following snowmelt events when the near-bed salinity peaked at 4.0-4.5 ppt, and $(\Delta\rho-\Delta\rho_0)/\Delta\rho$ peaked at 1 (see Figures 4-10a and 4-11b). By the third week of May, $(\Delta\rho-\Delta\rho_0)/\Delta\rho$ at IN was ~ 0 , indicating that spring chemical stratification due to the salt-laden inflows was now negligible because most of the water column salinity had been flushed or diluted by mixing (See Figure 4-11b and the salinity profile on May 21 in Figure 4-10a). However, densimetric stratification due to chemical stratification increased significantly again in the summer between May and August when $(\Delta\rho-\Delta\rho_0)/\Delta\rho$ increased above zero following most of the summer rainstorm events. For instance, the time series plot of salinity in Figure 4-12 shows that during the rainstorm events on June 7-8, 19-21, 27, July 4 and 16, the salinity at IN in Royal Oak decreased abruptly during the events, likely because of dilution. But the salinity increased significantly shortly after each event, likely due to the remobilization of the salt-laden bed sediment induced by turbulent mixing generated by the inflow events. Remobilizing the bed sediment at IN following significant inflow events increased water turbidity and reduced light penetration causing stronger vertical temperature gradients that persisted for longer at IN than at MID and OUT (Tables 4-4 and 4-5). At MID and OUT, $(\Delta\rho-\Delta\rho_0)/\Delta\rho$ was always approximately zero (i.e. < 0.1), indicating that chemical stratification was always negligible in the main cell and the outlet basin. The relative strength of chemical stratification to the total stratification $(\Delta\rho-\Delta\rho_0)/\Delta\rho$ averaged over the entire ice-free season was 22% at IN versus 0.5% and 0.3% at MID and OUT in Royal Oak and 0% everywhere in Rocky Ridge. This highlighted the importance of chemical stratification inside the sediment forebay of the Royal Oak wetland when it was negligible everywhere else in the two wetlands.

Daily fluctuations in the near-surface water temperatures generated diurnal cycles in the vertical density gradient between May and October (Figure 4-11a). The diurnal cycles of $\Delta\rho/\Delta d$ in Royal

Oak peaked at $1.8 \text{ kg/m}^3/\text{m}$ at IN on the hottest days in July and August (Figures 4-4a and 4-11a). The water column was stratified ($\Delta\rho/\Delta d > 0.08 \text{ kg/m}^3/\text{m}$) during most days and nights between May and October at IN for 79%. At MID and OUT, stratification was more ephemeral, with $\Delta\rho/\Delta d$ peaking at $1.5 \text{ kg/m}^3/\text{m}$ during the day and dropping to zero or lower during the night and persisting for 35 to 41% of the time (Figure 4-11a). In Rocky Ridge, diurnal patterns in the densimetric stratification peaked at higher values than Royal Oak, up to 3.8, 2.2, and $2.5 \text{ kg/m}^3/\text{m}$ at IN, MID and OUT (Figure 4-13), respectively. The water column in Rocky Ridge at IN was stratified 65% of the time, slightly less than in Royal Oak, likely due to the absence of chemical stratification in Rocky Ridge. However, Rocky Ridge stratified more often at OUT and MID than in Royal Oak at 42-54% versus 35-41%, likely due to the denser submerged aquatic vegetation in Rocky Ridge. In the two 3m deep stormwater ponds in chapter 3, the duration of the densimetric stratification above 0.25 kg/m^3 ($\Delta\rho/\Delta d \sim 0.08 \text{ kg/m}^3/\text{m}$) was 93% on average between May and September versus 65% in our wetlands. However, the diurnal fluctuations in the vertical density gradient in summer for these wet ponds peaked at significantly lower values of $0.5\text{-}1.0 \text{ kg/m}^3/\text{m}$, comparable to $1.5\text{-}3.8 \text{ kg/m}^3/\text{m}$ in our wetlands. This indicates that persistent stratification in the deeper wet ponds is the norm, while in shallower wetlands, diurnal cycles of densimetric stratification are the norm.

Unstable stratification, i.e., negative vertical density gradient when surface density was higher than at the bottom, was often observed during times of surface cooling. For example, unstable stratification was evident during most nights between June and October at MID and OUT in both wetlands (Figures 4-11a and 4-13b,c). In addition, unstable stratification occurred in October 2019 in Royal Oak at IN, MID and OUT for up to 9, 12 and 3 continuous days (Figure 4-11a) and for 18, 4 and 6 continuous days in Rocky Ridge, respectively (Figure 4-16). In total, unstable stratification occurred at these three locations for 8%, 47% and 47% in Royal Oak and 28%, 37%

and 41% in Rocky Ridge. This likely happened when surface cooling initially created unstable conditions before the sinking of the cooler water was inhibited by the dense aquatic vegetation (Jenter and Schaffranek, 2003; Chimney et al., 2006).

4.3.3 Consequences of stratification

Time series of the rainfall intensity, air temperature, vertical density gradient, and 2D colour contour plots of water temperature and DO profiles in Rocky Ridge in 2019 at OUT are presented in Figure 4-14. In May, the average air temperature was relatively low at 8.5 °C (Figure 4-14a). As a result, the water column was stratified (i.e., $\Delta\rho/\Delta d > 0.08 \text{ kg/m}^3/\text{m}$) for only 20% (Figure 4-14b) and was thermally mixed with $\Delta T/\Delta z < 1 \text{ }^\circ\text{C}/\text{m}$ 90% in May (Figure 4-14c). Simultaneously, the DO concentrations were approximately uniform with depth, and higher values were observed during drier and warmer days (Figure 4-14d). In June, July, and August, the average air temperature increased to 13, 15 and 15 °C resulting in a stratified water column (i.e., $\Delta\rho/\Delta d > 0.08 \text{ kg/m}^3/\text{m}$) for 51%, 73% and 77% of the time, respectively. In addition, continuous thermal stratification was observed for up to 2 and 3 consecutive days in July and August (Figure 4-14c). During prolonged stratification in July and August, vertical patterns in DO concentrations were evident, with dramatically decreased concentrations of $< 2 \text{ mg/L}$ near the bed, while concentrations near the surface were as high as 10-20 mg/L. Similarly, DO concentrations well above 100% saturation up to 16 mg/L near the surface were observed in constructed wetlands with submerged aquatic vegetation beds in south Florida under calm conditions with high illumination (Chimney et al., 2016). These types of vertical and temporal variations in DO concentrations in wetlands are affected by biogeochemical processes that consume oxygen, such as respiration and sediment oxygen demand, and processes that oxygenate the water column, like photosynthesis and reaeration from the atmosphere (Chimney et al., 2006). Reduced mixing of the water column due

to stratification can limit reaeration to the point where the downward transport of DO is insufficient to balance oxygen consumption (Singh et al., 2019; Ji and Jin, 2020; Nakhaei et al., 2021). Due to the prolonged stratification at OUT in Rocky Ridge in 2019, the DO concentrations near the bed were low, < 6 mg/L for 82% in August (Figure 4-14d). DO concentrations < 6 mg/L have detrimental effects on aquatic life and violate the requirements for receiving water (Alberta Environment, 1999; Swistock, 2016). For instance, some fish taxa do not tolerate DO concentrations < 6.0 mg/L (Chen et al., 2019), and hence the discharge of low DO water may harm the biodiversity and the available natural resources in the receiving water bodies (Swistock, 2016; Yadav et al. 2018)

In Royal Oak, the DO concentrations from the profiling data at IN and OUT in 2018 revealed an increasing DO concentration from 4-14 to 9-34 mg/L from the surface to the bed at IN versus decreasing trend from 6-14 to 1.5-5 mg/L from the surface to bed at OUT, see Figure 4-15. The DO concentration near the bed at OUT, which was as low as 1.5 mg/L, is likely explained by the reduced vertical mixing by wind due to sheltering by the dense riparian vegetation along the edges of the outlet basin. Hypoxic conditions near the bed in wetlands can enhance the remobilization of metals and nutrients, generate toxicants such as hydrogen sulphide and ammonia and cause eutrophication (Oberts, 2003; Teichreb, 2012; Song et al., 2013; D'Aoust et al., 2017; Chen et al., 2019; Singh et al., 2019; Nakhaei 2019 & 2021). Hence relocating the outlet pipe at or near the NWL away from the bed in Royal Oak might reduce the risk of discharging water of degraded quality.

4.3.4 Hydrodynamics and mixing

Time series of measured wind and water surface currents components in the middle of the two wetlands, location V_m , are presented in Figure 4-16. The average water currents measured 10 cm below the NWL were 0.007 m/s and 0.006 m/s when the average 10 m wind speed was 2.5 m/s at Royal Oak and 1.6 m/s at Rocky Ridge. Higher magnitude wind-induced near-surface currents up to 0.06 m/s in Royal Oak and 0.02 m/s in Rocky Ridge are evident in Figure 4-16b,d and coincided with maximum wind speeds of 11 and 5 m/s, respectively (Figure 4-16a,c). In Royal Oak, surface velocities tended to peak at times when the wind was from the west and windspeeds exceeded 5 m/s (e.g., July 11, 14, 18, 19, 21, 24, 25 and 27 in Figure 4-16a,b) since this wetland was less sheltered by mature vegetation and houses (Figure 4-1a). In Rocky Ridge, most largest surface velocities coincided with east, northeast and southeast winds (e.g., May 11, 15, 18, 19, 20 in Figure 4-16c,d). The east side of Rocky Ridge faces a major road where no nearby buildings or trees would provide sheltering (Figure 4-1a).

Linear regression analysis was performed between the magnitude of surface velocities, V_s , and wind speed, W , and the results of the strongest correlations are presented in Table 4-6. The wind speed was correlated to the surface velocity at Royal Oak regardless of direction, with $R^2 = 0.65$ and a regression slope $V_s/W = 0.25\%$. At Rocky Ridge, the correlation was weaker with $R^2 = 0.53$ and sloped at 0.27%. The strongest correlation was between the surface velocity and winds blowing from the west in Royal Oak ($R^2 = 0.78$; Slope = 0.34%) and the northeast in Rocky Ridge ($R^2=0.61$; Slope=0.31%), see Table 4-6. These results confirm previous observations in Figure 4-16. Therefore, the calculated slopes, V_s/W , can be used as a simple tool to estimate wind-driven currents in the study wetlands. The wetlands' surface velocity to wind speed ratios are comparable to the 0.2-0.6% observed in deeper (2-3 m) and bigger (up to 2.5 ha) stormwater ponds in Canada and Iceland (Andradóttir et al., 2016; chapter 3 of the current study).

The wind speed, surface velocity, solar radiation, air/water temperatures and water column density gradient are presented in Figure 4-17 between July 24 and August 6, 2019, in Royal Oak. These dry days with almost zero rain depths and air temperatures above 10 °C were chosen to investigate the significance of wind speed on mixing when other factors (e.g., continuous surface cooling and significant inflows) contributing to mixing were minimal. The continuous water column density gradient generally followed the air temperature diurnal fluctuations. They were positively correlated with $R^2 = 0.66$, indicating that air temperature is one of the main drivers of densimetric stratification (Figure 4-17d,e). The density gradients peaked at $< 1 \text{ kg/m}^3/\text{m}$ on July 24, 25, 27 and 28 on days of high wind speeds at 5-10 m/s and surface velocities $> 2 \text{ cm/s}$ (Figure 4-17a,b,e). The highest density gradients at 1.3-1.6 $\text{kg/m}^3/\text{m}$ on July 26, 29, and August 1, occurred on days of minimum cloud cover (as inferred from solar radiation) and low wind speed at $< 5 \text{ m/s}$. On August 2, the highest diurnal air temperature at 29 °C coincided with a significant wind speed peaked at 8 m/s and the highest cloud cover. As a result, the generated density gradient was slightly lower in magnitude than on other days with lower air temperatures, wind speeds and cloud cover, e.g. August 1 and 3. Hence, when the strongest wind events were observed in this wetland (i.e., $\geq 5 \text{ m/s}$) and cloud cover reduced the solar radiation, $\Delta\rho/\Delta d$ was reduced by 0.2-0.4 $\text{kg/m}^3/\text{m}$. Similarly, in a 3m deep stormwater pond in Calgary, Alberta, Canada, the diurnal peak in the density gradient decreased by $\sim 0.25 \text{ kg/m}^3/\text{m}$ when wind speeds exceeded 8 m/s and significant surface currents were generated (refer to chapter 3).

The wind speed required to thoroughly mix a stratified water column was estimated in the wetlands based on an approach developed by Boegman et al. (2008) and later applied by Rey et al. (2021) and in our stormwater wet ponds in chapter 3 (see Equation 3-8). This analysis found that a continuous wind speed of 2 m/s for 24 hours is required to thoroughly mix a density gradient of 1

kg/m³/m in Royal Oak and Rocky Ridge. Although a wind speed of > 2 m/s lasted for 40 hours on July 24 and 25 in Royal Oak (Figure 4-17a), diurnal density gradients of 1 kg/m³/m still occurred on these two days (Figure 4-17e). Similarly, previous studies reported a minor effect of wind on mixing and concluded that this was likely explained by low wind stresses at the water surface (Folkard et al., 2007; Song et al., 2013; Yang et al., 2018; Singh et al., 2019). Therefore, the low surface current to wind speed ratio of ~ 0.3% in the study wetlands might be the reason for the weak effect of wind on mixing. The sheltering by the mature vegetation and houses at both wetlands, in addition to the small length of their longest axis < 150 m and the presence of submerged plants, are vital factors in the weak wind-induced mixing (Jin and Ji, 2015; Andradóttir et al., 2016). As a result, it is not surprising that none of the observed wind-induced currents appeared to cause complete vertical mixing during the diurnal stratification in either study wetland.

4.4 Conclusions

This study is one of the most comprehensive field studies of constructed urban stormwater wetlands that aims to understand the role of stratification in governing physical and water quality processes. In contrast to the assumption of urban wetlands being well-mixed ecosystems, thermal stratification (vertical temperature gradient > 1°C/m) was observed in these two shallow wetlands (0.8 m deep) for up to two-thirds of the ice-free season and for up to 21 consecutive days in the summer. In addition, inverse stratification (vertical temperature gradient < 1°C/m) occurred for up to 18 consecutive days in the fall when bed sediments became a heat source and/or the sinking of cooler surface water was inhibited by the dense aquatic vegetation. Chemical stratification was also evident due to salt-laden inflows from road deicing salts resulting in a significant densimetric stratification for up to 79% between May and October. Furthermore, the mechanical interference

by the dense aquatic vegetation and the local landscaping resulted in weaker wind-induced surface currents, scaling at 0.3% of the wind speed, compared to the ~2% value often used in the ocean, causing a negligible impact on vertical mixing. For instance, the strongest wind events above 5 m/s reduced the vertical density gradient by less than 30%. As a result, stratification caused the water at depth to become hypoxic for extended periods in both wetlands, violating specific requirements of DO concentration for the receiving waters. Potential adverse effects of hypoxic conditions on water quality include the remobilization of the metals and nutrients in the bed sediment and the generation of toxicants and algal blooms due to eutrophication. In addition, discharging stormwater with low dissolved oxygen levels may cause a loss of biological diversity and available natural resources in the receiving waters.

The two study wetlands had different inlet and outlet designs, morphological characteristics, local landscaping, and vegetation designs. As a result, the study reported marked differences in the duration and strengths of thermal and chemical stratification and the hydrodynamics in the two nearby study wetlands, which are only 0.25 km apart. For instance, the wetland with double the volume and surface area had denser submerged aquatic vegetation, causing a localized increase in water temperature and increasing its average water temperature by up to 2 °C higher than the smaller wetland. Discharging stormwater water with elevated temperatures downstream could adversely limit the habitat viability of aquatic fish and invertebrates requiring cold water conditions. The wetland with double the length-to-width ratio, separated outlet basin and half the water volume and surface area had better mixing during inflow events and was efficiently shaded by the riparian vegetation and trees, reducing the strength of its thermal stratification by up to eight times. However, shading from the dense riparian vegetation along the edges of the wetland also reduced vertical mixing by wind, causing hypoxia near the bed. Hence, locating the outlet pipe at

or near the NWL away from the bed where anoxia/hypoxia was evident might be helpful. In chapters 5 and 6, the results presented in the current chapter will be linked to inflow/outflow and in-pond water quality data, including temperature, salinity and suspended sediment concentrations, to explore in-depth the role of the studied physical process in altering hydrodynamics and sediment transport and fate in wetlands.

Notation

The following symbols are used in this chapter:

d = water depth measured downward from the normal water level;

DO = dissolved oxygen;

h = height above the bed;

HWL = high water level;

I = rainfall depth;

NWL = normal water level;

R = solar radiation;

S = water salinity;

T_a = air temperature;

T_s = water surface temperature;

T_{wc} = depth-averaged water temperature;

u_w = eastward wind speed component;

V_{abs} = absolute water surface velocity;

V_E : eastward water surface velocity;

V_N = northward water surface velocity;

V_s = water surface velocity;

v_w = northward wind speed component;

w = wind speed;

W_{abs} = absolute wind speed;

z = water surface elevation;

ΔT = vertical top-bottom temperature differences;

$\Delta\rho$ = vertical bottom-top density differences;

$(\Delta\rho - \Delta\rho_0)/\Delta\rho$ = the ratio of the real minus freshwater bed-surface density difference to the real bed-surface density difference;

η = water depth above normal water level;

Table 4-1. Study wetlands' physical and drainage characteristics.

| | Unit | Royal Oak | Rocky Ridge |
|---|----------------|------------------|--------------------|
| Catchment type | / | Residential | Residential |
| Catchment area | ha | 18.3 | 15.1 |
| Imperviousness ratio | % | 51 | 60 |
| Surface area at NWL¹ | m ² | 5,500 | 11,400 |
| Wetland to watershed area ratio | / | 0.03 | 0.08 |
| Permanent wet pool volume | m ³ | 2,500 | 5,750 |
| Average normal depth | m | 0.8 | 0.8 |
| Length-to-width ratio | / | 2:1 | 1.25:1 |
| Depths at NWL¹ IN/MID/OUT² | m | 1.3/0.7 /0.6 | 0.8/0.8/0.8 |

1 Normal Water Level; 2 Monitoring locations in Figure 4-1b,c

Table 4-2. Summary of the meteorologic data statistics at the wetlands between May and October in 2018 and 2019. T_a dry and T_a wet are the air temperature during zero rain depth and rain depth > 0.2 mm. μ is the mean. The first six rows of the table are mean values (μ).

| | Royal Oak | | Rocky Ridge | |
|---|-----------|------|-------------|------|
| | 2018 | 2019 | 2018 | 2019 |
| T_a (μ), °C | 11.9 | 10.8 | 11.9 | 10.8 |
| T_a dry (μ), °C | 12.0 | 10.9 | 12.0 | 10.9 |
| T_a wet (μ), °C | 7.5 | 7.3 | 7.3 | 7.4 |
| Solar radiation (μ), W/m ² | 215 | 210 | 208 | 198 |
| Cloud cover (μ), - | 0.3 | 0.3 | 0.3 | 0.3 |
| Wind speed (μ), m/s | 1.7 | 2.7 | 1.6 | 1.7 |
| Total rain depth, mm | 201 | 400 | 185 | 397 |
| Wet days > 0.2 mm, % | 36% | 43% | 34% | 43% |

Table 4-3. Average temperatures between May and October at the three monitored locations of the two wetlands. T_{wc} , T_s and T_a are the depth-averaged water temperature, water surface temperature, and air temperatures.

| Average T (°C) | | 2018 | | | 2019 | | |
|----------------|-------------|------|------|------|------|------|------|
| | | IN | MID | OUT | IN | MID | OUT |
| RO | T_{wc} | 13.2 | 14.3 | 12.6 | 12.2 | 13.7 | 12.6 |
| | T_s | 14.2 | 14.4 | 12.9 | 13.6 | 13.8 | 12.8 |
| | $T_s - T_a$ | 2.3 | 2.5 | 1.0 | 2.8 | 3.0 | 1.9 |
| RR | T_{wc} | 13.7 | 14.2 | 14.1 | 13.8 | 14.5 | 14.5 |
| | T_s | 14.5 | 14.8 | 14.8 | 14.7 | 14.8 | 14.7 |
| | $T_s - T_a$ | 2.6 | 2.9 | 2.9 | 3.8 | 4.0 | 3.9 |

Table 4-4. Summary of the percentage of time between May and October when the water column in the two wetlands at the three locations IN, MID and OUT were thermally stratified by a vertical temperature gradient ($\Delta T / \Delta z > 1 \text{ }^\circ\text{C}$) and ($\Delta T / \Delta z < -1 \text{ }^\circ\text{C}$).

| Criteria/ wetland | IN | | MID | | OUT | | |
|---|------|------|------|------|------|------|-----|
| | 2018 | 2019 | 2018 | 2019 | 2018 | 2019 | |
| $\Delta T / \Delta z > 1 \text{ }^\circ\text{C/m}$ | RO | 55% | 62% | 28% | 35% | 41% | 28% |
| | RR | 51% | 62% | 43% | 46% | 37% | 34% |
| $\Delta T / \Delta z < -1 \text{ }^\circ\text{C/m}$ | RO | 15% | 15% | 10% | 24% | 15% | 19% |
| | RR | 6% | 20% | 3% | 18% | 1% | 12% |

Table 4-5. Summary of the statistics (mean \pm standard deviation) for the continuous temperature gradient at the two wetlands between May and October in 2018 & 2019.

| $\Delta T/\Delta z$ ($^{\circ}\text{C}/\text{m}$) | IN | | MID | | OUT | |
|---|---------------|---------------|---------------|---------------|---------------|---------------|
| | 2018 | 2019 | 2018 | 2019 | 2018 | 2019 |
| RO | 1.5 \pm 2.2 | 1.9 \pm 2.7 | 0.2 \pm 1.6 | 0.3 \pm 2.3 | 1.0 \pm 2.3 | 0.2 \pm 1.7 |
| RR | 2.6 \pm 3.7 | 2.6 \pm 4.5 | 1.6 \pm 2.4 | 0.9 \pm 2.1 | 1.4 \pm 2.0 | 0.9 \pm 2.3 |

Table 4-6. Results of a linear regression analysis (slope and correlation coefficient R^2) between the absolute surface velocity (V) and wind speed (W) in the Royal Oak and Rocky Ridge wetlands at location V_m . All regressions are statistically significant at a 0.1% level ($p < 0.001$).

| Royal Oak | | | Rocky Ridge | | |
|----------------|-------------|-------|----------------|-------------|-------|
| Wind Direction | V_s/W (%) | R^2 | Wind Direction | V_s/W (%) | R^2 |
| SE | 0.32 | 0.71 | NE | 0.31 | 0.61 |
| W | 0.34 | 0.78 | E | 0.31 | 0.57 |
| NW | 0.30 | 0.68 | SE | 0.27 | 0.61 |
| All wind | 0.25 | 0.65 | All wind | 0.27 | 0.53 |

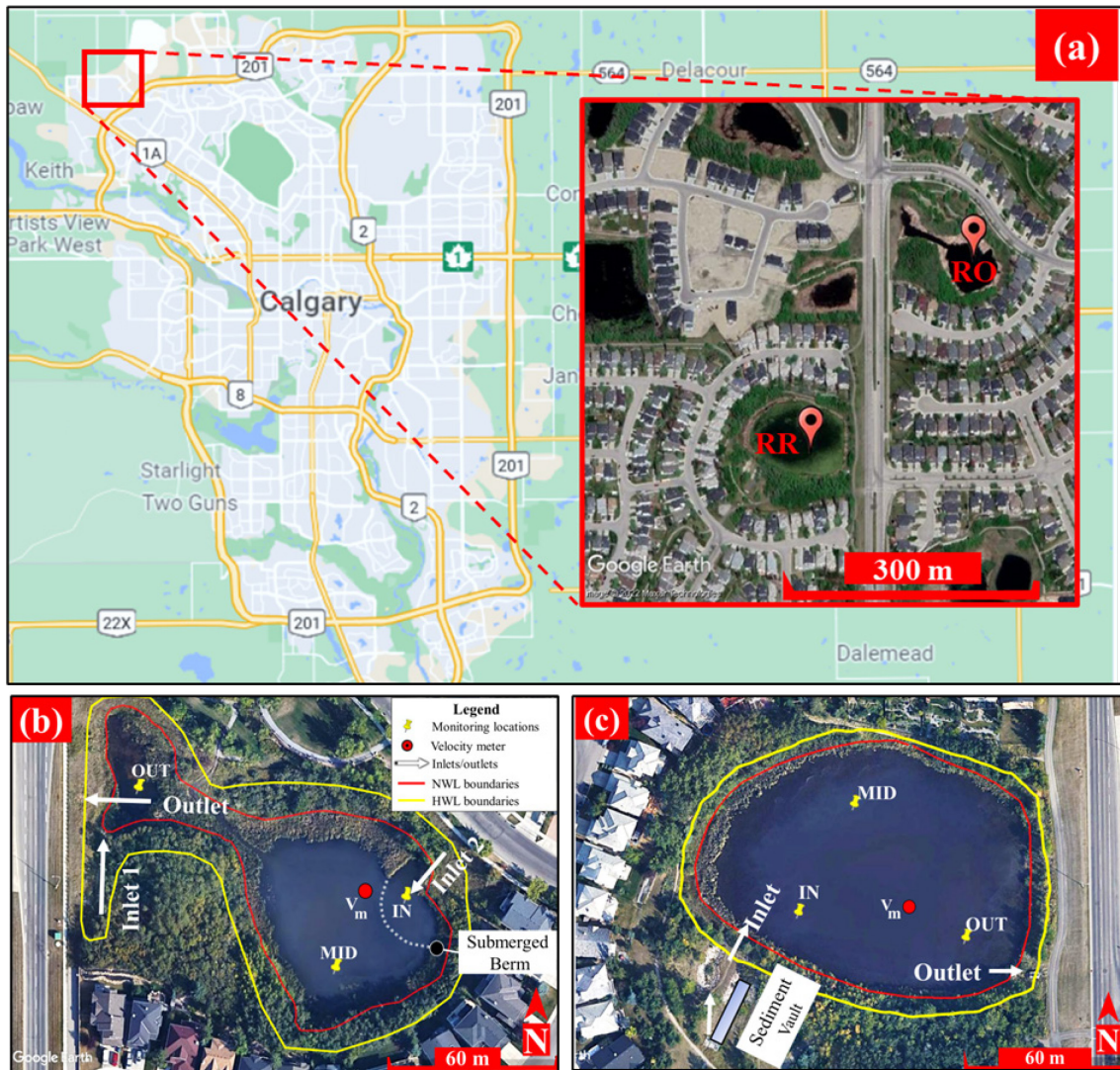


Figure 4-1 (a) Map of the City of Calgary, Canada, showing the location of the Royal Oak (RO) and the Rocky Ridge (RR) wetlands; (b) and (c) satellite images of the Royal Oak and Rocky Ridge wetlands, respectively. The red and yellow lines in (b) and (c) indicate the normal and high water level boundaries, respectively. The white arrows show the location of inlets and outlets. Yellow pins labelled IN, MID, and OUT in each wetland are in-pond monitoring locations near the inlet(s), middle, and outlet. The red dot, V_m , is the velocity measurement location. [Images' source: Google Earth Pro 7.3.4.8248. (August 31, 2017). City of Calgary, Alberta, Canada. <<http://www.google.com/earth/index.html> > (Accessed January 22, 2022)]. [Map's source: Google Maps. Retrieved January 22, 2022, from <https://goo.gl/maps/22uRPTqEVXdxUaYSA>]

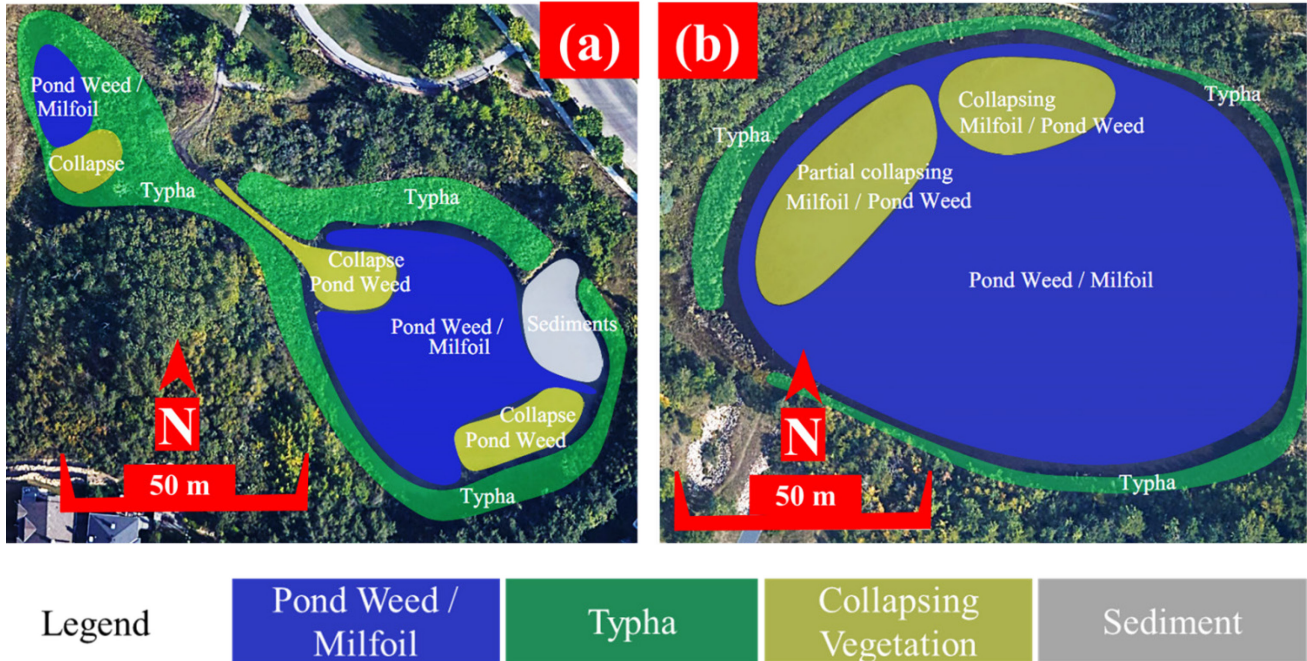


Figure 4-2 Boundaries and extents of the riparian and aquatic vegetation species at (a) the Royal Oak wetland and (b) the Rocky Ridge wetland.



Figure 4-3 Image from a game camera mounted at the weather station pole in (a) Rocky Ridge showing the dense submerged aquatic vegetation in July 2019, and in (b) Royal Oak showing the dense riparian vegetation at the outlet basin. The water level in the two images is the normal water level (NWL)

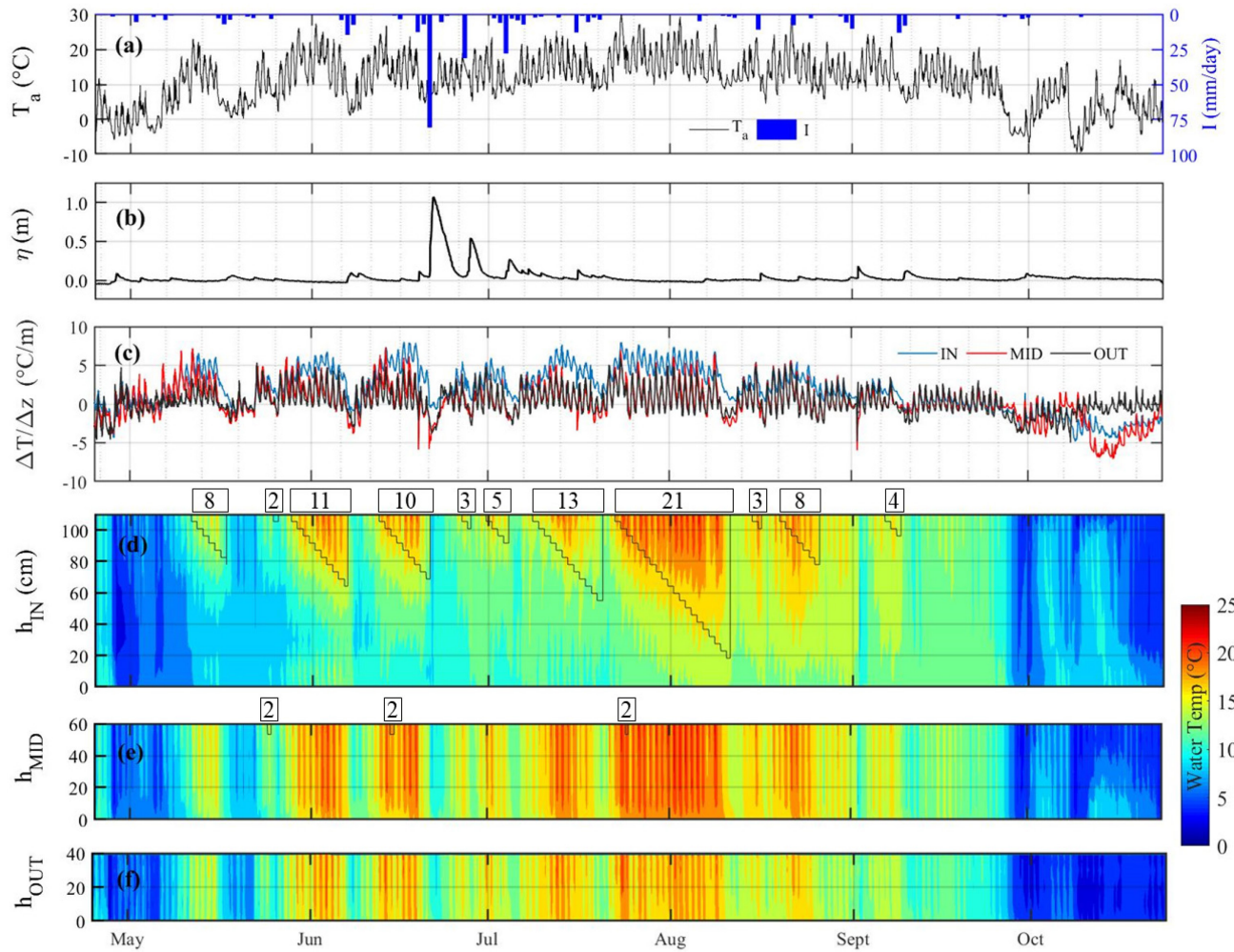


Figure 4-4 Results from the Royal Oak wetland in 2019 show time series of (a) air temperature (left axis) and rainfall intensity, I , (right axis), (b) measured water depth above the NWL, η , (c) vertical temperature gradients, $\Delta T/\Delta z$, (d), (e) & (f) colour contour plots of vertical water temperature profiles versus height above the bed at IN, MID, and OUT, respectively, numbers in boxes at the top of each colour contour plot and the black staircase lines represent days with continuous thermal stratification.

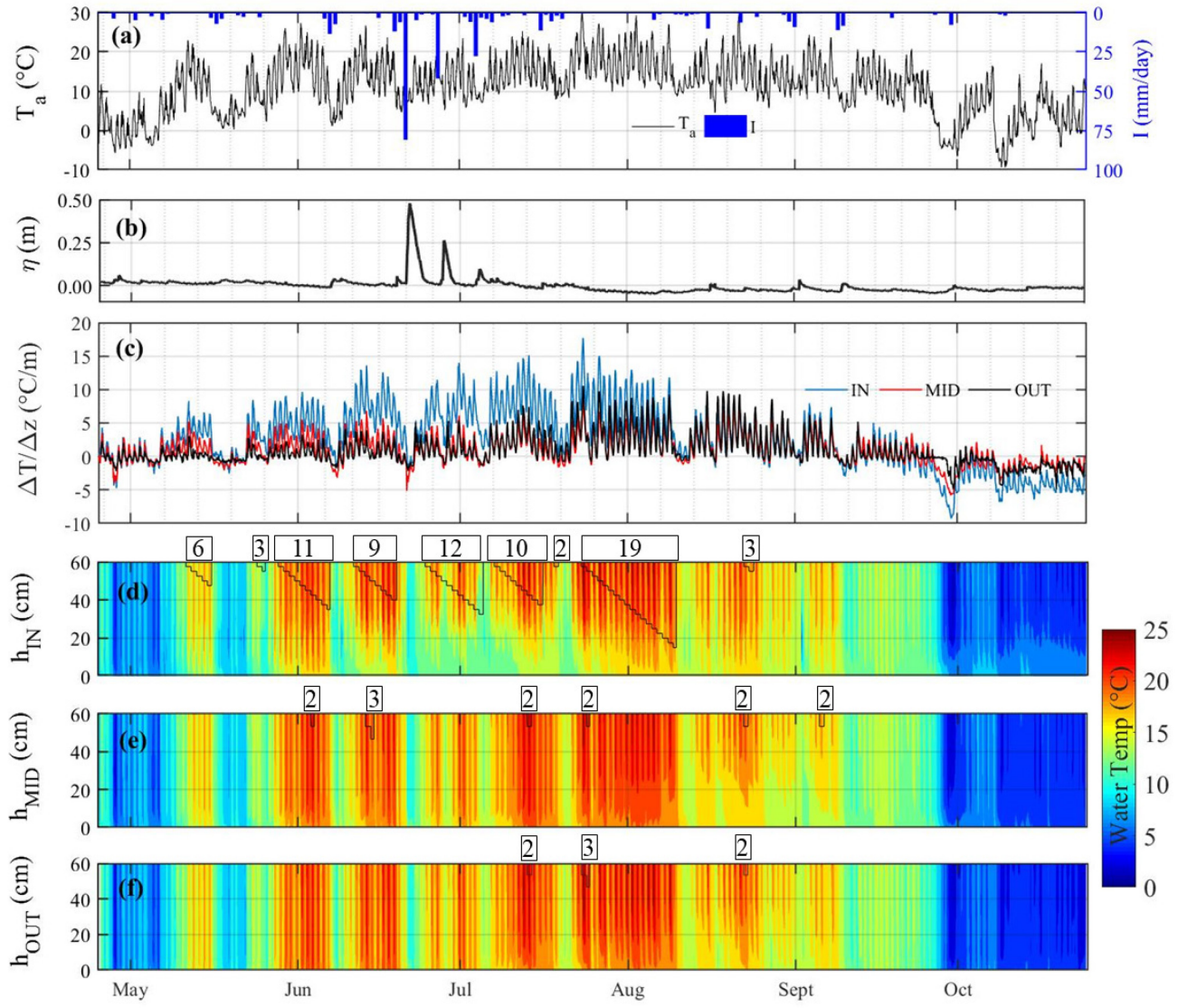


Figure 4-5 Results from the Rocky Ridge wetland in 2019 similar to that in Figure 4-4.

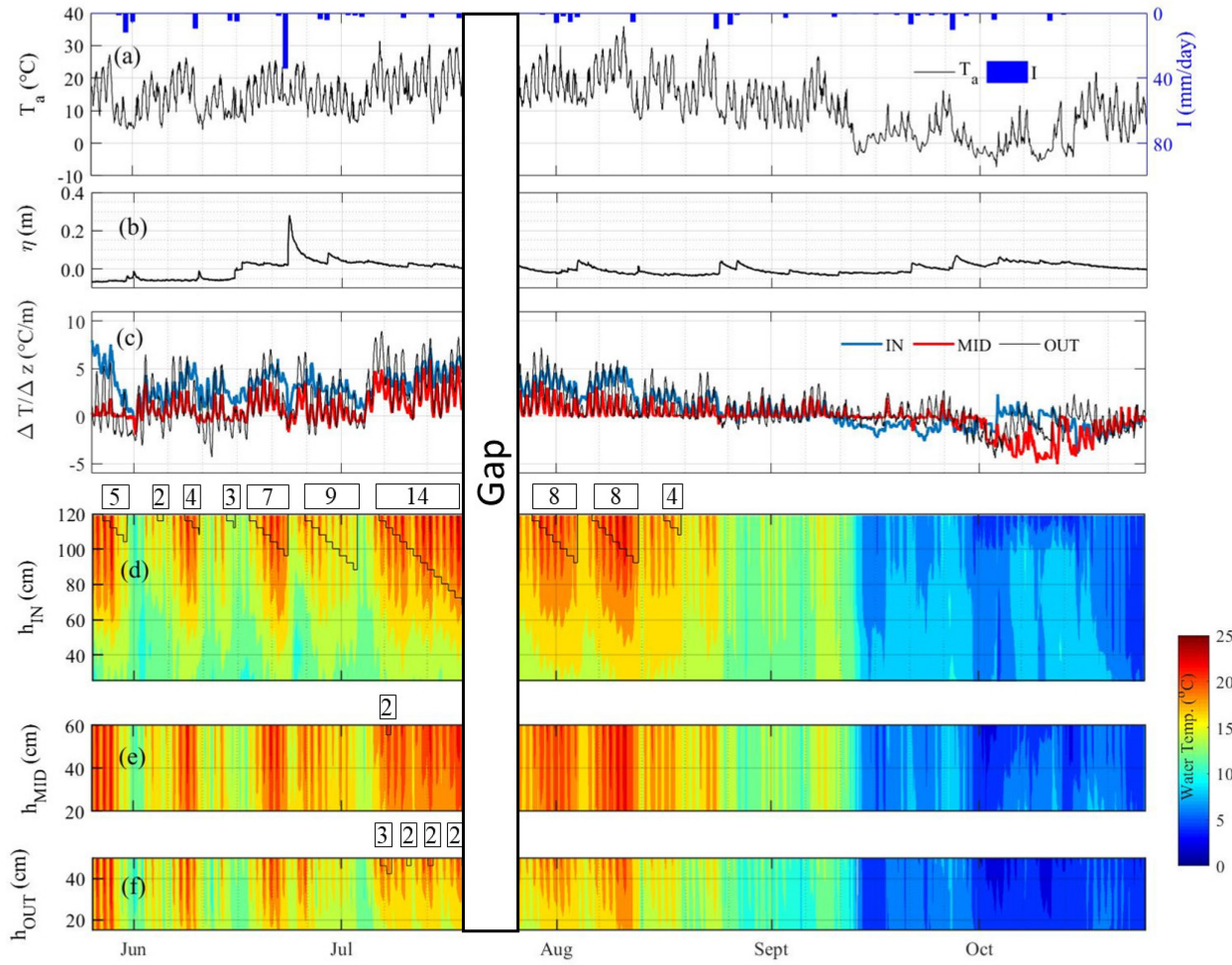


Figure 4-6 Results from the Royal Oak wetland in 2018 similar to that in Figure 4-4.

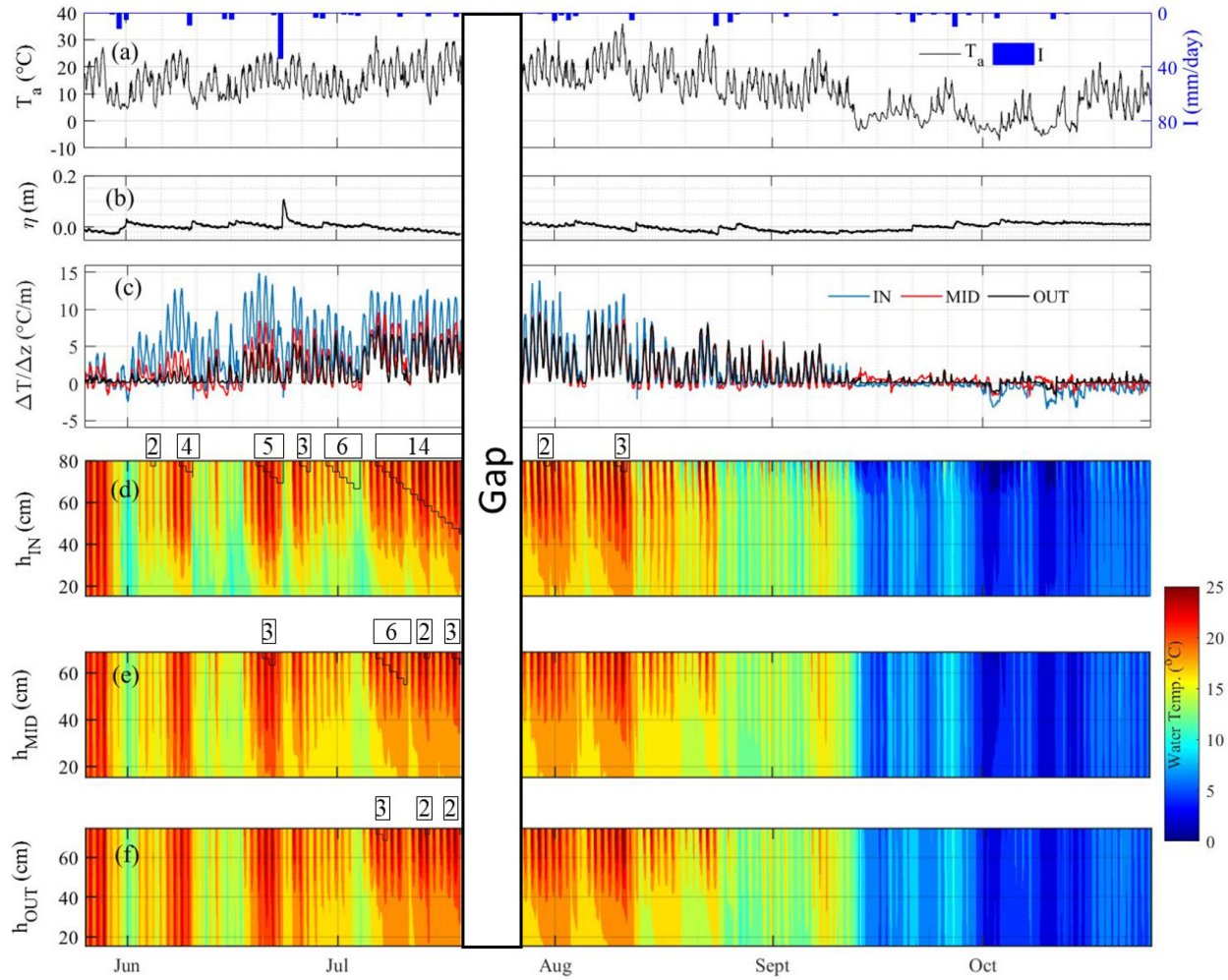


Figure 4-7 Results from the Rocky Ridge wetland in 2018 similar to that in Figure 4-4.

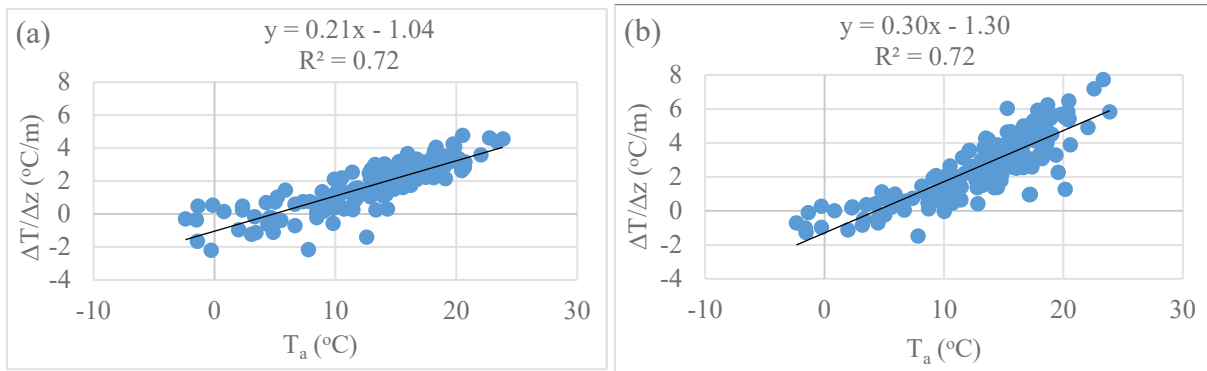


Figure 4-8 Linear correlation of the daily averaged air temperature, T_a , and the vertical water temperature gradient, $\Delta T/\Delta z$, daily averaged and averaged over the entire wetland between May and August in 2018 and 2019 in (a) Royal Oak and (b) Rocky Ridge.

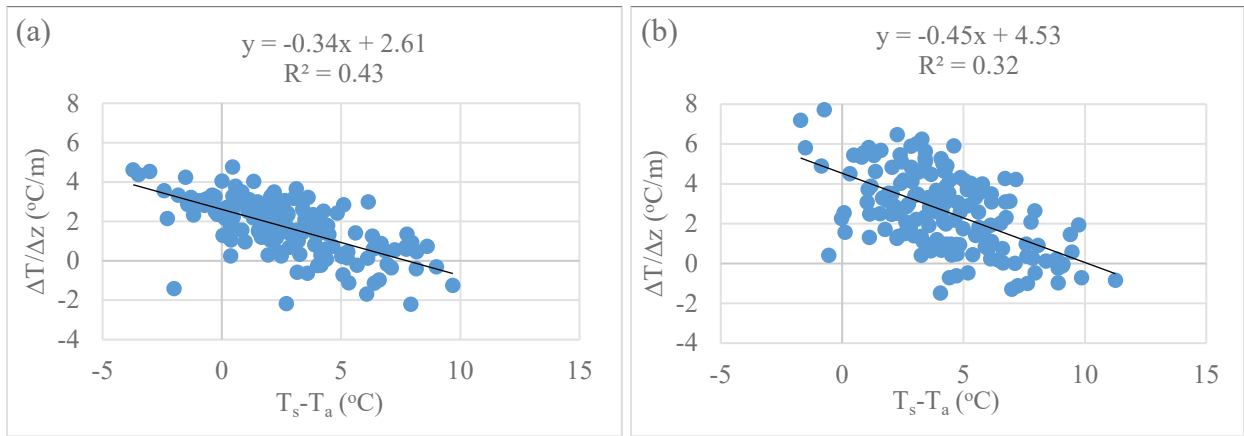


Figure 4-9. Linear correlation between the atmospheric instability, $T_s - T_a$, and the vertical water temperature gradient, $\Delta T / \Delta z$, daily averaged and averaged over the entire wetland between May and August in 2018 and 2019 in (a) Royal Oak and (b) Rocky Ridge.

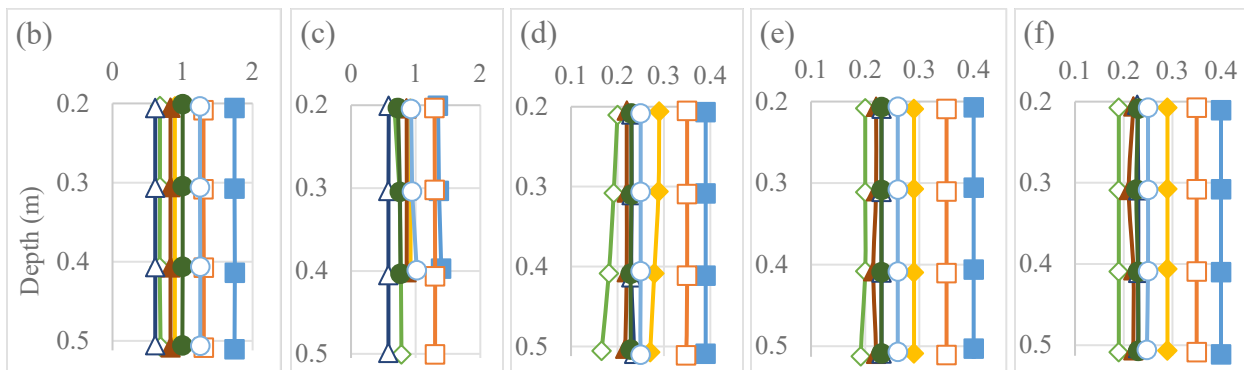
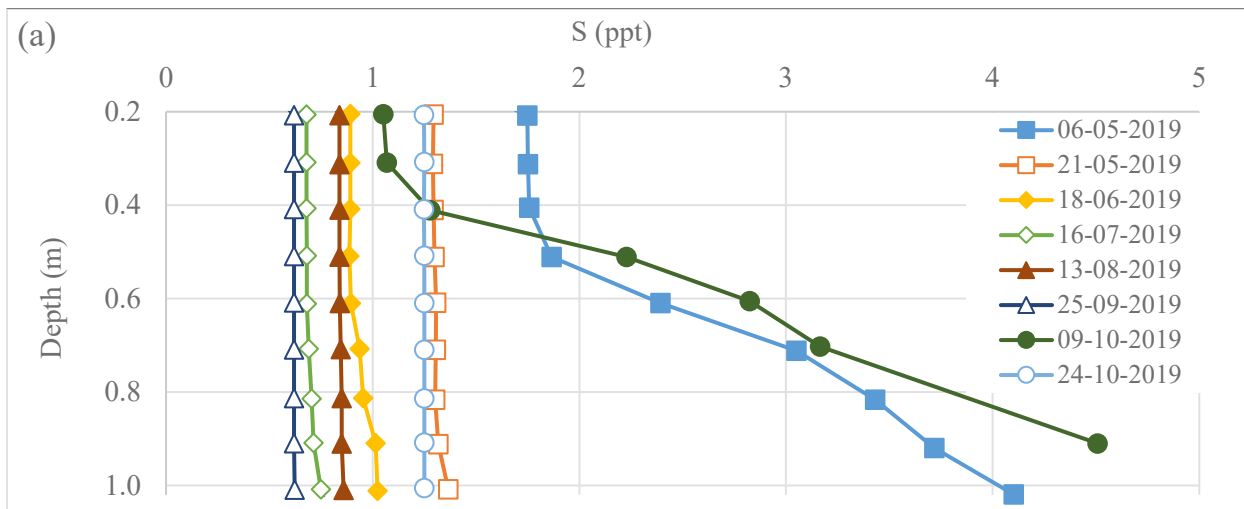


Figure 4-10 Water salinity profiles in 2019 at locations (a) IN, (b) MID, (c) OUT in the Royal Oak wetland, and (d) IN, (e) MID, and (f) OUT of the Rocky Ridge wetland.

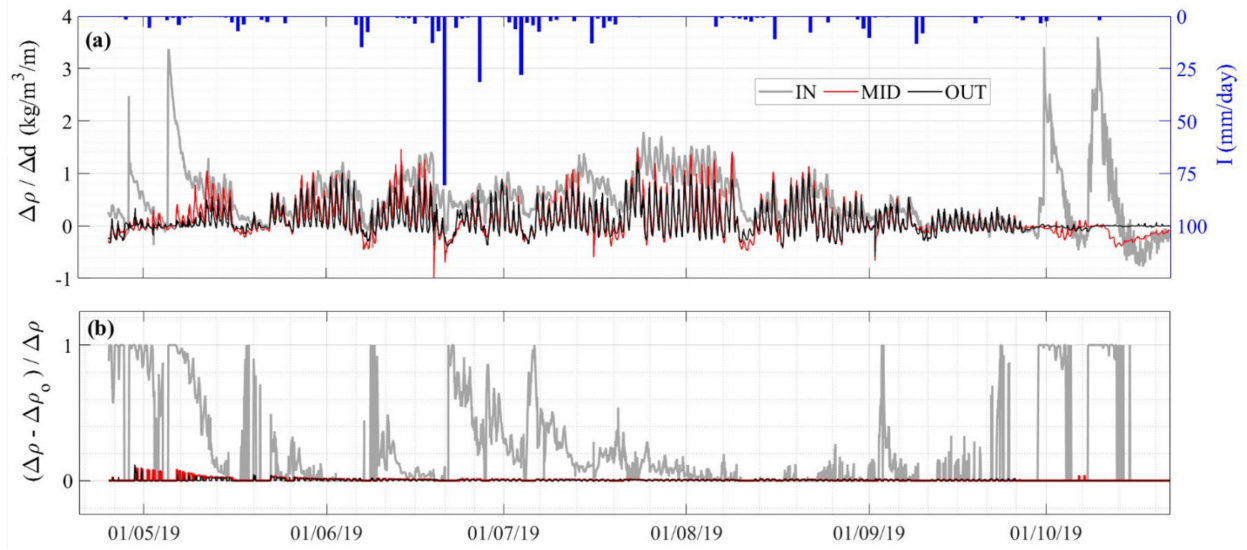


Figure 4-11 Results from the Royal Oak wetland in 2019 show time series of (a) the vertical density gradient $\Delta\rho/\Delta d$ at IN, MID and OUT and (b) $(\Delta\rho - \Delta\rho_0)/\Delta\rho$, the ratio of the real minus freshwater bed- surface density difference to the real bed- surface density difference.

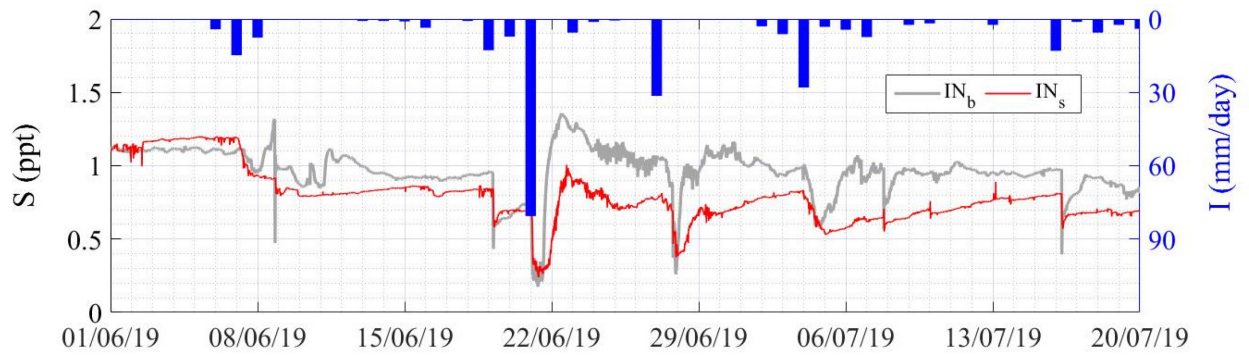


Figure 4-12 Results from the Royal Oak wetland in 2019 show the time series of water salinity measured at IN 30cm above the bed for IN_b and 30 cm below the NWL for IN_s (left axis) and rainfall intensity (right axis).

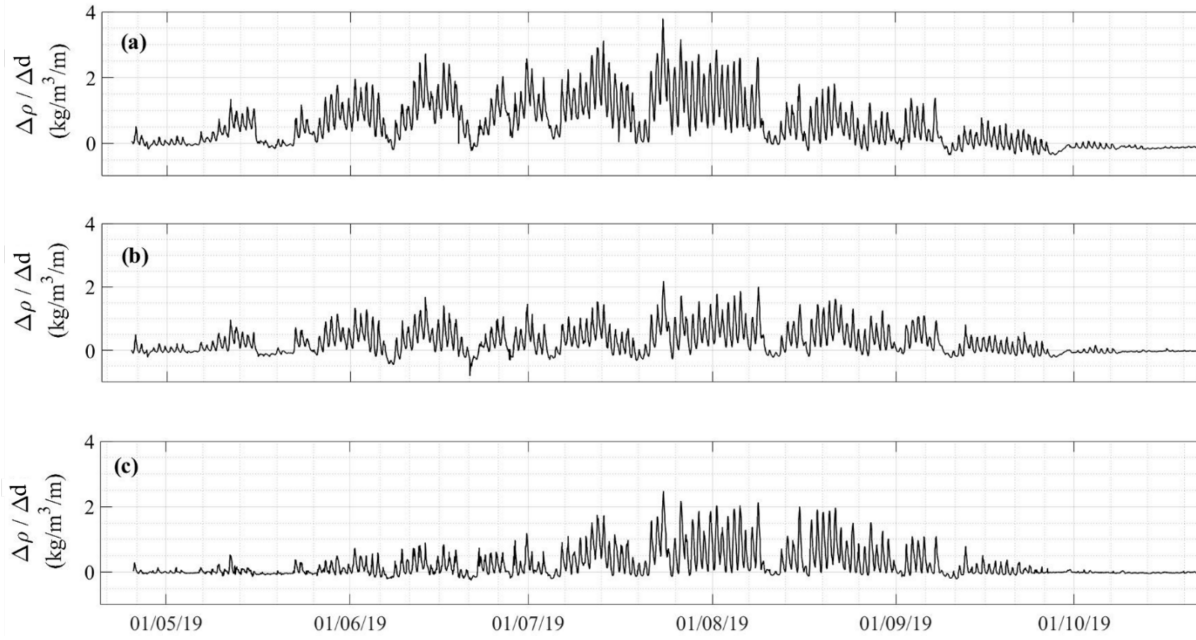


Figure 4-13 Vertical density gradient $\Delta\rho/\Delta d$ at the Rocky Ridge wetland in 2019 at locations IN, MID and OUT for plots (a,b,c).

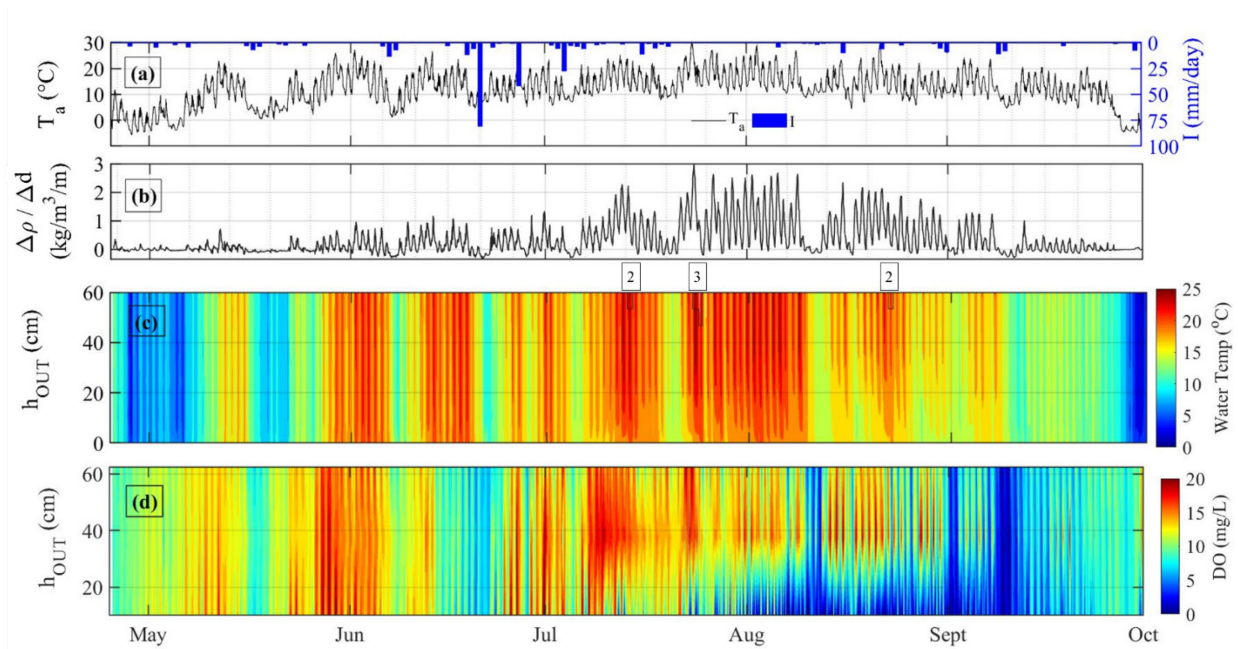


Figure 4-14 Data measured at the Rocky Ridge wetland in 2019, (a) air temperature (left axis) and rainfall intensity (right axis), (b) vertical density gradient $\Delta\rho/\Delta d$ at OUT, (c) colour contour plots of vertical water temperature profiles versus height above the bed at OUT, numbers in boxes at the top of the plot are days with continuous thermal stratification, and (d) colour contour plots of vertical dissolved Oxygen (DO) profiles versus height above the bed measured at h of 10, 37.5 and 62.5 cm at OUT.

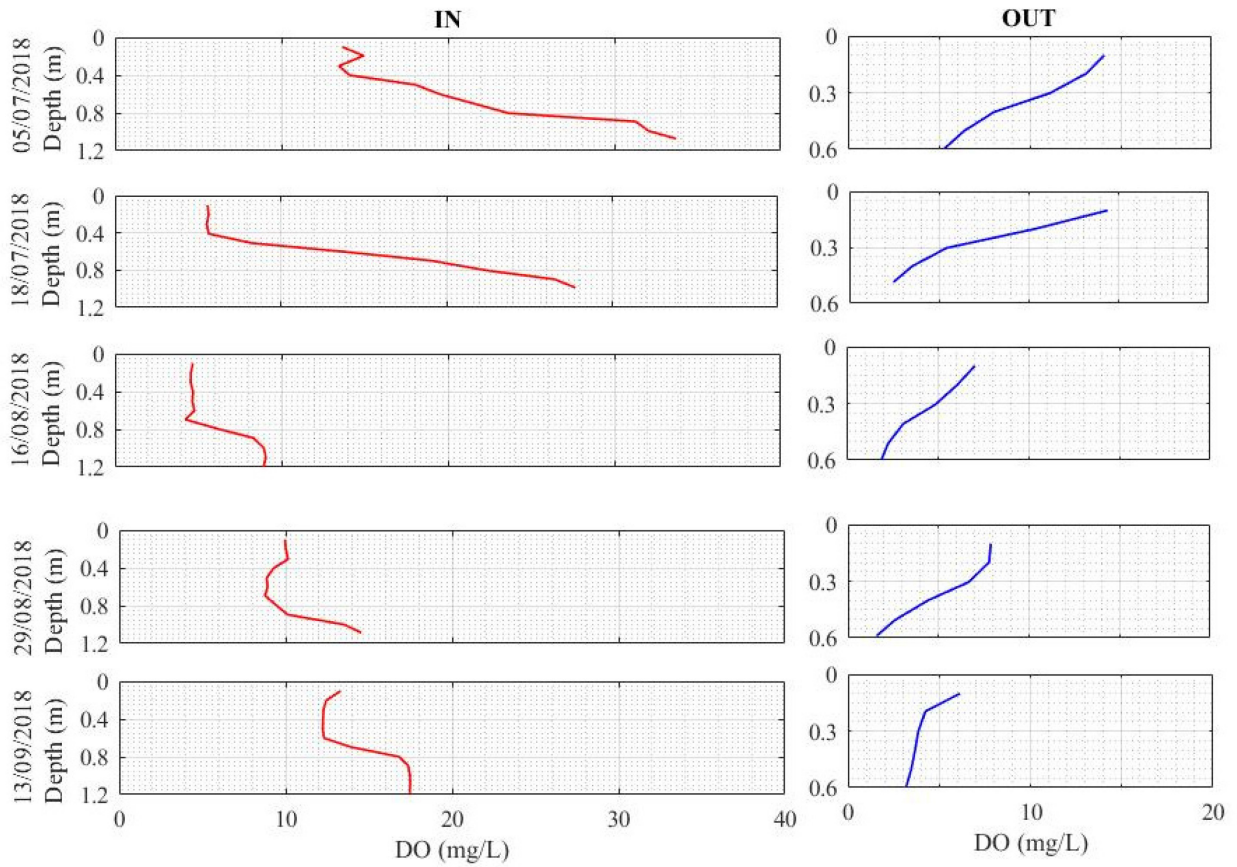


Figure 4-15 DO profiles in the Royal Oak wetland at IN and OUT between July 5 and September 13, 2018.

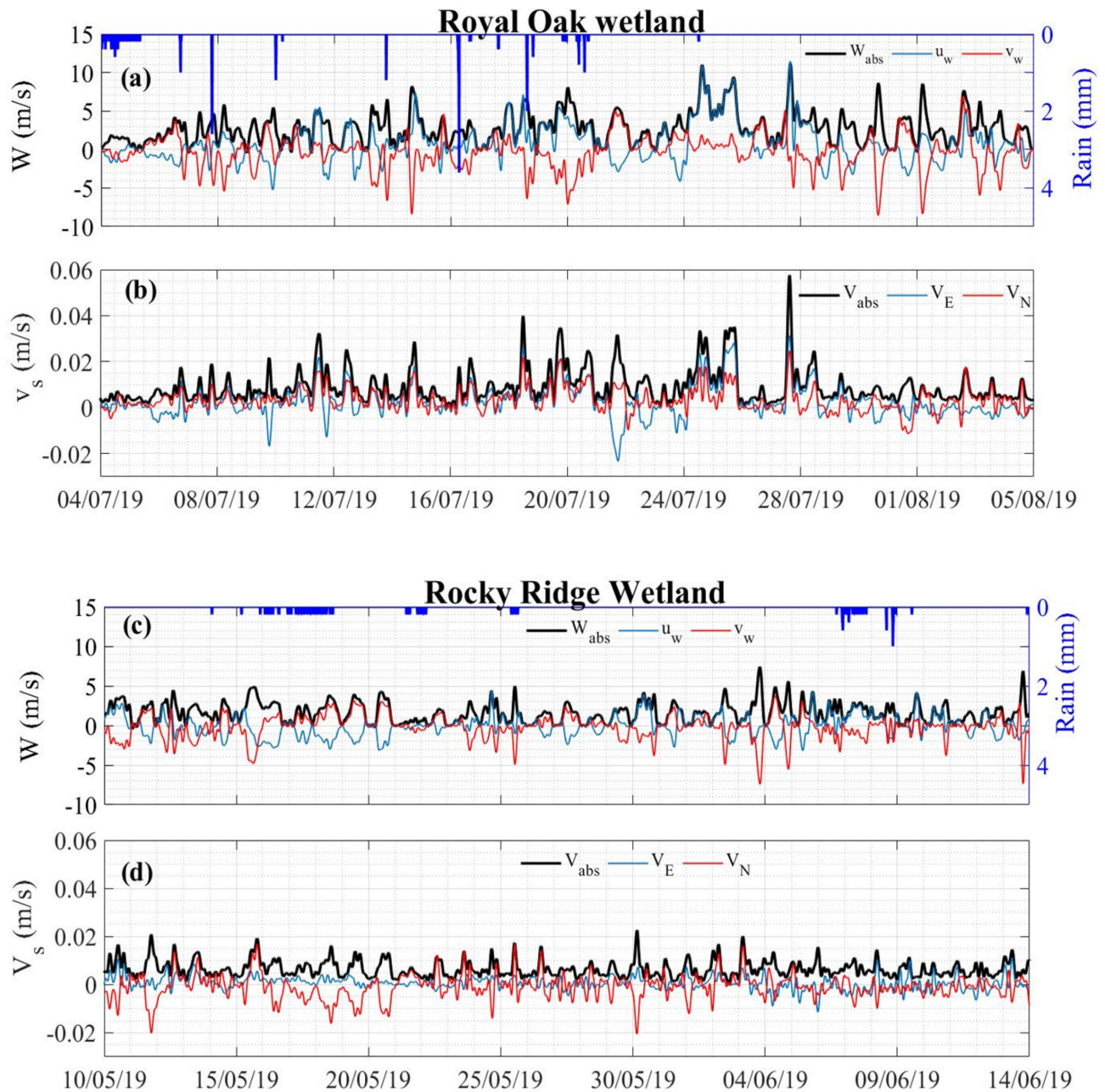


Figure 4-16 Data measured at the Royal Oak and Rocky Ridge wetlands show (a,c) wind components (u_w : positive eastward, v_w : positive northward, and W_{abs} : magnitude) (left axis), and 5-minute interval rain depth (I, right axis), (b,d) water surface velocity, location V_m , (V_E : positive eastward, V_N : positive northward, and V_{abs} : magnitude).

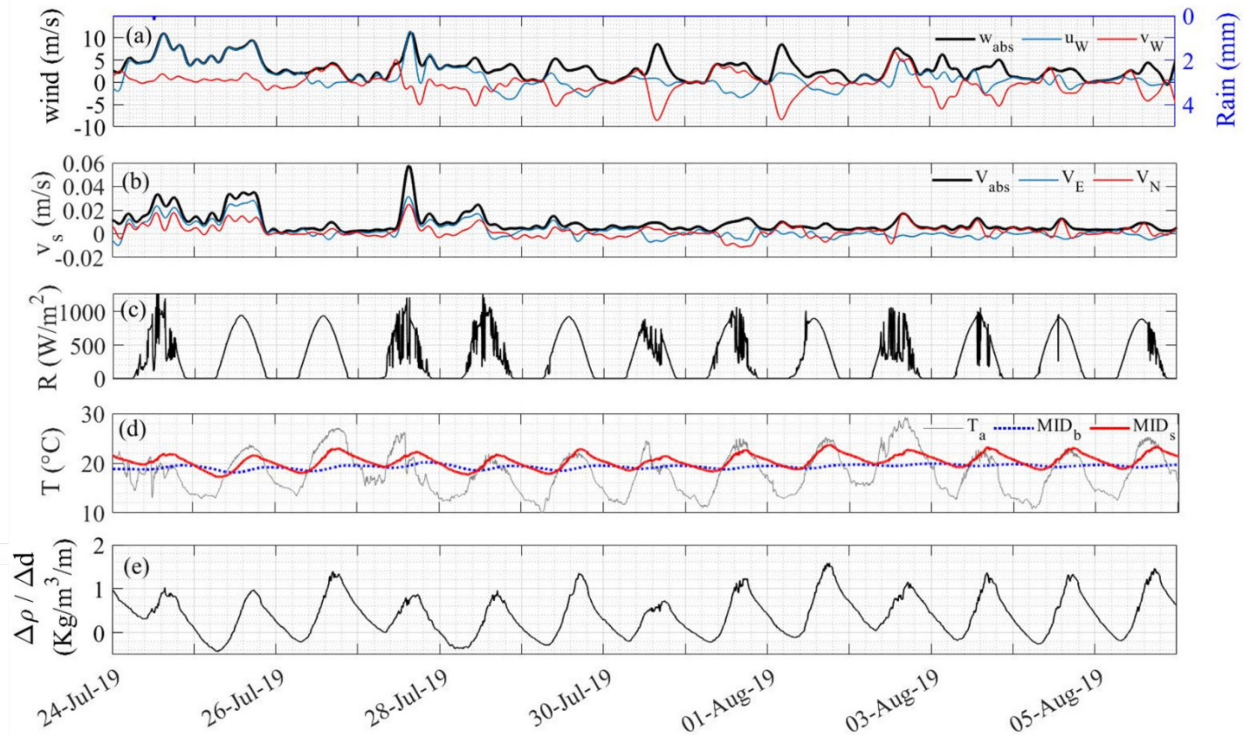


Figure 4-17 Data measured at the Royal Oak wetland between July 24 and August 6, 2019, (a) wind components (u_w : positive eastward, v_w : positive northward, and W_{abs} : magnitude) (left axis), and 5-minute interval rain depth (right axis), (b) water surface velocity (V_E : positive eastward, V_N : positive northward, and V_{abs} : magnitude), (c) solar radiation, (d) air temperature and water temperature at ~ 0 cm above the bed for MID_b and ~ 10 cm below the NWL for MID_s, and (e) vertical density gradient, location MID.

5. Hydrodynamic and physical processes modelling in an urban stormwater wet pond and a constructed wetland*

5.1 Introduction

Stormwater wet ponds and constructed wetlands are two structural best management practices (BMPs) used extensively for stormwater management (City of Calgary, 2011). They have also been used to improve the water quality of stormwater runoff by reducing sediment and nutrient concentrations (Song et al., 2013 & 2015; Gu et al., 2017; Ji and Jin, 2020). Their permanent pool acts as a settling chamber for sedimentation by reducing bottom shear stresses and bed erosion (City of Calgary, 2011; Jin and Ji, 2015). In addition, nutrients in stormwater runoff can be removed via mechanisms such as filtration by vegetation, sorption onto suspended sediment particles and uptake by vegetation and algae (City of Calgary, 2011; Schwammburger et al., 2020). However, the physical processes governing the transport and fate of these pollutants in stormwater wet ponds and constructed wetlands are complex and not yet fully understood (Song et al., 2013; Gu et al., 2017; Ji and Jin, 2020). Key considerations, including densimetric stratification, wind, inflow/outflow configurations, pond morphometric characteristics and vegetation design, will all affect the hydrodynamics and pollutants fate in ponds and wetlands (Marsalek 2003; Bentzen et al. 2008; Novotny et al. 2008; Song et al. 2013). Therefore, the complex flow fields in these facilities need to be modelled realistically to evaluate the performance of ponds and wetlands and define appropriate remediation design strategies to ensure desirable water quality.

Many studies have demonstrated that 3D models are required to accurately simulate the complex temporal and spatial variations in the flows in ponds and wetlands (Shaw et al., 1997; German et

* The content of this chapter is being prepared and will be submitted as a journal manuscript.

al., 2003; Hart et al., 2014; Androdóttir and Mortamet, 2016; Ji and Jin, 2020). For example, Shaw et al. (1997), using a 3D hydrodynamic model in stormwater ponds in Kingston, Ontario, Canada, showed that the ponds' horizontal and vertical flow patterns were complex and dynamic because of the combined effects of wind stress on the water surface and inflow momentum. In addition, high-resolution velocity measurements in a 2 m deep stormwater pond in Iceland showed that wind-induced vertical and basin-scale mixing create a complex 3D flow (Androdóttir and Mortamet 2016). Furthermore, the hydrodynamic LOEM-CW model applied to constructed wetlands in South Florida revealed that the flow resistance caused by the submerged and emergent aquatic vegetation was a vital factor in reducing the flow velocity and changing the flow pattern (Ji and Jin, 2020).

Thermal stratification is a physical process of considerable importance to small pond ecosystems (Song et al., 2013; Rey et al., 2021). The role of thermal and chemical stratifications in governing water quality processes in two stormwater wet ponds and two constructed wetlands in Calgary, Alberta, Canada, was investigated in chapters 3 and 4. Chapter 3 showed that the study ponds had vertical water temperature differences >1 °C from May to August 99% of the time. In addition, salt-laden inflows from road deicing salts led to strong chemical stratification up to five times stronger in the sediment forebays than in the main cells in spring. The vertical thermal and chemical structure forced the runoff from the inlet to the outlet to move above or below the pycnocline, creating dead zones and inhibiting wind-induced vertical mixing. The results demonstrate that the ponds' strong and prolonged stratification decreased pollutant retention capacity and caused the water at depth to become anoxic, degrading the quality of the water discharged downstream. Stratification and hydrodynamics were also investigated in two wetlands in chapter 4. Despite their small size (<1.5 ha) and shallow depths (0.8 m), stratification was

thoroughly and intensely present in the wetlands in contrast to the assumption that ponded water in urban wetlands is well-mixed. For instance, thermal stratification in the two urban stormwater-constructed wetlands in chapter 4 persisted at a vertical temperature gradient $> 1^{\circ}\text{C}/\text{m}$ for up to two-thirds of the ice-free season, May-October, and up to 21 consecutive days in the summer. In addition, chemical stratification was evident due to salt-laden inflows from road deicing salts resulting in a significant densimetric stratification of up to 79% of the time between May and October. Strong densimetric stratification and low wind stress on the water surface caused anoxic conditions near the bed, potentially adversely affecting water quality and downstream aquatic communities. Hence, additional stratification considerations are required when designing new stormwater ponds and constructed wetlands.

Stratification has also been suggested as an essential factor when determining the hydraulic residence time (HRT) in ponds and wetlands (Torres et al., 1997; Kellner and Pires, 2002; Wahl et al., 2010). Residence time is a measure of the duration that the stormwater resides in a pond's basin before exiting to the receiving water body and is sometimes used interchangeably with hydraulic retention time (Persson et al., 1999; Su et al., 2009; Wahl et al., 2010). Management practices should aim for adequate residence time to facilitate sediment and nutrient removal (Wahl et al., 2010; Song et al., 2013; Gu et al., 2017). However, existing guidelines do not typically account for hydraulic complexity and rely on zero-dimensional (completely mixed) or 1D (plug-flow) models to estimate HRT (e.g., Ontario Ministry of the Environment, 2003; City of Calgary, 2011). These methods can produce inaccurate HRT predictions and result in untreated stormwater (Gu et al., 2017).

Despite the numerous research studies on stormwater ponds and wetlands, the application of a 3D hydrodynamic model in urban stormwater wet ponds and constructed wetlands for extended

periods with extensive data sets for model calibration and verification is lacking (Chen et al., 2019; Ji and Jin, 2020). The application and long-term validation of a 3D hydrodynamic model would allow for crucial model calibration parameters (e.g., light attenuation, albedo, heat transfer coefficients, and eddy viscosity and diffusivity) to be identified, which would help improve the understanding of the relationship between temperature, turbidity and turbulence on thermal stratification and HRT. In addition, the 3D hydrodynamic models can also enhance understanding of the influence of the inflow/outflow rates, stratification, wind speed and direction, and pond geometry on the HRT and mixing. Therefore, the detailed field data presented in chapters 3 and 4 were used to calibrate/validate the 3D hydrodynamic model, Environmental Fluid Dynamics Code (EFDC), in an urban stormwater wet pond (Auburn Bay) and an urban stormwater constructed wetland (Royal Oak). Then the calibrated and validated models were used to systematically investigate the effect of inflow/outflow configuration, bathymetry, wind and stratification on the retention time in the study sites. In addition, a parametric study was conducted on varying design depth, inlet positioning, wind speed and direction.

5.2 Methodology

5.2.1 Study sites and field measurements for the hydrodynamic modelling

A stormwater wet pond, Auburn Bay, and a relatively smaller and shallower constructed wetland, Royal Oak, in the southeast and northwest Calgary, Alberta, Canada, were selected for this study (Figure 5-1). Table 5-1 presents the characteristics of the two facilities and their associated catchments. The bathymetry of the pond/wetland in Figure 5-1 was defined from survey data collected in 2018 using a real-time kinetic global positioning system (GPS). The study sites have different depths, sizes, and vegetation designs, allowing for a better understanding of the

hydrodynamics under various conditions. For example, the Auburn Bay wet pond has a surface area at NWL ~ four times larger and a loading ratio ~ three times larger than the Royal Oak wetland (Table 5-1). The aquatic and riparian vegetation communities were identified in Royal Oak and Auburn Bay during a ground-based field survey and areal photos using a drone in June 2019. In addition, the physical dimensions of aquatic plants were measured, and plant density was identified in situ as the number of stems inside a unit area hollow frame at multiple locations in the pond/wetland. For further information on the design characteristics of the two study sites and their catchment areas, refer to chapters 3 and 4.

The meteorological data were acquired using a solar-powered HOBO U30 or RX3000 data logger (Onset, USA) deployed at each site on a 10-m pole and sampled every 5 minutes. Solar radiation, wind speed, wind direction, air temperature, relative humidity, atmospheric pressure, and precipitation have been measured, and the cloud cover was calculated following Reed (1977). Figure 5-2 shows the time series of the meteorological data from the Auburn Bay station in 2019. For further information on the meteorological data at the two study sites, refer to chapters 3 and 4.

At the inlet structures of Auburn Bay and Royal Oak, area/velocity flow modules (model 750 or 2150, Teledyne ISCO, USA) were installed inside the inlet pipes to automatically calculate the inflow rates from the recorded water depths/velocities and the diameters of the given pipes. Three locations were chosen in the wet pond and the wetland near the inlet, the middle and the outlet for continuous water quality monitoring needed for calibration and validation, i.e., locations IN, MID and OUT (Figure 5-1). In addition, 25 fortnightly field trips to the ponds were conducted in 2018 and 2019. During each trip, Secchi disc measurements were recorded, and vertical temperature and salinity profiles with a vertical resolution of 30 cm in Auburn Bay and 10 cm in Royal Oak were collected manually from a boat. Furthermore, velocity profile measurements were continuously

collected at three locations, V_1 , V_2 and V_3 , along the main flow path in Auburn Bay using bottom-mounted acoustic Doppler current profilers (Aquadopp Profiler 1 MHz, Nortek, Norway) at 15 minutes intervals, see Figure 5-1a. The shallow wetland does not have enough depth to deploy the AquaDopp. Therefore, an Acoustic Doppler Velocimeter (ADV) (Vector-300m Cable Probe GA, Nortek, Norway) was deployed in Royal Oak downstream of the sediment forebay at location V_4 in Figure 5-1b. The Vector velocimeter captured the 3D velocities at ~10 cm below the water surface at 15 minutes intervals. For further information on the two years field program and the limnological data at the two study sites, refer to chapters 3 and 4.

5.2.2 Model description

The EFDC+ model (latest version, DSI LLC, 2022) solves the unsteady 3D Reynolds-averaged Navier–Stokes (RANS) and continuity equations with the Boussinesq approximation and Mellor–Yamada (Mellor and Yamada, 1982) second-moment turbulence closure model (Hamrick, 1992). In addition, the EFDC+ solves the advection-diffusion equations for the transport of salinity, heat, and dye. The governing equations of the model can be found in the EFDC+ theory guide (DSI LLC, 2022). The equations are presented in the curvilinear coordinate system in the horizontal direction and sigma-Z (Craig et al., 2014) transformation for the vertical direction. The sigma-Z-coordinate system adjusts the number of vertical layers per horizontal grid cell according to the depth below this cell. It provides an efficient way to balance vertical resolution, reducing the horizontal gradient error in sigma grids (DSI LLC. 2022).

The level 2.5 turbulence closure parameterization developed by Mellor and Yamada (1982) and modified by Galperin et al. (1988) determines the vertical mixing coefficients. The horizontal momentum and mass diffusivity are determined independently using the Smagorinsky (1963) eddy

parameterization with the multiplier (horizontal turbulence Prandtl number) set to 0.1 according to Mellor and Blumberg (1985). More information on Mellor-Yamada turbulent closure model and the Smagorinsky model is available in the EFDC+ theory guide (DSI LLC, 2022).

The surface heat exchange model includes heating due to longwave radiation, evaporation, and sensible heat fluxes calculated based on the approach proposed by Rosati and Miyakoda (1988) and Hamrick (1992) as follows:

$$-\frac{\rho_w c_{pw} A_b}{H} \frac{\partial T}{\partial z} = H_L + H_E + H_S \quad (\text{Equation 5-1})$$

$$H_L = \varepsilon (T_s + 273.15)^4 (0.39 - 0.05\sqrt{e_a}) (1 + B_c C) + 4\varepsilon\sigma (T_s + 273.15)^3 (T_s - T_a) \quad (\text{Equation 5-2})$$

$$H_E = c_e \rho_a L_E W (e_s - e_a) \frac{0.622}{p_a} \quad (\text{Equation 5-3})$$

$$H_S = c_s \rho_a C_{pa} W (T_s - T_a) \quad (\text{Equation 5-4})$$

where ρ_w is water density (kg/m^3); c_{pw} is the specific heat of water ($=4,182 \text{ J/kg/}^\circ\text{C}$); A_b is the vertical eddy diffusivity (m^2/s); H is the water depth (m); H_L , H_E and H_S are the heat exchange flux due to long wave back radiation, latent heat, and sensible heat (W/m^2); ε is the emissivity of the waterbody ($= 0.97$); T_a and T_s are the air and water surface temperatures ($^\circ\text{C}$); e_a and e_s are the vapour pressure of the air and the saturation vapour pressure at surface water temperature in (mbar); B_c is an empirical constant ($= 0.8$); C is the cloud fraction (dimensionless); σ is Stefan–Boltzmann constant ($= 5.67 \times 10^{-8} \text{ W/m}^2/\text{K}^4$); c_e and c_s are the latent and sensible heat transfer coefficients (calibration parameters, dimensionless); ρ_a is the atmospheric density ($= 1.2 \text{ kg/m}^3$),

L_E is the latent heat of evaporation of water ($= 2.501 \times 10^6$ J/kg); W is the 10-m wind speed (m/s); P_a is the atmospheric pressure (mbar); C_{pa} is the specific heat of air ($= 1005$ J/kg/°C).

The model also calculates the penetration of short-wave solar radiation in the water column as an exponential function of water depth and light extinction coefficient according to the Beer-Lambert law (Ji, 2008):

$$I_{ws} = I_0 \cdot S_f \cdot \min \{ \exp[-K_{e,me}(H_{rps} - H)], 1 \} \quad (\text{Equation 5-5})$$

$$I_z = I_{ws} e^{-\int_0^z K dz} \quad (\text{Equation 5-6})$$

where I_0 and I_{ws} (W/m^2) are the short wave radiation at the earth's surface (measured), and the short wave radiation at the water surface as modified by the terrain shading factor ($S_f = 1 - \text{albedo}$); $K_{e,me}$ is the light extinction coefficient for emergent shoots (m^{-1}); H_{rps} is the rooted plant shoot height (m); H is the water column depth (m). At depth z (m) below the water surface, the short wave radiation penetrating the water surface, I_z (W m^{-2}), is dependent on the light extinction coefficient, K (m^{-1}), which is a calibration parameter that plays a vital role in determining the depth of the thermocline and the degree of temperature stratification (Brown, 1984; DSI LLC. 2022).

In addition, the model changes the bed temperature (T_b) with time due to sediment-water interface heat exchange, which is analogous to Rosati and Miyakoda's expression for the water surface (Rosati and Miyakoda 1988) as follows:

$$\frac{\delta(D_b T_b)}{\delta t} = - \left(K_{b,v} \frac{\rho_w c_{pw}}{\rho_b c_{pb}} U_b + \frac{K_{b,c}}{\rho_w c_p} \right) (T_b - T_{bw}) \quad (\text{Equation 5-7})$$

where D_b is the sediment bed-thermal thickness (calibration parameter, m); $K_{b,v}$ is the convective heat transfer coefficient (= 0.001 following Jin et al., 2000); ρ_b , ρ_w are bed and water densities (Kg/m^3); c_{pw} is the specific heat of water (=4,182 J/kg/°C); c_{pb} is the specific heat of the water-solid bed mixture (J/kg/°C); U_b is the absolute water velocity at the bed-water interface (m/s); $K_{b,c}$ is the conductive heat exchange coefficient (= 0.3 W/m²/°C following Gong et al., 2016); T_{bw} is water temperature near the bed (°C). For simplicity, the model assumes $\rho_w c_{pw}$ equal to $\rho_b c_{pb}$, following Jin et al. (2000).

A dye constituent in EFDC+ is employed to compute the hydraulic residence time or age of water in days. It represents a tracer in the water column that does not impact the hydrodynamics, thermal or physical properties, including density and viscosity (DSI 2022). With this option, the water age in the model domain starts at zero at the beginning of each run. In addition, all incoming water to the model domain is assumed to have an age of zero days, i.e. new water. Every timestep, the age of water in days is transported following the advection-diffusion equation in a method similar to all other water column constituents (e.g., temperature and salinity). Then at the end of each time step, the water is aged by adding the time step in days to the age constituent. Suppose the model is run sufficiently long enough to achieve a dynamic steady state. In that case, residence times can be computed by time-averaging cell ages over all parts of the model domain (DSI LLC. 2022). Although this method neglects the initial age of water that starts at zero and underestimates the time-averaged age (average HRT), it might be a conservative way to evaluate the hydraulic performance of the study pond and wetland, assuming that they started their operation at the beginning of each simulation.

5.2.3 Model setup

The physical domains of the study sites were transported into computational meshes that accurately represent the shape of the water bodies with outer boundaries set to cover the inundated area during the designed High Water Level (HWL) (Figure 5-1). A mesh of 3x3 m grids was prepared to represent 3917 and 776 horizontal cells in Auburn Bay and Royal Oak, respectively. The number of layers used per cell varied over the model domain between 4 and 40 in the wet pond and 1 and 20 in the wetland, according to the depth below this cell. As a result, a fine vertical grid of 7–9 cm was used in the two systems. The adequacy of the grids is investigated by undertaking a mesh independency study by comparing the results of the water temperature, salinity and velocity modules under different mesh sizes of 3, 6, and 12 m and different vertical resolutions of 10, 20 and 40 vertical layers. Similarly, Nakhaei et al. (2019) used cell sizes between 2 and 4 m in their 3D Estuary and Lake Computer Model (ELCOM v. 3.0) for hydrodynamic and thermal stratification modelling in three stormwater wet ponds and wetlands of 1-2 ha surface area in Edmonton, Canada. In addition, Nakhaei et al. (2019) used a similar fine vertical grid of 5–10 cm to resolve the vertical gradients in their 0.5-1.8 m deep stormwater facilities. The large number of cells in the Auburn Bay domain was computationally demanding. Hence the dynamic time step option was used in which the EFDC code changed the time step between 0.1 and 1.6 seconds based on the Courant–Friedrichs–Lewy condition and the positivity of temperature, salinity, and dye results. In Royal Oak, the domain was much smaller, and hence a constant 0.3-second time step was computationally convenient to satisfy the stability criterion of the Courant–Fredrichs–Lewy condition.

The simulation start and end dates presented in Table 5-2 were set based on the available inflow data. The meteorological data for the boundary forcing at the air-water interface were obtained from onsite meteorological stations. Temperature and salinity profiles measured at the three

monitoring locations at the beginning of each monitoring year were spatially interpolated to initialize the water temperature and salinity of the two domains. EFDC+ can internally simulate different hydraulic structures, including weirs and orifices. Therefore, the flow boundary conditions were defined using the measured inflow time series at inlets and the as-built outlet structure dimensions. Inflow temperature and salinity boundary conditions were not measured. As a result, the water temperature profiles measured continuously near the inlet at IN at a vertical resolution of 25 cm in Auburn Bay and 10 cm in Royal Oak were set as the inflow temperature boundary condition. While the inflow salinity concentration was calibrated to achieve the least error between the observed and simulated in-pond water salinity. The continuous water surface elevations, temperature, salinity and velocity data collected at 5-15 minute intervals between May and October were used for calibration in 2019 and validation in 2018.

The input parameters used for the vegetation submodel in the Royal Oak wetland are shown in Table 5-3. For further information on the vegetation in the Royal Oak wetland and its spatial distribution, refer to chapter 4. Plant density, area covered, stem diameter and height for the aquatic and riparian communities were measured in situ. While the drag coefficient was considered a calibration parameter. Drag exerted by plants will reduce the mean flow within vegetated regions. Vegetation will also affect the turbulence intensity and its diffusion and solar radiation received at the water surface I_{ws} due to shading (Equation 5-5). The conceptual framework for vegetation in the EFDC+ is shown in (DSI 2022).

5.2.4 Model calibration

The simulated and measured water surface elevations, temperatures and salinity for the same time step were compared by calculating the root-mean-squared error (RMSE) given by:

$$RMSE = \sqrt{\frac{\sum_{i=1}^n (x_{i,observed} - x_{i,simulated})^2}{n}} \quad (\text{Equation 5-8})$$

A low-pass filtering with 2 hrs cutoff was applied to both modelled and observed water currents to minimize the noise in the data. Then, the agreement between the modelled and the observed easting and northing components and absolute velocities of the water surface currents was tested using a linear correlation coefficient of determination (R^2). Further, the normalized Fourier norm or the relative percentage of variance in the observed water currents that is unexplained by the model solutions was calculated to evaluate the hydrodynamic results, following Beletsky et al. (2006) as follows:

$$F_n = \left(\frac{1}{M} \sum_{t=\Delta t}^{M\Delta t} |V_m - V_o|^2 \right)^{0.5} / \left(\frac{1}{M} \sum_{t=\Delta t}^{M\Delta t} V_o^2 \right)^{0.5} \quad (\text{Equation 5-9})$$

where V_m and V_o are the modelled and observed water currents.

The latent and sensible heat transfer coefficients in Equations 5-3 and 5-4, albedo in Equation 5-5, light extinction coefficient in Equation 5-6, and the bed-thermal thickness D_b in Equation 5-7 were manually calibrated to minimize the RMSE between the modelled and the observed water temperature. Then, the background horizontal and vertical eddy viscosity, diffusivity, and vegetation drag coefficient were manually calibrated using values in previous EFDC models to maximize the R^2 between the observed and modelled water currents.

The EFDC code uses default latent and sensible heat transfer coefficients C_e and C_s of 1.1×10^{-3} (DSI LLC. 2020). Nakhaei et al. (2019) set the C_e and C_s coefficients at 1.3×10^{-3} in three stormwater ponds and wetlands in Edmonton, Alberta, Canada. These values of C_e and C_s match earlier observations obtained under moderate to strong wind conditions over the ocean (e.g., Fairall

et al. 1996). However, the heat transfer coefficients have been reported to increase at low wind speeds ($<4 \text{ m s}^{-1}$) (Wei and Miyano., 2016). The wind speeds recorded at our study sites were light at average values of 2.1 and 2.7 m/s in 2019 in Auburn Bay and Royal Oak, respectively (Figure 5-2). At these low wind conditions, the heat transfer coefficients, according to Wei and Miyano (2016), changed between 1.0×10^{-3} and 4.0×10^{-3} . As a result, this range for the latent and sensible heat transfer coefficients was used for the calibration and sensitivity analysis in our study pond and wetland.

The reflection coefficient of the short wave radiation (albedo) depends on the sun angle, watercolour, and emergent plants (Rouse, 2000; Nakhaei et al., 2019). For example, Albedo between 0.10-0.35 was used by Nakhaei et al. (2019) to calibrate their hydrodynamic models of urban stormwater ponds and wetlands in Edmonton, Alberta, Canada. These wet ponds and wetlands, located in Alberta, Canada, $< 300 \text{ KM}$ away from our study sites, had comparable solar angles and similar shading from surrounding trees and other vegetation to Auburn Bay and Royal Oak. In addition, the albedo in wetlands in Manitoba, Canada, from June through September, was reported to be 0.05-0.20 (Rouse, 2000). As a result, scenarios of varying albedo between 0.05 and 0.3 were used for the calibration and sensitivity analysis in our study sites.

The turbid water, suspended algae, and submerged aquatic vegetation in ponds and wetlands can inhibit light penetration through the water column (Brown, 1984). This can alter thermal stratification and needs to be addressed by adjusting the light extinction coefficient (Nakhaei et al., 2019). Values for the light extinction coefficient were selected based on a relation proposed by Brown (1984) between the Secchi disc measurements and the light extinction coefficient, K , (m^{-1}), $K = -\ln(I_0)/(\text{Secchi depth})$, where I_0 is the percentage of penetrated light at the Secchi depth. Assuming light penetration between 10-30% following Brown (1984), the calculated light

extinction between May and October varied between 1 and 6 m^{-1} and was higher, on average, at IN at 2.5 m^{-1} than MID and OUT at 2.0 m^{-1} . As a result, a calibration was performed, assuming a spatially varying light extinction coefficient at IN and MID/OUT between 1 and 6 m^{-1} .

Bed temperature can also influence the downward propagation of surface heating and cooling (DSI LLC, 2022). The rate of change of bed temperature depends on the sediment bed-thermal thickness D_b in Equation 5-7. The greater the thermal thickness, the slower the bed temperature will change. The selection of the thermal thickness is subject to initial approximation and subsequent calibration. Values between 0.1-0.3 m were used in the literature to calibrate stratified lakes (Jin et al., 2000; Dong et al., 2019).

For the water temperature calibration, time series of RMSE profiles between the simulated and observed water temperature were calculated at a vertical resolution of 25 cm in Auburn Bay and 10 cm in Royal Oak for each run. Then the time series of the RMSE profiles were averaged at IN, MID and OUT in (Figure 5-1) to give an averaged RMSE at each location. Next, the averaged RMSE of temperature from the different calibration runs was linearly interpolated in 2D plots by tuning two parameters from the heat transfer coefficients, albedo and light extinction coefficient, to define the model's sensitivity and the optimum calibration values as follows. Firstly, the RMSE of temperature was interpolated for 16 scenarios of albedo at 0.05, 0.1, 0.2 and 0.3 versus heat transfer coefficients $c_e=c_s$ at 1.0, 2.0, 3.0 and 4.0 $\times 10^{-3}$ with an initial approximation of spatially varying light extinction coefficients of 2.5 m^{-1} at the sediment forebay (IN) and 2.0 m^{-1} at the main cell (MID and OUT). After that, the best results for the heat transfer coefficients c_e and c_s from the first analysis were fixed for another 24 scenarios of light extinction at 1.0, 2.0, 3.0, 4.0, 5.0 and 6.0 m^{-1} versus albedo at 0.05, 0.1, 0.2 and 0.3 at the sediment forebay (IN) and the main cell (MID/OUT). Finally, the best results for the heat transfer coefficients, albedo and light

extinction coefficients were used to test the model's sensitivity against two scenarios of bed thermal thicknesses at 0.1 and 0.3 m.

For the hydrodynamic calibration, the background horizontal and vertical eddy viscosity and diffusivity were interrogated using values in previous EFDC models in Lake Ontario in Canada, Lake Arendsee in Germany and the shallow Upper Klamath Lake in the USA (Arfin et al., 2016; Dong et al., 2019; Chen et al., 2020). Values from 0 to 2.5 m²/s for the horizontal eddy viscosity, 10⁻⁶–0.01 m²/s for vertical eddy viscosity and 10⁻⁸–0.01 m²/s for vertical diffusivity were tested. In addition, the vegetation sub-model was tested for a wide range of vegetation parameters at stem diameters between 0.001-0.2m, plant density at 0-100 stem/m², stem height at 0-2m and drag coefficients between 0 and 1.

5.2.5 Hydraulic performance analysis

To evaluate the hydraulic performance of the study pond and wetland and to achieve optimized treatment efficiency, they are expected to experience an actual HRT equal to the theoretical or the nominal residence time t_n (Bodin and Persson, 2012; Jenkins and Greenway, 2005; Guo et al., 2017). The nominal residence time t_n is defined according to the plug-flow (1D) assumption as the ratio of the pond volume V to the average inflow rate (Andradóttir and Mortamet, 2016). However, ponds and wetlands can function below the optimized level due to unevenly distributed flow patterns in the three dimensions. Therefore, hydraulic efficiency, defined as the ratio of the simulated HRT over the nominal residence time t_n , is used to measure the extent of the effective usage of the water body. For instance, thermal stratification is a physical process that can inhibit vertical mixing and cause shortcircuiting and deviations in HRT between the nominal and

simulated values (Holland et al., 2004; Wahl et al., 2010; Guo et al., 2017), reducing pollutants retention capacity (refer to chapter 3). As a result, thermal stratification is also quantified and used as an index for hydraulic performance evaluation. First, a vertical temperature difference, ΔT , of at least 1.0 °C was used as the threshold to define significant thermal stratification following McEnroe et al. (2013), Nakhaei et al. (2019) and a similar approach used in our stormwater ponds in chapter 3. Then, the duration of the simulated thermal stratification predicted at IN, MID and OUT as a percentage of the overall runtime is determined.

5.3 Results and discussion

5.3.1 Sensitivity analysis

The albedo, turbulent heat exchange coefficients, C_e and C_h , and light extinction coefficients were chosen as input parameters for the sensitivity analysis in Figure 5-3. Two-dimensional colour contour plots of the RMSE of the water temperature from 64 runs were generated to estimate the model's sensitivity based on the RMSE gradients (see Figure 5-3). For example, in Figure 5-3ad, 16 scenarios of albedo versus turbulent heat exchange coefficients in Auburn Bay and Royal Oak show higher RMSE gradients in the heat exchange coefficient direction, which can also be defined as the proximity of the contour lines to each other, than in the albedo direction. In Auburn Bay, 24 scenarios of light extinction at IN and OUT versus albedo in Figure 5-3bc show that the model was equally sensitive to both light extinction and albedo when the contour lines were on average at 45°. Finally, in Royal Oak (Figure 5-3e,f), the model was equally sensitive to albedo and light extinction at IN (Figure 5-3e) and more sensitive to albedo than light extinction at OUT (Figure 5-3f), likely due to its shallow depth at 0.6 m, causing minimal vertical temperature gradient regardless of the light extinction coefficient (Song et al., 2013).

The sensitivity of the hydrodynamic model to the background horizontal eddy viscosity was investigated using two scenarios at 0.05 and 0.1 m²/s. The results of the modelled velocity profiles were compared to the observed profiles in Auburn Bay in Figure 5-4. The higher value resulted in predicted average velocities that were overestimated by ~50%, and the lower value underestimated the average velocities by a factor of two (Figure 5-4).

The simulated water surface elevations, temperature, salinity and water velocity profiles were not sensitive to the bottom roughness height, bed thermal thickness, background vertical eddy viscosity, or diffusivity. Furthermore, in Royal Oak, the velocity profiles were not sensitive to varying parameters in the aquatic vegetation sub-model over wide ranges (i.e., stem diameters between 0.001-0.2m, plant density at 0-100 stem/m², stem height at 0-2m and drag coefficients between 0 and 1).

5.3.2 Calibration and validation

The model parameters used in the EFDC simulations for Auburn Bay and Royal Oak are presented in Table 5-4. The water surface elevation was calibrated using appropriate turbulent exchange coefficients for evaporation and discharge coefficients for the outlet hydraulic structures (Table 5-4). Figure 5-5 shows the simulated water surface elevation compared to the observed data in Auburn Bay and Royal Oak during the calibration and validation runs, and errors are presented in Table 5-5. In Auburn Bay, the milder inflow events and the lower water surface elevation rises in 2019 likely resulted in an accurate simulation at a low RMSE of 1.6 cm (Table 5-5 and Figure 5-5a) versus 4.5 cm in 2018 due to the significant inflow events that induced a rapid and considerable increase in the water surface elevation (Table 5-5 and Figure 5-5b). Royal Oak's water surface elevation was modelled better during the validation run in 2018 when the RMSE was as low as 1.3

cm versus 3.3 cm in 2019 (Table 5-5). Uncertainties in the measured inflow rates during significant inflow events are the possible sources of the water surface elevation errors. Previous EFDC hydrodynamic models of wetlands and shallow Lakes in the USA and China had RMSE in water surface elevation at 2-13 cm, equivalent to 1-13% of their permanent pool volume (Gong et al., 2016; Chen et al., 2020; Ji and Jin, 2020) versus 1-4% in our study pond and wetland (Table 5-5). Hence, our models simulated the observed depths reasonably well compared to the literature.

The lowest RMSE in simulated water temperatures in Auburn Bay was achieved at an albedo of 0.05, heat exchange coefficients of 2.5×10^{-3} and light extinction coefficients of 4 and 2 m^{-1} at IN and OUT (Table 5-4 and Figure 5-3a,b,c). However, the most accurate simulations in Royal Oak were achieved at a higher albedo of 0.2, heat exchange coefficients of 3×10^{-3} and light extinction of 6 and 2 m^{-1} at IN and OUT (Table 5-4 and Figure 5-3d,e,f). These turbulent heat exchange coefficients are much larger than the 1.1×10^{-3} typically used in the open ocean because of the significantly lower wind velocities observed at these inland water bodies (Wei and Miyano, 2016). In addition, a higher albedo was likely needed in Royal Oak (Table 5-4) because a significant fraction of the water surface is shaded by the wetland's dense riparian vegetation. The calibrated light extinction at IN was twice as large as at OUT in both water bodies (Figure 5-3b,c,e,f). This was due to the higher turbidity inside the sediment forebays at IN, inferred from the lower Secchi depth measurements at IN than MID and OUT.

The RMSEs of the water temperatures were 1.0-1.3 °C in Auburn Bay and 1.7-1.9 °C in Royal Oak for the calibration and validation runs, respectively (Table 5-5). The higher RMSEs in Royal Oak suggest that the EFDC model can simulate temperatures more accurately in relatively deeper stormwater ponds compared to shallower wetlands (Nakhaei et al. 2019). However, the RMSEs of water temperature in our study sites are still better than most results found to be acceptable in other

published studies where hydrodynamic models have been applied to ponds, wetlands, and shallow lakes in North America and China. For example, Gong et al. (2016) in Lake Tianyihu in China, Nakhaei et al. (2019) in three stormwater ponds in Edmonton, Alberta, Canada, Ji and Jin (2020) in a wetland in south Florida, USA, and Rey et al. (2021) in a waste stabilization pond in Ontario, Canada, reported RMSEs in the water temperature of 1.0-3.5 °C.

The simulated vertical temperature profiles and thermocline height above the bed are compared to the observed values at IN and OUT in Auburn Bay in Figure 5-6. At IN, the model accurately simulated the water temperatures and the thermocline in May and June before it predicted a gradual deepening of the thermocline in mid-July and overestimated its depth significantly for the remainder of the time. For instance, the simulated thermocline depth was overestimated by 52 cm between May and October and up to 139 and 106 cm in July and August, respectively (Figure 5-6b,c). Therefore, the average ratio of the predicted versus observed thermocline depth was 1.7. At OUT, the thermocline depth was more reasonably simulated when the average predicted versus observed depth ratio was 1.3, and the thermocline depth was overestimated by only 28 cm (Figure 5-6d,e). In Royal Oak, the model overestimated the average thermocline depth between May and September at IN by 21 cm, and the average predicted versus observed depth ratio was 2.5 (Figure 5-7b,c). Yet, the model reasonably simulated the thermocline depth at OUT when the predicted versus observed depth ratio was 1.3 (Figure 5-7d,e). Nakhaei et al. (2019) also reported that the predicted average thermocline depth using a 3D hydrodynamic model in 0.4-1.8 m deep stormwater ponds and wetlands in Alberta, Canada, was overestimated by up to 1.0 m. They suggest that this was due to a higher light penetration throughout the water column in the model despite having a large calibrated light extinction coefficient (6.0 m^{-1}) in their model. The sensitivity analysis of light extinction at IN in Auburn Bay (Figure 5-3b) also suggests that

increasing the calibrated light extinction above 4 m^{-1} will not enhance the average RMSE of water temperature at IN.

Tables 5-6 and 5-7 presented the percentage of the time when the water columns in Auburn Bay and Royal Oak were thermally stratified at a vertical temperature difference $> 1 \text{ }^\circ\text{C}$ and the average magnitude of the vertical temperature difference, ΔT . The model in Auburn Bay underestimated the occurrence of stratification by $\sim 7\text{-}28\%$ and the strength of the stratification by $0.6\text{-}2.2 \text{ }^\circ\text{C}$ (Tables 5-6 and 6-7). Similar results were observed in Royal Oak when the model underestimated the strength of thermal stratification by $0.4\text{-}2.6 \text{ }^\circ\text{C}$ and the duration of thermal stratification by 30% at IN, and it failed to predict any thermal stratification event at OUT, where the depth was shallowest at 0.6 m (Tables 5-6 and 5-7). Nakhaei et al. (2019) also reported that their hydrodynamic model underestimated the duration and strength of thermal stratification by $7\text{-}50\%$ and $1.5\text{-}2.0 \text{ }^\circ\text{C}$ in three stormwater ponds in Alberta, Canada. They suggest that this was primarily due to challenges in accurately simulating the thermocline depth, especially in the shallow vegetated wet ponds.

The modelled time series of the water salinity at various depths in Auburn Bay were compared to the observations in Figure 5-8. Chapters 3 and 4 of the current study reported that the chemical stratification, high in winter and early spring and low in summer in the study pond and wetland, is due to inflows of salt-laden stormwater from road deicing salts. For instance, Auburn Bay was chemically stratified at the beginning of the calibration run in late April 2019 by more than 2.5 and 1.0 ppt of vertical salinity difference at IN and OUT (Figure 5-8). The high salinity in spring was gradually flushed by subsequent inflow events decreasing the chemical stratification with time (Figure 5-8). In general, the simulated seasonal variations in the water salinity agree well with the observations (Figure 5-8). During the calibration and validation runs, the RMSE of salinity in

Auburn Bay and Royal Oak was ≤ 0.2 ppt (Table 5-5). An error in salinity of 0.4 ppt is equivalent to the density difference between 24 and 25 °C (McEnroe et al., 2013). Hence the salinity RMSEs in Table 5-5, which are equivalent to less than 1°C error in temperature, are acceptable.

Figure 5-9 shows the time series of wind components, rain depth and the velocities observed and modelled in the middle of the Auburn Bay wet pond at V_2 . Wind speed influenced water surface currents when peak velocities between 2 and 3 cm/s coincided with stronger winds up to 7 m/s (Figure 5-9a-d). The effect of the wind direction is emphasized on May 30, June 2, 3,4, and 13, when the strongest along-axis winds from the east and northeast produced a significant current toward the west (Figure 5-9a,b). Water surface currents with magnitudes of 1-2 cm/s were observed following the rainfall event on June 8 (Figure 5-9a,d). The inflow water on June 8 was forced to travel above the berm of the sediment forebay from the inlet to the outlet toward the west when counter currents were generated at location V_2 in the opposite direction from outlet to inlet toward the east at d/H of ~ 0.6 (Figures 5-9e and 5-10a). Similarly, during the significant wind event on June 13 from the east, surface currents toward the west were generated when deeper return currents toward the east at d/H of 0.1-0.3 were evident (Figures 5-9e and 5-10b).

The vertical distribution of the normalized Fourier norms, F_n , between the modelled and observed currents at stations V_1 , V_2 and V_3 in Auburn Bay is presented in Figure 5-11. The normalized Fourier norm or the relative percentage of variance in the observed water currents that is unexplained by the model solutions was calculated following Equation 5-9. The vertical F_n values ranged between 0.45 and 0.7. The error peaked at subsurface layers of depth ratio d/H of 0.1-0.2, indicating an underestimation of the depth of the surface currents (Figures 5-9e,f and 5-11). Similarly, in Lake Ontario, the vertical F_n ranged from 0.4 to 0.9 when Huang et al. (2010) simulated the currents using three hydrodynamic models, namely, the Princeton Ocean Model

(POM), Canadian Version of Diecast Model (CANDIE), and Estuary, Lake, and Coastal Ocean Model (ELCOM). Huang et al. (2010) also reported that the three models underestimated both the current velocity at subsurface depths and the thickness of the upper mixed layer.

In the middle of the Auburn Bay pond, location V_2 , the error between the modelled and the observed water currents was the least near the surface when F_n was 0.45 (Figure 5-11). The magnitude of the modelled and observed surface velocities had a coefficient of determination R^2 of 0.24 at V_2 (Figure 5-9d). The correlation was even stronger during some shorter periods, e.g., between June 3 and 11 in Figure 5-9d, when R^2 was at 0.53. Chen et al. (2019) and Rey et al. (2020) observed R^2 up to 0.17-0.58 for the current magnitude in a stormwater pond and a waste stabilization pond in Canada. Hence, our model's prediction of the velocity magnitude is comparable to and sometimes better than that applied in recent studies. However, the agreement between the modelled and observed currents direction in Auburn Bay was poor at a coefficient of determination R^2 of 0.00 for v_x , v_y (Figure 5-9b,c). Rey et al. (2020) suggested that the challenges in modelling pond currents are due to their slow velocities. This might also explain the poor agreement between the modelled and observed currents in Auburn Bay, where velocities were < 3 cm/s.

In the middle of the Royal Oak wetland, location V_4 , the observed wind components and the modelled and observed water surface currents are presented in Figure 5-12. Wind speed peaked at higher values than in Auburn Bay, above 10 m/s at times (e.g., July 24 and 27 in Figure 5-12a). As a result, the observed currents measured 10 cm below the water surface peaked at 3-6 cm/s on July 24, 25 and 27 (Figure 5-12d) (Figure 5-9b-d). The modelled and observed water surface currents in Royal Oak were linearly correlated at R^2 between 0.13-0.61 in direction and 0.55 in magnitude. These results represent one of the best attempts to model water currents in ponds using

a hydrodynamic model in the literature (Chen et al., 2019; Rey et al., 2020). The better predictions of the water currents in the Royal Oak model than in Auburn Bay suggest that the poor results are due to slow velocities.

5.3.3 Hydraulic performance

Ponds and wetlands can function below the optimized level due to shortcircuiting and deviations in HRT between the nominal and simulated values. Therefore, hydraulic efficiency, defined as the ratio of the simulated HRT over the nominal residence time t_n , is used to measure the extent of the effective usage of the water body. The time series of the water depth fluctuation and the modelled domain averaged HRT in Auburn Bay in 2019 and 2018 are presented in Figure 5-13. The modelled HRT started at zero in the two years and increased steadily with time during no or mild water level rises before it decreased abruptly when surface runoff following rainstorm events entered the pond (Figure 5-13). For example, on June 28, day 62 in 2019 (Figure 5-13a), the inflow volume in Auburn Bay induced the highest water level rise in 2019, increasing the depth by ~ 0.4 m and reducing the HRT by 30% (Figure 5-13a). Further, on June 23, day 8 in 2018, during the most significant rainstorm inflow event and the highest water level rise observed in our field study in Auburn Bay, the water depth increased by 1.5 m, significantly reducing the HRT by 84% (Figure 5-13b).

Table 5-8 presents the simulated HRT, the nominal residence time t_n , and the hydraulic efficiency in Auburn Bay and Royal Oak in the two years. In Auburn Bay in 2019, an average stormwater inflow rate of 1,280 m³/day during the modelling period caused a nominal residence time of 44.1 days when the modelled HRT was only 28.6 days, resulting in a hydraulic efficiency of 65% (Table 5-8). During the validation run in 2018, the average inflow rate was higher at 2,900 m³/day when

the hydraulic efficiency hit 100% (Figure 5-13b). In Royal Oak, the average inflow rate was significantly higher in 2019 at 224 versus 43 m³/day in 2018, reduced t_n considerably in 2019, resulting in higher hydraulic efficiency in 2019 at 173% versus 58% in 2018. Hence, the hydraulic performance of stormwater ponds and wetlands is inconsistent and can vary annually according to the average inflow rates.

Using the continuous 15-minute interval time series in Figure 5-13 in the two years, the water depth rise, Δd , normalized to the average pond depth, H , and the corresponding reduction in the domain averaged HRT normalized to the initial HRT in each time step were correlated in Figure 5-14. The HRT decreased only during the water depth rising curve (Figure 5-13). Hence, the water level drops (i.e., negative Δd) were excluded from this correlation. This analysis intended to show the significance of the water level rise, representing inflow/outflow rate and bathymetry, on mixing in ponds. The correlation coefficient was strong at R^2 of 0.71 and 0.96 in Auburn Bay and Royal Oak, indicating that the normalized water depth rise is one of the main drivers of mixing in the study pond and wetland. In Auburn Bay, two distinct grouping points in the correlation in Figure 5-14a represent results from each year. Hence, the weaker correlation in Auburn Bay is likely explained by the interference of other factors in altering mixing in the deeper wet pond, particularly thermal stratification, which was different in the two years (Table 5-7). As a result, one should be careful in extrapolating the correlation results from our region to another region with completely different stratification conditions.

5.3.4 Design and operation guidelines

As a remediation option, the Auburn Bay model was simulated in 2019 with reduced pond storage by lowering the NWL by 0.5 and 1.0 m. As a result, HRT/ T_n slightly increased to 66% during the

first scenario and more significantly enhanced to 76% during the second scenario compared to 65% for the base case scenario. Furthermore, by lowering the NWL by 1.0 m, the model predicted a lower duration of thermal stratification by up to 12% near the outlet (Table 5-9). Reducing Auburn Bay's depth by 1 m was previously recommended in chapter 3 and validated in the current chapter.

The current study in chapter 3 also suggested locating inlets at or near the NWL surface as opposed to the pond bottom to allow complete mixing of the relatively colder inflow water with ambient pond water in the near-field of the inlet. The scenario of inlets located at the NWL for Auburn Bay and Royal Oak reduced the duration of thermal stratification at IN by 19% and 12%, respectively (Table 5-10). This might enhance the pond and the wetland's performance, as prolonged stratification decreased pollutant retention capacity and caused the water at depth to become anoxic, degrading the water quality (Song et al., 2013; Rey et al., 2021).

The calibrated models in 2019 were used to investigate the significance of wind direction on the hydraulic performance at the two study sites. Four scenarios of the observed wind speed consistently blowing from one of the four main cardinal directions were simulated in 2019, and the results are presented in Figure 5-15. These simulations intended to investigate the effect of wind direction on the residence time to point the direction for improved performance by shading a particular direction. At the two study sites, the HRT/T_n slightly increased by 1-2% above the base case scenarios in Auburn Bay and Royal Oak for winds consistently blowing from east and west (Figure 5-15). However, the HRT/T_n slightly decreased by 2-4% during wind from the north and the south (Figure 5-15). This suggests that the wind along the main flow path direction from east and west can slightly increase the effective volume. However, winds perpendicular to the flow path decreased the effective volume by up to 2 and 4% in Auburn Bay and Royal Oak. For

example, the north and south wind in Auburn Bay resulted in a horizontal shortcircuiting when the fresh inflow water travelled south of the main cell and poorly mixed the sediment forebay (Figure 5-15a). Hence, shading the north and south sides of the study pond and wetland by planting trees and riparian vegetation might slightly enhance their hydraulic performance. This finding disagrees with what Li et al. (2013) observed when modelled a rectangular-shaped waste stabilization pond. They observed short circuits harmed the hydraulic efficiency when the inlet/outlet orientation was aligned with the direction of the prevailing winds. The rectangular-shaped basin with no baffles modelled by Li et al. (2013) is much simpler than the irregular geometry and bathymetry of our pond and wetland with berms perpendicular to the flow path, creating more complex flow fields.

Three scenarios of wind speeds, defined as half the observed wind speed, the observed wind speed and doubled the observed wind speed, were tested against the HRT/T_n in 2019 at both sites (Figure 5-16). These simulations were performed for more insights into the significance of wind on hydraulic performance. The observed wind speeds during the model run at the two study sites were 2.1 and 2.7 m/s in the Auburn Bay wet pond and the Royal Oak wetland, respectively. In Auburn Bay, the high wind speed scenario caused a significant reduction in the duration of thermal stratification by up to 31% at OUT due to an increased latent and sensible heat loss from the water surface (Table 5-11). However, the effect of wind speed on the hydrodynamics was minimum in Auburn Bay when HRT/T_n changed by $\leq 1\%$ for both the high and low wind speed scenarios (Figure 5-16c).

For the Royal Oak wetland, the low wind speed scenario significantly increased the duration of thermal stratification by up to 12% due to a reduced heat loss at the water surface (see Equations 5-3, 5-4, and Table 5-10). In addition, the hydrodynamics in the wetland was affected when the HRT/T_n was reduced by 15% (Figure 5-16d), likely when the stratification reduced the hydraulic

retention capacity of the wetland. Double the observed wind speed scenario in Royal Oak caused significant mixing when the duration of thermal stratification was significantly reduced by 34%, the HRT decreased by 33% and the hydraulic efficiency in the wetland was reduced by 58% (Figure 5-16d). Hence, the hydraulic performance of the wetland might be more sensitive to significant changes in the wind speed than the larger and deeper wet pond that was three times deeper and 22 times larger in volume.

5.4 Conclusions

We present well-calibrated and validated EFDC models for simulating the hydrodynamics in an urban stormwater wet pond and a constructed stormwater wetland for exploring their physical processes between May and September in two years. Few studies have previously been published on 3D hydrodynamic modelling of a stormwater wet pond and a constructed stormwater wetland with extensive two-year data sets for model calibration and verification. The RMSEs of the water surface elevation (1.5-4.5 cm), temperature (1-2 °C), and salinity (< 0.2 ppt) during the calibration and validation runs were equal to or better than errors reported in similar modelling studies of wetlands or shallow lakes. Furthermore, although slow velocities at < 3 cm/s in the wet pond were not accurately simulated, the modelled and observed water surface currents in the wetland at 3-6 cm/s were reasonably linearly correlated at R^2 up to 0.61 in direction and 0.58 in magnitude. The hydrodynamic results in the wetland represent one of the most accurate attempts in the literature to model water currents. In the calibration process, the water currents were most sensitive to the background horizontal eddy viscosity. In addition, the modelled temperatures were most sensitive to the turbulent heat exchange coefficients, generally due to the low wind conditions at the study sites. Furthermore, the stormwater pond and wetland characterized by their highly variable

turbidity needed light extinction to be spatially varied in the model domain for more accurate temperature simulations.

The calibrated and validated models were used to evaluate the hydraulic performance of the study sites using the HRT/T_n ratio as an essential indicator of the ponds' retention capacity. Although HRT/T_n varied annually according to the average inflow rates, the normalized water depth rise during inflow events to the permanent pool depth was one of the main drivers of mixing in the study wet pond and wetland when it correlated to the corresponding normalized reduction in the HRT to the initial HRT, at R^2 of 0.71 and 0.96 in the wet pond and the wetland, respectively. The weaker correlation in the deeper 3m wet pond than the shallower 0.8 m wetland is likely explained by the interference of other factors in altering mixing in the wet pond, particularly thermal stratification. The hydraulic performance of the 3.0 m deep wet pond was not sensitive to changes in wind speed or direction. However, the hydraulic performance of the shallow 0.8 m wetland was more obviously sensitive to the wind when it was significantly mixed by double the observed wind speed resulting in a 33% reduction in the hydraulic residence time and a 34% reduction in the duration of the thermal stratification. The study also validated previously suggested remediation design options for better hydraulic performance. For instance, a shallower wet pond at 2 m depth instead of 3 m increased the HRT/T_n by 11% and decreased the duration of the thermal stratification (i.e., $\Delta T > 1^\circ\text{C}/\text{m}$) by 12%. In addition, the scenario of inlets located at or near the NWL, as opposed to near the bed inlets, mixed the water columns near the inlet, causing a significant reduction in the duration of thermal stratification by 19% and 12% in Auburn Bay and Royal Oak.

The developed models are expected to establish a modelling framework for extended wet pond and wetland studies. For instance, the generated 3D models presented in the current chapter will

incorporate the transport and fate of sediment linked to hydrodynamic parameters in chapter 6. This can evaluate the overall efficiency of the design and operation of the stormwater pond and wetland in capturing sediment from stormwater runoff before being discharged to rivers and lakes. It will also assist in optimizing the design and operation guidelines by simulating remediation options for less sediment released downstream.

Notation

The following symbols are used in this chapter:

A_b = vertical eddy diffusivity;

C = cloud fraction;

c_e = latent heat exchange coefficients;

c_{pa} = specific heat of air;

c_{pb} = specific heat of the water-solid bed mixture;

c_{pw} = specific heat of water;

c_s = sensible heat exchange coefficients;

d = water depth below the water surface;

d/H = water depth to the total water column depth ratio;

D_b = sediment bed-thermal thickness;

e_a = vapour pressure of the air;

e_s = the saturation vapour pressure at surface water temperature;

F_n = normalized Fourier norm;

H = water column depth;

H_E = latent heat flux;

H_L = long wave back radiation heat flux;

H_{rps} = rooted plant shoot height;

HRT = hydraulic residence time;

HRT/t_n = hydraulic efficiency;

H_S = sensible heat flux;

HWL = high water level;

I = rain depth;

I_0 = short wave radiation at the earth's surface;

I_{ws} = short wave radiation at the water surface;

I_z = short wave radiation penetrating the water surface at depth z below the water surface;

K = light extinction coefficient;

$K_{b,c}$ = conductive heat exchange coefficient of the bed;

$K_{b,v}$ = convective heat transfer coefficient of the bed;

$K_{e,me}$ = light extinction coefficient for emergent shoots;

L_E = latent heat of evaporation of water;

NWL = normal water level;

P_a = atmospheric pressure;

RMSE = root mean square error;

S = water salinity;

S_f = terrain shading factor;

T_a = air temperature;

T_b = bed temperature;

T_{bw} = water temperature at the bed-water interface;

t_n = nominal residence time;

T_s = water surface temperature;

U_b = absolute water velocity at the bed-water interface;

u_w = wind components (positive eastward);

V_{abs} = absolute water velocity;

V_m = modelled water currents;

V_o = observed water currents;

v_w = wind components (positive northward);

V_x = east water velocity;

V_y = north water velocity;

W = wind speed;

WSE = water surface elevation;

z = height above the bed;

ΔT = vertical top-bottom temperature differences;

ρ_a = atmospheric density;

ρ_b = sediment bed density;

ρ_w = water density;

ε = emissivity of the waterbody;

Table 5-1 Physical and drainage characteristics of the study sites.

| | Units | Auburn Bay Wet pond | Royal Oak Wetland |
|--|----------------|--------------------------------|------------------------------|
| Catchment type | / | Residential & Commercial | Residential |
| Catchment area | ha | 232 | 18.3 |
| Imperviousness ratio | % | 58 | 51 |
| Surface area at NWL¹ | m ² | 24,700 | 5,500 |
| Loading ratio² | / | 94 | 33 |
| Permanent wet pool volume | m ³ | 56,500 | 2,500 |
| Average Depth | m | 3.0 | 0.8 |
| Maximum Depth | m | 3.4 | 1.4 |

1 Normal Water Level

2 Ratio of the catchment to the pond area

Table 5-2 Start and end dates of the model runs in Auburn Bay and Royal Oak.

| Pond | Year | Start date | End date |
|------------------------|----------------------|------------|------------|
| Auburn Bay wet pond | Calibration/ 2019 | 2019-04-27 | 2019-09-21 |
| | Validation/ 2018 | 2018-06-15 | 2018-09-12 |
| Royal Oak wetland | Calibration/ 2019 | 2019-04-30 | 2019-08-28 |
| | Validation/ 2018 | 2018-06-21 | 2018-09-14 |

Table 5-3 Model parameters used in the vegetation submodel of the Royal Oak wetland

| Vegetation Class ID | Class 1 | Class 2 |
|--|-------------------|----------------|
| Description | Pond Weed/Milfoil | Typha |
| Plant Density (#/m²) | 100 | 100 |
| Stem Diameter (m) | 0.002 | 0.02 |
| Stem Height (m) | 0.2 | 1.5 |
| Drag Coeff Factor | 0.7 | 0.7 |

Table 5-4 Model parameters used in the simulations in Auburn Bay wet pond and Royal Oak wetland

| Parameter | Unit | Auburn Bay wet pond | Royal Oak wetland | Source |
|--|--------------------------------|--------------------------------|------------------------------|---------------------|
| Time Step | s | 0.2-1.6 | 0.3 | Model self-adaption |
| Bottom roughness height | m | 0.02 | 0.02 | Gong et al. (2016) |
| Albedo | / | 0.05 | 0.2 | Calibrated |
| Latent and sensible heat exchange coefficients, c_e and c_s | / | 2.5E-03 | 3.0E-03 | Calibrated |
| Light extinction coefficient, K | m^{-1} | 2-4 | 2-6 | Calibrated |
| Bed Thermal Thickness, D_b | m | 0.3 | 0.3 | Jin et al. (2000) |
| Heat transfer coefficient between the bed and bottom water layer | $W/(m^{-2} \text{ } ^\circ C)$ | 0.3 | 0.3 | Gong et al. (2016) |
| Background Horizontal Eddy Viscosity | m^2/s | 0.08 | 0.08 | Calibrated |
| Dimensionless horizontal momentum diffusivity | / | 0.1 | 0.1 | Dong et al. (2019) |
| Background Vertical Eddy Viscosity | m^2/s | 1E-05 | 1E-05 | Dong et al. (2019) |
| Background Molecular Diffusivity | m^2/s | 1E-07 | 1E-07 | Dong et al. (2019) |
| Outlet weir discharge coefficient | / | 0.45 | 0.75 | Calibrated |
| Outlet Orifice discharge coefficient | / | 1.0 | 0.75 | Calibrated |

Table 5-5 Root mean square errors (RMSE) between the observed data and modelled Water Surface Elevation (WSE), water temperature (T_w) and water salinity (S) in Auburn Bay and Royal Oak during calibration and validation runs.

| | Auburn Bay | | Royal Oak | |
|-----------------------|-------------------|------------|------------------|------------|
| | Calibration | Validation | Calibration | Validation |
| | 2019 | 2018 | 2019 | 2018 |
| WSE ¹ (cm) | 1.6 | 4.5 | 3.3 | 1.3 |
| T_w (°C) | 1.0 | 1.3 | 1.7 | 1.9 |
| S (ppt) | 0.13 | 0.04 | 0.20 | 0.08 |

Table 5-6 Comparison of the percentage of the time when the water columns at IN and OUT had vertical temperature difference $> 1\text{ }^{\circ}\text{C}$ (difference of near-surface and bottom temperatures) in the model and observation

| % of time $\Delta t > 1^{\circ}\text{C}$ | Auburn Bay | | Royal Oak | |
|--|------------|-----|-----------|-----|
| | IN | OUT | IN | OUT |
| 2019 - Observed | 98 | 92 | 86 | 25 |
| 2019 - Model | 91 | 70 | 60 | 0 |
| 2018 - Observed | 98 | 88 | 74 | 45 |
| 2018 - Model | 84 | 60 | 53 | 0 |

Table 5-7 Comparison of the average near-surface and bottom temperature difference between the model and observation

| Average Δt ($^{\circ}\text{C}$) | Auburn Bay | | Royal Oak | |
|--|-------------------|-----|------------------|-----|
| | IN | OUT | IN | OUT |
| 2019 - Observed | 6.0 | 5.1 | 4.1 | 0.4 |
| 2019 - Model | 5.4 | 3.0 | 1.5 | 0.0 |
| 2018 - Observed | 5.1 | 4.4 | 2.8 | 1.1 |
| 2018 - Model | 3.6 | 2.2 | 1.6 | 0.0 |

Table 5-8 Simulated HRT, computed nominal residence time, t_n , and hydraulic efficiency, HRT/ t_n results at both study sites in both years.

| Pond | Year | HRT (days) | t_n (Days) | HRT/ t_n (%) |
|------------------------|----------------------|------------|--------------|----------------|
| Auburn Bay wet pond | Calibration/ 2019 | 28.6 | 44.1 | 65% |
| | Validation/ 2018 | 19.5 | 19.5 | 100% |
| Royal Oak wetland | Calibration/ 2019 | 20.1 | 11.6 | 173% |
| | Validation/ 2018 | 35 | 60 | 58% |

Table 5-9 The modelled duration as a percentage of the time between May and September 2019 when the water columns at IN, MID and OUT in Auburn Bay had vertical temperature differences > 1 °C for three NWL scenarios.

| % of time $\Delta t > 1^\circ\text{C}$ in 2019 | | IN | MID | OUT |
|--|-----------------------|----|-----|-----|
| | Base Case (1041.0) | 91 | 64 | 70 |
| NWL (m) | 1039.5 | 92 | 64 | 68 |
| | 1039.0 | 90 | 56 | 57 |

Table 5-10 The modelled duration as a percentage of the time between May and September 2019 when the water columns in Auburn Bay and Royal Oak had vertical temperature differences >1 °C for the scenario of inlets located at the NWL versus the base case scenario of inlets located at the bed.

| % of time $\Delta t > 1^\circ\text{C}$ in 2019 | | IN | MID | OUT |
|--|--------------------|----|-----|-----|
| Auburn Bay | Base case | 91 | 64 | 70 |
| | Near-surface inlet | 72 | 67 | 72 |
| Royal Oak | Base case | 60 | 1 | 0 |
| | Near-surface inlet | 48 | 0 | 0 |

Table 5-11 The modelled duration as a percentage of the time between May and September 2019 when the water columns in Auburn Bay and Royal Oak had vertical temperature differences > 1 °C for three wind speed scenarios.

| % of time $\Delta t > 1^\circ\text{C}$ in 2019 | | IN | MID | OUT |
|--|------------|----|-----|-----|
| Auburn Bay | Base Case | 91 | 64 | 70 |
| | Wind x 0.5 | 93 | 64 | 72 |
| | Wind x 2.0 | 85 | 38 | 39 |
| Royal Oak | Base Case | 60 | 1 | 0 |
| | Wind x 0.5 | 72 | 8 | 0 |
| | Wind x 2.0 | 26 | 0 | 0 |

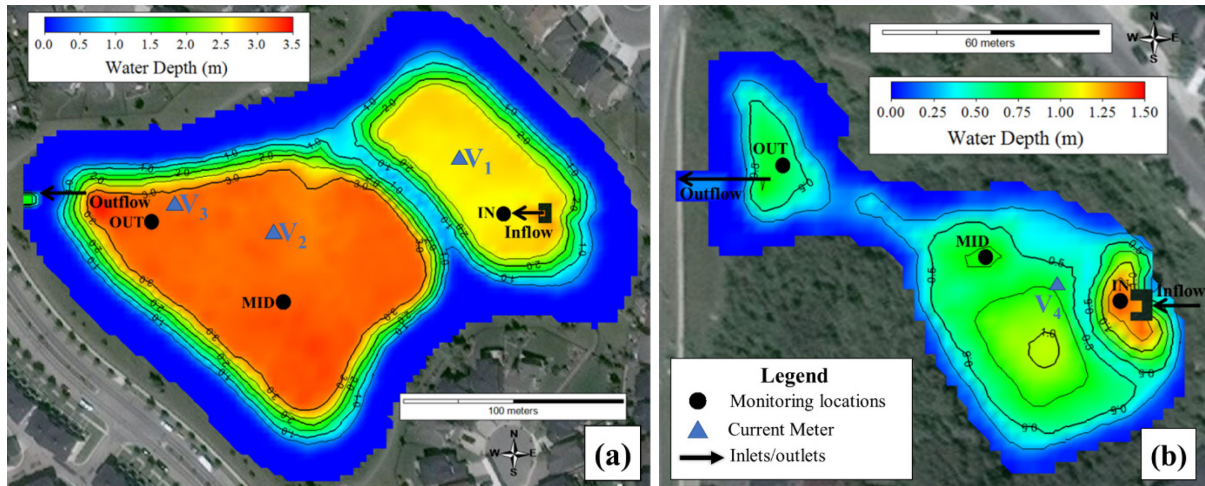


Figure 5-1 Model domain of (a) the Auburn Bay wet pond and (b) the Royal Oak wetland, indicating their permanent pool depths in Auburn Bay and Royal Oak. Note that dark blue values are zero water depth only during the NWL condition, i.e., during no live storage or rainstorm inflow events. The outer boundaries of the model domains cover the inundated area during the design High Water Level (HWL), 1043m and 1266m in Auburn Bay and Royal Oak. Black arrows show the location of inlets and outlets. Black circles labelled IN, MID and OUT are in-pond monitoring locations near the inlet, middle, and outlet. Blue triangles are the deployment locations of the current meters.

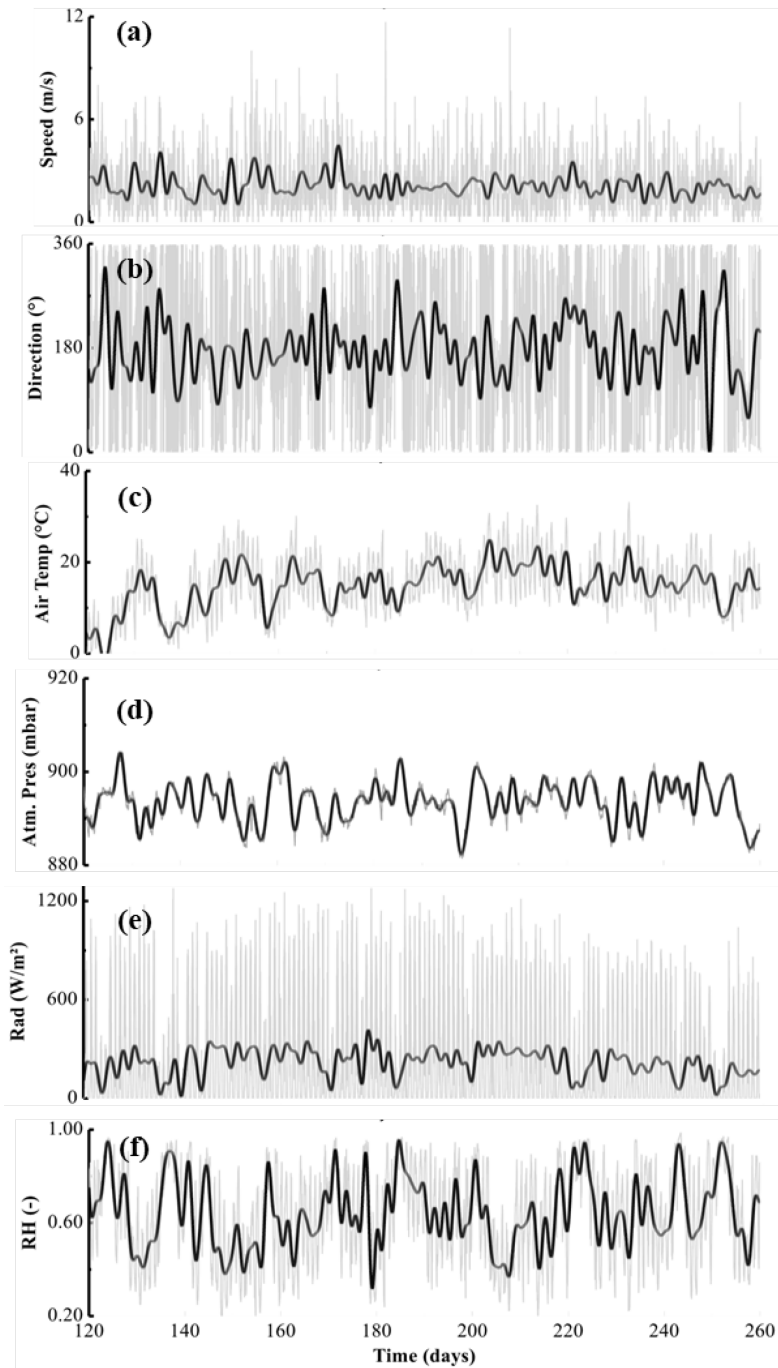


Figure 5-2 Time series from the Auburn Bay weather station showing the meteorological data versus Julian day in 2019. Gray and black time series are the continuous 5-minute interval and the 24 hr running average data.

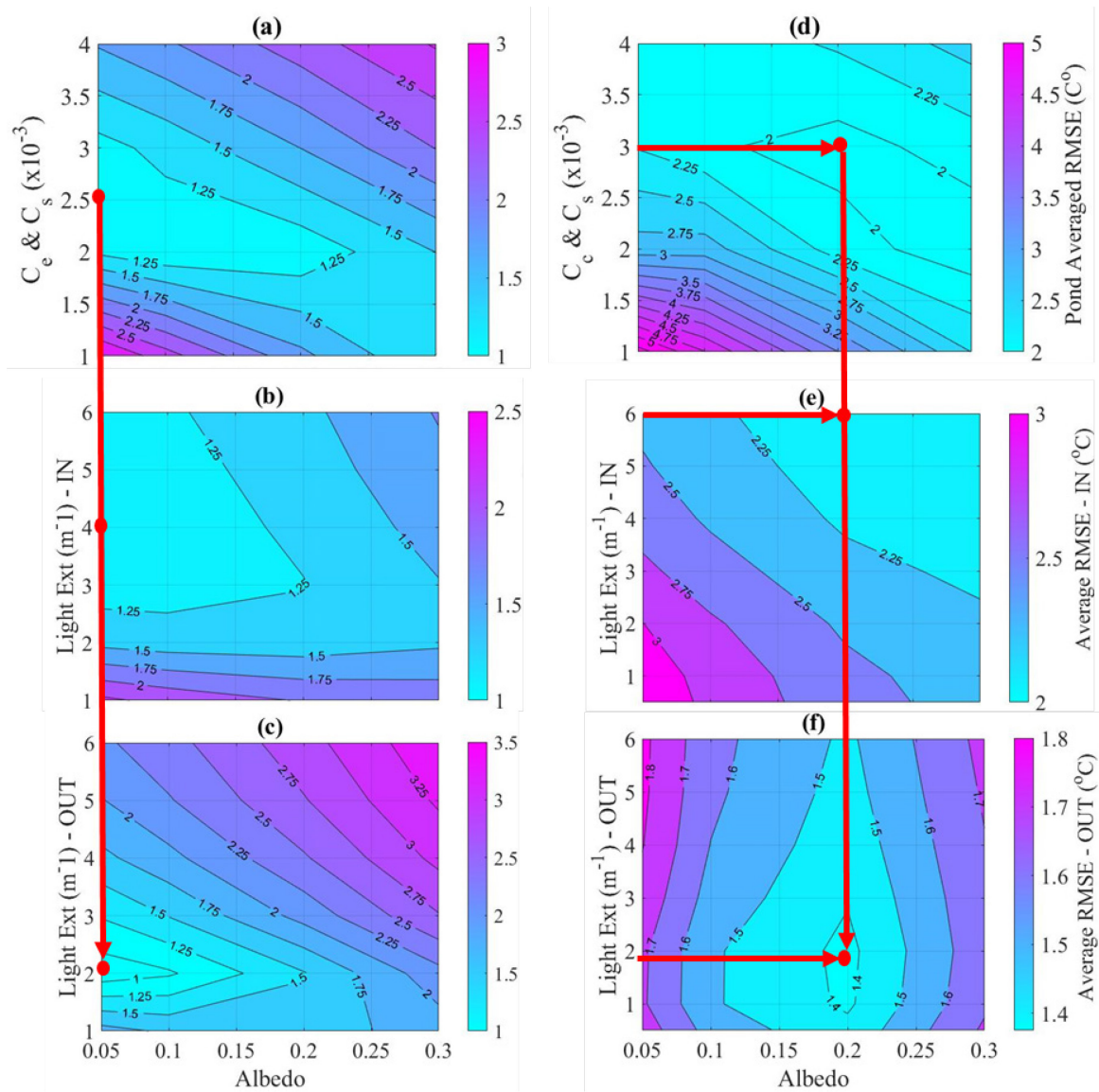


Figure 5-3 Two-dimensional RMSE contour plots of water temperature generated based on the calibration sensitivity analysis in Auburn Bay in (a,b,c) and Royal Oak in (d,e,f) for 16 scenarios of turbulent heat exchange coefficients and albedo in (a,d), 24 scenarios of light extinction coefficient at IN and albedo in (b,e), and 24 scenarios of light extinction coefficient at OUT and albedo in (c,f). Red arrows and dots are the scenarios for the calibration parameters with the least temperature RMSE.

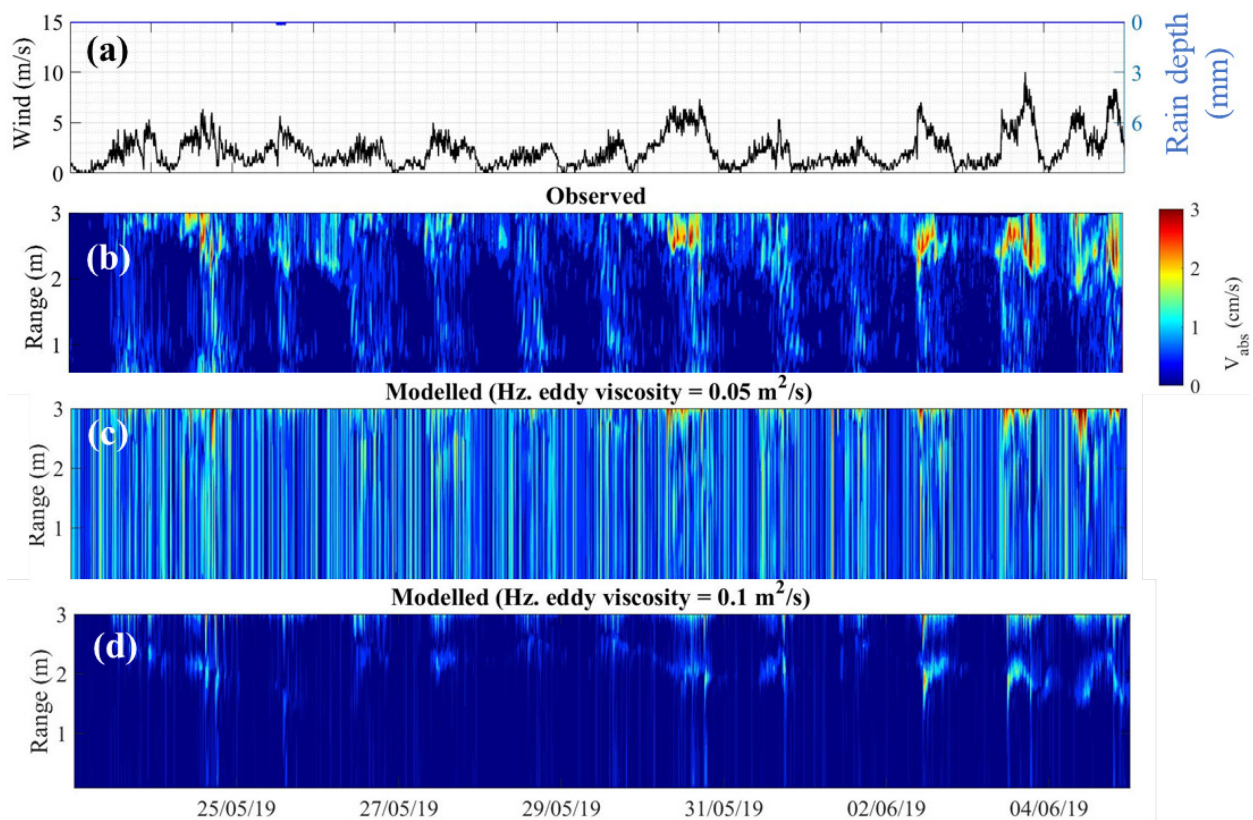


Figure 5-4 Results from the Auburn Bay pond in 2019 at V_2 show time series of (a) wind speed (left axis) and 5-minute interval rain depth (right axis), (b) colour contour plots of observed absolute water velocity profiles versus range from the bed, and (c),(d) colour contour plots of modelled absolute water velocity profiles versus range from the bed using horizontal eddy viscosities of 0.05 and 0.1 m²/s, respectively.

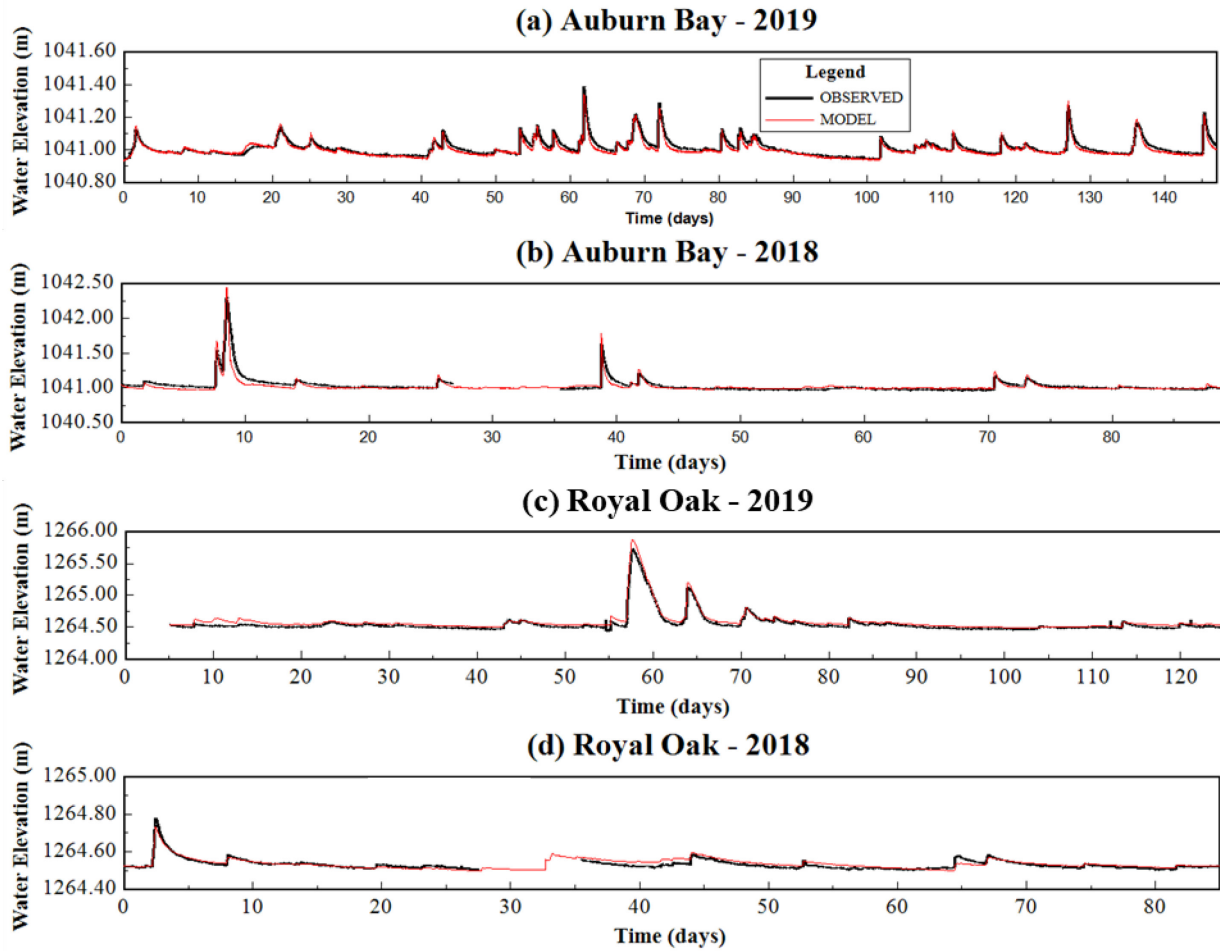


Figure 5-5 Time series of the modelled and measured water surface elevation in Auburn Bay (a,b) and Royal Oak (c,d) during calibration (a,c) and validation runs (b,d) in 2019 and 2018. The start date of each run is presented in Table 2.

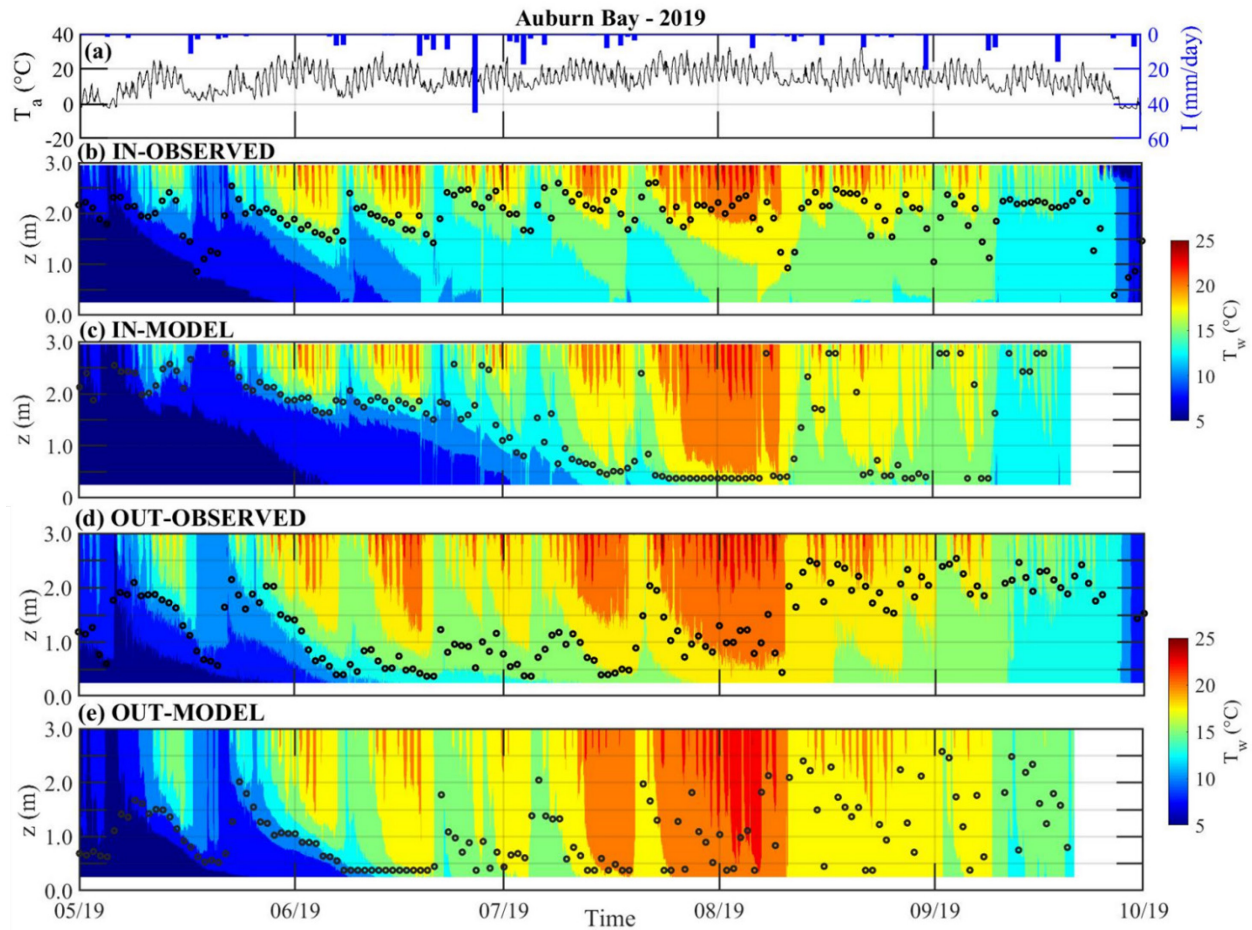


Figure 5-6 Results from the Auburn Bay wet pond in 2019 show time series of (a) air temperature (left axis) and rain depth (I , right axis), (b), (c), (d) and (e) colour contour plots of observed and modelled vertical water temperature profiles versus height above the bed (z) at IN, and MID. The black circles are the average daily thermocline height above the bed (z).

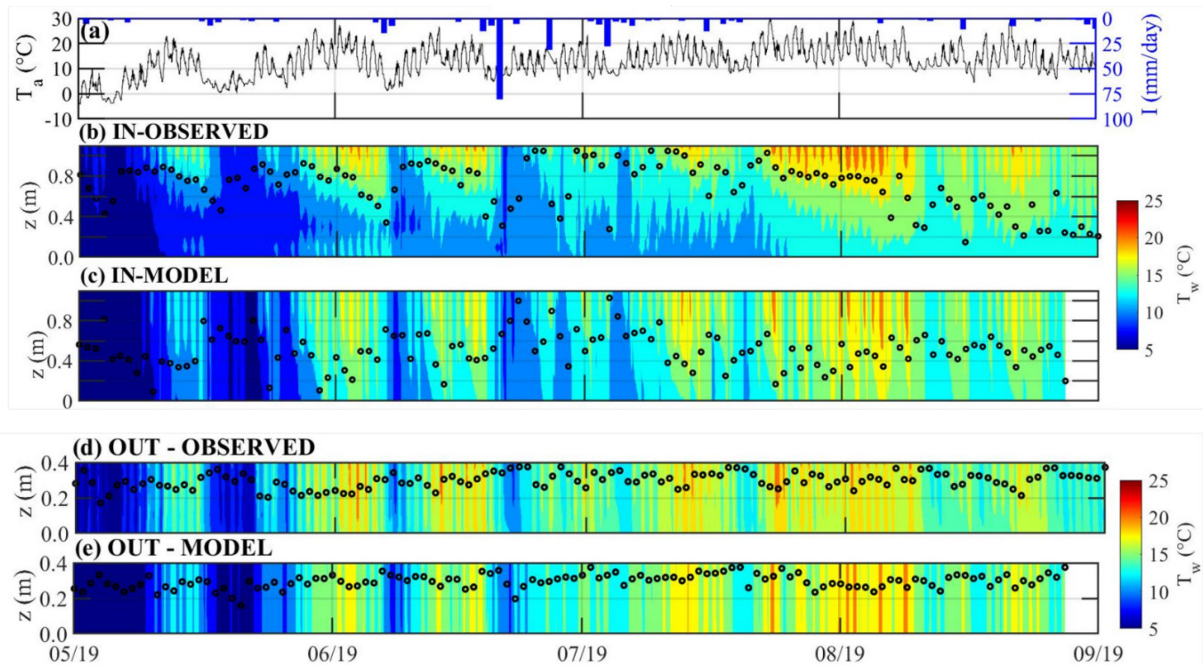


Figure 5-7 Results from the Royal Oak wetland in 2019 show time series of (a) air temperature (left axis) and rain depth (I , right axis), (b), (c), (d) and (e) colour contour plots of observed and modelled vertical water temperature profiles versus height above the bed (z) at IN, and MID. The black circles are the average daily thermocline height above the bed (z).

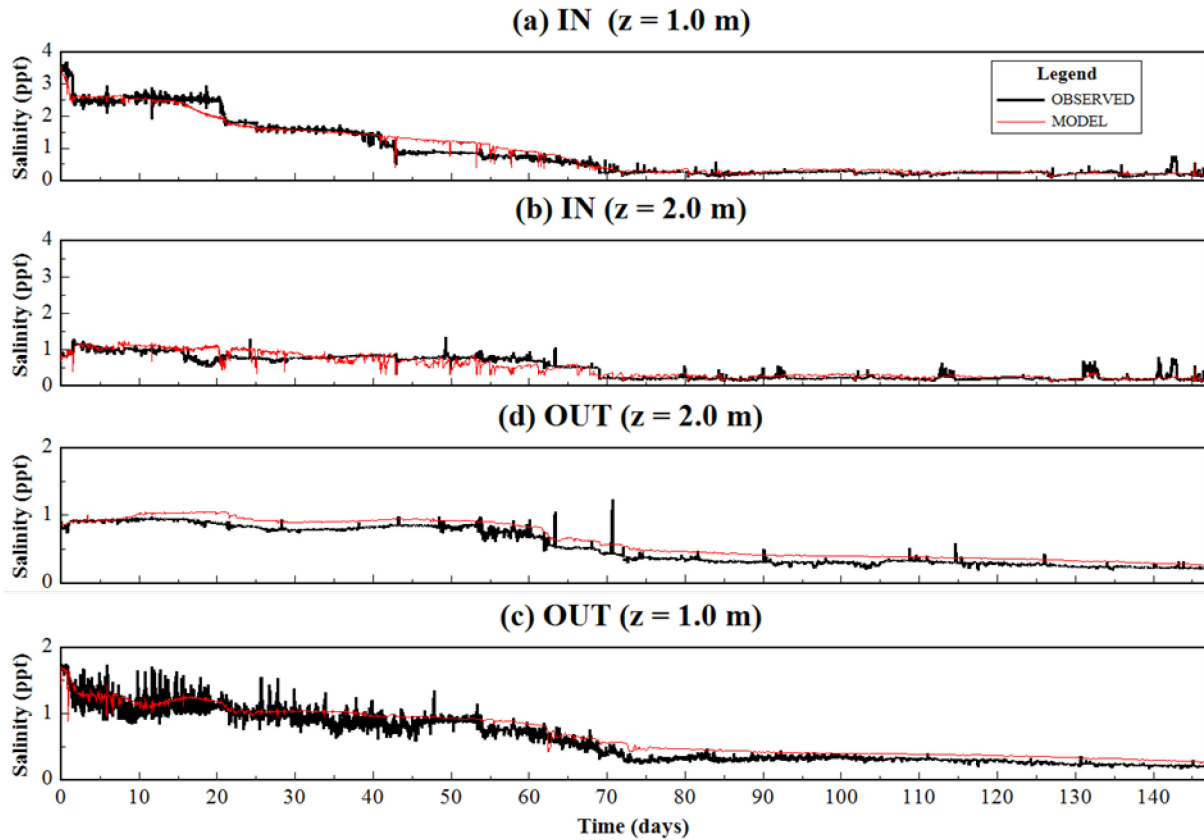


Figure 5-8 Observed and modelled time-depth variations of the water salinity in Auburn in 2019 at IN and OUT and heights above the bed (z) of 1.0 and 2.0 m. The start date of the calibration run in 2019 is presented in Table 2.

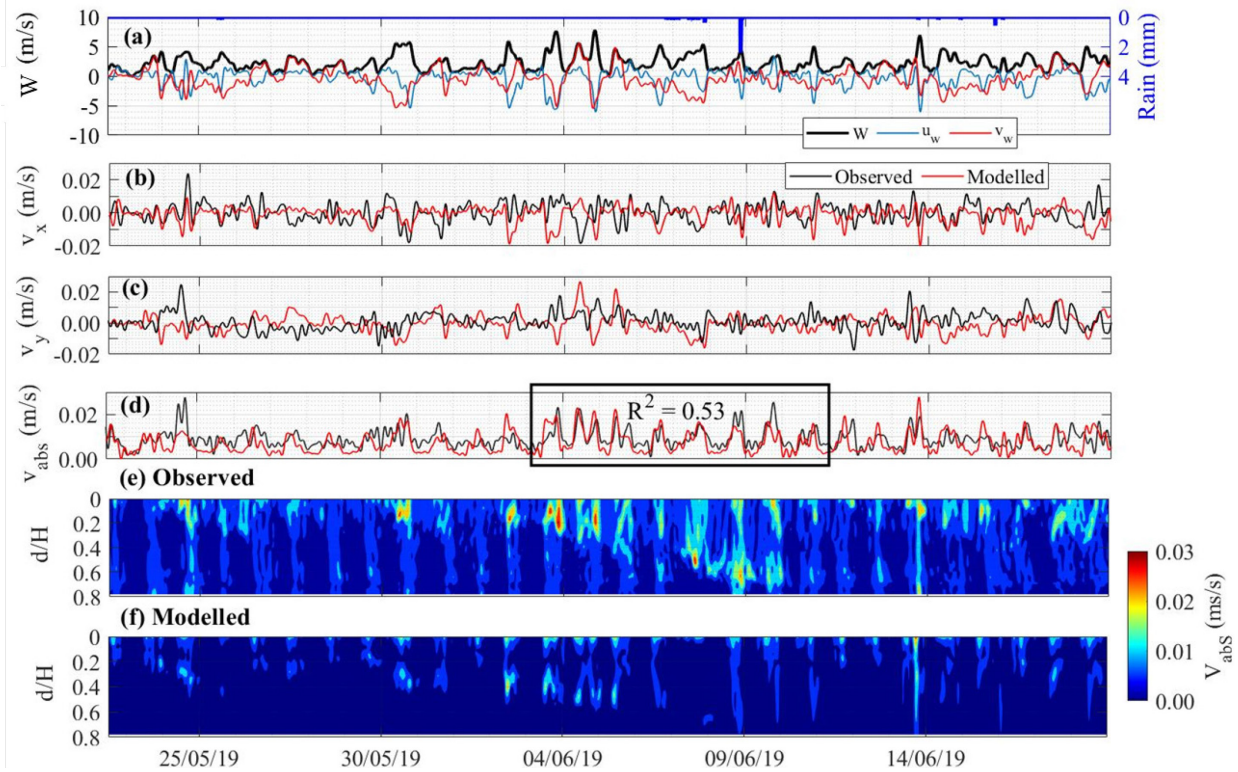


Figure 5-9 Results from the Auburn Bay pond in 2019 show time series of (a) wind components (u_w : positive eastward, v_w : positive northward, and magnitude, W) (left axis) and 5-minute interval rain depth (right axis), (b), (c), (d) observed and modelled east, V_x , north, V_y , and absolute, V_{abs} , water surface velocity at V_2 , (e), and (f) colour contour plots of observed and modelled absolute water velocity profiles versus depth ratio (d/H) at V_2 .

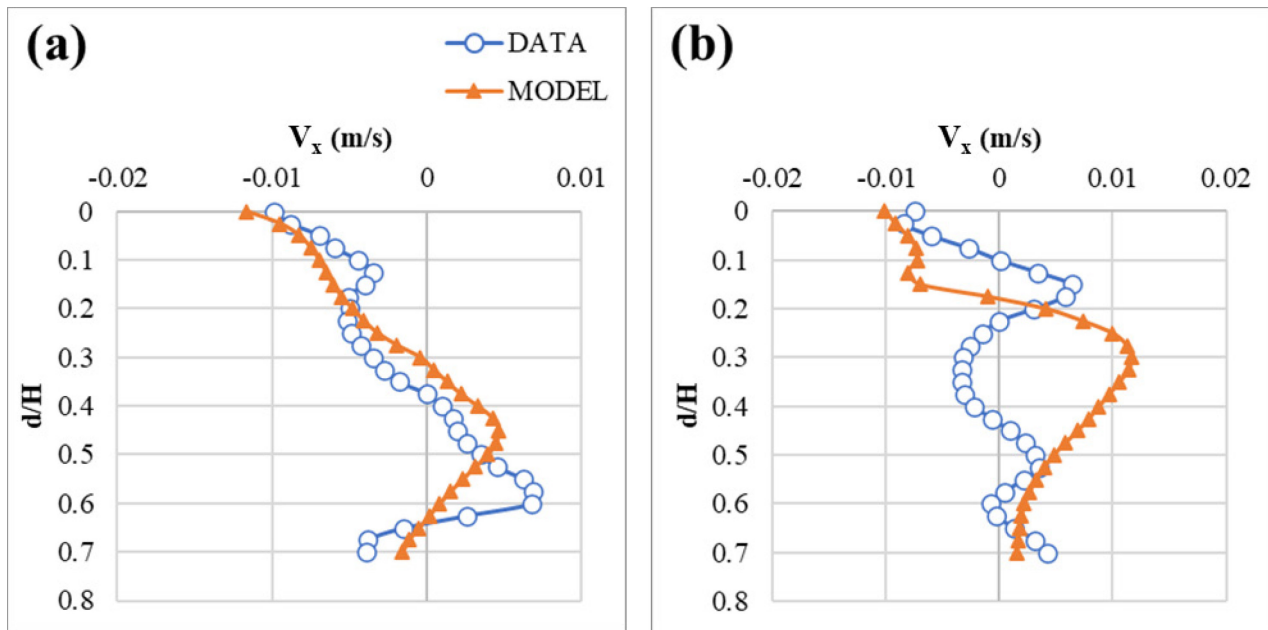


Figure 5-10 Observed and modelled East velocity, V_x , profiles versus depth ratio (d/H) at V_2 on (a) June 8, 2019, and (b) June 13, 2019.

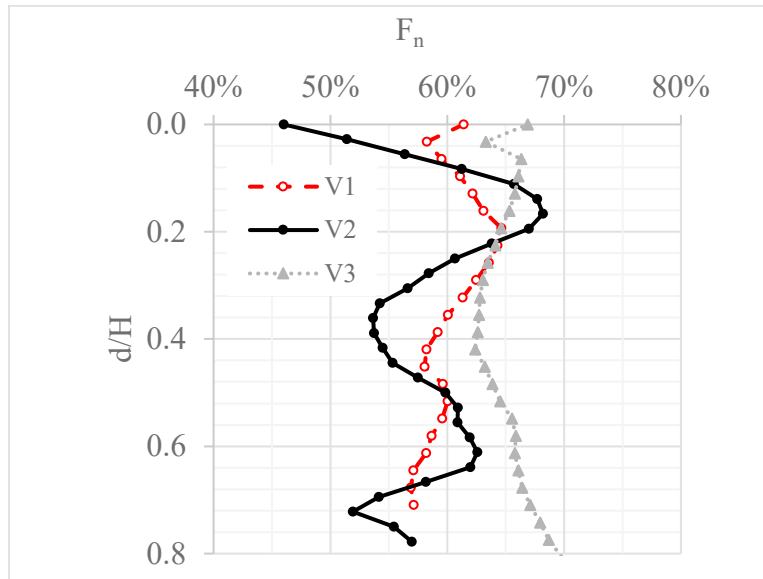


Figure 5-11 The vertical distribution of normalized Fourier norms between the modelled and observed currents at stations V₁, V₂ and V₃ in Auburn Bay.

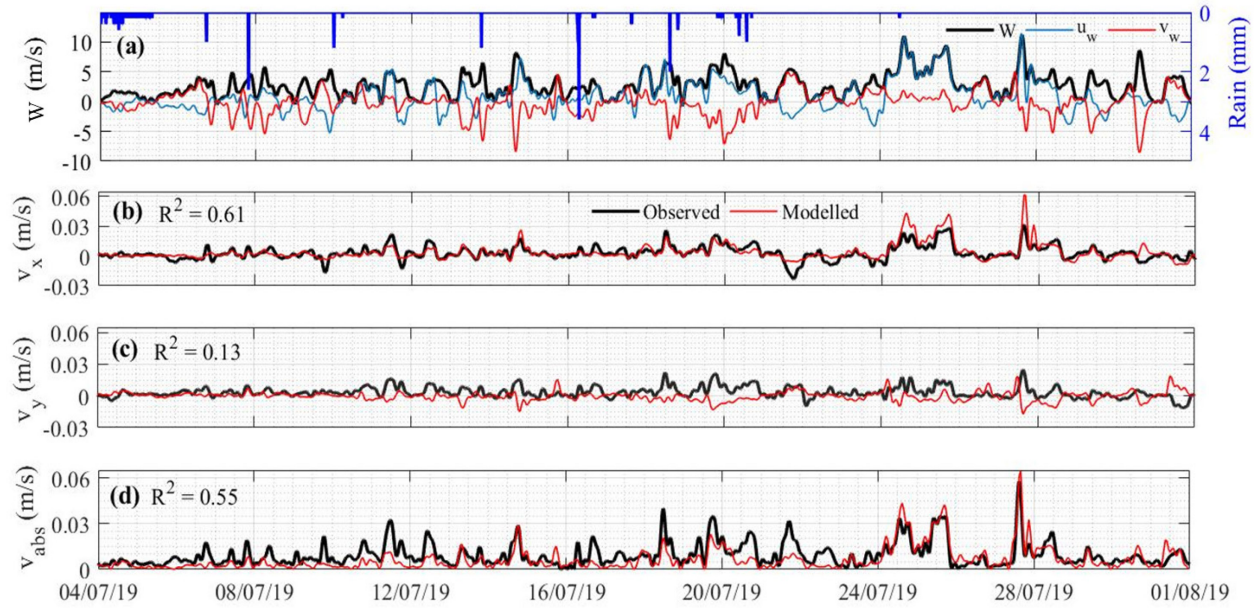


Figure 5-12 Results from the Royal Oak Wetland in 2019 show time series of (a) wind speed (left axis) and 5-minute interval rain depth (right axis), (b), (c) and (d) observed and modelled east, north and absolute water surface velocity at V_4 .

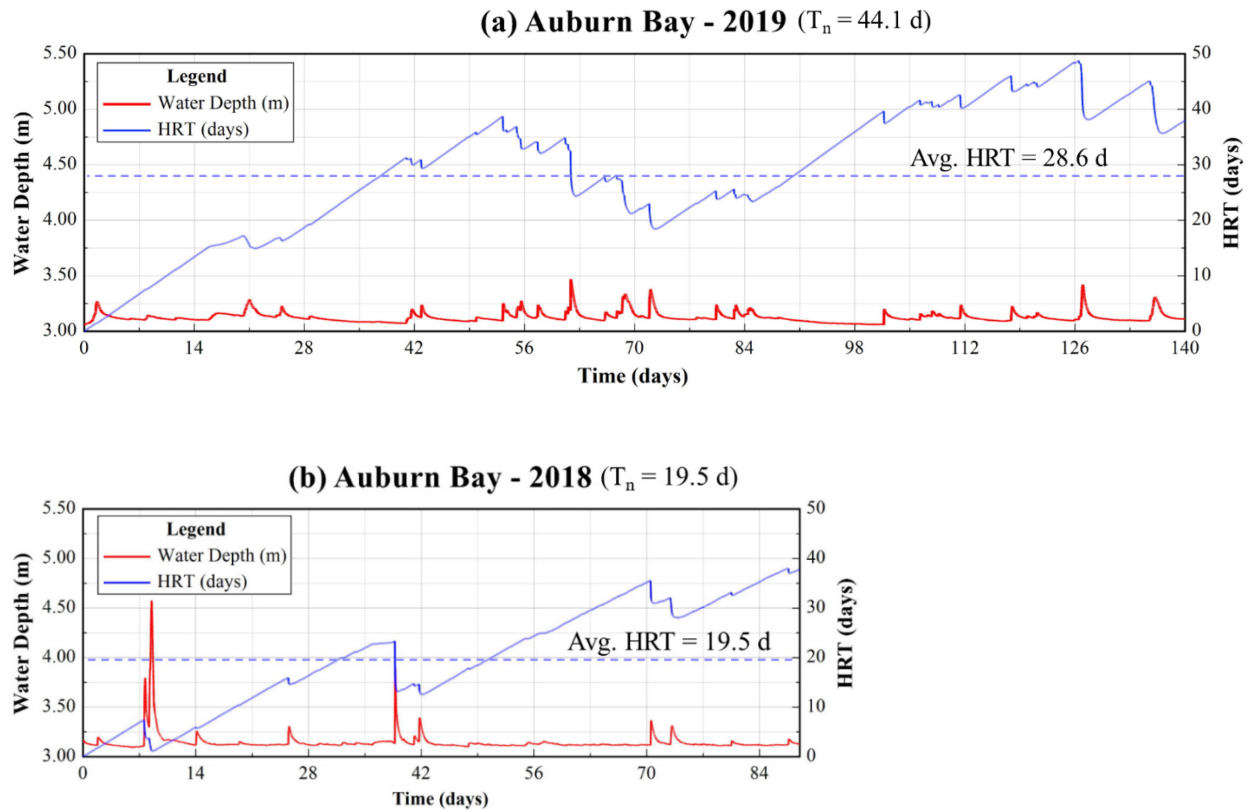


Figure 5-13 Results from the Auburn Bay wet pond model show time series of water depth at MID (left axis) and the modelled HRT averaged over the entire domain (right axis) in (a) 2019 and (b) 2018. Start dates are April 27 and June 15 in 2019 and 2018, respectively, Avg. HRT is the hydraulic residence time averaged over the entire model domain and run time. T_n is the nominal residence time in a given year.

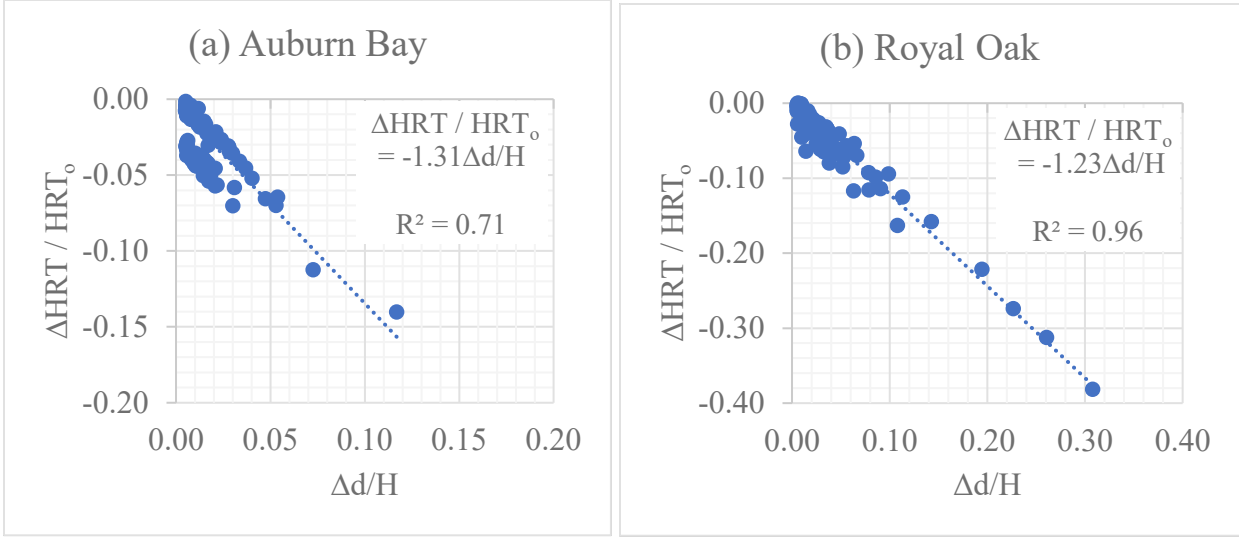


Figure 5-14 Linear correlation of the water depth rise normalized to the average pond depth, $\Delta d/H$, and the corresponding reduction in the domain HRT normalized to the initial HRT, $\Delta\text{HRT}/\text{HRT}_0$, in (a) Auburn Bay and (b) Royal Oak.

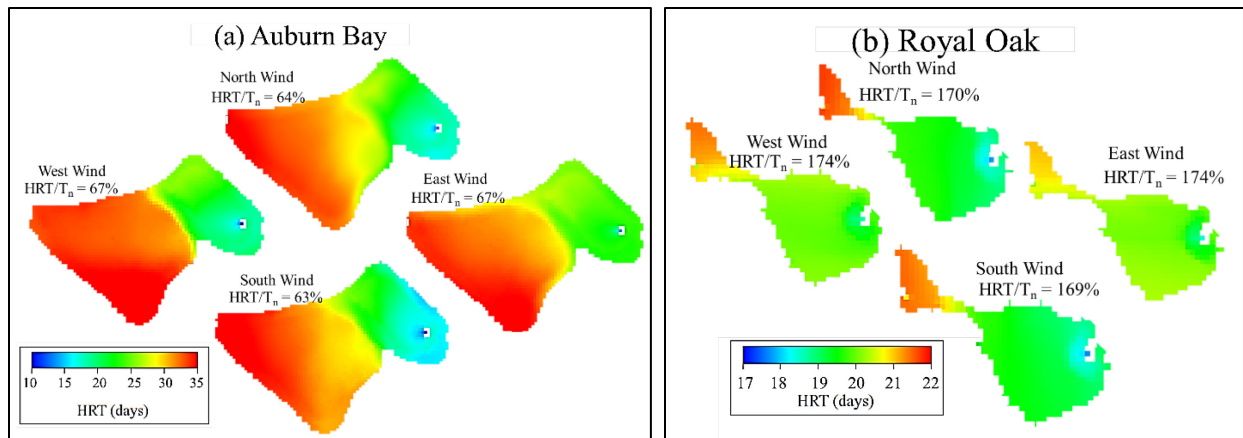


Figure 5-15 Model grids indicating the modelled HRT averaged over the entire run time in 2019 for four scenarios of the observed wind speed consistently blowing from north, south, east and west in (a) Auburn Bay and (b) Royal Oak.

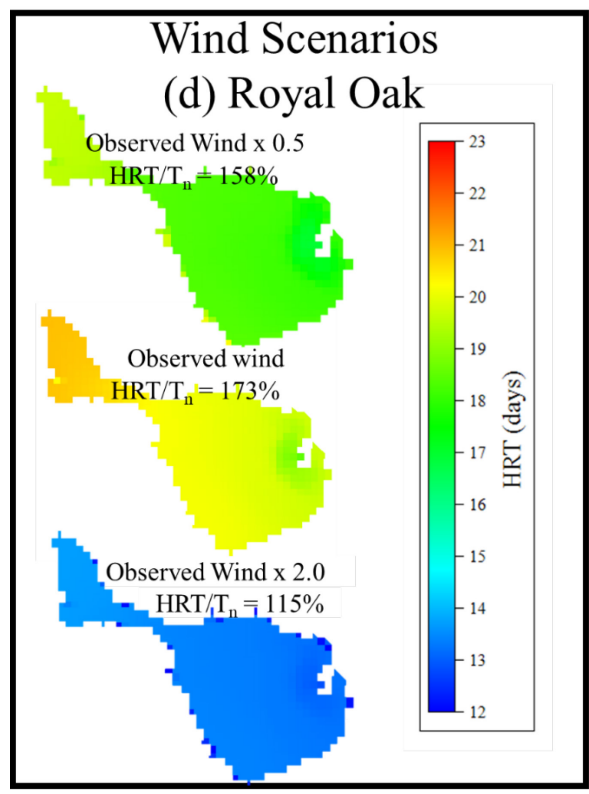
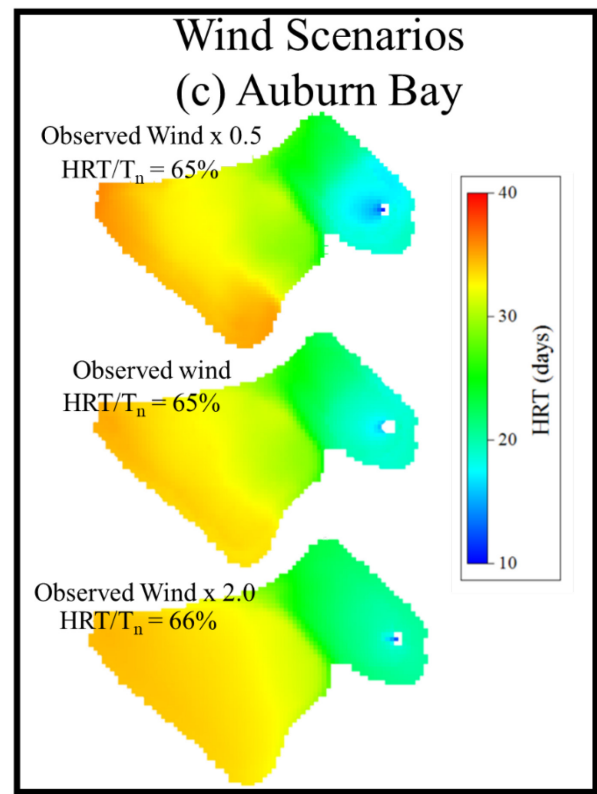
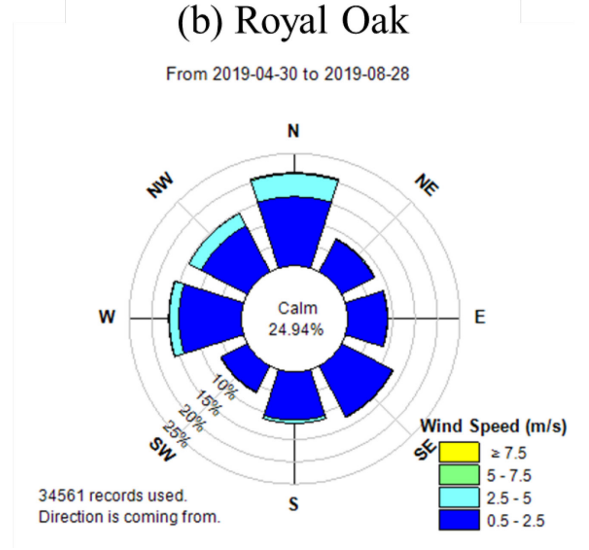
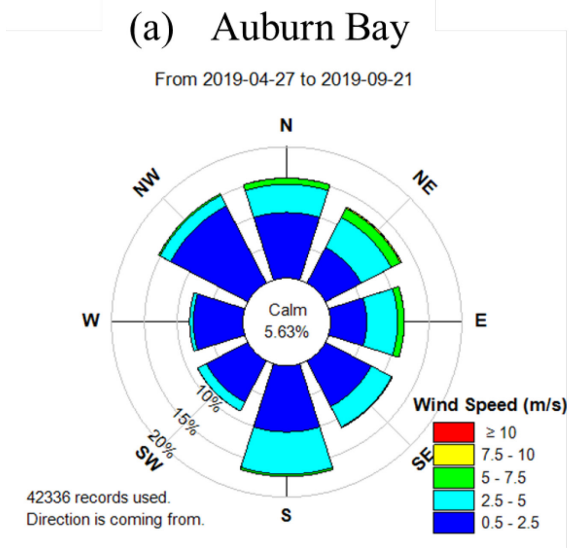


Figure 5-16 The wind rose plots in 2019 at (a) Auburn Bay and (b) Royal Oak, along with the HRT for the base case scenario for wind and scenarios of half and double the observed wind speed at (c) Auburn Bay and (d) Royal Oak.

6. Suspended sediment transport in an urban stormwater wet pond and a constructed wetland*

6.1 Introduction

Urban stormwater runoff is a major sediment source to the receiving water bodies (Alberta Environment 2007). For example, in Edmonton, Alberta, Canada, thousands of tons of sediment are released to the North Saskatchewan River annually, with about 70% of this loading attributed to stormwater runoff (Shammaa et al., 2002). In addition, according to a water quality study in 2005, 90% of sediment in the Bow River in Calgary, Alberta, Canada, was from the stormwater system (City of Calgary, 2005). Sediment can affect the physical and chemical environment of the receiving water body, adversely impacting aquatic life and fisheries, source waters for drinking water supplies, and recreational uses of the water body (USEPA 1999; Jin and Ji 2015). For instance, suspension sediments in the water column can reduce the light intensity and influence the growth of phytoplankton (Aryal and Lee, 2009; Jin and Ji, 2015). In addition, heavy metals (e.g. lead, copper, zinc), nutrients and other pollutants can be absorbed onto fine sediment particulates and pose direct threats to aquatic life and water quality (Chalov et al. 2015).

Stormwater ponds, including wet ponds and constructed wetlands, are one of the structural best management practices (BMPs) used extensively for stormwater management and water quality treatment (City of Calgary, 2011; Song et al., 2013 & 2015; Gu et al., 2017; Ji and Jin, 2020). Wet ponds and constructed wetlands maintain a permanent pool volume, provide detention volume for stormwater runoff, and reduce the peak runoff to control flooding (OMOE 2003). In addition, their permanent pool acts as a settling chamber for sedimentation (City of Calgary, 2011; Jin and Ji,

* The content of this chapter is being prepared and will be submitted as a journal manuscript.

2015), making the proportion of the incoming sediment that is deposited or trapped one of the essential properties of stormwater ponds.

In recent years, governments in North America have proposed best practices for sediment removal criteria for stormwater ponds. For example, the current Alberta guidelines (Alberta Environment, 2001) call for removing a minimum of 85% of sediment with a particle size $\geq 75 \mu\text{m}$. Additionally, the recent guidelines put by the City of Calgary have mandated the removal of a minimum of 85% total suspended solids (TSS) for particle sizes $\geq 50 \mu\text{m}$ (City of Calgary 2011). Further, Dane County in the U.S. requires removing at least 80% of the TSS in their stormwater manual (Dane County 2022). Given these requirements, it is crucial to assess the performance of existing ponds and predict their trap efficiency.

Substantial variations in removal efficiencies were reported in the literature, suggesting a gap between the real-life removal efficiency and the best practice standards for ponds and wetlands (USEPA 2002; Birch et al., 2006; GCI and WVEI 2014; Gu et al., 2017). For instance, Birch et al. (2006) found sediment removal efficiencies in stormwater ponds to vary from -12% to 93%. This was likely due to the highly variable sediment inflow load, physical particle characteristics (e.g. size, shape and density), inflow characteristics (e.g. flow rate, volume and duration), vegetation design, wind, stratification, and others (Gu et al., 2017). Thus, a comprehensive understanding of key factors in sediment removal efficiency in stormwater ponds and wetlands is essential.

Numerical modelling has been broadly developed and applied to investigate sediment dynamics and removal efficiencies in ponds, wetlands, and shallow lakes (Bentzen, 2009; Chung et al., 2009; Wang et al., 2013; Lv et al. 2013; Ji and Jin, 2014; Jin and Ji 2015; Liu et al. 2016). Three-

dimensional models seem particularly appropriate, owing to the complex flow fields created by inflow, wind, aquatic vegetation, bathymetries, vertical gradients in water temperature, and density currents, as presented in chapters 3 and 4. For instance, the current study in chapter 3 reported that the thermal and chemical stratifications in the study ponds forced the runoff from the inlet to the outlet to move above or below the pycnocline, creating dead zones and short-circuiting. Furthermore, chapter 4 documented that despite the shallow depth of the current study wetland at < 1.5 m, vertical stratification was present, inhibiting vertical mixing and causing hypoxic conditions near the bed. The strength of the vertical stratification also differed significantly between wetlands of comparable depths due to differences in the aquatic vegetation design and geometry. For example, although the two study wetlands in chapter 4 were only 0.25 KM apart and had the same average depth of 0.8 m, they differed in surface areas and length-to-width ratios, resulting in thermal stratification that differed significantly by up to 8 times between the wetlands. These results demonstrate that 3D models are required to accurately simulate the complex temporal and spatial variations in hydrodynamics and stratification.

The EFDC+ software based on the Environmental Fluid Dynamics Code (EFDC) (<https://www.eemodelingsystem.com/ee-modeling-system/efdc-plus/overview>) has been chosen in the current study for the sediment transport modelling in one stormwater wet pond and one constructed wetland. This is mainly due to its ability to stimulate the transport of multiple size classes of cohesive and non-cohesive sediment, including deposition and resuspension, as well as sediment particle sorting (Hamrick, 1996). In addition, non-cohesive sediment may be transported as bed and suspended loads, depending on the flow conditions. Furthermore, the aquatic vegetation module can represent the spatial and temporal variations of our wetland's submerged and emergent aquatic vegetation to account for flow resistance. The EFDC model has been extensively tested

and documented in more than 100 modelling studies (e.g., Jin et al., 2000; Yang and Hamrick, 2003; Ji et al., 2007; Wan et al., 2012; Shin et al., 2019). The model is presently being used by universities, research organizations, governmental agencies, and consulting firms.

Recent applications of sediment transport modelling using the EFDC include the 3D hydrodynamic and sediment transport modelling in the Yuan-Yang lake in the north-central region of Taiwan by Liu et al. (2015). This study used field-observed data to determine infrequently examined model parameters such as sediment settling velocity and resuspension rate. Sensitivity analysis indicated that the settling velocity is the most sensitive parameter to the suspended sediment concentration. The model was also used to probe the lake's mean current and suspended sediment distribution. Additionally, an integrated 3D hydrodynamic, sediment transport, and submerged aquatic vegetation in Lake Okeechobee Environmental Model (LOEM) were developed within the EFDC framework. The hydrodynamic and sediment model of LOEM was applied to stormwater treatment wetlands in South Florida (Jin and Ji 2015). It was shown that the flow pattern is primarily driven by rain and inflows/outflows. In addition, the flow resistance caused by the submerged/emergent aquatic vegetation significantly reduced the flow velocity and changed the flow pattern, which helped increase sediment settling. The hydrodynamic and sediment transport modules of the EFDC were also used by Shin et al. (2019) as a receiving water-body model. The EFDC model was coupled with the watershed loading model Soil and Water Assessment Tool (SWAT). The modelling framework in this study was applied to predict the spatial distributions of sediment depositions in an agricultural reservoir and quantify their uncertainty.

Computational modelling alone would provide a simplified picture of reality, synthesizing observations with theoretical knowledge, but it can never contain all the features of a real system

(Jørgensen & Fath, 2011). Hence, a mixed approach of a comprehensive field monitoring program and computer modelling investigations has been adopted for the current study. The field program was undertaken during two ice-free seasons (May-October) in 2018/2019 to continuously monitor stratification and hydrodynamics in two stormwater wet ponds and two constructed wetlands in Calgary, Canada. Results from the two years field program were presented in chapters 3 and 4. In addition, the two-year data were used to calibrate and validate the application of the hydrodynamic EFDC model in one wetland and one wet pond to simulate water depth, temperature, salinity and currents in chapter 5. Finally, in the current chapter, the sediment transport module of the EFDC model was applied to the calibrated/validated hydrodynamic models in chapter 5 to simulate sediment transport in 2019. The study's objectives are to: 1) conduct a detailed field monitoring investigation to measure sediment loadings in a stormwater wet pond and a constructed wetland to assess their ability to remove sediments, 2) set up a useful model capable of predicting resuspension, suspended sediment transport, and removal efficiency in the stormwater pond and the constructed wetland; and 3) use the validated models to optimize their design and operation guidelines by simulating different remediation options.

The current study's modelling framework simulated different normal water level operational options, inflow characteristics, vegetation design, wind speed/direction and stratification scenarios to discover the optimum design and operation guidelines for better sediment removal efficiency. For instance, the strength and duration of the vertical stratification in the two wet ponds and the two wetlands in chapters 3 and 4 differed significantly, mainly due to the differences in morphology, depths and vegetation design (see results in chapters 3 and 4). As a result, the significant duration and strength of the stratification observed in the 3m deep wet ponds in chapter 3 are compared in the current study to a milder stratification scenario when the normal water level

was lowered by 1 m. In addition, inflow characteristics during different inflow events and multiple scenarios of vegetation design and wind speed were tested against the sediment removal efficiency. Furthermore, the relatively weak stratification observed in the Royal Oak wetland in chapter 4 is compared in the current study to a more stratified scenario when the surface heat loss was deactivated, resulting in a ten-times increase in the strength of the thermal stratification. The stratification scenario in the Royal Oak wetland is intended to test a comparable stratification strength occurring in the nearby Rocky Ridge wetland, where the stratification strength was up to eight times higher (see chapter 4).

6.2 Materials and methods

6.2.1 Field measurements and data analysis of suspended sediment transport

One stormwater urban wet pond: Auburn Bay (AB), southeast of Calgary, and one stormwater urban constructed wetland: Royal Oak (RO), northwest of Calgary, were selected for this study. An aerial view of these facilities is presented in Figure 6-1. More detailed information on the two sites, their catchment characteristics, and meteorological data are available in chapters 3 and 4.

Field measurements conducted from May to August 2019 at AB and RO were used in the current study based on the available inflow and outflow suspended sediment data. Portable autosamplers (Model 6712 - Teledyne ISCO, USA) equipped with Model 750 or 2150 area/velocity flow modules were installed at the inlet/outlet structures of AB and RO. In AB, two autosamplers were installed at the inlet structure at two upstream branch pipes diverting flow to the inlet pipe (Figure 6-1a) and one autosampler at the outlet structure. The two samplers at the inlet measured inflows from 186 and 46 ha sub-catchments for inflows 1 and 2 that go into the same inlet pipe (Figure 6-1a). In RO, one autosampler was installed at the inlet structure and one at the outlet structure. The

6712 samplers were programmed to automatically collect flow proportionate water samples and continuous flow data from area velocity flow meters. The water samples were collected, labelled then sent to a commercial laboratory lab for TSS concentration and particle size analysis.

Three locations were chosen in AB and RO near the inlet, outlet and middle, away from the main flow path for water quality monitoring needed for calibration, i.e., locations IN, OUT and MID, respectively (Figure 5-1). Water depth, temperature, dissolved oxygen, conductivity, turbidity, chlorophyll-a, and velocity were continuously sampled at 5-15 minutes intervals at the two sites. In addition, fortnightly field trips to the ponds were conducted between April 23 and October 24, 2019. During each trip, water quality samples were collected near the surface and mid-depth of the three locations in AB and RO and then sent to a commercial laboratory in Calgary for water quality testing, including TSS concentration and particle size distribution analysis. More detailed information on the field program at the two sites in 2019 is available in chapters 3, 4 and 5.

Continuous and direct measurement of TSS in the water column is time-consuming due to the large number of water samples needed for the analysis. An alternative approach is using turbidity measurements as a surrogate for TSS concentrations (Daphne et al., 2011; DRI, 2008). Turbidity was continuously measured near the outlet in RO using an EXO3 turbidity sensor (YSI, USA) in formazin nephelometric units (FNU), which measure the intensity of light scattered in the water. In AB, turbidity data were not collected due to a malfunction in the turbidity unit. Hence, no continuous TSS data will be available, and only discrete inflow/outflow TSS concentrations will be used in the current study for the AB wet pond during rainfall events.

The bed sediment depth was determined from survey data collected using a real-time global positioning system (GPS) and a depth sounder by comparing the measured bed elevation with the

as-build elevation. In addition, sediment core samples were collected in September 2019 at AB and RO using a 5 cm diameter and 50 cm long Wildco® hand corer (Florida, USA) equipped with a 4.5 m long extension handle. Cores were collected from an inflatable boat or by wading whenever the water depth was less than 0.8 m. The corer was pushed vertically into the bottom sediments until the sediment was stiff enough to prevent the corer from penetrating it further or the deposited sediment depth was greater than the corer length (i.e. 50 cm). The cores were sampled at three locations along the main flow path in each pond/wetland. Cores were collected within the sedimentation bay, halfway along the primary flow path, and near the outlet, locations I, M and O in Figure 6-1a, 6-1b. Field duplicate core samples were collected at each location within 5 meters of the original sampling location. An additional core sample in AB and RO from the sediment forebay, location I, was collected for bulk density analysis.

Five sediment class sizes were used in the current study (see Table 6-2) with a size range and particle density defined following data adopted by the City of Calgary in their stormwater management and design manual (City of Calgary 2011). The sediment removal efficiency, RE, defined as the ratio between inflow minus outflow TSS load to the inflow TSS load for each sediment class, was calculated following Gu et al. (2017);

$$RE = \left(1 - \frac{M_{out}}{M_{in}}\right) \times 100\% \quad \text{(Equation 6-1)}$$

where M_{in} and M_{out} are the inflow and outflow TSS load in kg, respectively. First, the inflow and outflow sediment hydrographs in kg/s were determined by multiplying the water hydrograph in m^3/s and sediment concentrations in kg/m^3 (equivalent to 1000 mg/L). Then M_{in} and M_{out} in kg were determined by integrating the sediment inflow/outflow rate in kg/s along the sediment hydrographs. M_{in} and M_{out} between May and August were used to estimate the overall removal

efficiency in each pond/wetland based on the available inflow and outflow suspended sediment data. In addition, event-based M_{in} and M_{out} were calculated to determine the removal efficiency for each rainfall event. During the event-based removal efficiency analysis, a 95% upper bound for the sediment hydrograph was used as an integration cutoff to compensate for the effect of the long tail of declining sediment hydrographs (Li et al. 2013; Rey et al. 2021).

6.2.2 Model description

The EFDC+ software incorporates hydrodynamics, salinity, temperature, dye, and multiple-size classes of cohesive and non-cohesive sediments transport into a comprehensive model (DSI 2022). First, the hydrodynamic model predicts water surface elevation, velocities, and temperature. Then the sediment transport portion of the model uses the results from the hydrodynamic model to compute the settling of suspended sediment, resuspension of bottom sediments, and bed load movement of non-cohesive sediments (DSI 2022). A detailed description of the hydrodynamic equations and numerical scheme of the EFDC model can be found in DSI (2022).

Cohesive sediment

EFDC+ allows the choice from different settling approaches for the cohesive sediment, including; option 1 following a formulation proposed by Hwang and Mehta (1989), option 2 following Shrestha and Orlob (1996), option 3 following Ziegler and Nisbet (1994, 1995) and option 4 which is a generalized approach to computing the settling velocities based on sediment concentration and shear stress (DSI, 2022). In addition, user-defined settling velocities are allowed by the EFDC+. Hence, settling velocities adopted by the City of Calgary in their Stormwater management & design manual were also tested (City of Calgary 2011).

Surface erosion occurs gradually when bed shear stress, τ_b , is greater than a critical erosion or resuspension stress, τ_{ce} . Surface erosion flux in $\text{g/m}^2/\text{s}$ is generally expressed as a function of the erosion rate, M , in $\text{kg/m}^2/\text{s}$, bed shear stress, τ_b , in N/m^2 and critical stress for erosion, τ_{ce} , in N/m^2 . The erosion rate, M , and the critical stress for erosion, τ_{ce} , depend on the sediment type, bed water content, total salt content, ionic species in the water, pH, and temperature (Mehta et al., 1989). The EFDC+ can estimate M and τ_{ce} following built-in formulas proposed by Hwang and Mehta (1989) and Sanford and Maa (2001). In addition, values of 0.1 N/m^2 for τ_{ce} and $9 \times 10^{-6} \text{ kg/m}^2/\text{s}$ for M were tested following Liu et al. (2016).

The bed shear stress, τ_b , is computed as a function of the bottom horizontal velocity components and roughness height, z_0 (DSI, 2022). Values for z_0 from 0.008 to 0.1 m were previously used to simulate the effects of emergent and submerged plants and irregularities in bottom depth (Jin et al., 2000; Jin and Ji, 2005; Liu et al., 2016). As a result, the sensitivity of the sediment transport model was tested under z_0 of 0.01, 0.05 and 0.1 m.

Net deposition to the bed occurs as the bed shear stress decreases. The critical deposition stress is generally determined from in situ field observations, and values ranging from 0.05 to 1.1 N/m^2 have been reported in the literature (Liu et al., 2016; DSI, 2022). Given this wide range of reported values, the depositional stress is treated as a calibration parameter and values of 0.01, 0.1 and 1.1 N/m^2 were tested.

Non-cohesive sediment

For the settling velocity of non-cohesive sediment, the EFDC+ allows the choice from the method proposed by van Rijn (1984) or user-defined settling velocities. As a result, the sensitivity of the sediment transport model to settling velocities calculated following van Rijn (1984), settling

velocities adopted by the City of Calgary indicated in their Stormwater management & design manual (City of Calgary 2011) and others measured by the Nationwide Urban Runoff Program (NURP; USEPA 1983) were tested.

Non-cohesive sediment may be transported as bedload or suspended load. Several approaches have been used to distinguish whether a particular sediment size is transported as a bed or suspended load under a specific local flow condition. Both modes of transport begin with erosion or resuspension of sediment from the bed when the bed shear stress exceeds the critical Shield's stress. Formulation of these processes is developed in the EFDC as a function of the near-bed equilibrium concentration and its corresponding reference distance above the bed. Equilibrium distribution of sediment in the water column tends to be established, under steady, uniform flow and sediment loading conditions, with the resuspension and deposition fluxes cancelling each other. The EFDC+ allows the choice from different formulations for determining the near-bed equilibrium concentration, C_{eq} , including Smith and McLean (1977), van Rijn (1984), and Garcia and Parker (1991). Bedload transport of the non-cohesive sediment is determined using bedload transport rate q_B (mass per unit time per unit width) in the direction of the near-bed horizontal velocity vector. EFDC allows the calculation of q_B using widely used bedload formulations from Engelund and Hansen (1967), Van Rijn (1984), or Wu et al. (2000).

6.2.3 Model implementation

The hydrodynamic compartment of the EFDC model was calibrated and validated in AB and RO against water level, temperature, salinity and velocity profiles in two ice-free seasons between May and October 2018 and 2019 (refer to the hydrodynamic modelling results in chapter 5). In the current study, the sediment transport compartment of the EFDC was only applied to the validated

hydrodynamic model in AB and RO in 2019 based on the available inflow and outflow suspended sediment data to simulate the sediment dynamics between May and August 2019. The water and sediment inflows measured at the inlet structures were used for the inflow boundary conditions. The built-in modelling codes in the EFDC+ for hydraulic systems, including weirs and orifices, were considered outflow boundary conditions. The initial sediment concentration and bedload were assigned based on the collected in-pond water samples, sediment depth survey and bed sediment core samples.

6.3 Field measurement results

Figures 6-2 and 6-3 present time series for the inflow, outflow and collected water samples (aliquots) in AB and RO. In addition, Table 6-1 shows the information on the observed inflow/outflow events and the collected aliquots' representativeness, defined as the inflow volume between the start and end of sampling to the event total inflow volume in AB and RO. The inflow/outflow water quality was monitored during eleven rainfall events between April 27 and August 25 in AB and RO (Table 6-1 and Figures 6-2 and 6-3). The collected aliquots' representativeness was less than 50% for only 5 out of 26 successful samples in AB and 7 out of 18 in RO. The inflow volume to AB between April 27 and August 25 was significantly higher from inflow 1 than inflow 2 at 22.93 and 0.11 million m³, respectively (Figure 6-2a,b). No water samples were acquired in AB for 6 out of 11 events at inflow 2 due to its low inflow rate, which was lower than the anticipated set point to enable the autosampler (Table 6-1 and Figure 6-2b). In RO, the total inflow volume was 0.26 million m³. Water sampling was unsuccessful during one and two events at the inflow and outflow, respectively, due to the autosampler's power failure (Table 6-1). In AB, composite samples representing event mean concentration were acquired

during 8, 5 and 8 events at the inflow1, 2 and outflow, respectively (Table 6-1). In addition, discrete samples between 4 and 9 aliquots for each event were collected during 3, 0 and 2 events at the inflow1, 2 and outflow, respectively (Table 6-1). In RO, composite samples were acquired during 7 and 6 inflow and outflow events, and discrete samples were collected during 4 and 3 inflow and outflow events, respectively (Table 6-1).

The particle size distribution for the water samples collected in AB and RO is presented in Table (6-2). More than 60% of the inflow and in-pond suspended sediment were cohesive at particle sizes $< 50 \mu\text{m}$. However, the outflow water samples showed a higher percentage of non-cohesive sediment above $50 \mu\text{m}$ than the inflow and in-pond water samples (Table 6-2). For instance, the percentage of the non-cohesive sediment at the inflow and the outflow was 37% and 55% in AB and 30% and 39% in RO, respectively.

Table 6-3 provides information on the collected bed sediment samples in AB and RO. Fourteen cores were collected (seven in each water body) and Core depths ranged from 10 to 50 cm. Between 1 and 3 sediment samples were extracted from each core at different depths based on a visual inspection of the strata in each core. Accordingly, 15 samples were extracted from each facility. Samples were sent to a commercial laboratory to determine the particle size distribution and bulk density. The soil bulk density measured in AB and RO were 2442 and 2192 kg/m^3 , respectively. And the percentage of cohesive sediment less than $50 \mu\text{m}$ at locations I, M and O was 63%, 67% and 58% in AB, versus 72%, 38% and 39% in RO. This confirms the previous observation that the percentage of the non-cohesive sediment is higher near the outlet than near the inlet in AB and RO.

The TSS concentration and turbidity level were measured in 29 water samples collected from different locations, depths, and at different times in Royal Oak. The plotted data in Figure 6-4 shows a positive correlation between TSS and turbidity, with a coefficient of correlation R^2 of 0.95. Overall, measuring turbidity has shown a potential cost-saving option to estimate an approximate continuous TSS concentration in RO. Yet, in AB, turbidity data were not collected due to a malfunction in the turbidity unit. As a result, only discrete inflow/outflow TSS concentrations will be available in the current study for AB.

Tables 6-4 and 6-5 show the observed suspended sediment inflow and outflow load in kg and the removal efficiency for different sediment classes in RO and AB. The total suspended sediment inflow load observed between April 30 and August 28 in RO was 2768 kg. As a result, the overall observed removal efficiency between May and August in RO was 93% (Table 6-4). In AB, the total inflow load between May and August was 24,564 kg, and the outflow load was 1740 kg (Table 6-5). As a result, the observed removal efficiency in AB was 93% (Table 6-5). The removal efficiency was the highest for the finest class size $< 10 \mu\text{m}$ at 98% and 95% in AB and RO and the lowest for the coarsest class size $> 150 \mu\text{m}$ at 88% and 87% in AB and RO, respectively. This was because the fraction of the non-cohesive sediment was higher near the outlet than near the inlet in AB and RO (Table 6-2). Both water bodies could remove more than 85% of the suspended sediment with particle size greater than $75 \mu\text{m}$ per the Alberta guideline requirements (AENV 2001). Further, they met the requirements of the city of Calgary (2011) that calls for removing a minimum of 85% of sediment with a particle size of $50 \mu\text{m}$ or greater. Hence, the performance of AB and RO between April 25 and August 28 in terms of sediment removal efficiency was overall acceptable.

6.4 Model calibration and sensitivity analysis

6.4.1 Model calibration

The model was calibrated by tuning the bottom roughness height, z_0 , settling velocity, w_s , surface erosion flux, J_r , and critical deposition stress, τ_{cd} , for the cohesive sediment, in addition to the settling velocity, w_s , the near-bed equilibrium concentration, C_{eq} and the bedload transport rate, q_B , for the non-cohesive sediment using values and formulations reported in the literature and discussed in section 6.2.2. The root means square error (RMSE) between the modelled and observational outflow's TSS concentration between April 27 and August 25, 2019, in AB and between April 30 and August 28 in RO were used to calibrate the model and validate its capability to predict the sediment removal efficiency, according to the availability of the inflow data and the observed inflow/outflow TSS concentration.

The best calibration results were achieved when the settling velocity of the cohesive sediment was calculated based on sediment concentration and shear stress following an approach presented in DSI (2022; option 4) for RO and Ziegler and Nisbet (1994, 1995) for AB. In addition, a low roughness height of 0.005 m was needed for the best calibration results in RO versus 0.01 m in AB. Through the model runs in AB and RO, values of 0.1 N/m^2 , $9 \times 10^{-6} \text{ kg/m}^2 \cdot \text{s}$ and 0.05 N/m^2 for τ_{ce} , M and τ_{cd} were used following Liu et al. (2016). In addition, the most recent formulations developed by Garcia and Parker (1991) for C_{eq} and by Wu et al. (2000) for q_B were chosen. Furthermore, settling velocities for non-cohesive sediment following NURP (1983) were adopted. Although NURP (1983) significantly underestimated the settling velocity compared to OMOE (2003) and the City of Calgary (2011), NURP (1983) does provide a conservative estimate for stormwater treatment practice design (Gulliver et al. 2010).

Figure 6-5 compares the simulated and observed outflow's TSS concentration in RO and AB. In addition, the vertical profiles of the simulated and observed TSS concentration in ponds are shown in Figures 6-6 and 6-7. The RMSE results for the calibrated models in RO and AB are presented in Table 6-6. The RMSEs between the computed and measured suspended sediment concentrations in RO are between 3.0 and 4.0 mg/L (Table 6-6). This reveals that the simulated outflow's TSS in RO reasonably matches the observed values (Figure 6-5a). It also indicates that the model predicted the measured TSS in vertical profiles (Figure 6-6). However, in AB, the RMSEs for the calibrated model were more than twice those in RO (Table 6-6).

On May 20, an absolute relative error of 56% was evident between the modelled and the observed outflow's TSS concentration in AB (Figure 6-5b). Simultaneously, high chlorophyll-a levels were observed at mid-depth near the outlet in AB, which persisted until early June (Figure 6-8). The high chlorophyll-a concentrations can be explained as escalations of algal biomass quantity (Chung et al., 2009; Chen et al., 2019). This might explain the high observed outflow's TSS concentration on May 20 when algal biomass was internally produced in the pond before exiting during outflow events. However, this biogeochemical process was not modelled by the sediment transport module of the EFDC, which likely resulted in the underestimation of the outflow's TSS in AB (Figure 6-5b) and the significant RMSEs between the computed and measured TSS concentrations in AB (Table 6-6).

On August 14, the TSS profile near the outlet (Location OUT) in AB (Figure 6-7c) showed a significant error between the observed and the modelled TSS near the surface at an absolute relative error of 92%. On that day, we managed to document the existence of big floating algal blooms near the outlet of AB (Figure 6-9), which most likely resulted in the high observed TSS concentration near the surface at this time when the model failed to predict it. This confirms that

the uncertainties in modelling the sediment transport in AB arise from the biological processes that generated floating and suspended algal biomass contributing to the TSS concentration that was not modelled by the EFDC. Similarly, Nakhaei et al. (2021) reported that Alberta stormwater ponds may suffer from algal blooms because of excessive nutrient loads causing eutrophication, where suspended algae growth increases in response to nutrient enrichment. While in the vegetated wetlands, similar to the RO wetland, the suspended algae and macro-algae must compete with aquatic vegetation (macrophytes) for nutrients, resulting in lower phytoplankton biomass and increased water clarity (Nakhaei et al., 2021). As a result, coupled sediment transport and biogeochemical models in AB are necessary to enhance its ability to predict the outflow's TSS concentration (Arhonditsis and Brett, 2004).

The model in RO could predict a total outflow load of 168 kg versus 190 kg for the observed value (Table 6-4). As a result, the total removal efficiency in RO was 93 and 94% for the observed and simulated results (Table 6-4). However, the model significantly underestimated the outflow load of the non-cohesive sediment of particle sizes $> 50 \mu\text{m}$ at 7 kg compared to 74 kg for the observed value (Table 6-4). In AB, the inflow load was 24,564 kg, and the modelled outflow load was half the observed outflow load at 909 and 1740 kg (Table 6-5). As a result, the modelled removal efficiency was overestimated at 96% compared to 93% for the observed value (Table 6-5). This underestimation was likely due to the fact that the internal loading of the floating and suspended algal biomass by biological processes was not modelled by the EFDC. Similar to RO, the model in AB significantly underestimated the outflow load of the non-cohesive sediment at 0 kg compared to 692 kg for the observed outflow load (Table 6-5). The particle size distribution for the water samples collected in AB and RO showed a higher percentage of non-cohesive sediment above $50 \mu\text{m}$ at the outflow than the inflow and in-pond water samples (Table 6-2). As a result,

the resuspension of previously settled non-cohesive sediment at the outlet structure might have been the source of the observed non-cohesive outflow that was not predicted by the model due to the lack of sediment data at the outlet structures.

6.4.2 Sensitivity analysis

A sensitivity analysis was performed to examine the response of the prototype in AB and RO to changing the previously mentioned calibration parameters using the RMSE between the modelled and observational outflow's TSS concentration. The input values for the parameters used in the sensitivity analyses were determined using values and methods reported in the literature and discussed in section 6.2.2. Figure 6-10 presents the model sensitivity results in RO for all parameters in May when the observed outflow's TSS concentration was the highest in 2019. In AB, the sensitivity analysis was performed between June 20 and July 15, during the most significant rainstorm inflow events in 2019 (Figure 6-2). Table 6-7 summarizes the RMSE values of the different sensitivity runs in AB and RO. In RO, the outflow TSS concentration was somehow sensitive to the bed roughness height when the RMSE changed between 5.4 and 6.4 mg/L for a z_o range of 0.01-0.1 m (Table 6-7 and Figure 6-10a). However, the outflow TSS in AB was not sensitive to z_o (Table 6-7). The different formulations of the settling velocities for the cohesive sediment in AB and RO resulted in the broadest range of RMSE 14-27 mg/L in AB and 5-67 mg/l in RO (Table 6-7 and Figures 6-10b & 6-11). These results indicate that cohesive sediment settling velocity would be the most sensitive parameter to the outflow's suspended sediment concentration (Lee et al., 2005; Liu et al., 2016). The erosion flux for cohesive sediment, J_r , critical deposition shear stress for cohesive sediment, τ_{cd} , settling velocity for non-cohesive sediment, w_s , bed equilibrium concentration for non-cohesive sediment, C_{eq} and bed load transport rate for non-

cohesive sediment, q_B , were slightly sensitive parameters to the modelled outflow TSS in both AB and RO (Table 6-7).

6.5 Model application and discussion

6.5.1 Effect of lowering the operational NWL.

In AB, lowering the NWL by 1.0 m decreased the permanent pool volume by a third from 56500 to 35300 m³ and the duration of thermal stratification by up to 12% in the main cell. In addition, lowering the dead storage will increase the live capacity in wet ponds, reducing the risk of flooding by accommodating runoff volumes larger than the designed values, which might be a concern due to climate change. However, the current study revealed that lowering the NWL by 1 m will increase the outflow's TSS concentration during most inflow events (Figure 6-12), resulting in an increase in the total outflow load by a third from 909 kg during the base case simulation to 1200 kg during the reduced NWL scenario. In addition, the TSS removal efficiency will decrease from 96% during the base case scenario to 95% during the lowered NWL scenario. Figure 6-13 shows longitudinal sections from the inlet to the outlet for the in-pond TSS concentration following the June 27 inflow event during the base case scenario and the reduced NWL scenario. Both scenarios were subjected to a clear short-circuiting when the inflow load of TSS concentration at more than 100 mg/L travelled down the water column in the main cell and did not mix with the entire volume. However, the higher water column depth during the base case scenario slowed down the inflow load's transport, allowing for more settling and resulting in a lower outflow concentration (Figure 6-12). Yet this result needs more validation by adding the water quality module to simulate the benefits/drawbacks of lowering the NWL on the biological processes and the internal loading of the algal biomass.

6.5.2 Effect of inflow characteristics

Table 6-8 presents the simulated inflow load, outflow load and removal efficiencies for different rainstorm events in AB and RO. In AB, The highest removal efficiencies occurred on June 8 and August 6 at 100% when the inflow volume and duration were minimum at 2800-2900 m³ and 3-5 hrs, respectively. The removal efficiencies were minimum at 92% and 90% on April 27 and July 3 (Table 6-8) when the inflow duration was maximum at 2.0-2.5 days. The TSS removal efficiency in AB showed no correlation with the sediment inflow load or the maximum inflow rate at $R^2 < 0.2$, and it was weakly correlated with the inflow volume at R^2 of 0.47 (Figure 6-14). Yet the sediment removal efficiency in AB was well correlated with the inflow duration (i.e., the duration between the start and the end of the inflow hydrograph) at R^2 of 0.71 (Figure 6-14).

In RO, the highest removal efficiencies occurred on August 6 and 22 at 100% when the inflow volume was minimum at $< 200 \text{ m}^3$ (Table 6-8). The removal efficiencies decreased to 91 and 82 on June 20-21 and 27 (Table 6-8) due to the significant turbulence following the highest inflow rates peaking at 1.4 and 1.2 m³/s (Figure 6-3) and inflow volumes at 9850 and 4800 m³ (i.e., 4 and 2 times the permanent pool volume). Yet, On July 3, the removal efficiency was the minimum at 72% when the inflow duration was the highest at 2.7 days, and the sediment loading was low at 29 kg. The TSS removal efficiency in RO showed almost no correlation with the sediment inflow load, inflow volume, and maximum inflow rate at $R^2 < 0.25$ and was weakly correlated to the inflow duration at R^2 of 0.43 (Figure 6-15).

The energy dissipation by the submerged berms at the inlets of AB and RO intends to stop particles from moving greater distances before settling during high inflow rates (Gu et al., 2017). Thus the removal efficiency at both facilities was not significantly correlated with the inflow rate. However,

the duration of the inflow events at both sites showed a notable correlation with the RE. This is because continuous inflows keep particles suspended for longer before settling, allowing more sediment to transport to the outlet. This also explains the declining removal efficiency as we move forward from the June 19 to the July 3 events at both sites. The four significant inflow events in a short period resulted in the lowest removal efficiency during the last event in this series of inflows on July 3 (Table 6-8).

6.5.3 Effect of vegetation

The model simulations in the RO wetland were not sensitive to varying parameters in the aquatic vegetation sub-model over wide ranges (i.e., stem diameters between 0.001-0.2m, plant density at 0-100 stem/m², stem height at 0-2m and drag coefficients between 0 and 1). Similarly, by analysis of data from 46 wet ponds and constructed wetlands, Larm and Alm (2014) found the coefficient of correlation (R^2) between the vegetation and sediment removal efficiency to be 0.042.

In numerical modelling, vegetation can be considered a bed roughness and is modelled by assigning very high friction factors (Somes et al. 1999). The model results in RO have shown a slight sensitivity to the fact that the bottom roughness can reduce the flow velocity and change the flow pattern, which helps increase sediment settling and reduce the outflow's TSS concentration (Figure 6-10a & Table 6-7). Therefore, to improve the removal efficiencies of sediments, it was suggested that vegetation be located within the main flow path of stormwater wetlands similar to RO to serve as an obstacle (Gu et al., 2017). Denser submerged aquatic vegetation might increase bed roughness and slightly reduce the outflow TSS concentration. Yet, it might also cause a localized increase in water temperature near the surface, increasing thermal stratification (refer to chapter 4). Therefore, riparian vegetation might be a better option to serve as an obstacle. This is

because shading from the dense riparian vegetation reduces surface heating and thermal stratification, allowing for better mixing and lower TSS concentration in the outflow. However, sheltering by riparian vegetation does also reduce vertical mixing by wind, causing anoxic conditions near the bed (refer to chapter 4). Hence, the vegetation design in wetlands needs further investigation through the water quality compartment of the EFDC that models the biological and chemical processes.

6.5.4 Effect of wind

The measured data and the model results reveal that the average wind-induced currents in AB and RO are low at 1–2 cm/s (see chapters 3 and 4). However, significant wind events at 12 m/s can induce surface currents up to 9 and 25 cm/s in AB and RO. Figure 6-16 shows the EFDC results of the surface velocity vectors and longitudinal sections from the inlet to the outlet for the velocity vector profiles and the TSS profiles in AB associated with the significant wind event and dry weather on July 1 at 12 m/s from the northeast. The simulated results reveal that the surface currents were in phase with the wind direction (Figure 6-16a). In addition, the bottom currents were in the opposite direction as surface currents due to return flows (Figure 6-16b) (Liu et al. 2016). In the sediment forebay, the water circulation due to wind was limited to the top 1 m of the water column, likely due to the smaller size of the forebay and the complex bathymetry due to the submerged berm (Figure 6-16b). In the main cell, where the fetch is double that of the sediment forebay (Figure 6-1a), and the morphology was less complex, the water circulated occurred from the top to the bottom of the water column (Figure 6-16b), allowing for better mixing of the TSS than in the sediment forebay (Figure 6-16c).

In RO, the simulated results during the significant wind event on July 24 at 12 m/s from the west reveal that the surface currents were significantly higher in RO than in AB at 25 cm/s (Figure 6-17a). In addition, vertical circulation was also evident when bottom currents were in the opposite direction as surface currents (Figure 6-17b). As a result, the induced currents due to this significant wind event in RO caused resuspension of the deposited sediment near the bed at the main cell and the narrow channel (Figure 6-17c).

Figure 6-18a shows the outflow's TSS concentration between April 27 and August 25 in AB under three wind speed scenarios defined as the observed, double and half the observed wind speed. The observed wind speed between April 27 and May 25 was 2.2 m/s on average from all directions (i.e., no prevailing wind direction), with a maximum speed of 12 m/s. The outflow load for half the observed wind speed, the observed wind speed and double the observed wind speed scenarios were 874, 909, and 1021 kg, respectively. However, the differences between the outflow load were insignificant and did not cause a notable change to the TSS removal efficiency, which was 96% for all three scenarios.

Figure 6-19 shows longitudinal sections from the inlet to the outlet for the TSS concentration in AB on April 28 following the significant inflow event on April 27. At that time, the water column in the wet pond was significantly stratified at a bottom-top vertical density difference above 1 kg/m³. In addition, the wind blew from east to west along the main flow path direction. As a result, the scenario of double the observed wind speed caused short-circuiting and transported more TSS load above the pycnocline from the sediment forebay to the outlet (Figures 6-18a & 6-19). In Figure 6-20, the TSS concentration is presented in AB on June 28, following the significant inflow event of June 27. At that time, the bottom-top vertical density difference in AB was milder at < 0.5 kg/m³. In addition, the wind speed was blowing from the west, opposite to the inflow direction.

As a result, the scenario of double the observed wind speed retarded, the transport of the inflow load above the berm. In addition, the circulation during the significant wind scenario was able to better mix the TSS load in the main cell before exiting the pond (Figures 6-18a and 6-20). Similarly, Condie and Webster (2001) noted that mixing in a shallow lake in southeastern Australia is enhanced by strong winds through mechanical stirring and evaporative cooling at the water surface.

In RO, Figure 6-18b shows the outflow's TSS concentration between April 30 and May 30 under the three wind speed scenarios. The observed wind speed between April 30 and May 30 was 2.5 m/s on average, predominantly from north and west (i.e., opposite to the flow direction in RO), with a maximum speed of 13 m/s. The simulated outflow's TSS was the least under the double wind speed scenario and the highest during the half wind speed scenario (Figure 6-18b). For instance, the outflow load was 32, 25, and 16 kg for the half, observed and double wind speed scenarios, respectively. As a result, the removal efficiency was the lowest at 97% during the low wind speed scenario and the highest at 99% for the high wind speed scenario. Hence, the sediment removal efficiency was more sensitive to wind speed in RO than in AB. Similarly, wind forces were previously reported to be transferred more efficiently in shallower ponds (Józsa, 2014; Andradóttir and Mortamet, 2016). The higher removal efficiency during the higher wind speed scenario in RO was due to the prevailing wind direction being opposite to the inflow direction and the hydraulic mixing, which enhanced the effective volume of the wetland. For instance, the pond averaged vertical temperature gradient between April 30 and May 30 was 0.72, 0.03 and -0.17 °C/m for the half, observed and double wind speed scenarios, respectively.

6.5.5 Effect of stratification

A scenario of significant thermal stratification in RO was modelled by deactivating the sensible and latent heat loss at the water surface, increasing the vertical temperature gradient between May 1 and August 28 from 0.4 °C/m to 4.6 °C/m. The stratification scenario in RO is intended to test the effect of the high stratification strengths observed in the nearby Rocky Ridge wetland, where the stratification strength was up to eight times higher than in RO (see chapter 4). Figure 6-21 shows the outflow's TSS during the base case and the stratification scenarios in RO. Following the first inflow event on May 2, it was revealed that stratification delayed the peaking of the outflow's TSS concentration when TSS peaked on May 3 for the base case scenario versus May 5 for the stratification scenario. However, the total outflow load between May 1 and 15 was higher during the stratification scenario at 26 kg compared to 19 kg for the base case scenario. Figure 6-22 shows the plan view and longitudinal section from the inlet to the outlet for the TSS in RO when the outflow's TSS peaked on May 3 and May 5 for the two scenarios. On May 3 of the base case scenario, RO was entirely at a TSS of 22 mg/L or above, which is the peak outflow's TSS concentration following the May 2 inflow event (Figure 6-22a). However, on May 5 of the stratification scenario, part of the outlet basin in RO had a lower TSS concentration than the outflow peak concentration at 27 mg/L (Figure 6-22b). Hence, it was concluded that stratification can create preferential flow paths within the wetland, reducing the effective volume, which increases the TSS outflow load.

Following the May 17 and June 8 inflow events, the stratification scenario had lower TSS concentrations than the base case scenario between May 14 and June 18 (Figure 6-21), resulting in a lower outflow load for the stratification scenario at 6 kg versus 12 kg for the base case scenario. Figure 6-23 shows the plan view and longitudinal section from the inlet to the outlet for the TSS in RO following the May 17 inflow event. During the base case scenario, some of the inflow's

TSS managed to exit the forebay, travel to the main cell, and then to the outlet basin. However, during the stratification scenario, most of the inflow's TSS settled in the sediment forebay and could not overtop the berm. This was likely due to the low inflow rates at less than $0.05 \text{ m}^3/\text{s}$ on May 17 and June 8 (Figure 6-3) that could not overcome the predominant stabilizing effect of stratification in the sediment forebay. However, during the significant inflow events at flow rates above $0.75 \text{ m}^3/\text{s}$ between June 19 and July 3 (Figure 6-3), the inflow momentum was able to overcome the stratification and act similarly to the base case scenario (Figure 6-21). Hence, the internal hydrodynamic behaviour of a stratified wetland significantly influences the movement of suspended particles in the water column according to the strength of the inflow momentum (Condie and Webster 2001). Similarly, He et al. (2015) found that the concentrations of suspended solids during low inflow events were higher in bottom waters than in surface waters, suggesting stratification's predominant influence on resuspension.

6.5.6 Model limitation and future work

The current study provides a valuable tool for predicting sediment transport and fate in the study pond and wetland, which is a crucial component for water quality and ecology simulations. In addition, it can be used to optimize design and operation for improved sediment removal through various remediation options. Yet, the models can be further improved through coupled hydrodynamic, sediment transport and biogeochemical models. This can enhance the predicted outflow's TSS concentration when the internal loading of algal biomass is accurately simulated. In addition, the biogeochemical compartment might better investigate the significance of the aquatic vegetation on the water quality. A sediment survey at the outlet structures is also needed to explain the source of the non-cohesive sediment at the outflow of the stormwater facilities that the models could not predict. This is important as some guidelines mandate removing a certain

percentage of non-cohesive sediment before releasing downstream (e.g., 85% by the City of Calgary, 2011). As a result, an accurate investigation of the outflow's non-cohesive sediment concentration and its source is crucial.

6.6 Conclusions

Sediment removal efficiency in urban stormwater ponds and wetlands usually varies greatly in the literature, and hence, it is essential to identify the key influencing factors to improve their design and operation to minimize the outflow of sediment that degrades downstream water quality. In the current study, 3D sediment transport models were validated in an urban stormwater wet pond and a constructed wetland in residential areas of Calgary, Alberta, Canada, using comprehensive field monitoring data to investigate the key parameters governing sediment transport.

The sensitivity analysis using the sediment transport compartment of the EFDC model indicates that the settling velocity of the cohesive sediment is the most critical parameter influencing the outflow's TSS concentration. Cohesive sediment concentration obtained from the validated model generally agreed with field observations. However, the model underestimated the outflow's non-cohesive sediment fraction. The validated model revealed that the sediment removal efficiency is not correlated with the inflow rate between 0.02 and 3.98 m³/s, likely due to the energy dissipation by the submerged berms. But the inflow duration was significantly negatively correlated with the TSS removal efficiency at R² up to 0.71. This occurred when higher inflow durations inhibited settling and kept suspended sediment longer in the water column, allowing more sediment to travel to the outlet. The deeper depth of the stormwater pond at 3m versus 2m dissipated the inflow momentum and slowed the suspended sediment transport, allowing more settling and reducing the outflow load by a third. Wind forces transferred more efficiently in the shallower wetland,

increasing the hydraulic mixing and reducing the outflow load. For instance, the effect of double the observed wind speed on sediment removal efficiency was negligible in the 3m deep wet pond but significant in the 0.8m deep wetland when vertical mixing by wind decreased its sediment outflow load by half.

Notation

The following symbols are used in this chapter:

C_{eq} = near-bed equilibrium concentration for non-cohesive sediment;

HWL = high water level;

I = rainfall depth;

J_f = surface erosion flux for cohesive sediment;

M = erosion rate for cohesive sediment;

M_{in} = the sediment masses entering the stormwater ponds;

M_{out} = the sediment masses leaving the stormwater ponds;

NWL = normal water level;

q_B = bedload transport rate for non-cohesive sediment;

RE = sediment removal efficiency;

RMSE = root mean square error;

TSS = total suspended solids;

Tu = water turbidity;

w_{sj} = settling velocity sediment particles of class j ;

z_0 = bottom roughness height;

τ_b = bed shear stress;

τ_{cd} = critical deposition shear stress for cohesive sediment;

τ_{ce} = critical erosion shear stress for cohesive sediment;

Table 6-1 Information on the observed inflow/outflow events and the collected aliquots representativeness, defined as the inflow volume between the start and end of sampling to the total inflow volume during 11 rainfall events in the AB wet pond and the RO wetland. "√" represents successful composite sampling, "√D" represents successful discrete sampling, and red highlighted cells labelled "X" represents unsuccessful sampling.

| Storm Event | AB | | |
|--------------------------|-----------|---------------|------------------------|
| | Inflow 1 | Inflow 2 | Outflow |
| 27-Apr-19 | √ (88%) | √ (83%) | √ (100%) |
| 17-May-19 | √D (94%) | √ (100%) | √ (69%) |
| 08-Jun-19 | √ (43%) | X (no sample) | √ (72%) |
| 19-Jun-19 | √ (61%) | √ (56%) | √ (composite) (93%) |
| 23-Jun-19 | √ (79%) | √ (60%) | |
| 27-Jun-19 | √D (69%) | X (no sample) | √D (94%) |
| 03-Jul-19 | √ (85%) | X (no sample) | √ (81%) |
| 16-Jul-19 | √D (65%) | √ (98%) | √D (58%) |
| 06-Aug-19 | √ (50%) | X (no sample) | √ (42%) |
| 16-Aug-19 | √ (31%) | X (no sample) | √ (60%) |
| 22-Aug-19 | √ (24%) | X (no sample) | √ (36%) |
| Storms | 11 | 5 | 10 |
| Discrete Samples | 3 | 0 | 2 |
| Composite Samples | 8 | 5 | 8 |

| Storm Event | RO | |
|--------------------------|---------------|------------------------|
| | Inflow | Outflow |
| 02-May-19 | √D (79%) | √ (33%) |
| 16-May-19 | X (no sample) | √ (55%) |
| 08-Jun-19 | √ (29%) | X (no sample) |
| 19-Jun-19 | √ (81%) | √ (composite) (94%) |
| 20-Jun-19 | √ (7%) | |
| 27-Jun-19 | √D (16%) | √D (26%) |
| 03-Jul-19 | √ (78%) | √ (45%) |
| 16-Jul-19 | √D (67%) | √D (82%) |
| 06-Aug-19 | √ (72%) | X (no sample) |
| 16-Aug-19 | √ (60%) | √ (63%) |
| 22-Aug-19 | √D (58%) | √D (41%) |
| Storms | 10 | 8 |
| Discrete Samples | 4 | 3 |
| Composite Samples | 6 | 5 |

Table 6-2 The mean particle size distribution for the water samples collected at the inflow/ in-pond and outflow in the AB wet pond and the RO wetland. "n" are the number of water samples collected at each location.

| Sediment type | Sediment Size (μm) | AB | | | RO | | |
|---------------|---------------------------------|---------------|----------------|---------------|--------------|----------------|---------------|
| | | Inflow (n=13) | In-Pond (n=41) | Outflow (n=9) | Inflow (n=5) | In-Pond (n=41) | Outflow (n=6) |
| Cohesive | <10 μm | 25 | 24 | 9 | 22 | 23 | 16 |
| | 10-20 μm | 19 | 21 | 14 | 22 | 20 | 23 |
| | 20-50 μm | 20 | 21 | 22 | 26 | 24 | 22 |
| Non-Cohesive | 50-150 μm | 23 | 22 | 33 | 21 | 19 | 22 |
| | >150 μm | 14 | 13 | 22 | 9 | 15 | 17 |

Table 6-3 The characteristics of the bed sediment core samples collected in the AB wet pond and RO wetland. Locations I, M and O, where the bed sediment core samples were collected in AB and RO, are shown in Figure 6-1.

| Core number | AB-I | AB-M | AB-O | RO-I | RO-M | RO-O |
|-----------------------------|------|------|------|------|------|------|
| Distance from the inlet (m) | 35 | 105 | 245 | 5 | 35 | 115 |
| Water depth (m) | 3.1 | 3 | 3.15 | 1.4 | 0.8 | 0.7 |
| Total core depth (cm) | 50 | 35 | 10 | 50 | 35 | 25 |
| Number of cores | 3 | 2 | 2 | 3 | 2 | 2 |
| | 5 | 5 | 5 | 5 | 5 | 5 |
| Sampling depths (cm) | 15 | 15 | - | 15 | 15 | - |
| | 25 | - | - | 25 | - | - |

Table 6-4 Simulated and observed sediment removal efficiency (RE) for different sediment classes in the RO wetland

| Class size (μm) | M_{in} (kg) | Simulated | | Observed | |
|------------------------------|----------------------|-----------------------|------------|-----------------------|------------|
| | | M_{out} (kg) | RE (%) | M_{out} (kg) | RE (%) |
| <10 | 609 | 51 | 92% | 30 | 95% |
| 10-20 | 609 | 50 | 92% | 44 | 93% |
| 20-50 | 720 | 60 | 92% | 42 | 94% |
| 50-150 | 581 | 7 | 99% | 42 | 93% |
| >150 | 249 | 0 | 100% | 32 | 87% |
| Total | 2768 | 168 | 94% | 190 | 93% |

Table 6-5 Simulated and observed sediment removal efficiency (RE) for different sediment classes in the AB wet pond

| Class size (μm) | M_{in} (kg) | Simulated | | Observed | |
|------------------------------|----------------------|-----------------------|------------|-----------------------|------------|
| | | M_{out} (kg) | RE (%) | M_{out} (kg) | RE (%) |
| <10 | 6435 | 352 | 95% | 156 | 98% |
| 10-20 | 4765 | 277 | 94% | 237 | 95% |
| 20-50 | 4793 | 279 | 94% | 386 | 92% |
| 50-150 | 5218 | 0 | 100% | 575 | 89% |
| >150 | 3353 | 0 | 100% | 387 | 88% |
| Total | 24564 | 909 | 96% | 1740 | 93% |

Table 6-6 Root mean square errors (RMSE) between the simulated and measured TSS concentrations. Locations IN, MID and OUT are shown in Figure 5-1.

| RMSE (mg/L) | Profiles | | | Time Series |
|----------------|----------|-----|-----|-------------|
| | IN | MID | OUT | Outflow |
| RO | 3.0 | 2.8 | 2.9 | 4.0 |
| AB | 10.5 | 4.9 | 7.7 | 14.0 |

Table 6-7 Results of the sensitivity run for different sediment transport parameters

| Parameter | Value/Model | RO | AB |
|-------------------------|---------------------------------|-------------|-------------|
| | | RMSE (mg/L) | RMSE (mg/L) |
| z_o | 0.01m | 5.4 | 13.7 |
| | 0.05m | 6.1 | 13.7 |
| | 0.1m | 6.4 | 13.7 |
| w_s (cohesive) | Hwang and Mehta (1989) | 59.1 | 21.9 |
| | Ziegler and Nisbet (1994, 1995) | 6.6 | 16.5 |
| | Shrestha and Orlob (1996) | 66.6 | 27.1 |
| | City of Calgary (2011) | 8.3 | 13.7 |
| | DSI (2022) - Option 4 | 5.4 | 23.0 |
| J_r (cohesive) | Hwang and Mehta (1989) | 5.4 | 13.7 |
| | Sanford and Maa (2001) | 5.3 | 13.7 |
| | Liu et al. (2016) | 5.3 | 13.7 |
| τ_{cd} (Cohesive) | 0.01N/m ² | 5.3 | 13.7 |
| | 0.1N/m ² | 5.4 | 13.7 |
| | 1.1N/m ² | 5.4 | 13.7 |
| w_s (Non-Cohesive) | NURP; USEPA (1983) | 5.4 | 13.7 |
| | van Rijn (1984) | 5.4 | 13.7 |
| | City of Calgary (2011) | 5.4 | 13.7 |
| C_{eq} (Non-Cohesive) | Smith and McLean (1977) | 5.4 | 13.7 |
| | van Rijn (1984) | 5.4 | 13.7 |
| | Garcia and Parker (1991) | 5.3 | 13.7 |
| q_B (Non-Cohesive) | Engelund and Hansen (1967) | 5.4 | 13.7 |
| | van Rijn (1984) | 5.4 | 13.7 |
| | Wu et al. (2000) | 5.3 | 13.7 |

Table 6-8 Simulated sediment removal efficiency (RE) for different inflow events in the AB wet pond and RO wetland in 2019

| Storm Event | AB | | | Storm Event | RO | | |
|--------------------|-----------------|----------------------------|-----------------------------|--------------------|---------------|-----------------|----------------------------|
| | (mmm-dd) | M_{in} (kg) | M_{out} (kg) | | RE (%) | (mmm-dd) | M_{in} (kg) |
| Apr 27- 29 | 2543 | 202 | 92 | May 02-03 | 533 | 7 | 99 |
| May 17-18 | 1227 | 27 | 98 | May 16-18 | 161 | 4 | 98 |
| Jun 08 | 2181 | 0 | 100 | Jun 08-09 | 153 | 2 | 98 |
| Jun 19 | 1110 | 7 | 99 | Jun 19 | 107 | 2 | 98 |
| Jun 23-24 | 845 | 13 | 98 | Jun 20-21 | 360 | 34 | 91 |
| Jun 27-28 | 4564 | 147 | 97 | Jun 27-28 | 451 | 85 | 81 |
| Jul 03-05 | 2071 | 197 | 90 | Jul 03-06 | 29 | 8 | 72 |
| Jul 16 | 719 | 13 | 98 | Jul 16 | 42 | 1 | 97 |
| Aug 06 | 862 | 1 | 100 | Aug 06-07 | 16 | 0 | 100 |
| Aug 16 | 406 | 3 | 99 | Aug 16 | 42 | 1 | 99 |
| Aug 22 | 201 | 3 | 99 | Aug 22 | 19 | 0 | 100 |



Figure 6-1 Satellite images of the (a) AB wet pond and (b) RO wetland. The red lines indicate the normal water level boundaries, and the white arrows show the location of inlets and outlets. Yellow circles labelled I, M, and O are bed sediment cores sampling locations along the flow path near the inlet, middle, and outlet, respectively. Red arrows show the location of the branch pipes to the inlet in AB. [Images' source: Google Earth Pro 7.3.4.8248. (August 31, 2017). City of Calgary, Alberta, Canada. <<http://www.google.com/earth/index.html>> (Accessed January 22, 2022)].

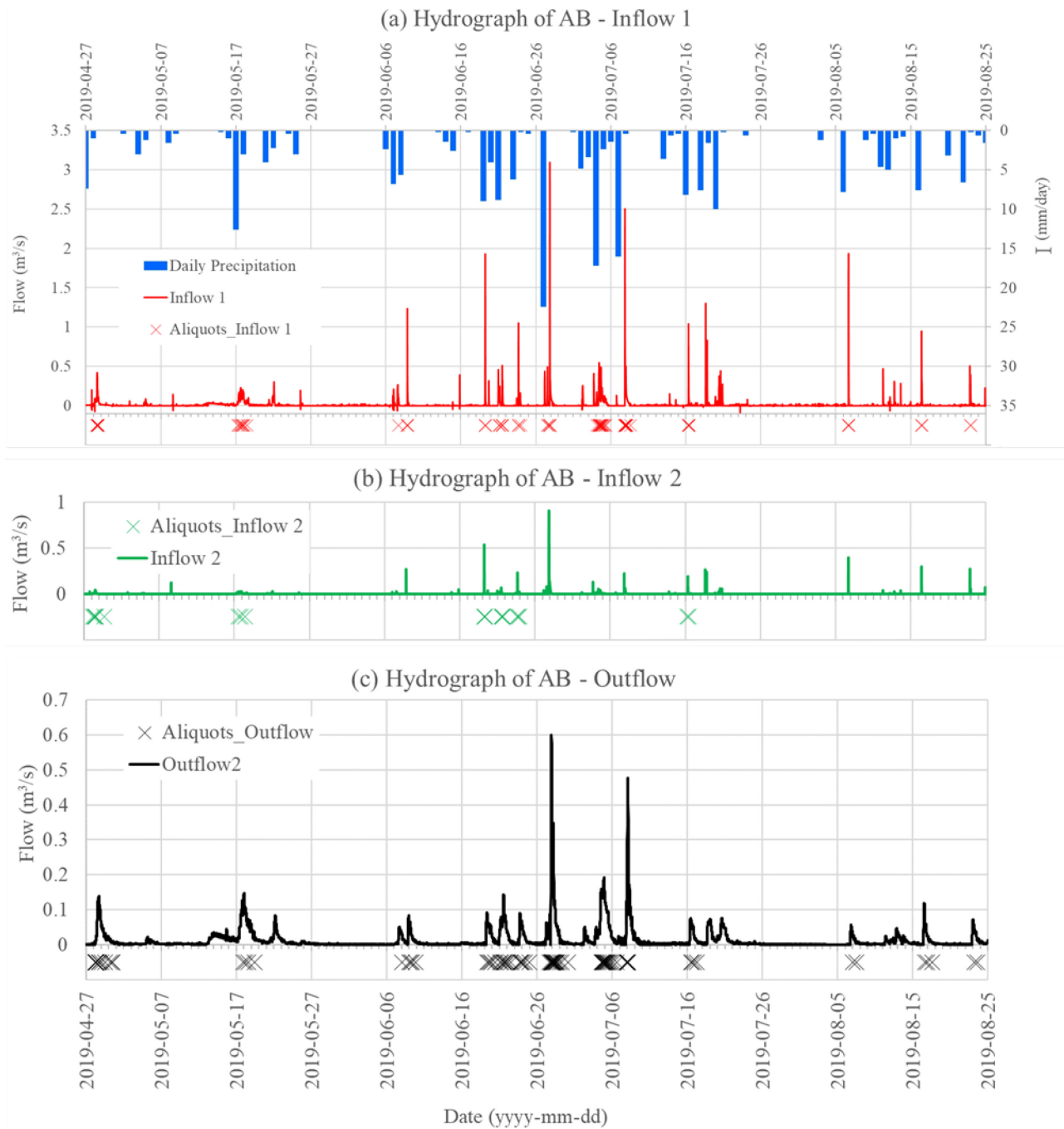


Figure 6-2 Time series measured in the AB wet pond showing the measured (a) inflow rate from branch pipe 1 (left axis) and rainfall depth (I, right axis), (b) inflow rate from branch pipe 2, and (c) outflow rate. Crosses in (a), (b), and (c) indicate the timing of the successfully collected aliquots.

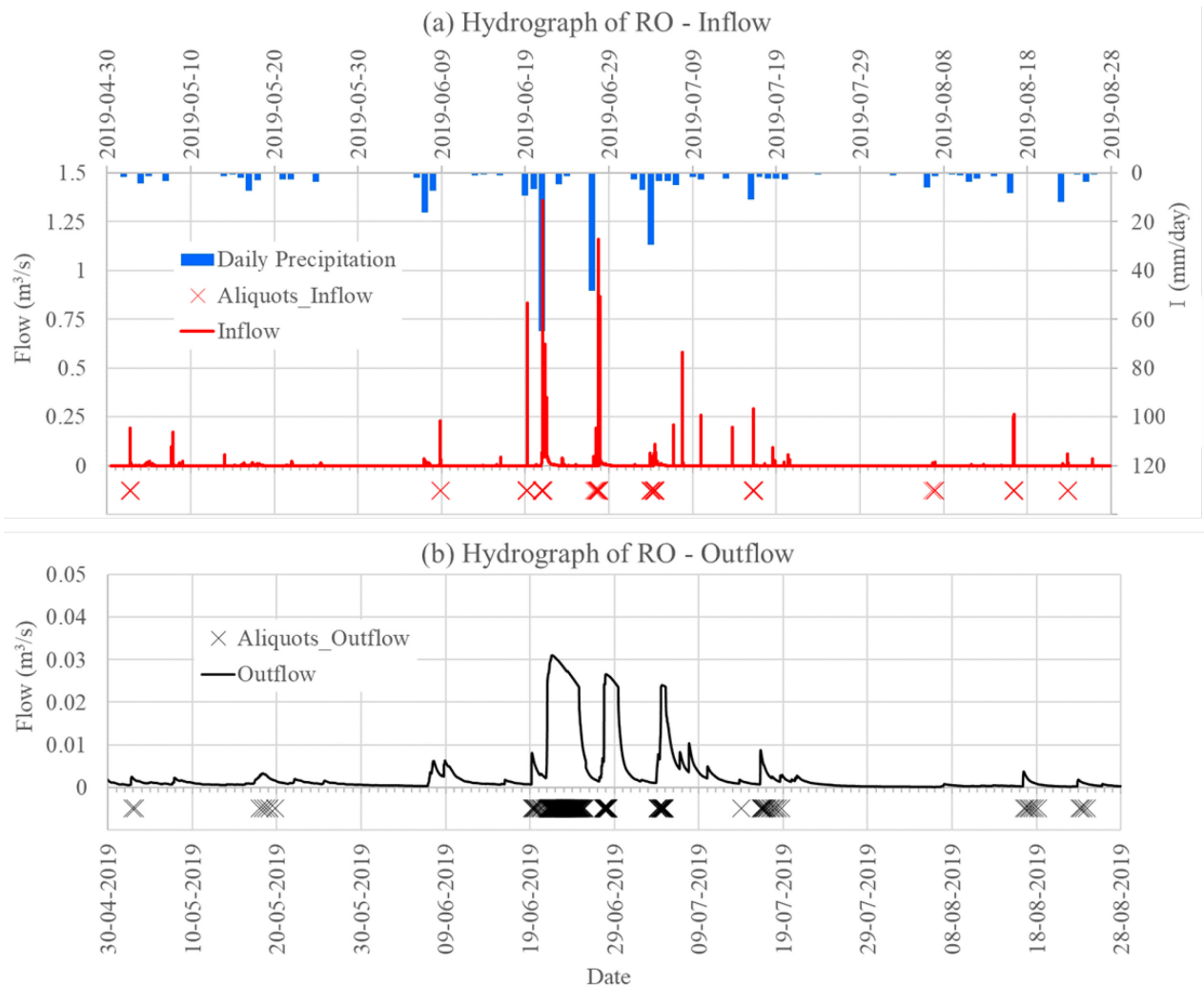


Figure 6-3 Time series measured in the RO wetland showing the measured (a) inflow rate (left axis) and the rainfall depth (I, right axis), (b) outflow rate. Crosses in (a) and (b) indicate the timing of the successfully collected aliquots.

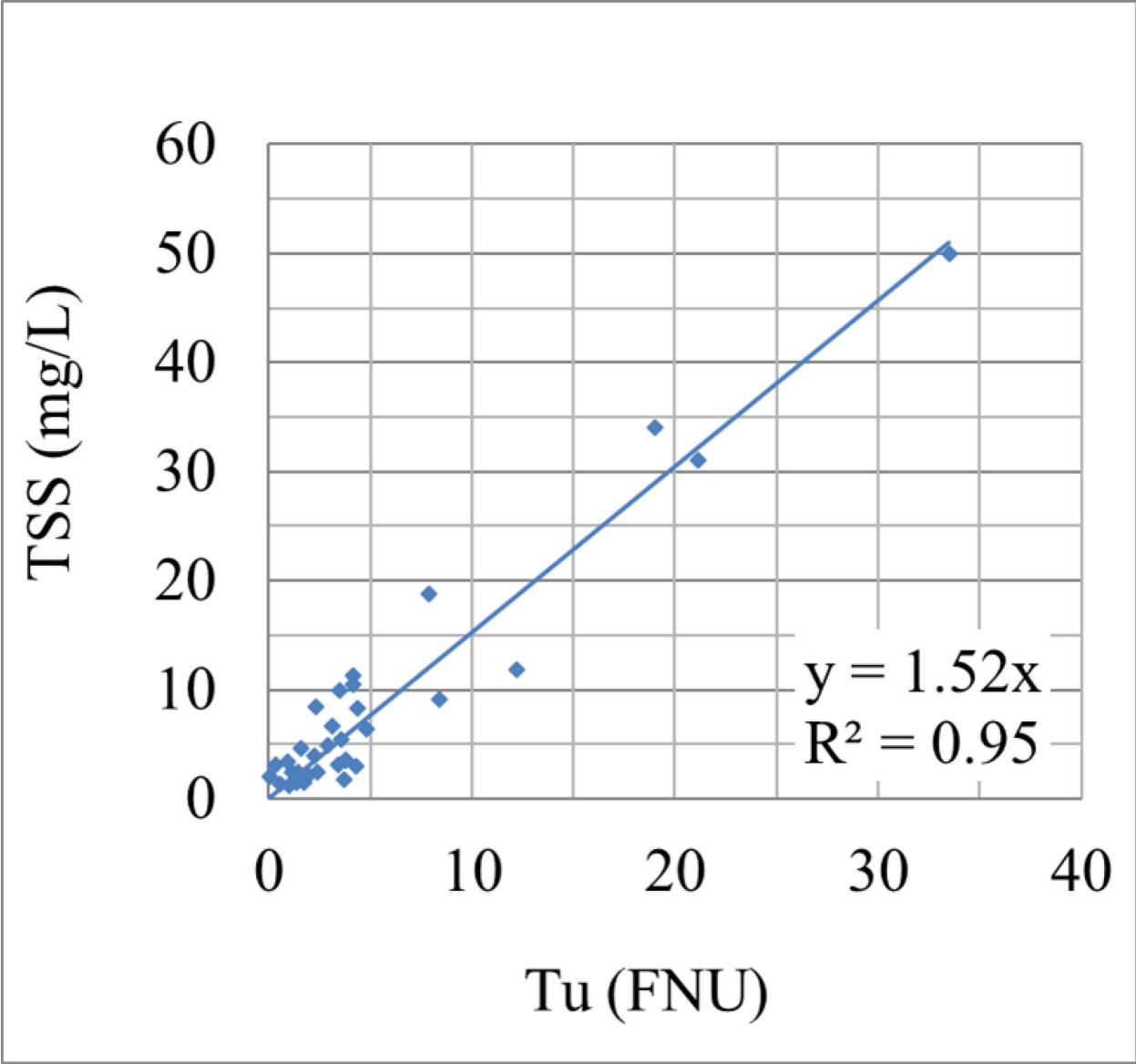


Figure 6-4 Linear correlation between TSS in (mg/L) and Turbidity level in (FNU) from water samples collected in the RO wetland.

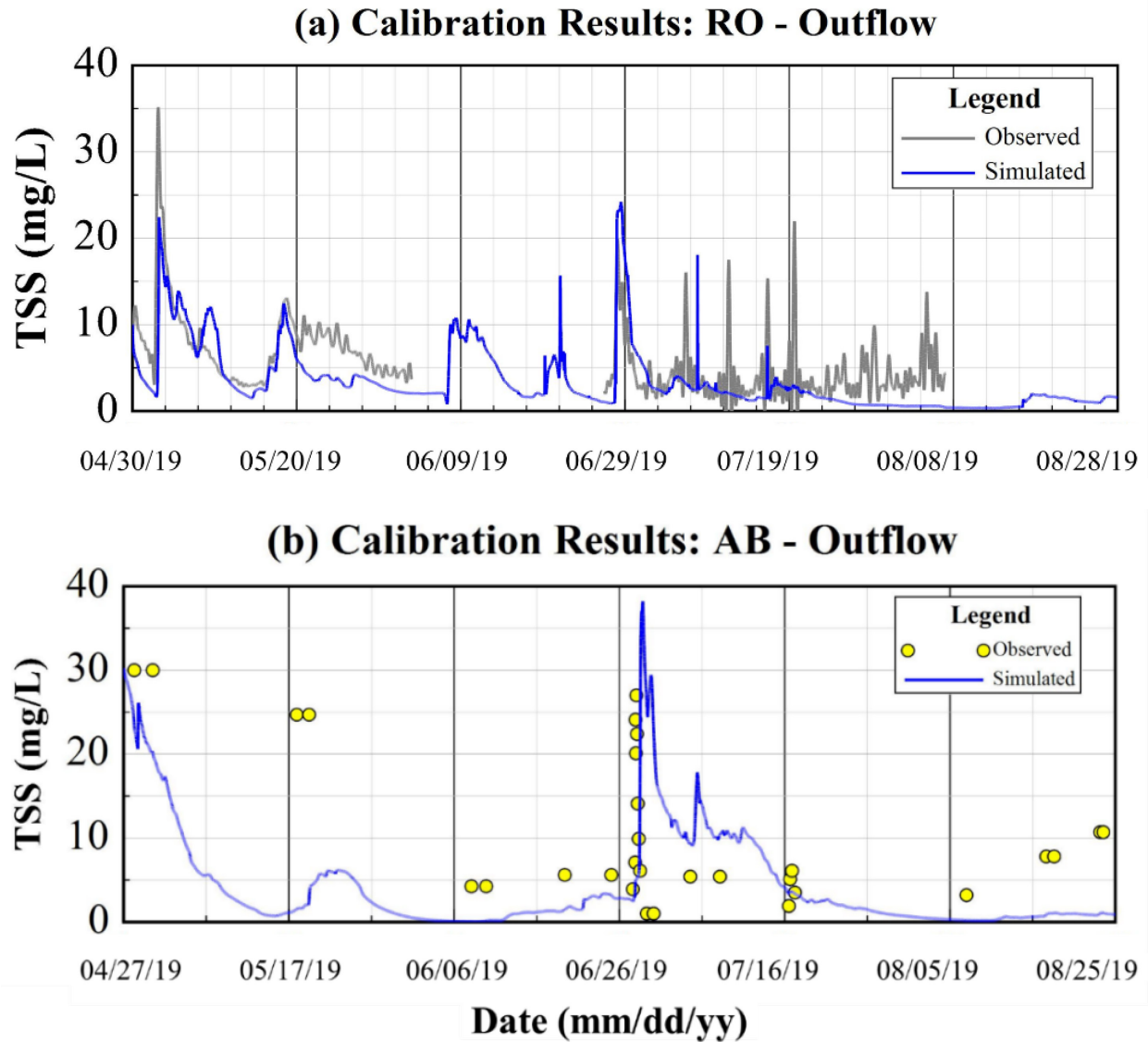


Figure 6-5 Comparison of the simulated and measured outflow’s TSS concentration in the (a) RO wetland and (b) AB wet pond.

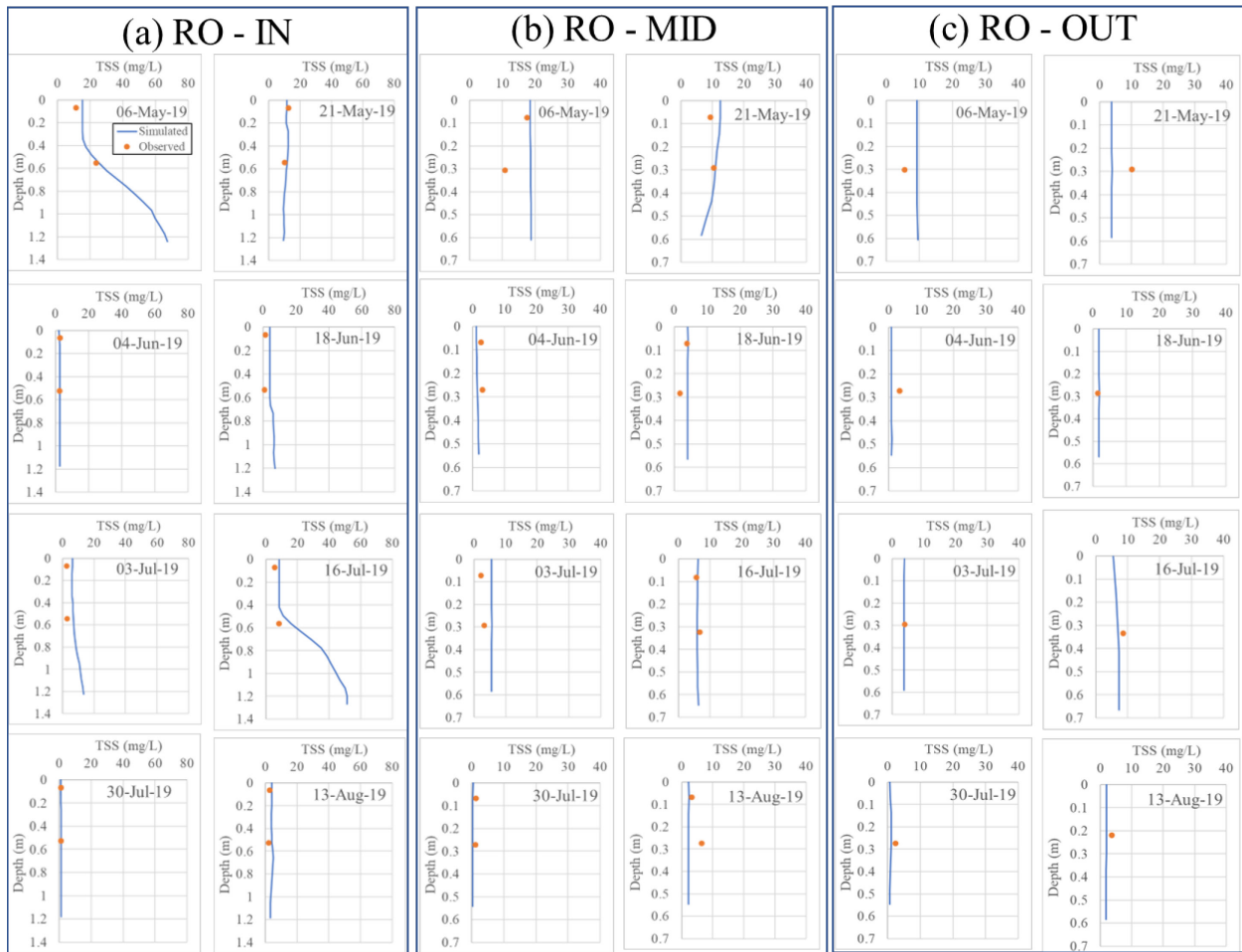


Figure 6-6 Comparison of the model-predicted and measured water column TSS concentration in the RO wetland at locations (a) IN, (b) MID and (c) OUT. Locations are shown in Figure 5-1b.

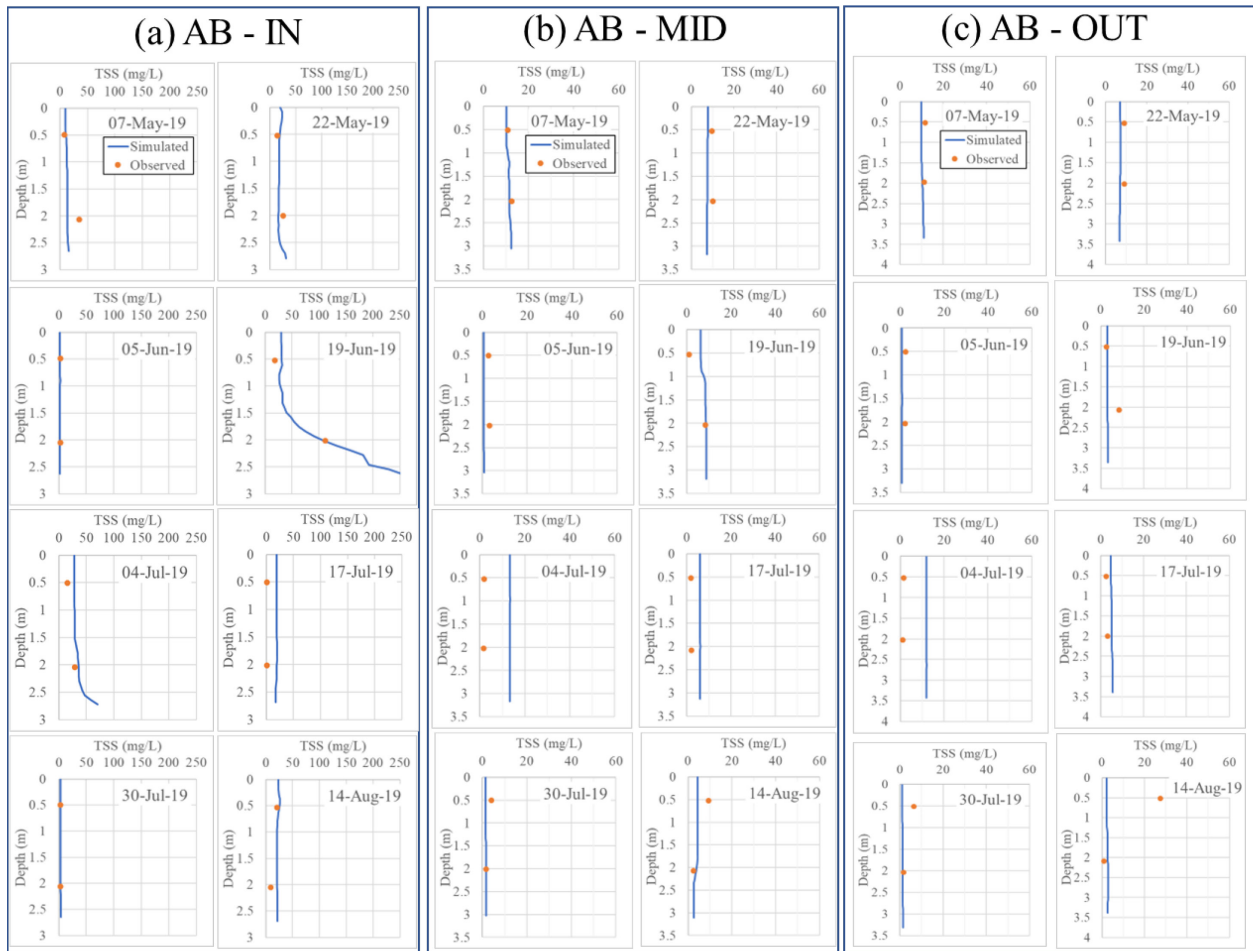


Figure 6-7 Comparison of the model-predicted and measured water column TSS concentration in the AB wet pond at locations (a) IN, (b) MID and (c) OUT. Locations are shown in Figure 5-1a.

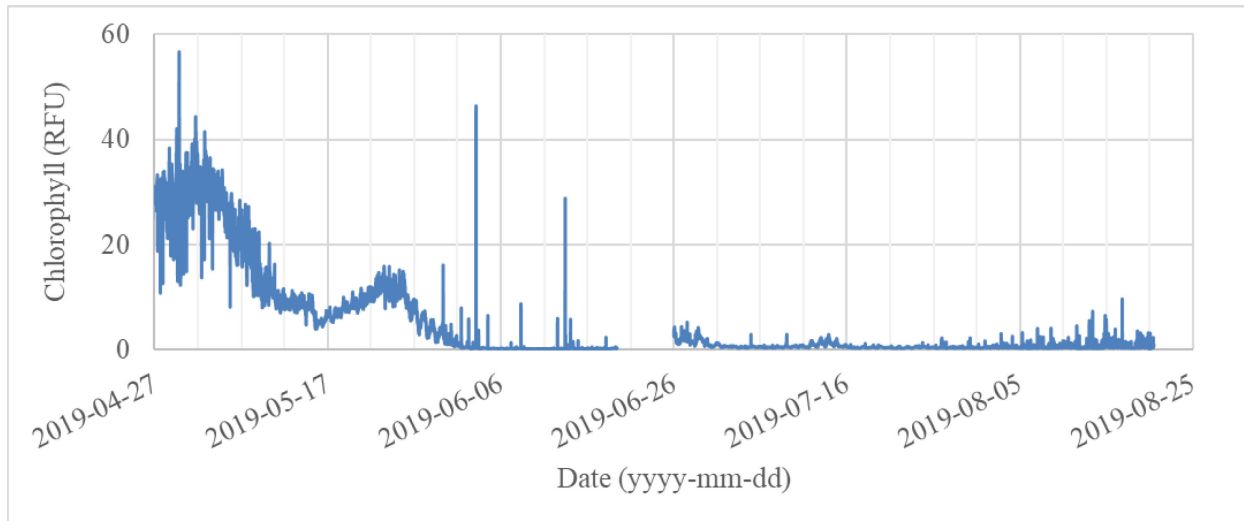


Figure 6-8 Time series of the measured chlorophyll-a concentration in (RFU) at mid-depth of location "OUT" in the AB wet pond. Location OUT in AB is shown in Figure 5-1a.



Figure 6-9 Pictures from the AB wet pond were taken on August 14, 2019.

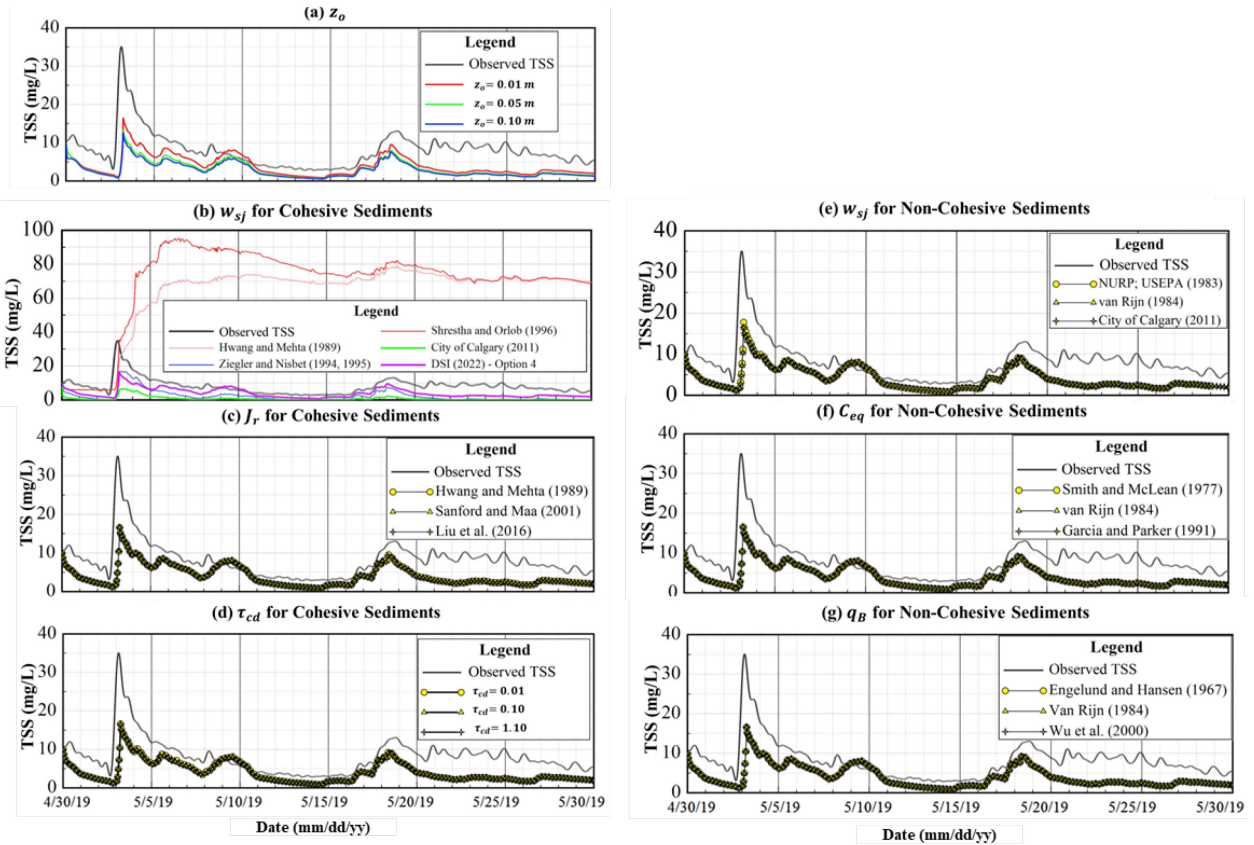


Figure 6-10 Model sensitivity results for different parameters in the RO wetland.

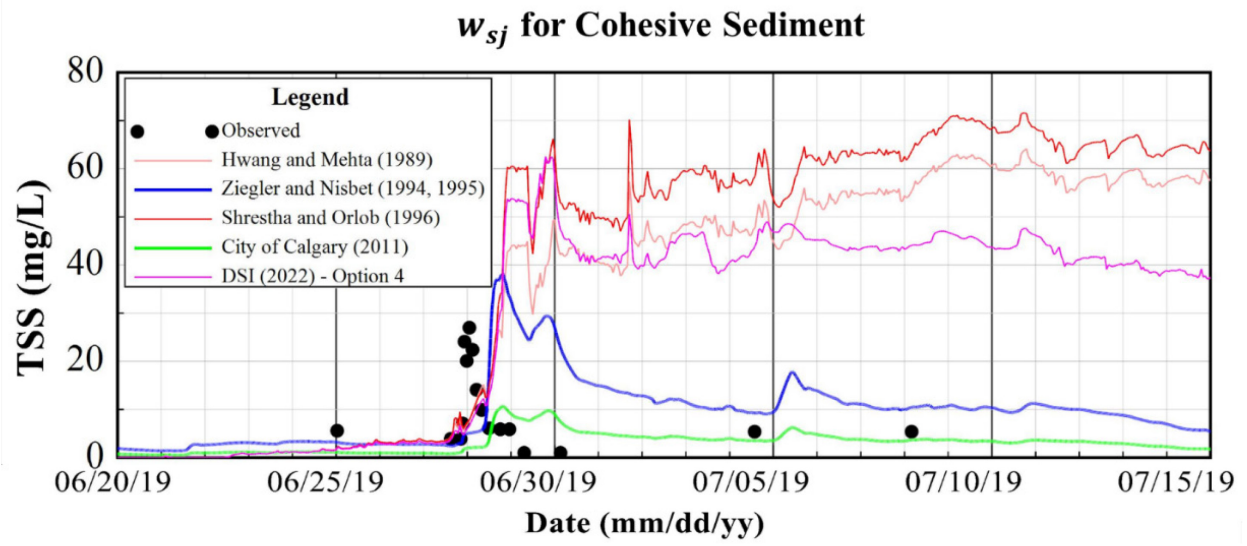


Figure 6-11 Model sensitivity results for different runs of the settling velocity of the cohesive sediment in AB.

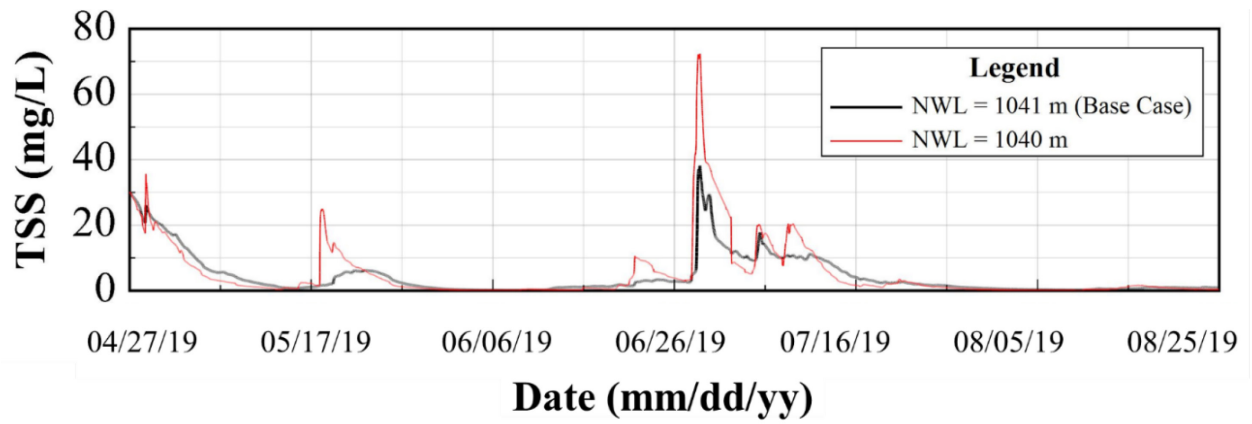


Figure 6-12 Comparison of the model-predicted outflow's TSS concentration in the AB wet pond between the base scenario and lowered NWL scenario.

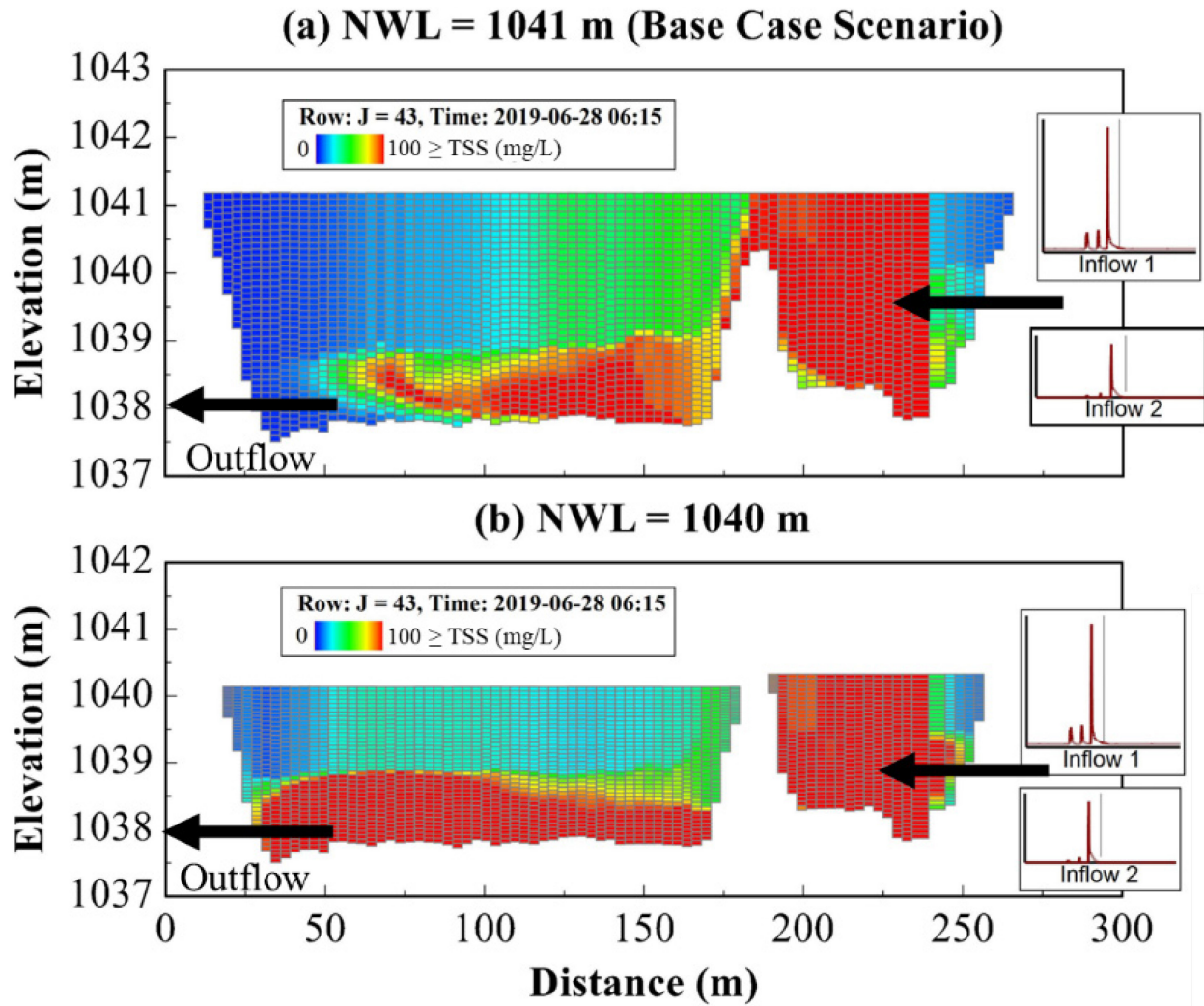


Figure 6-13 Comparison of the model-predicted TSS concentration using longitudinal sections from the inlet to the outlet in the AB wet pond on June 28 following the significant inflow event on June 27 during two scenarios of the operational NWL: (a) the base case scenario of NWL at 1041m and (b) the lowered NWL scenario at 1040m.

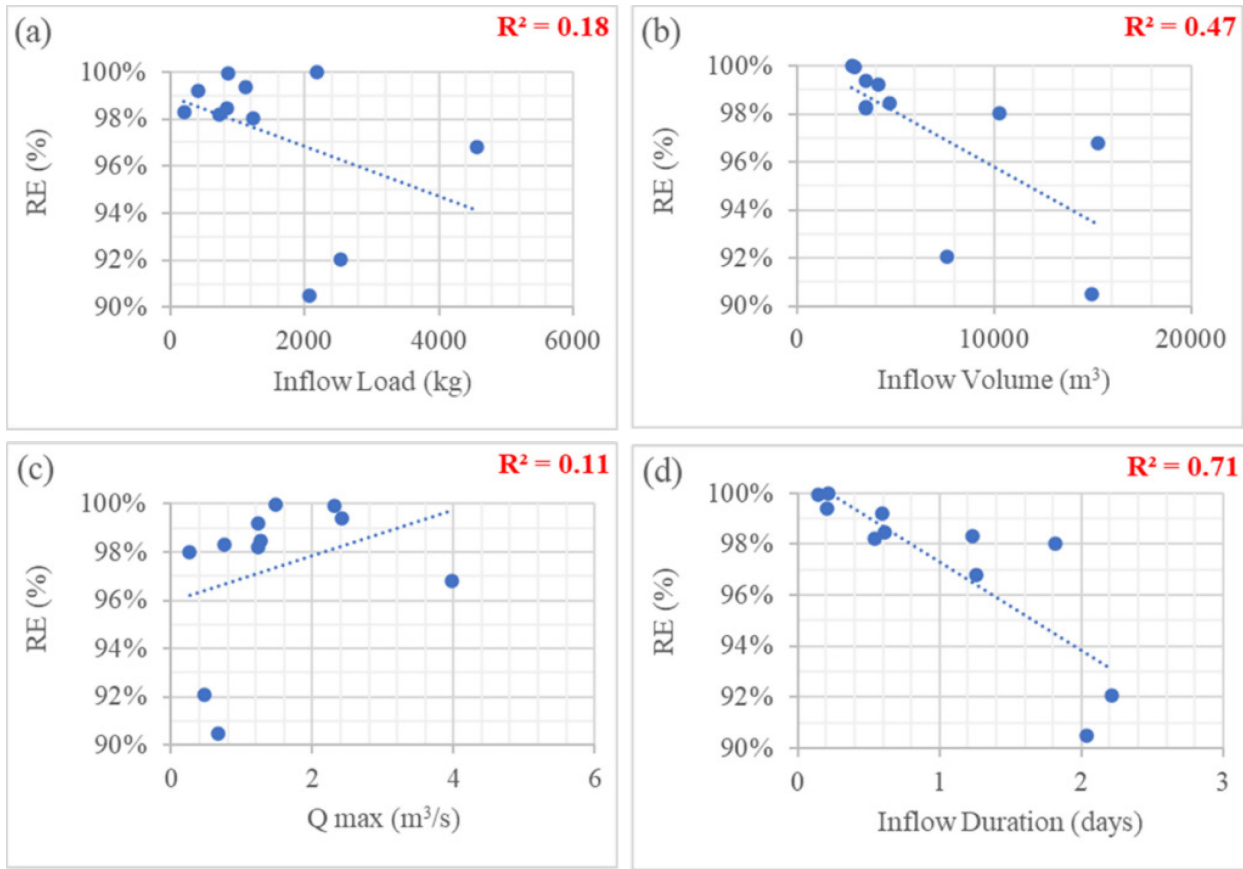


Figure 6-14 Linear correlation between the TSS removal efficiency and inflow characteristics in the AB wet pond.

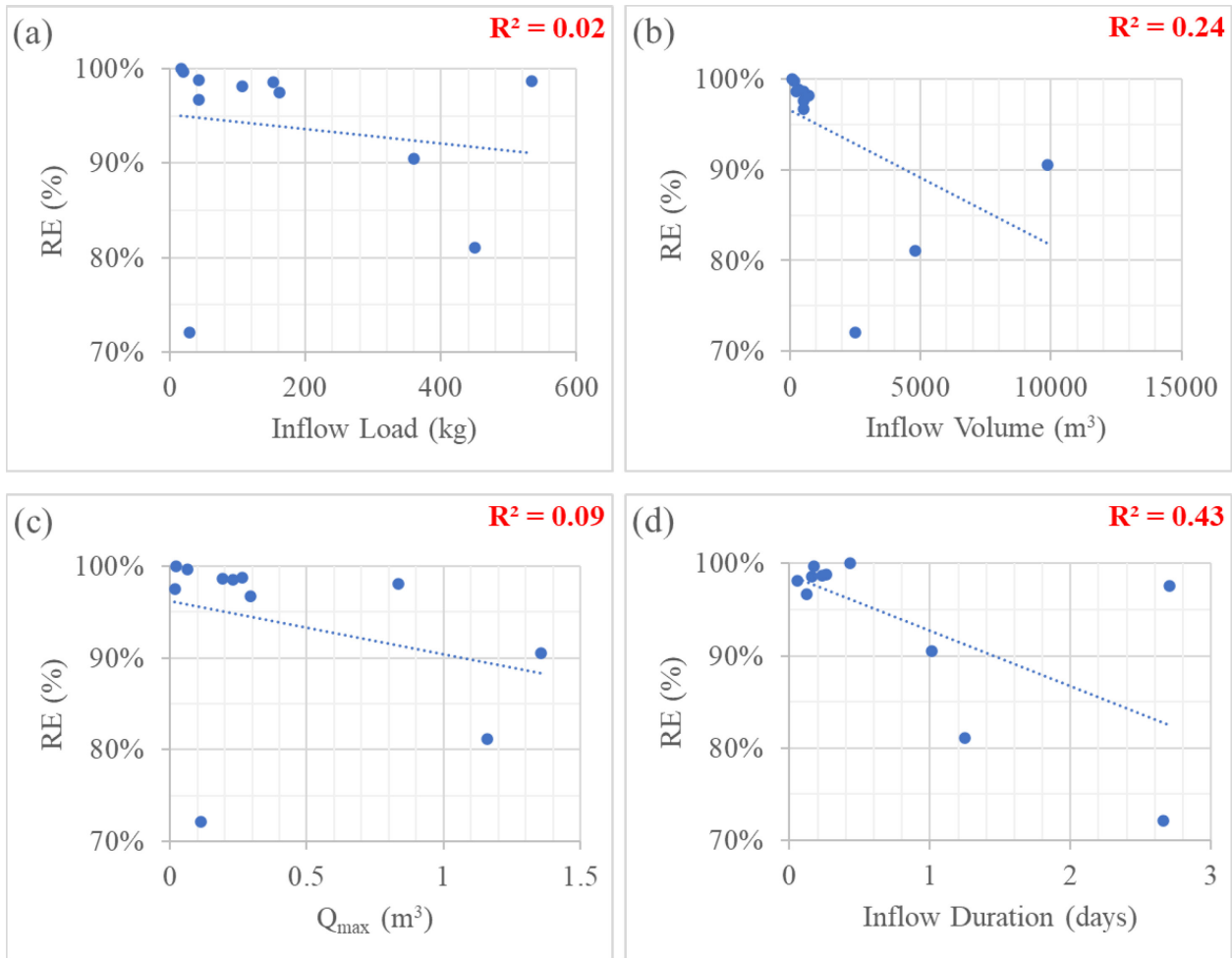


Figure 6-15 Linear correlation between the TSS removal efficiency and inflow characteristics in the RO wetland.

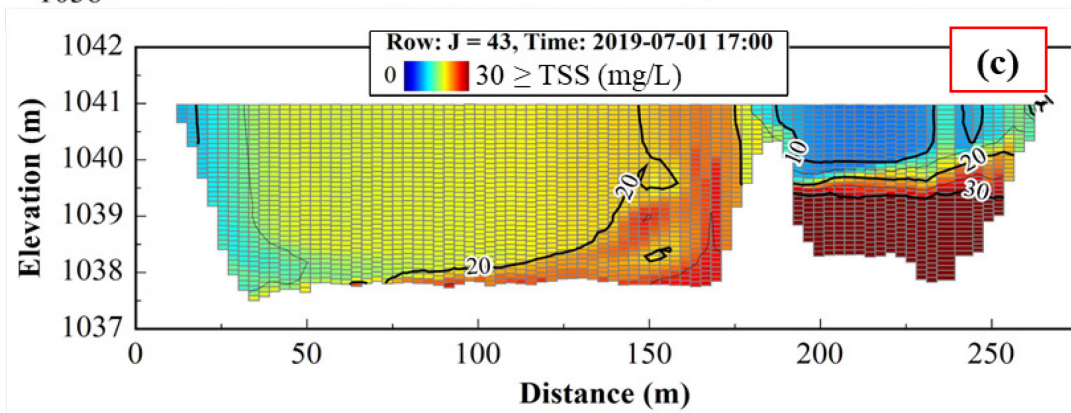
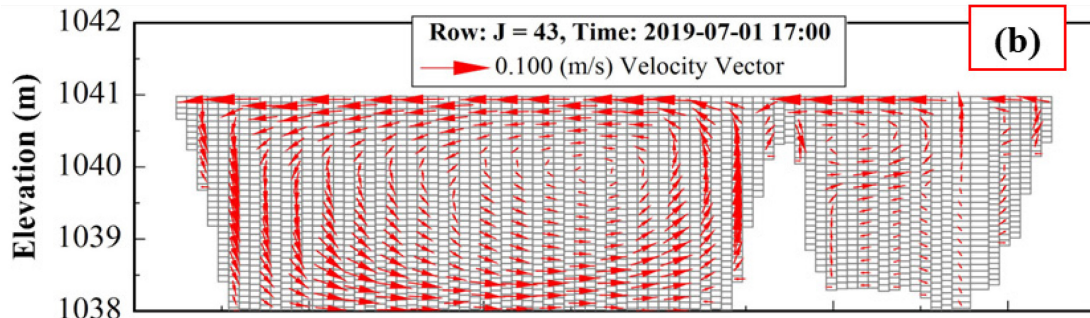
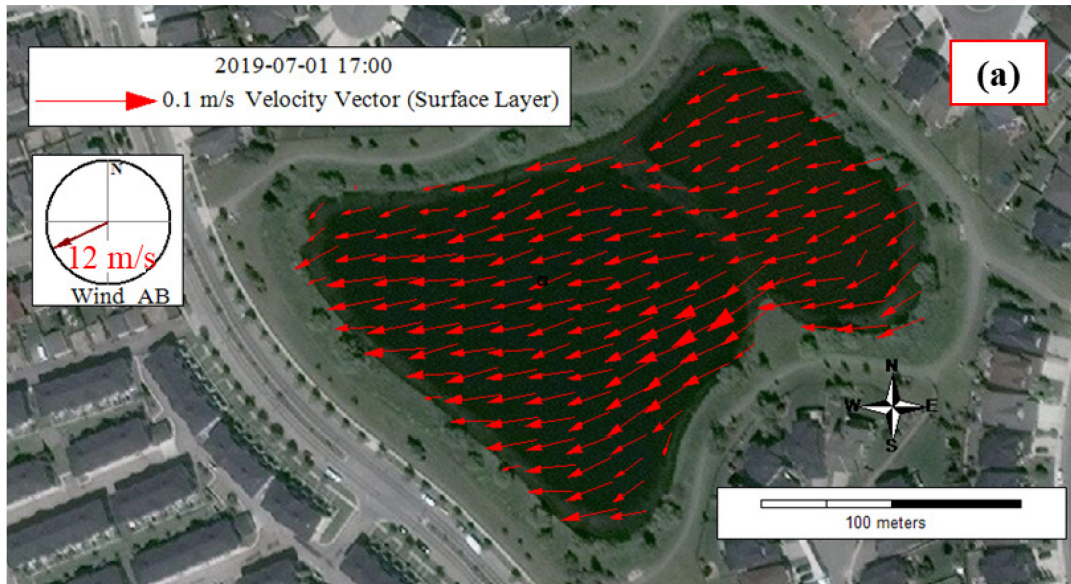


Figure 6-16 Modelling results during the highest observed wind speed in the AB wet pond on July 1, showing (a) a plan view for the surface velocity vector, (b) a longitudinal section from the inlet to the outlet for the velocity vector, and (c) a longitudinal section from the inlet to the outlet for the TSS concentration.

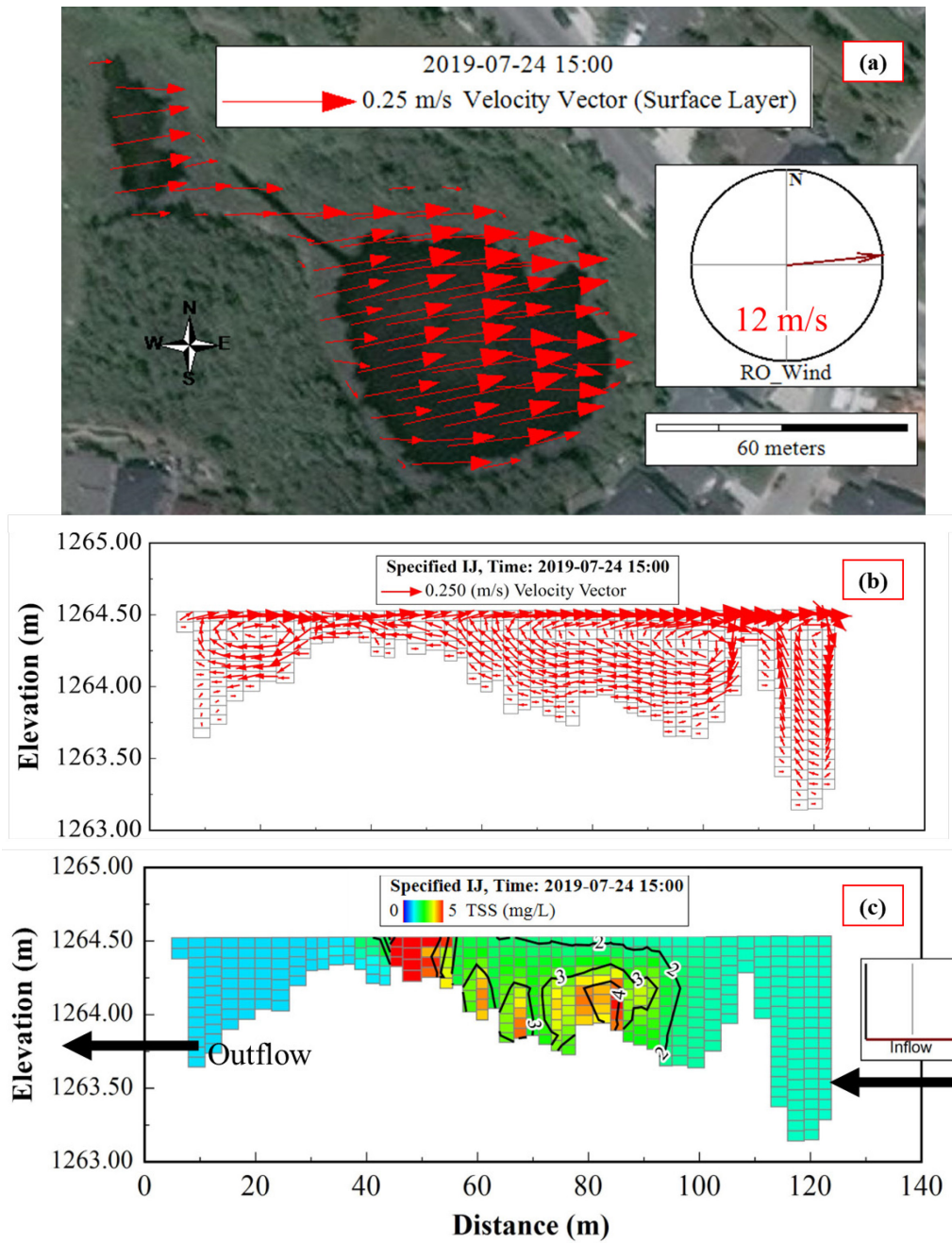


Figure 6-17 Modelling results during a significant wind event in the RO wetland on July 24, showing (a) a plan view for the surface velocity vector, (b) a longitudinal section from the inlet to the outlet for the vertical velocity vector, and (c) a longitudinal section from the inlet to the outlet for the TSS concentration.

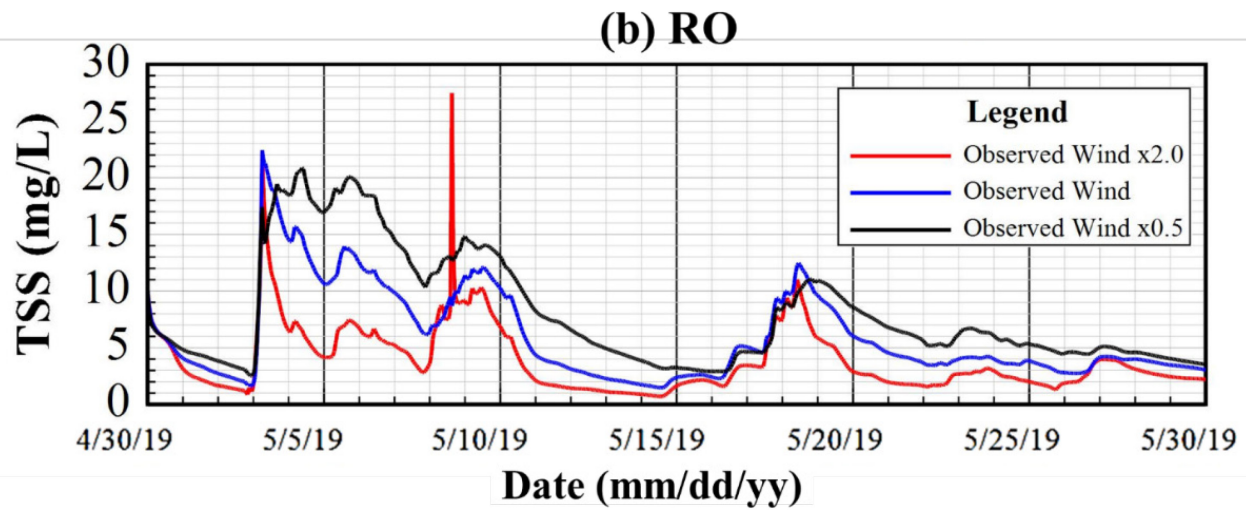
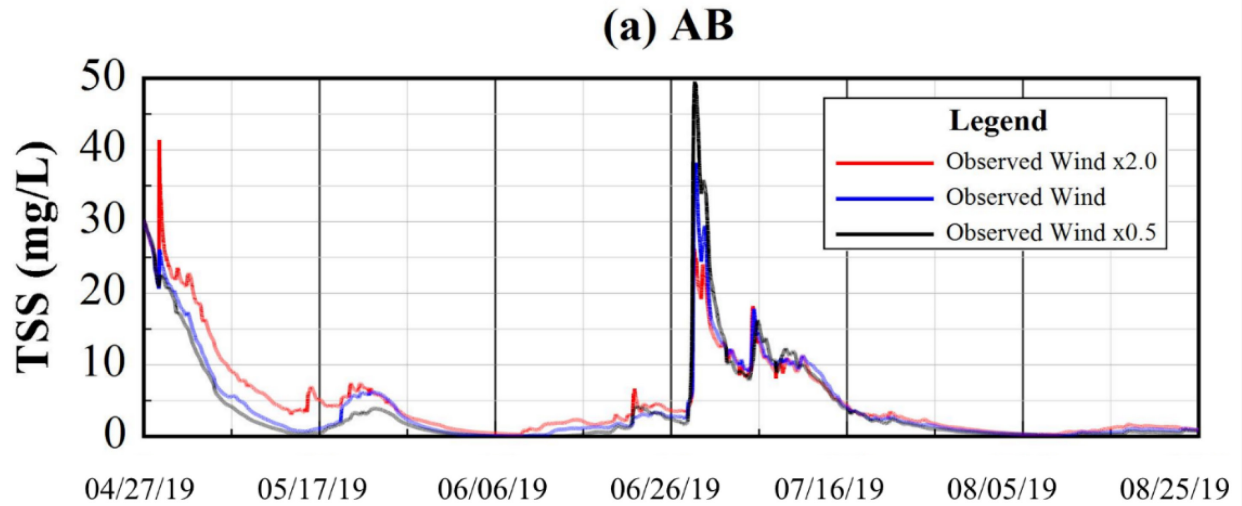


Figure 6-18 Comparison of the model-predicted outflow's TSS concentration under three wind speed scenarios: the observed wind speed, double and half the observed wind speed in the (a) AB wet pond and (b) RO wetland.

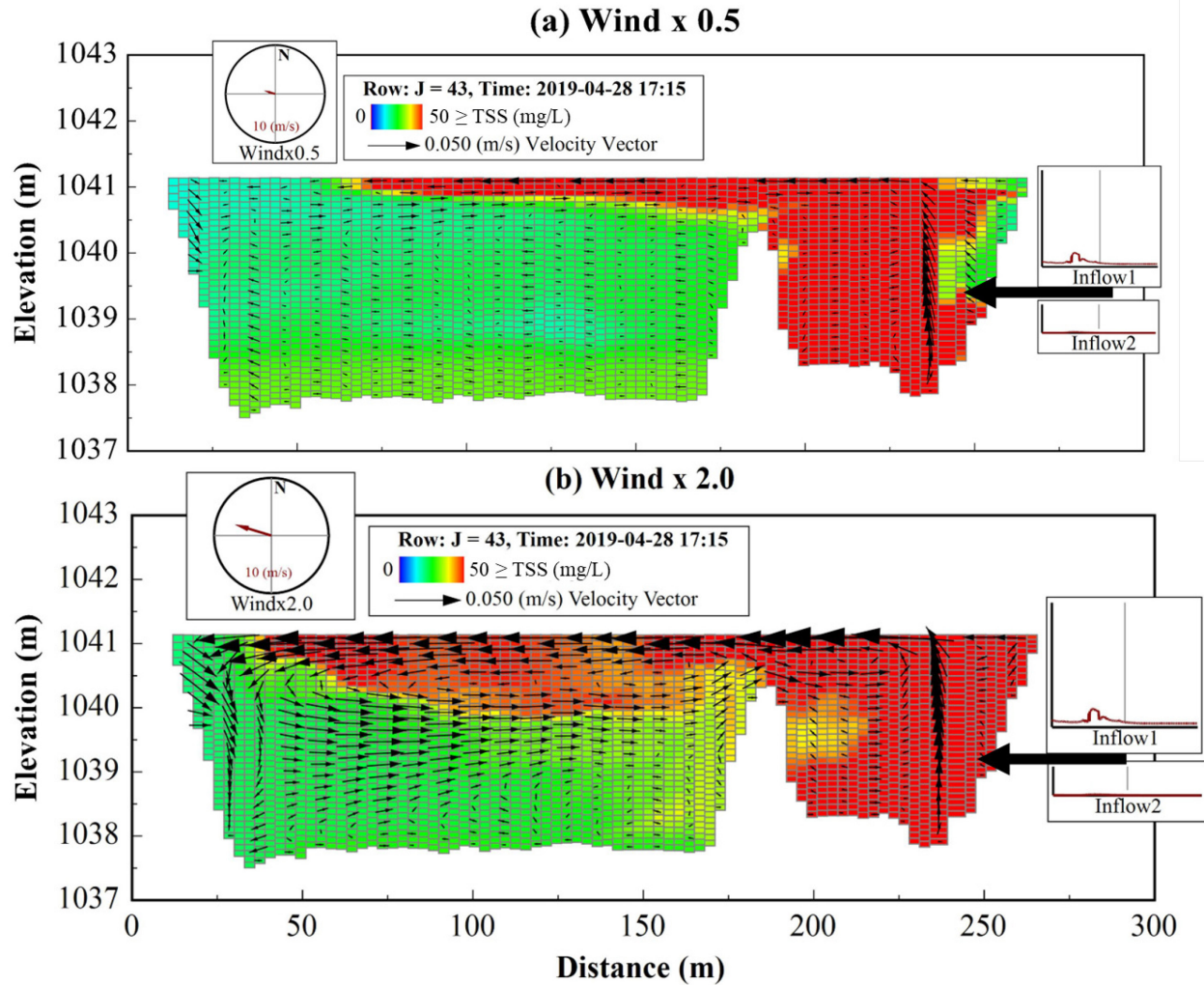


Figure 6-19 Modelling results in the AB wet pond on April 28 show longitudinal sections from the inlet to the outlet for the TSS concentration and velocity vector during the scenarios of (a) half the observed wind speed and (b) double the observed wind speed.

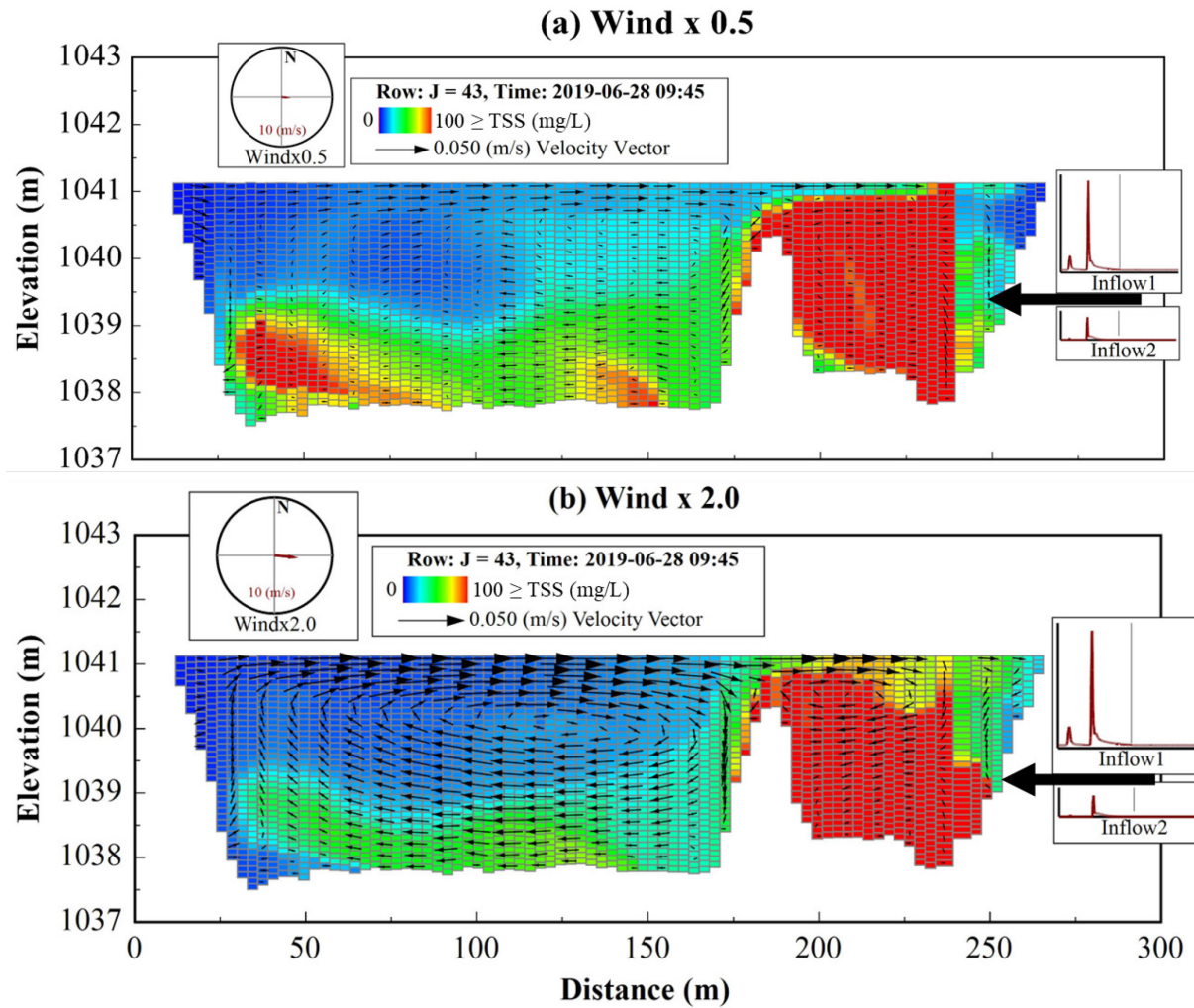


Figure 6-20 Modelling results in the AB wet pond on June 28 show longitudinal sections from the inlet to the outlet for the TSS concentration and velocity vector during the scenarios of (a) half the observed wind speed and (b) double the observed wind speed.

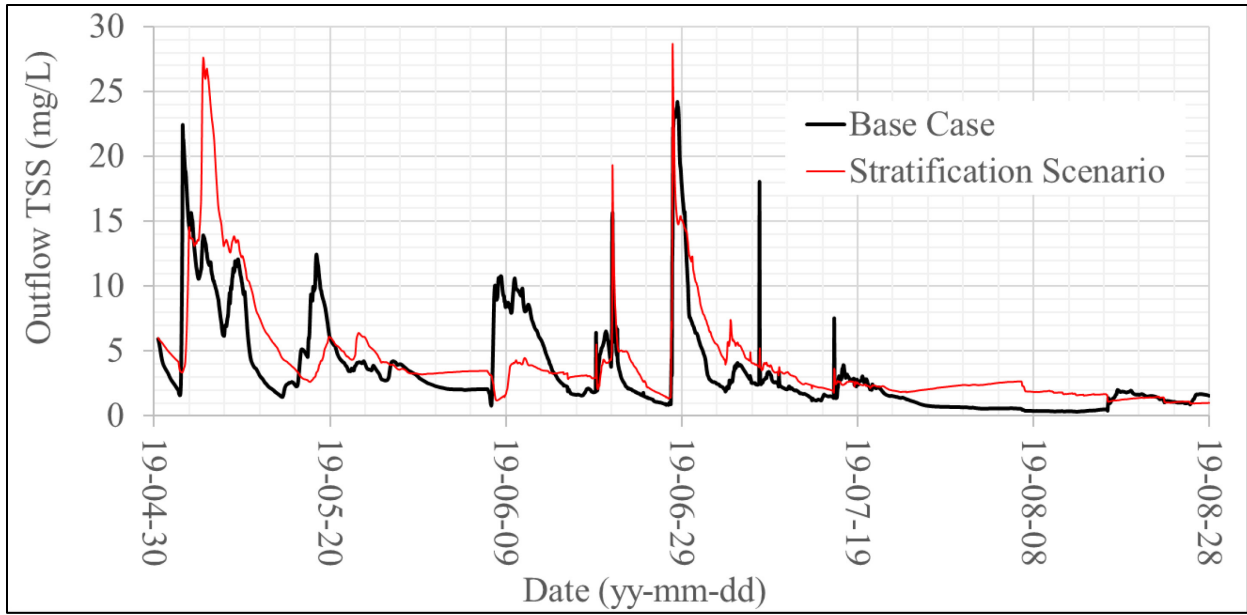


Figure 6-21 Comparison of the model-predicted outflow's TSS concentration in the RO wetland between the base scenario and stratification scenarios.

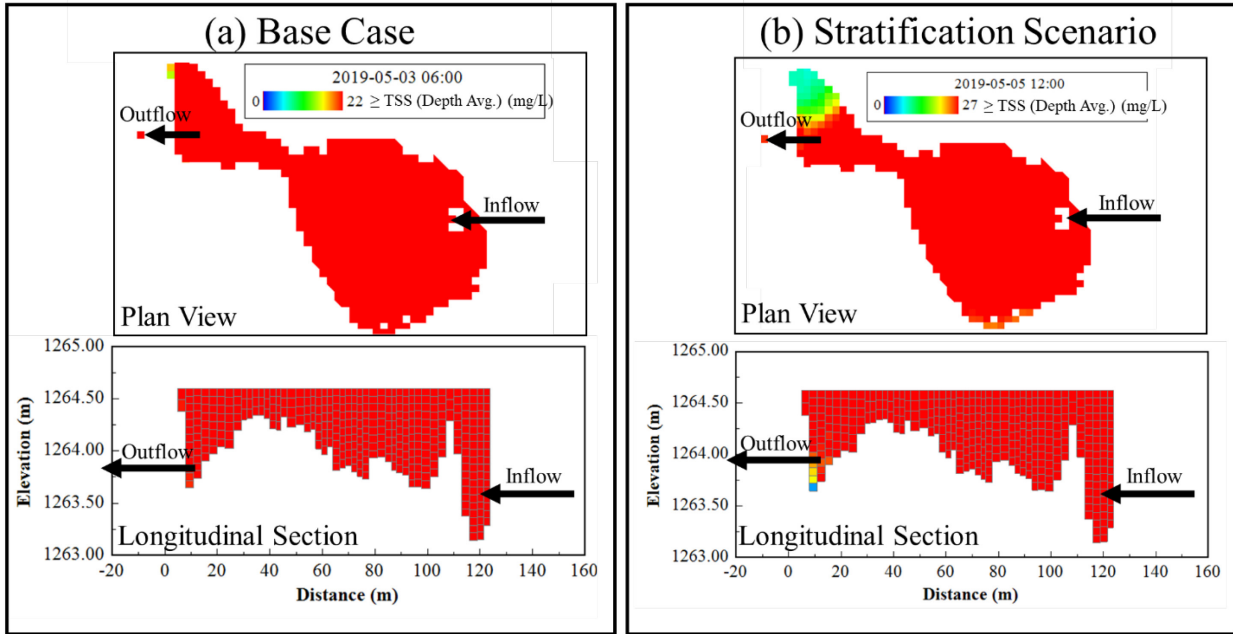


Figure 6-22 Modelling results in the RO wetland during the peak outflow concentration following the April 27 inflow event, showing plan views for the depth average TSS concentration and longitudinal section from the inlet to the outlet for the TSS concentration for (a) the base case scenario, and (b) the stratification scenario.

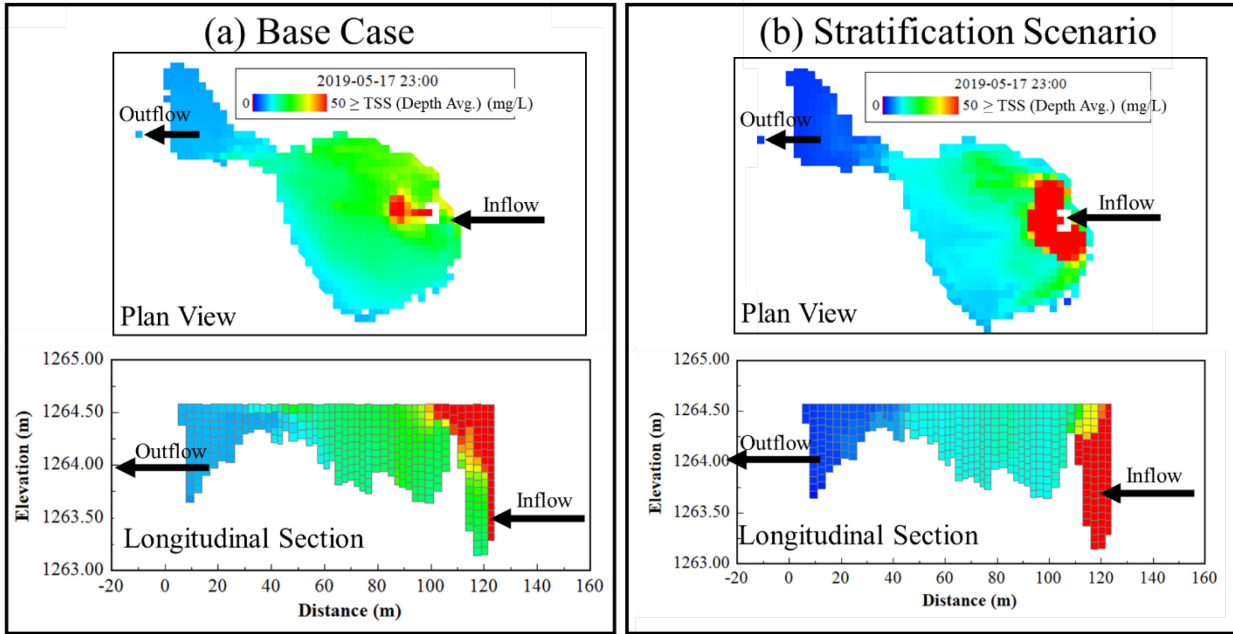


Figure 6-23 Modelling results in the RO wetland during the peak outflow concentration following the May 16 inflow event, showing plan views for the depth average TSS concentration and longitudinal section from the inlet to the outlet for the TSS concentration for (a) the base case scenario, and (b) the stratification scenario.

7. Conclusions and recommendations

7.1 Conclusions

In this thesis, a comprehensive 2-year field monitoring program was undertaken in two urban stormwater wet ponds and two constructed urban stormwater wetlands in Calgary, Alberta, Canada, during the ice-free seasons from May to October in 2018 and 2019: (1) the field data were used to investigate thermal, chemical and densimetric stratifications, thermocline depth and strength, and hydrodynamics as well as the interaction between stratification and hydrodynamics in the two stormwater wet ponds as fundamental physical processes that may significantly impact their water quality; (2) stratification and hydrodynamics were also investigated in the two constructed urban stormwater wetlands with different inlet, outlet, morphometric and vegetation designs and the potential adverse effect of stratification on water quality were identified; (3) then the field data supported the application of the Environmental Fluid Dynamics Coding (EFDC) hydrodynamic model to simulate the hydrodynamic and physical processes in one stormwater wet pond and one constructed wetland to evaluate their hydraulic performance and investigate key factors affecting their hydraulic behavior; (4) Finally, the sediment transport compartment of the EFDC model was applied to the validated hydrodynamic models to simulate the sediment dynamics in the stormwater wet pond and the constructed wetland to predict the annual mass of deposits and sediment removal efficiency, and to evaluate the current design and operation guidelines as a function of the key considerations, inflow, wind stratification, and vegetation design. Some general conclusions from the field and modelling investigations that were limited to the local weather of Calgary, Alberta, Canada, during the ice-free seasons between May and October are listed below:

- 1) Stormwater wet ponds experienced strong and prolonged thermal and chemical stratifications when the bed-surface density difference of $\Delta\rho > 0.25 \text{ kg/m}^3$ (equivalent to the density change in freshwater between 24 and 25 °C) occurred for up to 96% of the time May-September, negatively affecting their performance. In particular, the vertical thermal and chemical structure forced the runoff from the inlet to the outlet to move above or below the thermocline at times, creating dead zones. In addition, the densimetric stratification inhibited vertical mixing due to wind, causing the water at depth to become anoxic (DO concentration $< 1 \text{ mg/L}$) for up to 88 % of the time between May and mid-September. Potential consequences of the observed stratification include decreased pollutant retention capacity, discharge of poorer quality water downstream and increased stress on aquatic communities. As a result, it is recommended to lower the design depth from 3 to 2 m to be shallow enough to avoid persistent stratification and deeper than the photic zone to prevent aquatic growth and eutrophication.
- 2) In contrast to the assumption of urban wetlands being well-mixed ecosystems, thermal stratification in the two shallow wetlands, 0.8 m deep, persisted for up to two-thirds of the ice-free season between May and October. In addition, the mechanical interference by the dense aquatic vegetation and the local landscaping caused insignificant wind-induced surface currents, scaling at 0.3% of the wind speed, seven times lower than the ~2% value often occurring in the ocean, causing a negligible impact on vertical mixing. Stratification resulted in the water at depth becoming hypoxic at $\text{DO} < 2\text{-}3 \text{ mg/L}$ for extended periods in both wetlands, violating specific requirements of DO concentration for the receiving waters. Potential adverse effects of anoxic conditions on water quality include the remobilization of the metals and nutrients in the bed sediment and the generation of

toxicants. As a result, additional consideration of stratification may be required when designing newly constructed urban wetlands. For instance, the wetland with double the length-to-width ratio, separated outlet basin from the main cell and half the water volume and surface area was efficiently shaded by the riparian vegetation and trees, reducing its thermal stratification by up to 8 times.

- 3) The hydrodynamic simulations of the EFDC model are one of the most accurate attempts in the literature to model water level, temperature, salinity and velocity. The calibrated hydrodynamic models revealed that the water currents were most sensitive to the background horizontal eddy viscosity, the temperatures were most sensitive to the turbulent heat exchange coefficients generally due to the low wind conditions, and that light extinction needed to be spatially varied in the model domain due to the highly variable turbidity. The normalized water depth rise during inflow events to the permanent pool depth was one of the main drivers of mixing in the study pond and wetland. The hydraulic performance of the shallow 0.8 m wetland was more obviously sensitive to the wind speed than the 3.0 m deep wet ponds when it was significantly mixed by double the observed wind speed resulting in a 33% reduction in the hydraulic residence time versus $\leq 1\%$ in the wet pond.
- 4) The sensitivity analysis using the sediment transport compartment of the EFDC model indicates that the settling velocity of the cohesive sediment is the most critical parameter influencing the outflow's suspended sediment concentration. The model could predict resuspension, sediment transport, and overall removal efficiency with reasonable accuracy in the constructed wetland. Yet it underestimated the outflow's TSS concentration in the deeper wet pond when significant internal loading of algal biomass due to eutrophication

was evident during the field study but was not modelled. In addition, the model significantly underestimated the outflow load of the non-cohesive sediment $> 50 \mu\text{m}$ at both the wet pond and the wetland. The models revealed that the sediment removal efficiency is not linearly correlated with the inflow rate between 0.02 and $3.98 \text{ m}^3/\text{s}$, likely due to the energy dissipation of the submerged berms that separated the sediment forebay from the main cell. Yet inflow duration was negatively correlated to the TSS removal efficiency at R^2 up to 0.71 as turbulent mixing by inflow kept suspended sediment longer in the water column. The deeper 3.0m depth of the stormwater pond dissipated the inflow momentum and slowed the suspended sediment transport allowing for more settling compared to a 2.0 depth scenario. Double the observed wind speeds resulted in short-circuiting from the inlet to the outlet at times. Yet, it did not change the overall removal efficiency in the 3.0 m deep wet pond. However, mixing by the double observed wind speed scenario was significant in the 0.8 m deep wetland, reducing the outflow concentration by half and increasing sediment removal efficiency by 2% .

7.2 Recommendations

This research covers the physical processes and sediment transport in two stormwater wet ponds and two constructed wetlands in Calgary, Canada. However, some aspects still exist for further studies. Some recommendations for further studies are listed below:

- 1) The sediment transport modelling in the wet ponds can be further improved through coupled hydrodynamic, sediment transport and biogeochemical models. This might enhance the predicted outflow's TSS concentration when eutrophication and the internal loading of algal biomass are accurately simulated. In addition, adding the biogeochemical compartment to the

wetland's hydrodynamic and sediment transport modules might better investigate the role of the aquatic vegetation in altering water quality processes like filtration or the internal generation of suspended matter and biomass.

- 2) The particle size distribution for the water samples collected at both sites showed a higher percentage of non-cohesive sediment above 50 μm at the outflow than the inflow. Hence, a sediment survey at the outlet structures and storm sewers is needed to explore the source of the outflow's non-cohesive sediment that the current models could not predict. The accurate prediction of the outflow's non-cohesive sediment is important as the City of Calgary has mandated the removal of a minimum of 85% of the TSS for particle sizes $\geq 50 \mu\text{m}$.
- 3) The optimal design, operation and management of stormwater wet ponds and constructed wetlands have not yet been determined due to the lack of adequately monitored sites. As a result, the modelling framework from the current research can be used for extended ponds and wetlands studies by simulating numerous remediation design and operation options to discover the optimum design and operation guidelines.
- 4) Considering a full-year study including the role of winter, early spring and late fall flow, pond storage, sediment, and salinity loading would be next to consider to enhance the understanding of the role of urban stormwater ponds in water quantity and quality during non-growing season dynamics in Calgary.

Bibliography

- Aalderink, R.H., Lijklema, L., Breukelman, J., et al. (1985). Quantification of Wind Induced Resuspension in a Shallow Lake. *Water Sci Technol*, **17**(6-7): 903-914.
<https://doi.org/10.2166/wst.1985.0189>
- Abis, KL, & Mara, D. (2006). Temperature Measurement and Stratification in Facultative waste Stabilisation Ponds in the UK Climate. *Environ Monit Assess*, **114**(1-3): 35-47.
<https://doi.org/10.1007/s10661-006-1076-7>
- Alberta Environment (2007). Information Synthesis and Initial Assessment of the Status and Health of Aquatic Ecosystems in Alberta: Surface Water Quality, Sediment Quality and Non-Fish Biota. Technical Report # 278/279-01, <https://open.alberta.ca/dataset/a78a1f12-b471-4ab9-8e16-2102472151d7/resource/500ee1cc-1a64-4e2b-b195-4598fc48704a/download/7861.pdf> (accessed November 20, 2022).
- Alberta Environment. (1999). Surface water quality guidelines for use in Alberta. Alberta: Science and Standards Branch, Alberta Environment.
<https://open.alberta.ca/dataset/e0074537-88f6-4cc4-af5c-808161fa9af8/resource/ea13d7b1-c155-4fad-8b85-4f12443352f2/download/5713.pdf>
- Alberta Environment. (2001). Municipal policies and procedures manual. Province of Alberta, Edmonton, Alta: Alberta Environment, <https://open.alberta.ca/dataset/add022a6-33de-414f-a246-f4f2d4fb78f0/resource/84bb9f12-0de0-4295-95c1-9c73ab3a7b5c/download/2001-municipalpoliciesproceduresmanual-2001.pdf> (accessed November 20, 2022).
- Anagnostou, E., Gianni, A., & Zacharias, I. (2017). Ecological Modeling and Eutrophication— a Review. *Nat. Resour. Model.*, **30**(3), <https://doi.org/10.1111/nrm.12130>
- Andradóttir, H.Ó., & Mortamet, M.L. (2016). Impact of wind on storm water pond particulate removal. *J. Environ. Eng*, **143**(8). [https://doi.org/10.1061/\(ASCE\)EE.1943-7870.0001221](https://doi.org/10.1061/(ASCE)EE.1943-7870.0001221)
- APHA (1989). Standard Methods for the Examination of Water and Wastewater. 17th, American Public Health Association, Washington DC, 164.
- Arhonditsis, G.B. & Brett, M.T. (2004). Evaluation of the current state of mechanistic aquatic biogeochemical modeling. *Mar. Ecol. Progr. Series*, **271**:13-26,
<https://www.jstor.org/stable/24867420>
- Arifin, R.R., James, S.C., de Alwis Pitts, D.A., et al. (2016). Simulating the thermal behavior in Lake Ontario using EFDC. *Journal of Great Lakes Research*, **42**(3):511-523,
<https://doi.org/10.1016/j.jglr.2016.03.011>

- Aryal, R.K., & Lee, B.K. (2009). Characteristics of suspended solids and micropollutants in first flush highway runoff. *Water, Air and Soil Pollution: Focus*, **9**(5-6):339-346.
<https://doi.org/10.1007/s11267-009-9243-9>
- Bash, J., Berman, C., & Bolton, S. (2001). Effects of turbidity and suspended solids on salmonids. Washington State Transportation Center (TRAC) Report No. WA-RD 526.1, Olympia, WA, 92 pp
- Beletsky, D., Schwab, D.J., & McCormick, M. (2006). Modelling the 1998–2003 summer circulation and thermal structure in Lake Michigan. *J. Geophys. Res.*, **111**(C10),
<https://doi.org/10.1029/2005JC003222>
- Bentzen, T.R., Larsen, T., & Rasmussen, M. R. (2009). Predictions of Resuspension of Highway Detention Pond Deposits in Interrain Event Periods due to Wind-Induced Currents and Waves. *J. Environ. Eng.*, **135**(12):1286-1293.
[https://doi.org/10.1061/\(ASCE\)EE.1943-7870.0000108](https://doi.org/10.1061/(ASCE)EE.1943-7870.0000108)
- Bentzen, T.R., Larsen, T., & Rasmussen, M.R. (2008). Wind Effects on Retention Time in Highway Ponds. *Water Science and Technology*, **57**(11):1713-1720.
<https://doi.org/doi:10.2166/wst.2008.267>
- Birch, G.F., Matthai, C., & Fazeli, M.S. (2006). Efficiency of a retention/detention basin to remove contaminants from urban stormwater, *Urban Water Journal*, **3**(2): 69-77,
<https://doi.org/10.1080/15730620600855894>
- Bloesch, J. (1994). A review of methods used to measure sediment resuspension. *Hydrobiologia* **284**:13-18, <https://doi.org/10.1007/BF00005728>
- Bodin, H. & Persson, J. (2012). Hydraulic performance of small free water surface constructed wetlands treating sugar factory effluent in western Kenya. *Hydrol.Res.*, **43**(4):476-488,
<https://doi.org/10.2166/nh.2012.133>
- Boegman, L., Loewen, M.R., Hamblin, P.F., et al. (2008). Vertical mixing and weak stratification over zebra mussel colonies in western Lake Erie. *Limnol. Oceanogr.*, **53**(3):1093-1110. <https://doi.org/10.4319/lo.2008.53.3.1093>
- Brown, R. (1984). Relationships between suspended solids, turbidity, light attenuation, and algal productivity. *Lake Reserv Manag*, **1**(1):198-205,
<https://doi.org/10.1080/07438148409354510>
- Burban, P.Y., Lick, W., & Lick, J. (1989). The flocculation of fine-grained sediments in estuarine waters. *J. Geophys. Res. Oceans*, **94**(C6), 8323-8330,
<https://doi.org/10.1029/JC094iC06p08323>

- Burban, P.Y., Xu, Y.J., McNeil, J., et al.(1990). Settling speeds of floes in fresh water and seawater. *J. Geophys. Res. Oceans*, **95**(C10), 18213–18220, <https://doi.org/10.1029/JC095iC10p18213>
- Cappiella K., Fraley-McNeal, L., Novotney, M., et al. (2008). Article 5:The Next Generation of Stormwater Wetlands. Center for Watershed Protection, 2008. Web: http://www.cwp.org/documents/cat_view/73-wetlands-and-watersheds-article-series.html
- Carleton, J.N., Grizzard, T.J., Godrej, AN, et al., (2001). Factors affecting the performance of stormwater treatment wetlands. *Water Research*, **35**:1552-1562. [https://doi.org/10.1016/S0043-1354\(00\)00416-4](https://doi.org/10.1016/S0043-1354(00)00416-4)
- Chalov, S.R., Jarsjo, J., Kasimov, N.S., et al. (2015). Spatio-temporal variation of sediment transport in the Selenga River Basin, Mongolia and Russia. *Environ Earth Sci*, **73**:663-680, <https://doi.org/10.1007/s12665-014-3106-z>
- Chao, X., Jia, Y., Shields Jr., F.D., et al. (2007). Numerical modeling of water quality and sediment related processes. *Ecol Model*, **201**(3-4):385-397, <https://doi.org/10.1016/j.ecolmodel.2006.10.003>
- Chao, X., Jia, Y., Shields Jr., F.D., et al. (2008). Three dimensional numerical modeling of cohesive sediment transport and wind wave impact in a shallow oxbow lake. *Adv Water Resour*, **31**:1004-1014, <https://doi.org/10.1016/j.advwatres.2008.04.005>
- Chen, F., Zhang, C., Brett, M.T., et al. (2020). The importance of the wind-drag coefficient parameterization for hydrodynamic modeling of a large shallow lake. *Ecological Informatics*, **59**, <https://doi.org/10.1016/j.ecoinf.2020.101106>
- Chen, L., D'Aoust, P.M., Rennie, C.D., et al. (2019). Numerical investigation on the impact of wind-induced hydraulics on dissolved oxygen characteristics in a shallow stormwater pond. *Water Qual. Res. J.*, **54**(4):309-325, <https://doi.org/10.2166/wqrj.2019.002>
- Chen, L., Delatolla, R., D'Aoust, P.M., et al., (2019). Hypoxic conditions in stormwater retention ponds: potential for hydrogen sulfide emission, *Environmental Technology*, **40**(5):642-653, <https://doi.org/10.1080/09593330.2017.1400112>
- Chiandet, A.S., & Xenopoulos, M.A. (2016). Landscape and morphometric controls on water quality in stormwater management ponds. *Urban Ecosystems*, **19**:1645-1663. <https://doi.org/10.1007/s11252-016-0559-8>
- Chimney, M.J., Wenkert, L., & Pietro, K.C. (2006). Patterns of vertical stratification in a subtropical constructed wetland in south Florida (USA). *Ecol. Eng.* **27**(4):322-330, <https://doi.org/10.1016/j.ecoleng.2006.05.017>

- Choi, A.L., Sun, G., Zhang, Y. & Grandjean, P. (2012). Developmental fluoride neurotoxicity: a systematic review and meta-analysis. *Environmental Health Perspectives.*, **120**(10):1362-8, <https://doi.org/10.1289/ehp.1104912>
- Chung, E.G., Bombardelli, F.A., Schladow, S.G. (2009). Modeling linkages between sediment resuspension and water quality in a shallow, eutrophic, wind-exposed lake. *Ecol Model*, **220**(9-10):1251-1265, <https://doi.org/10.1016/j.ecolmodel.2009.01.038>
- City of Calgary (2005). Stormwater quality retrofit program, the City of Calgary. <https://www.calgary.ca/planning/water/stormwater-quality-retrofit-program.html> (accessed November 20, 2022).
- City of Calgary (2011). Stormwater management & design manual. Water Resources, <https://publicaccess.calgary.ca/lldm01/livelink.exe?func=ccpa.general&msgID=KTTTTqeKcW&msgAction=Download> (accessed November 20, 2022).
- City of Calgary (2022). salt management plan. Accessed January 25, 2022. Available at <https://www.calgary.ca/roads/conditions/snow-ice-salt.html>
- City of Calgary (2022). Snow and ice clearing update. Accessed August 22, 2022, from <https://www.calgary.ca/roads/conditions/snow-ice.html>
- Committee on Environment and Natural Resources (CENR). (2000). Integrated Assessment of Hypoxia in the Northern Gulf of Mexico. National Science and Technology Council, Washington, D.C
- Condie, S.A., & Webster, I.T. (2001). Estimating stratification in shallow water bodies from mean meteorological conditions. *J. Hydraul. Eng.*, **127**(4):286-292, <https://ascelibrary.org/doi/10.1061/%28ASCE%290733-9429%282001%29127%3A4%28286%29>
- Craig, P.M., Chung, D.H., Lam, N.T., et al. (2014). Sigma-Zed: A Computationally Efficient Approach to Reduce The Horizontal Gradient Error in the EFDC's Vertical Sigma Grid. Proceedings of the 11th International Conference on Hydrodynamics (ICHHD 2014), October 19 – 24, 2014, Singapore. Available at https://www.eemodelingsystem.com/wp-content/uploads/2017/08/2014-10_ICHD-Sigma-ZED_R04.pdf
- Crowther, R.A., & Hynes, H.B.N. (1977). The effect of road deicing salt on the drift of stream benthos. *Environ. Pollut.*, **14**:113-26. [https://doi.org/10.1016/0013-9327\(77\)90103-3](https://doi.org/10.1016/0013-9327(77)90103-3)
- D'Aoust, P.M., Delatolla, R., Poulain, A., et al. (2017). Emerging investigators series: hydrogen sulfide production in municipal stormwater retention ponds under ice covered conditions: a study of water quality and SRB populations. *Environ. Sci. Water Res. Tech.* **3**(4):686-698, <https://doi.org/10.1039/C7EW00117G>

- Dale, H.M., & Gillespie, T.J. (1977). The influence of submersed aquatic plants on temperature gradients in shallow water bodies. *Can. J. Bot*, **55**:2216-2225, <https://doi.org/10.1139/b77-251>
- Dane County (2022). Stormwater Manual: Management Practices, Wet pond, Available at https://danecountystormwatermanual.com/doku.php?id=wet_pond, (accessed December 08, 2022).
- Delft3D. (2022). Simulation of multi-dimensional hydrodynamic flows and transport phenomena, including sediments, User Manual, Version 4.05. Available at https://content.oss.deltares.nl/delft3d/manuals/Delft3D-FLOW_User_Manual.pdf
- Derecki, J.A. (1981). Stability effects on Great Lakes evaporation. *J Great Lakes Res* **7**(4):357-362. [https://doi.org/10.1016/S0380-1330\(81\)72064-1](https://doi.org/10.1016/S0380-1330(81)72064-1)
- Diaz, R.J., Rosenberg R. (2008) Spreading dead zones and consequences for marine ecosystems. *Science* **321**(5891):926-929, <https://doi.org/10.1126/science.115640>
- Dong, F., Mi, C., Hupfer, M., et al. (2019). Assessing vertical diffusion in a stratified lake using a three-dimensional hydrodynamic model. *Hydrological Processes*, **34**:1131-1143. <https://doi.org/10.1002/hyp.13653>
- DSI, LLC. (2020). EFDC+ Theory, Version 8.5. Published by DSI LLC, Edmonds, WA. Available at https://www.eemodelingsystem.com/wp-content/Download/Documentation/EFDC_Theory_Document_Ver_8.5_3.4.2020.pdf
- DSI, LLC. (2022). EFDC+ Theory, Version 10.3. Published by DSI LLC, Edmonds, WA. Available at https://www.eemodelingsystem.com/wp-content/Download/Documentation/EFDC_Theory_Document_Ver_10.3_2022.05.03.pdf
- Engelund, F. & Hansen, E. (1967). A Monograph on Sediment Transport in Alluvial Streams. Copenhagen, Denmark; Teknisk Forlag, Geology, Engineering, <http://resolver.tudelft.nl/uuid:81101b08-04b5-4082-9121-861949c336c9>
- Environment Canada and Health Canada (2001). Road salts: Priority Substances List Assessment Report. Canadian Environmental Protection Act, 1999. Ottawa, Ontario. Available at https://www.canada.ca/content/dam/hc-sc/migration/hc-sc/ewh-semb/alt_formats/hecs-sesc/pdf/pubs/contaminants/psl2-lsp2/road_salt_sels_voirie/road_salt_sels_voirie-eng.pdf
- Environmental Protection Agency (EPA). (2002). Methods for Measuring the Acute Toxicity of Effluents and Receiving Waters to Freshwater and Marine Organisms. U.S. Environmental Protection Agency Office of Water. Book. 5th Edition. 266 pp

- Environmental Protection Agency (EPA). (2023). Mississippi River/Gulf of Mexico Hypoxia Task Force. Web: <https://www.epa.gov/ms-htf/hypoxia-101>
- Fischer, H., List, J., Koh, C., et al. (1979). Mixing in inland and coastal waters. San Diego: Elsevier.
- Folkard, A.M., Sherborne, AJ, & Coates, M.J. (2007). Turbulence and stratification in Priest Pot, a productive pond in a sheltered environment. *Limnology*, **8**:113–120. <https://doi.org/10.1007/s10201-007-0207-3>
- Ford, P.W., Boon, P.I., and Lee, K., (2002). Methane and oxygen dynamics in a shallow floodplain lake: the significance of periodic stratification. *Hydrobiologia*, **485**:97-110, <https://doi.org/10.1023/A:1021379532665>
- Galperin, B., Kantha, L.H., Hassid, S., et al. (1988). A quasi-equilibrium turbulent energy model for geophysical flows. *J. Atmos. Sci.*, **45**(1), 55-62, [https://doi.org/10.1175/1520-0469\(1988\)045<0055:AQETEM>2.0.CO;2](https://doi.org/10.1175/1520-0469(1988)045<0055:AQETEM>2.0.CO;2)
- Garcia, M. & Parker, G. (1991). Entrainment of bed sediment into suspension. *J. Hydraul. Eng.*, **117**(4), 414-435, <https://ascelibrary.org/doi/10.1061/%28ASCE%290733-9429%281991%29117%3A4%28414%29>
- Gatch, A.J. (2019). Negative effects of sedimentation on lithophilic spawning fish embryos and methods to potentially mitigate these effects. Purdue University Graduate School. Thesis, <https://doi.org/10.25394/PGS.11253308.v1>
- German, J., Svensson, G., Gustafsson, L.G., et al. (2003). Modelling of temperature effects on removal efficiency and dissolved oxygen concentrations in stormwater ponds. *Water Sci Technol*, **48**(9):145-54. <https://doi.org/10.2166/wst.2003.0513>
- Gharabaghi, B., Fata, A., Seters T.V., et al. (2006). Evaluation of sediment control pond performance at construction sites in the greater Toronto area. *Canadian Journal of Civil Engineering*, **33**(11):1335-1344, <https://doi.org/10.1139/106-074>
- Gibbs, R.J. (1985). Estuarine flocs: their size, settling velocity and density. *J. Geophys. Res. Oceans*, **90**(C2):3249-3251, <https://doi.org/10.1029/JC090iC02p03249>
- Gong, R., Xu, L., Wang, D., et al. (2016). Water Quality Modeling for a Typical Urban Lake Based on the EFDC Model. *Environ Model Assess*, **21**:643-655, <https://doi.org/10.1007/s10666-016-9519-1>
- Gorham, E., and Boyce, F.M. (1989). Influence of lake surface area and depth upon thermal stratification and the depth of the summer thermocline. *J. Great Lakes Res.* **15**(2):233-245, [https://doi.org/10.1016/S0380-1330\(89\)71479-9](https://doi.org/10.1016/S0380-1330(89)71479-9)

- Gu, L., Dai, B., Zhu, D.Z., et al. (2017) Sediment modelling and design optimization for stormwater ponds. *Canadian Water Resources Journal / Revue canadienne des ressources hydriques*, **42**(1):70-87, <https://doi.org/10.1080/07011784.2016.1210542>
- Gulliver, J.S., Erickson, A.J., & Weiss, P.T. (editors). (2010). Stormwater treatment: Assessment and maintenance. Minneapolis, MN: University of Minnesota, St. Anthony Falls Laboratory, <http://stormwaterbook.safl.umn.edu/>
- Guo, C., Cui, Y., Dong, B., et al. (2017). Tracer study of the hydraulic performance of constructed wetlands planted with three different aquatic plant species. *Ecological Engineering*, **102**:433-442, <https://doi.org/10.1016/j.ecoleng.2017.02.040>
- Hamrick, J.M. (1992). A three-dimensional environmental fluid dynamics computer code: Theoretical and computational aspects. Technical report, Virginia Institute of Marine Science, College of William and Mary, <https://doi.org/10.21220/V5TT6C>
- Hamrick, J.M. (1996). A User's Manual for the Environmental Fluid Dynamics Computer Code (EFDC), Special Report 331. The College of William and Mary, Virginia Institute of Marine Science. 234 pp.
- Hamrick, J.M. & Wu, T.S., (1997). Computational design and optimization of the EFDC/HEM3D surface water hydrodynamic and eutrophication models. In: Delich, G., Wheeler, M.F. (Eds.), Next Generation Environmental Model and computational Methods. Society of Industrial and Applied Mathematics, Philadelphia, pp. 143–161.
- Hart, J., Tiev, V., Stovin, V., et al. (2014). The effects of vegetation on the hydraulic residence time of stormwater ponds. 21-24. Paper presented at 19th IAHR-APD Congress, Viet Nam.
- He, J., Valeo, C., & Chu, A. (2015). Variation in Water Quality of a Stormwater Pond from Diurnal Thermal Stratification. *J. water resour. hydraul. eng.*, **4**(2):181-190, [DOI:10.5963/JWRHE0402008](https://doi.org/10.5963/JWRHE0402008)
- Headley T.R. & Tanner C.C. (2012) Constructed Wetlands With Floating Emergent Macrophytes: An Innovative Stormwater Treatment Technology, *Critical Reviews in Environmental Science and Technology*, **42**(21):2261-2310, <https://doi.org/10.1080/10643389.2011.574108>
- Holland, J.F., Martin, J.F., Granata, T., et al. (2004). Effects of wetland depth and flow rate on residence time distribution characteristics. *Ecol. Eng*, **23**(3):189-203, <https://doi.org/10.1016/j.ecoleng.2004.09.003>
- Huang, A., Rao, Y.R., Lu, Y., et al. (2010). Hydrodynamic modeling of Lake Ontario: An intercomparison of three models. *J. Geophys. Res.*, **115**(C12), <https://doi.org/10.1029/2010JC006269>

- Hwang, K.N. & Mehta, A.J. (1989). Fine sediment erodibility in Lake Okeechobee, Florida. Coastal & Oceanographic Engineering Department, University of Florida.
- Imberger, J., Patterson, J.C. (1989). Physical limnology. *Adv Appl Mech*, **27**:303-475.
[https://doi.org/10.1016/S0065-2156\(08\)70199-6](https://doi.org/10.1016/S0065-2156(08)70199-6)
- Jenkins, G.A., & Greenway, M. (2005). The hydraulic efficiency of fringing versus banded vegetation in constructed wetlands. *Ecol. Eng*, **25**(1):61-72,
<https://doi.org/10.1016/j.ecoleng.2005.03.001>
- Jenter, H.J., & Schaffranek, R.W. (2003). Thermally-driven vertical mixing in the Everglades. In: Joint Conference on the Science and Restoration of the Greater Everglades and Florida Bay Ecosystem, Palm Harbor, FL, pp. 290-292.
- Ji, Z.G. & Jin, K.R. (2006). Gyres and Seiches in a Large and Shallow Lake. *Journal of Great Lakes Research*, **32**(4):764-775, [https://doi.org/10.3394/0380-1330\(2006\)32\[764:GASIAL\]2.0.CO;2](https://doi.org/10.3394/0380-1330(2006)32[764:GASIAL]2.0.CO;2)
- Ji, Z.G. & Jin, K.R. (2020). Three-Dimensional Modeling of Hydrodynamic and Water-Quality Processes in a Wetland. *J. Environ. Eng*, **146**(11):04020126
<https://ascelibrary.org/doi/abs/10.1061/%28ASCE%29EE.1943-7870.0001804>
- Ji, Z.G. (2008). Hydrodynamics and Water Quality: Modeling Rivers, Lakes, and Estuaries. John Wiley & Sons.
- Ji, Z.G. (2017). Hydrodynamics and water quality: Modeling rivers, lakes, and estuaries. 2nd ed. Hoboken, NJ: Wiley.
- Ji, Z.G., and Jin, K.R. (2014). Impacts of wind waves on sediment transport in a large, shallow lake. *Lakes and Reservoirs: Research and Management*, **19**:118-129,
<https://doi.org/10.1111/lre.12057>
- Ji, Z.G., Hamrick, J. H., & Pagenkopf, J. (2002). Sediment and Metals Modeling in Shallow River. *Journal of Environmental Engineering, American Society of Civil Engineers*, **128**(2):105-119, [https://doi.org/10.1061/\(ASCE\)0733-9372\(2002\)128:2\(105\)](https://doi.org/10.1061/(ASCE)0733-9372(2002)128:2(105))
- Ji, Z.G., Hu, G., Shen, J., Wan, Y. (2007). Three dimensional modeling of hydrodynamic processes in the St. Lucie Estuary. *Estuar. Coast. Shelf Sci.*, **73**(1-2):188-200,
<https://doi.org/10.1016/j.ecss.2006.12.016>
- Jin, K.R., & Ji, Z.G. (2001). Calibration and verification of a spectral wind-wave model for Lake Okeechobee. *Ocean Engineering*, **28**(5):571-584, [https://doi.org/10.1016/S0029-8018\(00\)00009-3](https://doi.org/10.1016/S0029-8018(00)00009-3)

- Jin, K.R., & Ji, Z.G. (2004). Case study: modeling of sediment transport and wind-wave impact in Lake Okeechobee. *J. Hydraul. Eng.*, **130**(11):1055-1067, [https://doi.org/10.1061/\(ASCE\)0733-9429\(2004\)130:11\(1055\)](https://doi.org/10.1061/(ASCE)0733-9429(2004)130:11(1055))
- Jin, K.R., & Ji, Z.G. (2005). Application and validation of three-dimensional model in a shallow lake. *J. Waterw. Port, Coast. Ocean Eng.*, **131**(5):213-225, [https://doi.org/10.1061/\(ASCE\)0733-950X\(2005\)131:5\(213\)](https://doi.org/10.1061/(ASCE)0733-950X(2005)131:5(213))
- Jin, K.R., & Ji, Z.G. (2013). A long term calibration and verification of a submerged aquatic vegetation model for Lake Okeechobee. *Ecological Processes*, **2**, 23. <https://doi.org/10.1186/2192-1709-2-23>
- Jin, K.R., & Ji, Z.G. (2015). An integrated environment model for a constructed wetland – Hydrodynamics and transport processes. *Ecol. Eng.*, **84**:416-426, <https://doi.org/10.1016/j.ecoleng.2015.09.022>
- Jin, K.R., Hamrick, J. H., & Tisdale, T. (2000). Application of Three-Dimensional Hydrodynamic Model for Lake Okeechobee. *J. Hydraul. Eng.*, **126**(10):758-771, [https://doi.org/10.1061/\(ASCE\)0733-9429\(2000\)126:10\(758\)](https://doi.org/10.1061/(ASCE)0733-9429(2000)126:10(758))
- Jin, K.R., Ji, Z.-G., & James, R.T. (2007). Three-dimensional water quality and SAV modeling of a large shallow lake. *J. Great Lakes Res.*, **33**(1):28-45, [https://doi.org/10.3394/0380-1330\(2007\)33\[28:TWQASM\]2.0.CO;2](https://doi.org/10.3394/0380-1330(2007)33[28:TWQASM]2.0.CO;2)
- Jørgensen, S. E., & Fath, B.D. (2011). Fundamentals of ecological modelling, applications in environmental management and research, Amsterdam: Elsevier Science, Developments in Environmental Modelling. Book, 4th ed, 399 pp
- Józsa, J. (2014). On the internal boundary layer related wind stress curl and its role in generating shallow lake circulations. *J. Hydrol. Hydromech.*, **62**(1):16-23, <https://doi.org/10.2478/johh-2014-0004>
- Kadlec, R.H., & Knight, R.L. (1996). Treatment Wetlands. Boca Raton: Lewis Publishers, 893 pp.
- Kalff, J. (2002). Limnology. Inland Water Ecosystems. Prentice Hall, Upper Saddle River. New Jersey. 592 pp
- Katsaros, K.B. (1998). Turbulent flux of water vapor in relation to the wave field and atmospheric stratification. In: Imberger J (ed) Physical processes in lakes and oceans. American Geophysical Union, Washington, DC, pp 37–46, <https://doi.org/10.1029/CE054p0037>

- Kellner, E., & Pires, E.C. (2002). The influence of thermal stratification on the hydraulic behavior of waste stabilization ponds. *Water Sci Technol*, **45**(1):41-48, <https://doi.org/10.2166/wst.2002.0006>
- Kjaraan, S.P., Holm, S.L., Myer, E.M. (2004). Lake circulation and sediment transport in Lake Myvatn. *Aquat Ecol*, **38**:145-162, <https://doi.org/10.1023/B:AECO.0000032049.94886.5a>
- Lake Simcoe Region Conservation Authority. (2010). Stormwater Pond Maintenance and Anoxic Conditions Investigation - FINAL REPORT. https://www.lsrca.on.ca/Shared%20Documents/reports/stormwater_maintenance.pdf
- Larm, T., & Alm, H. (2014). Revised design criteria for stormwater facilities to meet pollution reduction and flow control requirements, also considering predicted climate effects. *Water Pract. Technol.*, **9**(1):9-19, <https://doi.org/10.2166/wpt.2014.002>
- Lee, C., Schwab, D.J., Hawley, N. (2005). Sensitivity analysis of sediment resuspension parameters in coastal area of southern Lake Michigan. *J Geophys Res*, **110**, <https://doi.org/10.1029/2004JC002326>
- Lee, H., Chung, S., Ryu, I., et al. (2013). Three-dimensional modeling of thermal stratification of a deep and dendritic reservoir using ELCOM model. *J Hydro-Environ Res* **7**(2):124-133, <https://doi.org/10.1016/j.jher.2012.10.002>
- Li, M., Zhang, H., Lemckert, C., et al. (2013). Three-dimensional Investigation of Retention Time Distribution of Waste Stabilisation Ponds. 20th International Congress on Modelling and Simulation, Adelaide, Australia, 1–6 December 2013, <https://doi.org/10.36334/modsim.2013.L9.li>
- Liu, W.C., Chan, W.T. & Tsai, D.DW. (2016). Three-dimensional modeling of suspended sediment transport in a subalpine lake. *Environ Earth Sci*, **75**(2), <https://doi.org/10.1007/s12665-015-5069-0>
- Lv, C., Zhang, F., Liu, Z., et al. (2013). Three-dimensional numerical simulation of sediment transport in Lake Tai based on EFDC model. *J Food Agric Environ*, **11**(2):1343-1348.
- MacIntyre, S., Crowe, A.T., Cortes, A., et al. (2018). Turbulence in a small arctic pond. *Limnol. Oceanogr.*, **63**:2337-2358. <https://doi.org/10.1002/lno.10941>
- MacIntyre, S., Fram, J.P., Kushner, P.J., et al. (2009). Climate-related variations in mixing dynamics in an Alaskan arctic lake. *Limnol. Oceanogr.*, **54**:2401-2417, https://doi.org/10.4319/lo.2009.54.6_part_2.2401
- Marsalek, J. (2003). Road salts in urban stormwater: An emerging issue in stormwater management in cold climates. *Water Science and Technology*, **48**(9):61-70, <https://doi.org/10.2166/wst.2003.0493>

- Marsalek, P., Watt, W.E., Marsalek, J., et al. (2000). Winter flow dynamics of an on-stream stormwater management pond. *Water Qual Res J Can*, **35**(3):505-523, <https://doi.org/10.2166/wqrj.2000.030>
- Mayer, T., Rochfort, Q., Borgmann, U., et al. (2008). Geochemistry and toxicity of sediment porewater in a salt-impacted urban stormwater detention pond. *Environmental Pollution*, **156**(1):143-151, <https://doi.org/10.1016/j.envpol.2007.12.018>
- Mazda, Y., Magi, M., Ikeda, Y., et al., (2006). Wave reduction in a mangrove forest dominated by *Sonneratia* sp. *Wetlands Ecology and Management*. **14**(4): 365–378, <https://doi.org/10.1007/s11273-005-5388-0>
- McEnroe, N.A., Buttle, J.M., Marsalek, J. et al. (2013). Thermal and chemical stratification of urban ponds: Are they 'completely mixed reactors'?. *Urban Ecosystems*, **16**:327-339. <https://doi.org/10.1007/s11252-012-0258-z>
- Megahan, W.F. (1999). Sediment, sedimentation. In: *Environmental Geology. Encyclopedia of Earth Science*. Springer, Dordrecht, https://doi.org/10.1007/1-4020-4494-1_296
- Mehta, A.J., Hayter, E.J., Parker, W.R., et al., (1989). Cohesive sediment transport. i: Process description. *J. Hydraul. Eng.*, **115**(8), 1076-1093, <https://ascelibrary.org/doi/abs/10.1061/%28ASCE%290733-9429%281989%29115%3A8%281076%29>
- Melbourne Water, 2017. Design, construction and establishment of constructed wetlands: design manual. Retrieved from <https://www.melbournewater.com.au/building-and-works/developer-guides-and-resources/standards-and-specifications/constructed-wetlands>
- Mellor, G.L. & Yamada, T. (1982). Development of a turbulence closure model for geophysical fluid problems. *Rev. Geophys.*, **20**(4):851-875, <https://doi.org/10.1029/RG020i004p00851>
- Mellor, G.L., & Blumberg, A.F. (1985). Modelling vertical and horizontal diffusivities with the sigma coordinate system, *Mon. Weather Rev.*, **113**(8):1380-1383, [https://doi.org/10.1175/1520-0493\(1985\)113<1379:MVAHDW>2.0.CO;2](https://doi.org/10.1175/1520-0493(1985)113<1379:MVAHDW>2.0.CO;2)
- MIKE Powered by DHI (2023). MIKE 3 Flow Model FM, Hydrodynamic Module User Guide. Available at https://manuals.mikepoweredbydhi.help/latest/Coast_and_Sea/MIKE_FM_HD_3D.pdf
- Nakhaei, N., Boegman, L., Mehdizadeh, M., et al. (2019). Hydrodynamic modeling of Edmonton stormwater ponds. *Environ Fluid Mech*, **19**:305-327. <https://doi.org/10.1007/s10652-018-9625-5>

- Nakhaei, N., Boegman, L., Mehdizadeh, M., et al. (2021). Three-dimensional biogeochemical modeling of eutrophication in Edmonton stormwater ponds. *Ecol. Modell.*, **456**.
<https://doi.org/10.1016/j.ecolmodel.2021.109684>
- Nasiha, H. J., & Shanmugam, P. (2018). Estimation of settling velocity of sediment particles in estuarine and coastal waters. *Estuarine, Coastal and Shelf Science*, **203**:59-71,
<https://doi.org/10.1016/j.ecss.2018.02.001>
- Nezu, I. (1993). Turbulence in open-channel flows. IAHR-monograph.
- Novotny, E.V & Stefan, H.G. (2012). Road Salt Impact on Lake Stratification and Water Quality. *Journal of Hydraulic Engineering*, **138**(12):1069-1080,
[https://doi.org/10.1061/\(ASCE\)HY.1943-7900.0000590](https://doi.org/10.1061/(ASCE)HY.1943-7900.0000590)
- Novotny, E.V, Murphy, D., & Stefan, H.G. (2008). Increase of urban lake salinity by road deicing salt. *Science of The Total Environment*, **406**(1-2):131-144,
<https://doi.org/10.1016/j.scitotenv.2008.07.037>
- Oberts, G.L. (2003). Cold climate BMPs: solving the management puzzle. *Water Science and Technology* **48**(9): 21–32. <https://doi.org/10.2166/wst.2003.0483>
- Olding, D.D., Hellebust, J.A., & Douglas, M.S.V. (2000). Phytoplankton community composition in relation to water quality and water-body morphometry in urban lakes, reservoirs, and ponds. *Canadian Journal of Fisheries and Aquatic Sciences*, **57**(10): 2163–2174, <https://doi.org/10.1139/f00-176>
- Ontario Ministry of the Environment. (2003). Stormwater Management Planning and Design Manual. Ministry of Environment, Ontario. Available at
<https://www.ontario.ca/document/stormwater-management-planning-and-design-manual-0>
- Passos, R.G., von Sperling, M., & Ribeiro, T.B. (2014). Hydrodynamic evaluation of a full-scale facultative pond by computational fluid dynamics (CFD) and field measurements. *Water Sci Technol*, **70**(3):569-575, <https://doi.org/10.2166/wst.2014.265>
- Paturi, S., Boegman, L., & Rao, Y.R. (2012). Hydrodynamics of eastern Lake Ontario and the upper St. Lawrence River. *J. Gt. Lakes Res*, **38**(4):194-204,
<https://doi.org/10.1016/j.jglr.2011.09.008>
- Persson, J., Somes, N.L.G., Wong, T.H.F. (1999). Hydraulics efficiency of constructed wetlands and ponds. *Water Sci. Technol*, **40** (3), 291-300, [https://doi.org/10.1016/S0273-1223\(99\)00448-5](https://doi.org/10.1016/S0273-1223(99)00448-5)
- Reed, R.K. (1977). On estimating insolation over the ocean. *J Phys Oceanogr*, **7**(3):482–485,
[https://doi.org/10.1175/1520-0485\(1977\)007<0482:OEIOTO>2.0.CO;2](https://doi.org/10.1175/1520-0485(1977)007<0482:OEIOTO>2.0.CO;2)

- Rey, A., Mulligan, R., Ferreira da Silva, A.M., et al. (2020). Three-Dimensional Hydrodynamic Behavior of an Operational Waste-Stabilization Pond. *Journal of Environmental Engineering*, **147**(2), [https://doi.org/10.1061/\(ASCE\)EE.1943-7870.0001834](https://doi.org/10.1061/(ASCE)EE.1943-7870.0001834)
- Rey, A.J.M., Mulligan, R.P., Filion, Y., et al. (2021). Temperature Stratification in an Operational Waste-Stabilization Pond. *Journal of Environmental Engineering*, **147**(6), [https://doi.org/10.1061/\(ASCE\)EE.1943-7870.0001876](https://doi.org/10.1061/(ASCE)EE.1943-7870.0001876)
- Rosati, A. & Miyakoda, K. (1988). A general circulation model for upper ocean simulation. *Journal of Physical Oceanography*, **18**(11):1601-1626, [https://doi.org/10.1175/1520-0485\(1988\)018<1601:AGCMFU>2.0.CO;2](https://doi.org/10.1175/1520-0485(1988)018<1601:AGCMFU>2.0.CO;2)
- Rouse, W.R. (2000) The energy and water balance of high-latitude wetlands: controls and extrapolation. *Glob Change Biol*, **6**(S1):59–68, <https://doi.org/10.1046/j.1365-2486.2000.06013.x>
- Rouse, W.R., Oswald, C.M., Binyamin, J., et al. (2003). Interannual and seasonal variability of the surface energy balance and temperature of central Great Slave Lake. *Journal of Hydrometeorology*, **4**(4):720-730, [https://doi.org/10.1175/1525-7541\(2003\)004<0720:IASVOT>2.0.CO;2](https://doi.org/10.1175/1525-7541(2003)004<0720:IASVOT>2.0.CO;2)
- Rousseau, D., Lesage, E., Story, A., Vanrolleghem, P., De Pauw, N. (2008). Constructed wetlands for water reclamation. *Desalination*, **218**:181-189, <https://doi.org/10.1016/j.desal.2006.09.034>
- Schulz, R., & Peal, S.K.C, (2001). Effectiveness of a constructed wetland for retention of nonpoint-source pesticide pollution in the Lourens River catchment, South Africa. *Environmental Science and Technology*, **35**:422–426. <https://doi.org/10.1021/es0001198>
- Schwammburger, P.F., Yule, C.M., & Tindale, N.W. (2020). Rapid plant responses following relocation of a constructed floating wetland from a construction site into an urban stormwater retention pond. *Science of The Total Environment*, **699**, <https://doi.org/10.1016/j.scitotenv.2019.134372>
- Semadeni-Davies, A., & Semadeni-Davies, A. (2006). Winter performance of an urban stormwater pond in southern Sweden. *Hydrological Processes*, **20**(1):165-182, <https://doi.org/10.1002/hyp.5909>
- Shammaa, Y., Zhu, D.Z., Gyurek, L., et al. (2002). Effectiveness of dry ponds for stormwater total suspended solids removal. *Canadian Journal of Civil Engineering*, **29**(2), <https://doi.org/10.1139/102-008>
- Shaw, J., Watt, W., Marsalek, J., et al. (1997). Flow pattern characterization in an urban stormwater detention pond and implications for water quality. *Water Quality Research Journal of Canada*, **32**(1):53-71, <https://doi.org/10.2166/wqrj.1997.005>

- She, Y., Kemp, J., Richards, L., et al. (2016). Investigation into freezing point depression in stormwater ponds caused by road salt. *Cold Regions Science and Technology*, **131**:53-64, <https://doi.org/10.1016/j.coldregions.2016.09.003>
- Shilton, A., & Harrison, J. (2003). Guidelines for the Hydraulic Design of Waste Stabilization Ponds. Institute of Technology and Engineering, Massey University, Palmerston North, New Zealand.
- Shin, S., Her, Y., Song, J., & Kang, M. (2019). Integrated sediment transport process modeling by coupling Soil and Water Assessment Tool and Environmental Fluid Dynamics Code. *Environ. Model. Softw.*, **116**:26-39, <https://doi.org/10.1016/j.envsoft.2019.02.002>
- Shrestha, P.L. & Orlob, G.T. (1996). Multiphase distribution of cohesive sediments and heavy metals in estuarine systems. *J. Environ. Eng.*, **122**(8), 730-740, <https://ascelibrary.org/doi/10.1061/%28ASCE%290733-9372%281996%29122%3A8%28730%29>
- Singh, P., Bagrania, J. & Haritash, A.K. (2019). Seasonal behaviour of thermal stratification and trophic status in a sub-tropical Palustrine water body. *Appl Water Sci* **9**, 139, <https://doi.org/10.1007/s13201-019-1011-z>
- Smagorinsky, J. (1963). General circulation experiments with the primitive equations: I. the basic experiment. *Monthly weather review*, **91**(3):99-164, [https://doi.org/10.1175/1520-0493\(1963\)091<0099:GCEWTP>2.3.CO;2](https://doi.org/10.1175/1520-0493(1963)091<0099:GCEWTP>2.3.CO;2)
- Smith, J.D. & McLean, S. (1977). Spatially averaged flow over a wavy surface. *J. Geophys. Res.*, **82**(12):1735-1746, <https://doi.org/10.1029/JC082i012p01735>
- Somes, N., Warwick, L.G., Bishop, A., et al. (1999). Numerical simulation of wetland hydrodynamics. *Environ. Int.*, **25**(6):773-779, [https://doi.org/10.1016/S0160-4120\(99\)00058-6](https://doi.org/10.1016/S0160-4120(99)00058-6)
- Song, K., Xenopoulos, M.A., Buttle, J.M., et al. (2013). Thermal stratification patterns in urban ponds and their relationships with vertical nutrient gradients. *J. Environ. Manage.*, **127**:317-323, <https://doi.org/10.1016/j.jenvman.2013.05.052>
- Song, K., Xenopoulos, M.A., Marsalek, J., et al. (2015). The Fingerprints of Urban Nutrients: Dynamics of Phosphorus Speciation in Water Flowing through Developed Landscapes. *Biogeochemistry*, **125**(1):1-10, <https://doi.org/10.1007/s10533-015-0114-3>
- Stefan, H.G, Hondzo, M., Fang, X., et al. (1996). Simulated long-term temperature and dissolved oxygen characteristics of lakes in the north-central United States and associated fish habitat limits. *Limnol. Oceanogr.*, **41**(5):1124-1135, <https://doi.org/10.4319/lo.1996.41.5.1124>

- Stewart, F., Mulholland, T., Cunningham, A., et al. (2008). Floating islands as an alternative to constructed wetlands for treatment of excess nutrients from agricultural and municipal wastes - results of laboratory-scale tests. *Land Contam. Reclam.* **16**:25-33, <https://scholarworks.montana.edu/xmlui/handle/1/13182>
- Su, T.-M., Yang, S.-C., Shih, S.-S., et al. (2009). Optimal design for hydraulic efficiency performance of free-water-surface constructed wetlands. *Ecol. Eng.* **35**, (8), 1200-1207, <https://doi.org/10.1016/j.ecoleng.2009.03.024>
- Swistock, B. (2016). Interpreting water tests for ponds and lakes. State College: The Pennsylvania State University.
- Takamatsu, M., Barrett, M., & Charbeneau, R.J. (2010). Hydraulic model for sedimentation in stormwater detention basins. *Journal of Environmental Engineering*, **136** (5):527- 534, [https://doi.org/10.1061/\(ASCE\)EE.1943-7870.0000175](https://doi.org/10.1061/(ASCE)EE.1943-7870.0000175)
- Tanner, C., Sukias, J., Park, J., et al. (2011). Floating Treatment Wetlands: A New Tool for Nutrient Management in Lakes and Waterways. National Institute of Water and Atmospheric Research (NIWA), Auckland, New Zealand.
- Teichreb, C. (2012). Lake and Watershed Management Options for the Control of Nuisance Blue-Green Algal Blooms in Pigeon Lake, Alberta/Prepared by Chris Teichreb. In [Edmonton]: Alberta Environment and Sustainable Resource Development, [2012].
- Tetra Tech. (2002). Theoretical and computational aspects of sediment and contaminant transport in the efcd model. Technical report, US Environmental Protection Agency.
- Torres A., Kouyi, G.L., Bertrand-Krajewski, J.L., et al. (2008). Modelling of hydrodynamics and solid transport in a large stormwater detention and settling basin. In 11th International Conference on Urban Drainage, ICUD, Edinburgh, Scotland, UK, August 31-September 5, 2008.
- Torres, J.J., Soler, A.J. & Ortuno, J.F. (1997). Hydraulic performance of a deep wastewater stabilization pond. *Wat.Res.*, **31**(4), 679–688, [https://doi.org/10.1016/S0043-1354\(96\)00293-X](https://doi.org/10.1016/S0043-1354(96)00293-X)
- Troitsky, B., Zhu, D.Z., Loewen, M., et al. (2019). Nutrient processes and modeling in urban stormwater ponds and constructed wetlands, *Canadian Water Resources Journal / Revue canadienne des ressources hydriques*, <https://doi.org/10.1080/07011784.2019.1594390>
- U.S. Environmental Protection Agency (USEPA). (1999). Protocol for Developing Sediment TMDLs. Office of Water (4503F). U.S. Environmental Protection Agency, Washington, DC.

- U.S. Environmental Protection Agency (USEPA). (1983). Results of the nationwide urban runoff program, volume I- final report. NTIS PB84-185552. U.S. Environmental Protection Agency, Washington, DC.
- Van Buren, M.A., Watt, W.E., Marsalek, J., et al. (2000). Thermal enhancement of stormwater runoff by paved surfaces. *Water Res*, **34**(4):1359-1371, [https://doi.org/10.1016/S0043-1354\(99\)00244-4](https://doi.org/10.1016/S0043-1354(99)00244-4)
- van Rijn, L.C. (1984). Sediment transport, part ii: suspended load transport. *J. Hydraul. Eng.*, **110**(11):1613-1641, <https://ascelibrary.org/doi/10.1061/%28ASCE%290733-9429%281984%29110%3A11%281613%29>
- Vaze, J., Chiew, F.H.S. (2004) Nutrient loads associated with different sediment sizes in urban stormwater and surface pollutants. *J Environ Eng ASCE*, **130**(4):391-396, [https://doi.org/10.1061/\(ASCE\)0733-9372\(2004\)130:4\(391\)](https://doi.org/10.1061/(ASCE)0733-9372(2004)130:4(391))
- Verburg, P., & Antenucci, J.P. (2010). Persistent unstable atmospheric boundary layer enhances sensible and latent heat loss in a tropical great lake: lake Tanganyika. *Journal of Geophysical Research: Atmospheres*, **115**(D11), <https://doi.org/10.1029/2009JD012839>
- Wahl, M.D., Brown, L.C., Soboyejo, A.O., et al. (2010). Quantifying the hydraulic performance of treatment wetlands using the moment index. *Ecol.Eng.* **36**(1):1691-1699, <http://dx.doi.org/10.1016/j.ecoleng.2010.07.014>
- Wakelin, S.C., Elefsiniotis, P., & Wareham, D. G. (2003). Assessment of stormwater retention basin water quality in Winnipeg, Canada. *Water Quality Research Journal of Canada*, **38**(3): 433-450, <https://doi.org/10.2166/wqrj.2003.028>
- Wan, Y., Ji, Z., Shen, J., et al. (2012). Three dimensional water quality modeling of a shallow subtropical estuary. *Marine environmental research*, **82**:76-86, <https://doi.org/10.1016/j.marenvres.2012.09.007>
- Wand, H., Vacca, G., Kusch, P., Krüger, M., Kästner, M. (2007). Removal of bacteria by filtration in planted and non-planted sand columns. *Water Res.* **41**:159-167, <https://doi.org/10.1016/j.watres.2006.08.024>
- Wang, C., Shen, C., Wang, P.F., et al. (2013). Modeling of sediment and heavy metal transport in Taihu lake, China. *J Hydrodyn*, **25**(3):387–397, [https://doi.org/10.1016/S1001-6058\(11\)60376-5](https://doi.org/10.1016/S1001-6058(11)60376-5)
- Wei, Z., & Miyano, A. (2016). Drag and Bulk Transfer Coefficients OverWater Surfaces in Light Winds. *Boundary-Layer Meteorol*, **160**:319-346, <https://doi.org/10.1007/s10546-016-0147-8>
- Wetzel, R.G. (2001). Limnology : lake and river ecosystems, Academic Press.

- Winston, R.J., Hunt, W., Kennedy, S.G., et al. (2013). Evaluation of floating treatment wetlands as retrofits to existing stormwater retention ponds. *Ecol. Eng.* **54**:254-265, <https://doi.org/10.1016/j.ecoleng.2013.01.023>
- Wu, W., & Vieira, D.A. (2002). One-Dimensional Channel Network Model CCHE1D Version 3.0 – Technical Manual, Technical Report No. NCCHE-TR-2002-1, National Center for Computational Hydroscience and Engineering, University of Mississippi, USA.
- Wu, W., Wang, S.Y., & Jia, Y. (2000). Nonuniform sediment transport in alluvial rivers. *J. Hydraul. Res.*, **38**(6):427-434, <https://doi.org/10.1080/00221680009498296>
- WWEI & GCI. (2017). International Stormwater Best Management Practices (BMP) Database 2016 Summary Statistics.
- Yadav, A., Kataria, A., Singh, K., et al., (2015). Seasonal Assessment of Trophic State of a Palustrine Water Body, INTERNATIONAL JOURNAL OF ENGINEERING RESEARCH & TECHNOLOGY (IJERT) RACEE, **4**(3), 37-40, <https://www.ijert.org/seasonal-assessment-of-trophic-state-of-a-palustrine-water-body>
- Yang, F., Gato-Trinidad, S., & Hossain, I. (2022). New insights into the pollutant composition of stormwater treating wetlands. *Science of the Total Environment*, **827**, <https://doi.org/10.1016/j.scitotenv.2022.154229>
- Yang, Y., Wang, Y., Zhang, Z. et al. (2018). Diurnal and Seasonal Variations of Thermal Stratification and Vertical Mixing in a Shallow Fresh Water Lake. *J Meteorol Res*, **32**, 219-232, <https://doi.org/10.1007/s13351-018-7099-5>
- Yang, Z., & Hamrick, J.M. (2003). Variational inverse parameter estimation in a cohesive sediment transport model: An adjoint approach. *J. Geophys. Res. Oceans*, **108**, <https://doi.org/10.1029/2002JC001423>
- Yuan, F. (2008). Land cover change and environmental impact analysis in the Greater Mankato area of Minnesota using remote sensing and GIS modelling. *International Journal of Remote Sensing*, **29**(4):1169-1184, <https://doi.org/10.1080/01431160701294703>
- Ziegler, C.K. & Nisbet B. (1995). Long-term simulation of fine-grained sediment transport in large reservoir. *J. Hydraul. Eng.*, **121**(11), 773-781, <https://ascelibrary.org/doi/10.1061/%28ASCE%290733-9429%281995%29121%3A11%28773%29>
- Ziegler, C.K. & Nisbet, B. (1994). Fine-grained sediment transport in Pawtuxet river, Rhode island. *J. Hydraul. Eng.*, **120**(5), 561-576, <https://ascelibrary.org/doi/10.1061/%28ASCE%290733-9429%281994%29120%3A5%28561%29>